hhu

Heinrich Heine
University Düsseldorf

Metabolic investigations in patients
with hepatic encephalopathy
by magnetic resonance imaging and spectroscopy

Inaugural Dissertation

aus dem Institut für klinische Neurowissenschaften und medizinische Psychologie
der Heinrich-Heine-Universität Düsseldorf

Meinen Eltern.

Danksagung

Mein außerordentlicher und herzlichster Dank gilt Prof. Dr. Alfons Schnitzler, für die Möglichkeit meine Arbeit an seinem Institut anzufertigen. Die ausgezeichnete wissenschaftliche Unterstützung sowie die Ermutigung und Fürsprache während der Einwerbung von externen Förderungen, waren bei der Erstellung dieser Dissertation ein grundlegender Rückhalt.

Weiterhin bedanke ich mich bei Prof. Dr. Thomas Heinzel für die Übernahme der Mentoren Rolle meiner Dissertation und für die nützliche Unterstützung während der Anmeldung und Eröffnung des Promotionsverfahrens.

Prof. Dr. Dieter Häussinger ist an dieser Stelle für die Möglichkeit in einem etablierten Sonderforschungsbereich arbeiten zu können und für die infrastrukturelle Bereitstellung der benötigten Patienten zu danken.

Prof. Dr. Gerald Antoch ist für die Einbindung meines Arbeitsplatzes in die Infrastruktur des Instituts für Diagnostische und Interventionelle Radiologie, ohne die die Durchführung dieses Projekts nicht möglich gewesen wäre zu danken.

Meine besondere Wertschätzung gilt Prof. Dr. Hans-Jörg Wittsack, der in den letzten 7 Jahren ein immerwährender und vorbildhafter Quell von genialen fachlichen Impulsen und trockenem Humor gewesen ist, was ein wesentlicher Leitfaden für meine persönliche und wissenschaftliche Entwicklung darstellte.

Ebenso besonderer Dank gilt auch PD Dr. Markus Butz. Auch Ihn zeichnet die Kombination aus wissenschaftlicher Kompetenz und humorvoller Persönlichkeit aus, welche nicht selbstverständlich ist. Die lückenlose Erreichbarkeit, unerschütterlicher Optimismus, lektorische Unterstützung und persönliche Aufmunterung waren wesentlich am Erfolg der Arbeit beteiligt. Das Zusammenspiel aus freier Entwicklung und nötiger Impulse zur gegebenen Zeit sowie der täglich zelebrierte Gruß auf dem Weg zur Mensa sind vorbildlicher Weise zu erwähnen.

In der Reihe bilderbuchartiger Mentoren darf natürlich Dr. Georg Oeltzschner nicht fehlen. Als Betreuer meiner früheren wissenschaftlichen Arbeiten hat er maßgeblich zu meinem Werdegang beigetragen. Ihm verdanke ich auch den Initalkontakt zum Institut für klinische Neurowissenschaften. In den letzten 4 Jahren hat er sich als Tele-Mentor meiner Arbeit durch fachliche, lektorische und persönliche Tipps besonders eingebracht und mir auch den Zugang in das Netzwerk der Wissenschaft maßgeblich erleichtert. Nicht unerwähnt sollten hier auch die kreativen Pausen beim Zusammentreffen auf wissenschaftlichen Tagungen sein, die uns von der Pazifikküste Kanadas bis an das karibische Meer von Mexico brachten.

Author's Declaration

I, Helge Jörn Zöllner, hereby declare, that the work for my dissertation

Metabolic investigations in patients with hepatic encephalopathy by magnetic resonance imaging and spectroscopy

was realized independently and without using illicit help. Only the declared sources have been used, and all direct and analogous quotes have been marked as such. The work has not been submitted in identical or similar variety at any other institution. This is my first attempt at acquiring a doctoral degree.

Düsseldorf, September 26th 2019

HELGE JÖRN ZÖLLNER

Contents

First Authorships

H. J. Zöllner, M. Butz, G. Kircheis, S. Klinker, D. Häussinger, B. Schmitt, A. Schnitzler, and H.-J. Wittsack. "Ammonia-weighted imaging by chemical exchange saturation transfer MRI at 3 T". In: *NMR in Biomedicine* 31.9 (2018), e3947. DOI: 10.1002/nbm.3947.

H. J. Zöllner, M. Butz, M. Jördens, N.-D. Füllenbach, D. Häussinger, B. Schmitt, H.-J. Wittsack, and A. Schnitzler. "Chemical exchange saturation transfer imaging in hepatic encephalopathy". In: *NeuroImage: Clinical* 22 (2019), p. 101743. DOI: 10.1016/j.nicl.2019.101743.

H. J. Zöllner, G. Oeltzschner, A. Schnitzler, and H.-J. Wittsack. "In silico GABA+ MEGA-PRESS: Effects of signal-to-noise ratio and linewidth on modeling the 3-ppm GABA+ resonance". In: *NMR in Biomedicine, under review* (2019).

This dissertation is based on these publications. Personal contributions and impact factors are listed in Appendix B.

Abstract

Hepatic encephalopathy (HE) is a neuropsychiatric disease and a common complication in liver cirrhosis. Several pathogenetic concepts of HE have been proposed in the literature, yet the interplay between those concepts remain a matter of debate. A key factor is attributed to dysfunctional hepatic clearance of neurotoxins in particular, ammonia and its subsequent accumulation in the brain. The neurotransmitter balance in the brain is altered during the detoxification of ammonia, and in consequence, the cognitive, visual, sensorimotor, and eye-hand coordination abilities are hampered. These changes vary from subtle attention and motor deficits to flapping tremor, stupor, and in extreme cases, hepatic coma.

To further explore the mechanisms of HE, this dissertation describes improvements of magnetic resonance (MR) imaging and spectroscopy methods to gather metabolic information from brain tissue. In the process, a brain ammonia- or HE-sensitive MR imaging method was established. Thus, the metabolic MR imaging technique chemical exchange saturation transfer (CEST) was optimized for ammonia sensitivity, and subsequently applied in a clinically well-defined cohort of HE patients. Additionally, a simulation framework was designed to investigate limitations in the analysis of γ-aminobutyric acid (GABA)+ due to signal-to-noise ratio (SNR) and linewidth constraints during the acquisition of GABA-edited magnetic resonance spectroscopy (MRS) in deep brain regions. Finally, the neurometabolism in the cerebello-thalamo-cortical pathway of HE patients was investigated with GABA-edited MRS.

For the CEST optimization, several model solutions (ammonia, BSA + ammonia & tissue homogenate + ammonia) with varying ammonia concentrations were used to find optimal saturation parameters for an ammonia-weighted contrast. To scrutinize the mechanisms underlying the CEST experiments, protein denaturation and aggregation were assessed in the BSA sample. Finally, the optimal parameters were determined and tested in a healthy control and two patients suffering from HE.

In agreement with literature, it was found that amide proton transfer-weighted (APT$_w$) CEST contrast changes in the model solutions were introduced through protein denaturation mediated by ammonia, and an ammonia-sensitive MR imaging contrast was therefore established.

In a subsequent study, further phantom measurements revealed ammonia to be the primary driver of the observed contrast changes, while changes associated with other neurometabolites were negligible. In an application study, a cohort of 14 healthy controls, 10 minimal HE and 10 manifest

HE patients underwent computer neuropsychometry, critical flicker frequency (CFF) measurements, and blood sample testing prior to the CEST imaging. The processing pipeline of the CEST data included movement correction, magnetization transfer ratio asymmetry (MTR_{asym}) analysis, B_0- and B_1-correction as well as normalization to minimize possible confounders of the CEST effect. Finally, all MTR_{asym} datasets were normalized to a template (created from the study cohort) to establish pixel-based group statistics over the whole brain volumes.

A reduction of APT_w signals was found in the cerebellum and the occipital cortex of manifest HE patients. These reduction correlated with blood ammonia levels, as well as several neuropsychometric scores, including motor performance and reaction times. Additionally, increased APT_w signals were associated with individual CFF, and thalamic APT_w signal alterations were linked to gamma-glutamyltransferase levels.

This *in vivo* study showed patterns and correlations previously found in $^{13}NH_3$-positron emission tomography (PET) studies [1], which supports the interpretation that APT_w imaging is sensitive to ammonia concentrations. The presented results substantiate literature findings on the involvement of the cerebellum in HE, which is proposed to be involved in motor skill deterioration in HE patients. Additionally, neurotransmitter level alterations, slowed neural oscillations, and decreased visual performance are a common finding in HE, potentially linked to ammonia detoxification in the visual cortex.

In the future, the implementation of more advanced CEST techniques may allow to better distinguish underlying contributions - e.g. from CEST mediated by ammonia and contributions from nuclear Overhauser enhancement (NOE) mediated by hepatocerebral degeneration.

In vivo MR spectroscopy suffers from low SNR and poor linewidth, resulting in overlapping metabolic resonances. To investigate the impact of spectral quality on data modeling, a nearly noise-free template spectrum was created as the mean of 48 *in vivo* data sets. Several line broadening and noise level combinations were used to create different scenarios of B_0 homogeneity and GABA+ SNR by manipulating template. 100 spectra per condition were quantified with two commonly used MRS quantification tools (Gannet 3.0 and Tarquin). The GABA+ estimation error was quantified as the relative difference between the known modeled GABA+ resonance in the template spectrum, and the modeled GABA resonance of the manipulated spectra. Furthermore, fit error, standard deviation, and the number of rejected spectra were calculated for each combination, and the agreement between the simulations and two *in vivo* scenarios with varying linewidth and the GABA+ SNR was quantified.

The GABA+ estimation error was found to be below 5 % over the entire range of GABA+ SNR for medium linewidth (9.7 Hz) for Gannet 3.0 or all linewidth expect 10.6 Hz for Tarquin. The

standard deviation over 100 measurements varied between 3.1 and 17 % for Gannet 3.0 and between 1 and 11 % for Tarquin over the *in vivo* relevant GABA+ SNR range between 26 and 3.5.

The results are in line with other studies on the impact of SNR on the quantification of GABA+. Simulations and *in vivo* scenarios showed good agreement. The results suggest that GABA-edited studies can be realized for voxels with low GABA+ SNR at the cost of higher group-level variance. Furthermore, B_0 homogeneity had negligible effects on the GABA+ modeling. Also, the developed simulation framework could be used to test other quantification approaches.

In a final study, the neurometabolism in the cerebello-thalamo-cortical pathway of HE patients was investigated with GABA-edited spectroscopy. The voxels were designed based on the implications drawn from the previous simulation study. The cohort included 16 healthy controls and 16 HE patients (2 minimal HE, 14 HE I), who were assessed via CFF testing, Grooved PEG board testing for motor performance, and blood sample testing. GABA-edited MEscher-GArwood Point RESolved Spectroscopy (MEGA-PRESS) MRS was employed in the cerebellum, the thalamus, and the motor cortex. The GABA-edited difference spectra were analyzed with Gannet 3.0, while the OFF spectra were post-processed with FID-A and quantified with LCModel v6.3.

The preliminary results showed increased GABA-to-creatine levels in the cerebellum linked to visual and motor performance scores, which is in line with recent animal and transcranial magnetic stimulation studies. No GABA changes were found in the thalamus and the motor cortex, which contrasts the findings of the animal studies. Further, systemic effects on glutamine, myo-inositol, and aspartate were found in all regions, and were closely linked to visual and motor performance scores. Increased glutamine and myo-inostiol depletion are linked to ammonia detoxification and commonly reported in HE, while changes in aspartate are not reported, yet. Furthermore, increased levels of glutathione, a putative marker of oxidative stress, were found in all regions. The preliminary results indicate an active involvement of the cerebellum in the alterations of the cerebello-thalamo-cortical pathway in HE.

The principal results of the present dissertation are the ammonia sensitivity of optimized APT_w imaging, and the interpretation of APT_w signals as a brain ammonia level correlate. Therefore, APT_w imaging could be used to facilitate the understanding of the pathogenesis of HE. Furthermore, the simulation framework for MR spectroscopy could be used during the design and data quality evaluation of GABA-edited MRS studies. Finally, increased levels of GABA in the cerebellum and other systemic effects affecting the neurometabolism in the cerebello-thalamo-cortical pathway were found in HE patients.

Zusammenfassung

Die hepatische Enzephalopathie (HE) ist eine neuropsychiatrische Erkrankung, die infolge einer Leberzirrhose auftreten kann. Die Pathogenese der HE ist Gegenstand der aktuellen Forschung und wird in verschiedene Konzepte unterteilt. Ausschlaggebend ist hierbei die verminderte Filterung von Neurotoxinen durch die Leber, wie beispielsweise Ammoniak, welches sich anschließend im Gehirn sammelt. Durch die Belastung mit Neurotoxinen kommt es zu einer Verschiebung des Neurotransmittergleichgewichts im Gehirn und infolgedessen zu einer Veränderung der kognitiven, visuellen, sensorimotorischen und visuomotorischen Fähigkeiten des Patienten. Die Schwere der Symptome variiert zwischen subtilen Defiziten (Aufmerksamkeit- und Motordefizite) und mit Fortschreiten der Krankheit Asterixis, Stupor bis hin zum hepatischen Koma.

Die vorliegende Dissertation beschäftigt sich mit der Entwicklung einer HE- bzw. Ammoniaksensitiven Magnetresonanz (MR)-Bildgebungsmethode. Dazu wurde eine Optimierung an einer metabolischen chemical exchange saturation transfer (CEST) Bildgebung im Hinblick auf ihre Sensitivität für Ammoniak durchgeführt und in einer Kohorte von HE Patienten getestet. Zusätzlich wurde eine Simulation entwickelt, welche die Modellierung von GABA+ in 'spectral edited' MR-Spektroskopie unter Berücksichtigung verschiedener Signal-zu-Rausch-Verhältnisse (SNR) und Linienbreiten untersucht. Diese Bedingungen spielen vor allem bei der Untersuchung von tiefen Hirnregionen eine Rolle. Schlussendlich wurde der Neurometabolismus der HE innerhalb der cerebello-thalamo-kortikalen Nervenbahn mittels GABA-editierter MRS untersucht.

Im Verlauf der Arbeit wurden verschiedene Modelllösungen (Ammoniak, Albumin + Ammoniak & Ammoniak + Gewebehomogenisat) mit variierender Ammoniakkonzentration verwendet, um die optimalen Sättigungsparameter des Ammoniak-gewichteten Kontrasts zu finden. Weitergehend wurde die Denaturierung und Aggregation der Proteine bestimmt, um die zugrundeliegenden Mechanismen des CEST-Effekts zu evaluieren. Die optimalen Parameter wurden an einem gesunden Probanden und zwei HE-Patienten getestet.

In Übereinstimmung mit der Literatur zeigte sich die Amidprotonentransfer-gewichtete (APT$_\text{w}$) CEST-Bildgebung sensitiv für Proteindenaturierung. Durch Phantommesungen wurde gezeigt, dass die Kontraständerungen durch veränderte Proteinfaltung induziert wurden. Damit konnte ein ammoniaksensitiver MR-Bildkontrast etabliert werden.

In einer anschließenden Studie deckten weitere Phantommessungen auf, dass hauptsächlich Ammoniak die Kontraständerungen hervorruft, wohingegen der Einfluss anderer Neurometaboliten vernachlässigbar ist. Anschließend wurde eine Kohorte von 14 gesunden Kontrollen, 10 Patienten mit minimaler HE sowie 10 Patienten mit manifesten HE vor der MR Untersuchung psychometrisch getestet. Zusätzlich wurden Bluttests und eine Ermittlung der kritischen Flimmerfrequenz durchgeführt.

Die Nachverarbeitung der CEST-Daten umfasste eine Bewegungskorrektur, die Quantifizierung des CEST Effekts mittels einer Asymmetrieanalyse, eine Korrektur der B_0- und B_1-Effekte, sowie eine Normalisierung, um die möglichen Relaxationseffekte des CEST-Effekts zu minimieren. Zuletzt wurden die CEST-Bilder in ein gemeinsames Koordinatensystem normalisiert, welches basierend auf den gemeinsamen Eigenschaften der Studienkohorte erstellt wurde.

Eine Verminderung des APT_w-Signals wurde im Kleinhirn und im okzipitalen Kortex beobachtet. Das Ausmaß dieser Verminderung korrelierten zusätzlich mit den Blutammoniakwerten sowie mehreren neuropsychometrischen Testergebnissen, welche motorische Leistung und Reaktionszeiten umfassten. Zusätzlich wurden erhöhte APT_w-Signale im Putamen mit der kritischen Flimmerfrequenz, und APT_w-Signaländerungen im Thalamus konnten mit gamma-Glutamyltransferase Konzentrationen in Verbindung gebracht werden.

Die *in vivo* Studie zeigte vergleichbare Verteilungen und Korrelationen wie verschiedene $^{13}NH_3$-PET Studien, was die Interpretation stärkt, dass APT_w-Bildgebung sensitiv für Ammoniakkonzentrationen ist. Die Entdeckung untermauert die Beteiligung des Kleinhirns in der HE, welche in der Literatur als Auslöser der reduzierten motorischen Fähigkeiten bei HE-Patienten diskutiert wird. Veränderungen in Neurotransmittersystemen, verlangsamte neuronale Oszillationen und die verminderte Fähigkeit zur visuellen Differenzierung sind typische Beobachtungen in der HE, welche dem Ammoniakentgiftungspozess im visuellen Areal zugeschrieben werden.

Eine Überlagerung benachbarter Resonanzen in der *in-vivo*-MR-Spektroskopie wird durch ein niedriges SNR und erhöhte Lienenbreiten hervorgerufen. Zur Untersuchung der Auswirkungen der spektralen Qualität auf die Modellierung der Daten wurde der Mittelwert aus 48 *in-vivo*-Spektren zur Erstellung eines rauschfreien Musterspektrums verwendet. Anschließend wurde das Musterspektrum mit unterschiedlichen Linienverbreiterungen und Rauschwerten manipuliert, um variierende Magnetfeldhomogenität und GABA+ SNR Bedingungen zu simulieren.

Jeweils 100 Spektren wurden mit zwei verschiedenen Programmen (Gannet 3.0 und Tarquin) zur Analyse von MRS-Daten modelliert. Der GABA+-Messfehler wurde als relative Differenz zwischen dem Musterspektrum und den modellierten GABA+-Resonanzen der manipulierten Spektren berechnet. Außerdem wurden der Fehler des Fits, die Standardabweichung sowie die

Zahl der abgelehnten Spektren bestimmt. Der GABA+-Messfehler war kleiner als 5 % über den gesamten GABA+-SNR Bereich für mittlere Linienbreiten (9,7 Hz) für Gannet 3.0 und allen Linienbreiten außer 10,6 Hz für Tarquin. Die Standardabweichung im Bereich *in-vivo*-relevanter GABA+-SNR -Werte variierte zwischen 3,1 und 17 % für Gannet 3.0 und zwischen 1 und 11 % für Tarquin.

Diese Ergebnisse bestätigen andere Studien zur Auswirkung des SNR auf die Quantifizierung von GABA. Außerdem zeigte sich eine gute Übereinstimmung zwischen den Simulationen und den *in-vivo*-Szenarien. Dies legt nahe, dass GABA-editierte MR-Spektroskopie-Studien in Regionen mit geringerem GABA+ SNR durchgeführt werden können, jedoch auf Kosten einer höheren Varianz. Zusätzlich zeigte sich, dass die Magnetfeldhomogenität vernachlässigbare Effekte auf die Modellierung des GABA-Signals hat.

In der letzten Studie wurde der Neurometabolismus der cerebello-thalamo-kortikalen Nervenbahn mittels GABA-editierter MRS untersucht. Die Voxeldimensionen wurden entsprechend der Indikation aus der Simulationsstudie entworfen. Die vorläufige Kohorte umfasste 16 gesunde Kontrollprobanden und 15 HE Patienten (2 minimal HE, 14 HE I), bei denen zuvor die CFF ermittelt, Messungen der motorischen Leistung (grooved peg board) erstellt und Bluttests durchgeführt wurden. GABA-editierte MEGA-PRESS MR Spektroskopie wurde im Kleinhirn, Thalamus und Motorkortex durchgeführt. Die Differenzspektren wurden mit Gannet 3.0 analysiert, während die OFF Spektren mit FID-A verarbeitet und mit LCModel v6.3 quantifiziert wurden.

Die vorläufigen Ergebnisse zeigten erhöhte GABA-Konzentrationen im Kleinhirn, welche mit den Änderungen in der visuellen Wahrnehmung und den motorischen Fähigkeiten verknüpft waren. Diese Ergebnisse wurden auch innerhalb von Tierversuchen und einer aktuellen TMS-Studie in der Literatur gezeigt. Im Gegensatz zum Tiermodell wurden in der aktuellen Studie im Thalamus und Motorkortex dagegen keine Änderungen in den GABA-Konzentrationen festgestellt. Weiterhin wurden systemische Veränderungen der Konzentrationen von Glutamin, Myo-Inositol und Aspartat festgestellt, welche zusätzlich mit Änderungen der visuellen Wahrnehmung und den motorischen Fähigkeiten verbunden waren. Glutamin und Myo-Inositol sind im Gehirn von HE-Patienten durch die Stoffwechselprozesse zur Auflösung des Ammoniaks verändert, während Veränderungen in Aspartat Konzentrationen *in vivo* bisher nicht festgestellt wurden. Zusätzlich wurden erhöhte Glutathion-Konzentrationen in allen Regionen festgestellt, welche vielfach ein Indikator für erhöhten oxidativen Stress darstellt. Die vorläufigen Ergebnisse zeigen die wichtige Rolle des Kleinhirns für HE-spezifischen Änderungen der cerebello-thalamo-kortikalen Verbindung.

Zusammenfassend wurde in der vorliegenden Dissertation die Ammoniak-Sensitivität der APT_w Bildgebung und die Interpretation der APT_w-Signale als Korrelat des Gehirn-Ammoniakspiegels festgestellt. Deshalb kann die APT_w Bildgebung zur weiteren Untersuchung der Pathogenese der HE verwendet werden. Die entwickelten Simulationen können zum Entwerfen und zur Evaluation der Datenqualität von GABA-editierten MR-Spektroskopie-Studien verwendet werden. Schlussendlich wurden erhöhte GABA-Konzentrationen im Kleinhirn und systemische Effekte auf den Neurometabolismus der cerebello-thalamo-kortikalen Nervenbahnen in der HE gefunden.

1 Introduction

The human brain is the most differentiated organ in the human body. It is responsible for the processing of sensory perception and the coordination of behavior. Basic approaches to describe and understand the brain range across various scales and disciplines, from behavioral outcome to firing rates of single neurons, and from psychoanalysis over mathematical modeling of behavior to metabolic **magnetic resonance (MR)** imaging and spectroscopy. The extraordinary complexity of the brain can hardly be described by single numbers: about 86 billion neural cells form the human brain [2], providing a memory capacity of approximately 2.5 petabytes [3]. Neuroscience has evolved as an independent and highly interdisciplinary research field that is dedicated to expanding the understanding of this outstandingly complex system.

On a macroscopic scale, the brain is divided into telencephalon, diencephalon, cerebellum, and brainstem. The telencephalon is divided into two hemispheres, which are mainly connected by the corpus callosum. The surface is heavily folded into gyri and sulci, which feature a dense layers of neuronal cells. This layer is known as the cortex or gray matter, and is connected to other cortical regions and brain parts by neuronal tracts, also known as white matter [4]. External information are processed in different cortical regions. The visual cortex, for example, processes visual input from the retina [5], while the prefrontal cortex is responsible to regulate behavior with regard to internal reference systems [6]. The diencephalon located in the deeper brain regions underlying the white matter includes the thalamic subsystem. The thalamus is mainly categorized as a mediator between sensory and motor input [7], while the hypothalamus orchestrates several vital processes. The cerebellum is located caudal to the occipital lobe, and is mainly involved in motor and balance coordination [8]. Other sensory impressions are processed in the brainstem, which is also crucial to reflexive behavior.

The main components of the brain on a microscopic scale are neurons. These cells are electrically excitable, and responsible for the communication in the brain via synapses. Synapses form conjunctions between the neurons and transfer information between them. Generally, they are divided into chemical and electrical synapses. In the case of electrical synapses, pre- and postsynaptic neurons are connected via gap junctions which allow the passage of electrical current between the neurons. In chemical synapse, electrical signals are converted into chemical signals relayed by a neurotransmitter. These neurotransmitters are released into the synaptic cleft to bind to receptors on the postsynaptic neuron. Changes in the conformation of the receptor proteins introduce

changes to the membrane potential, or a cascade of secondary pathways to modulate the excitatory or inhibitory state of the postsynaptic neuron. There are possible neurotransmitter by which the chemical synapses are classified. The main excitatory neurometabolite is glutamate, while γ-**aminobutyric acid (GABA)** is the most prevalent inhibitory counterpart in the human brain. Changes in the baseline concentrations of those neurometabolites can cause severe dysfunction in the brain. Metabolic imaging and MR spectroscopy allow the investigation of concentration changes of several neurometabolites *in vivo*, such as GABA or glutamate. Therefore, it is a useful tool to study disease-related changes in the active neurometabolism in a living subject.

As a consequence of the brain's complexity, a subtle alteration in this clockwork-like system can ripple down into several subsystem inducing cognitive changes on a behavioral and clinically accessible scale. The brain is usually protected from outer influences via the blood brain barrier. This protection can be deliberately bypassed by medication, or inadvertently by various diseases. The neuropsychiatric disease **hepatic encephalopathy (HE)** is caused by a dysfunctional hepatic clearance of neurotoxins (e.g., ammonia, glutamate, mercaptan) from the blood. In Western countries, the most common form of liver cirrhosis is the ethyl-toxic cirrhosis introduced by ethanol abuse [9]. The effects of HE on the human brain are assumed to be multifactorial [10, 11].

In neuroscience, **magnetic resonance imaging (MRI)** is a valuable tool to noninvasively study the living brain. It is capable of providing structural information, but more advanced approaches allow for the investigation of the living metabolism. This could be done via **metabolic imaging** - which forms image contrasts based on the underlying cellular metabolism [12, 13, 14, 15] - or via **magnetic resonance spectroscopy (MRS)** - which allows for the evaluation of changes in the concentration of certain neurometabolites [16, 17, 18, 19, 20]. Although these techniques are valuable tools to investigate disease-related changes to gain a deeper understanding of the underlying pathophysiology of various brain diseases, such as HE, these techniques require a considerable amount of post-processing and expertise in the interpretation. This dissertation aims to adapt a magnetic resonance metabolic imaging as well as a spectroscopy approach to investigate the metabolic underpinnings of hepatic encephalopathy.

2 Hepatic Encephalopathy: From hepatic dysfunction to cognitive impairment

The pathophysiology of **hepatic encephalopathy (HE)** is assumed to be multifactorial but remains a matter of debate in the literature until today [10, 11]. The following parts describe the most common concepts on the pathophysiology of HE and its clinical assessment.

2.1 Pathophysiology of hepatic encephalopathy

HE arises from increased concentrations of numerous neurotoxins in the blood. The roots of the abnormal concentrations is presumably the loss of the liver's clearance ability due to cirrhosis, the formation of portosystemic shunts, or the artificial creation of a transjugular intrahepatic portosystemic shunt. Cirrhosis is possibly caused by ethanol abuse, leading to an ethyl-toxic cirrhosis [9]. Other forms of toxic cirrhosis include non-alcoholic steatohepatitis (non-alcoholic fatty liver disease) and drug-induced liver disease. Liver inflammation through chronic viral hepatitis (B, C, D) can also lead to cirrhosis. The multifactorial aspects of HE in the brain can be summarized as follows without being mutually exclusive:

- ammonium hypothesis [21, 22, 23]

- neuroinflammation and oxidative stress [24, 25, 26]

- other neurotoxins [27, 28]

- neurotransmitter imbalance [29, 30, 31, 32]

- false neurotransmitter hypothesis [33]

- neuropathological alterations [34, 35, 36]

Figure 2.1 summarizes the **ammonium hypothesis**. The increased concentration of the neu-rotoxin ammonia in the brain is assumed to be crucial in the pathogenesis of HE [21, 22, 23].
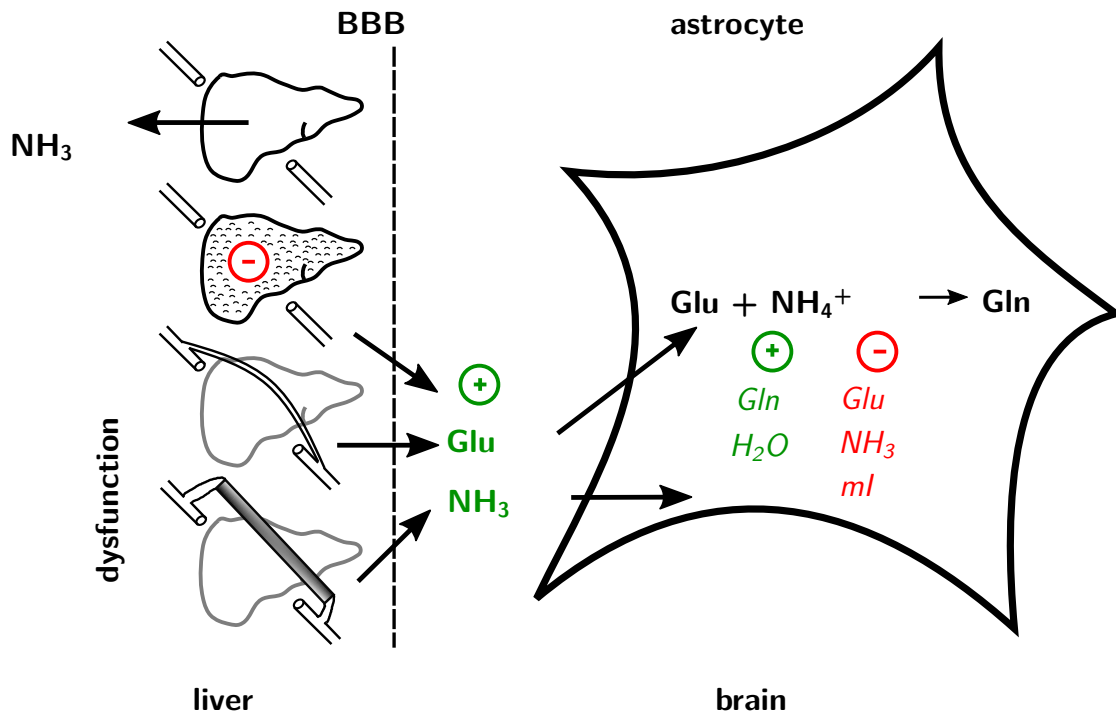
Figure 2.1 – Pathophysiology of HE - The ammonium hypothesis describes the detoxifica-tion of ammonium which has diffused through the blood brain barrier (BBB), by glutamine synthetase in astrocytes. Adapted from [37].

The elevated ammonia levels are reduced through the formation of glutamine, particularly in astrocytes. During ammonia detoxification, glutamine synthetase amidates glutamate and am-monium to create glutamine and water. This process alters the glutamine/glutamate ratio in the astrocytes [38, 17, 39, 40] and creates an osmotic gradient, which generates cell swelling [21, 41] and on a macroscopic scale the characteristic low-grade edema of HE [42, 43]. As a counter-reaction, the osmolyte myo-inositol is released, and therefore depleted in the cells [38]. Glutamate is the main excitatory neurotransmitter in the brain. Therefore, dysbalance in the glu-tamate concentration could affect glutamatergic neurotransmission [40]. Glutamate, glutamine, and myo-inositol are MR-visible metabolites, which allow the direct investigation of HE associated changes of these with MRS [38, 17].

In contrast, ammonia itself can not be detected by MRS due to its high exchange rates, but has extensively been investigated via **positron emission tomography (PET)**. Key findings are increased radiation of radioactively marked ammonia, as well as increased metabolic clearance rates of ammonia in HE patients [44, 1].

Additionally, ammonia has other direct effects on the brain, such as changes in excitatory and inhibitory neurotransmission (increased amino acid transport through the **blood brain barrier (BBB)** and effects on the sodium-potassium pump [45]), as well as alterations in the energy metabolism in higher stages of HE [46]. The ammonium hypothesis is a matter of discussion for two reasons: First, HE appears in about 10% of patients with normal serum ammonia levels, and second, the serum ammonia levels do not necessarily correlate with disease severity [47].

The increasing ammonia levels trigger **neuroinflammation and oxidative stress** [24, 25, 26], and interrupt several signaling pathways and protein synthesis. As an oxidative stress response, glutathione, the most abundant antioxidant in the human brain, is elevated in HE, and closely coupled to the hyperammonemia [19]. **Other neurotoxins** are mercaptans, which are potentiating the neurotoxicity of ammonium in the brain by inhibiting the sodium-potassium pump. Short- and middle-chain fatty acids are also suggested to interfere with the sodium-potassium pump, but their role is not fully understood [27]. Manganese is another common neurotoxin accumulating in the basal ganglia of HE patients [28].

Apart from the imbalance in the glutamine/glutamate ratio, **neurotransmitter imbalance** is a general concept in the pathophysiology. The GABA hypothesis, claiming that GABA forming in the gut passes the impaired BBB, has become obsolete [29]. Nevertheless, regional alterations in GABAergic tone [32], mediated through increasing endogenous benzodiazepines [30, 31], are a crucial characteristic in HE. Ammonia, benzodiazepines, and GABA itself have different effects which potentiate the GABAergic tone. Elevated ammonia levels modulate the affinity of the $GABA_A$ receptors for GABA. Furthermore, the selective binding of GABA and benzodiazepine agonists to the $GABA_A$ receptor complex and the stimulation of peripheral benzodiazepine receptors on the astrocytes increase the synthesis of neurosteroid agonists of the $GABA_A$ receptor complex. Moreover, the GABA uptake of astrocytes is decreased, while the release is increased, resulting in enhanced inhibitory neurotransmission [32]. Other neurotransmitters, such as serotonin are part of the present research on HE.

Impairment of the BBB allows increased diffusion of phenylalanine, tyrosine, and tryptopahn, which have a small excitatory effect. These neurotransmitter changes, as well as changes in dopaminergic neurotransmission, are summarized in the **false neurotransmitter hypothesis** [33], but their exact role in the emergence of HE remains unclear.

Reduced specificity and higher permeability of the BBB [23] and formation of Alzheimer Type-II astrocytes [34] are two HE-related **neuropathological alterations**. A swollen nucleus with chromatin concentrated at the edge of the nucleus characterizes these astrocytes. Additionally, hepatocerebral degeneration is a common feature in HE, leading to the loss of cells especially in the cerebellum [35, 36]

2.2 Clinical assessment and graduation of Hepatic Encephalopathy
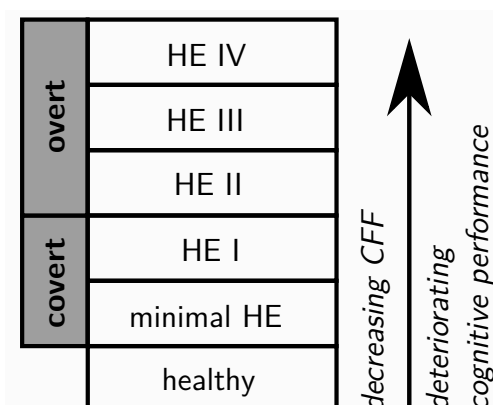
Figure 2.2 – Graduation of HE - The graduation system outlined in the consensus papers [48, 49, 50]. Adapted from [49, 50].

There are several consensus papers on HE classification [48, 49, 50]. Figure 2.2 presents the current graduation system. In this description ***minimal HE (mHE)*** is the lowest disease stage of the graduation system, which increases up to HE IV. The stages I to IV are clinically graded by the West-Haven criteria. Minimal HE and HE I are grouped together into covert HE and the other stages are grouped into overt HE [49]. Cognitive impairment increases in the course of the disease progression. Subclinical changes in psychomotor speed and executive functions are frequently observed in mHE. These changes can be detected with line-following, paper-pencil or number tracking tests, or more elaborately (and expensively) with computer psychometric testing.

The West-Haven criteria are used to classify clinically overt changes in patient behavior [48]. Patients with HE I show a general lack of awareness, a shortened attention span, and altered sleep patterns. Yet, they are still oriented in space and time. HE II patients are disoriented in time, apathetic and exhibit personality changes. They may also display dyspraxia and asterixis (flapping tremor). In the HE III stage, patients may present confusion, disorientation in space, somnolence to semistupor, and bizarre behavior. Finally, hepatic coma eventuates at stage IV.

A relatively new approach to reflect and quantify the continuous nature of HE is the **critical flicker frequency (CFF)** [51, 52]. The CFF is suitable to substantiate the psychometric findings. The patient indicates the frequency at which he/she perceives a fast flickering light, which is perceived as continuous for high flickering frequencies in the beginning of the experiment, as flickering. Patients with a CFF below 39 Hz are defined as impaired. This neurophysiological method is suggested to be independent of learning effects, age, and education, and shows a high correlation with the disease stage [51]. It reflects the deterioration of the visual perception during disease progression, and also correlates with neurophysiological (GABA concentrations [18]) and neuronal oscillatory (α band peak frequency [53]) measures.

3 Nuclear Magnetic Resonance: From physical phenomenon to metabolic investigation

The **nuclear magnetic resonance (NMR)** describes the nuclear-physical effect of atomic nuclei absorbing and emitting alternating electromagnetic fields while placed in a constant magnetic field. All modern *MR* scanners are designed to exploit NMR to create a number of qualitative or quantitative imaging contrasts.

The electromagnetic interactions between atoms and magnetic fields were first described by Stern and Gerlach [54], who observed the splitting of the focal spot of silver atoms after their passage through a magnetic field. It was the first time quantum-mechanical space quantization was observed during an experiment, which was proposed as a consequence of the Zeeman experiment two decades earlier [55]. The Zeeman effect describes the splitting of spectral lines of a gas discharge lamp, and is based on the interactions between the external magnetic field and the atomic magnetic moment.

NMR, in particular, was described in the mid-20th century by two independent experiments [56, 57], which paved the way for the concept of NMR tomography and imaging, developed by Mansfield and Lauterbur [58]. Until now, MRI and MRS research undergo rapid evolution allowing vast capabilities of image contrasts and advanced biomedical imaging methods. Finally, the emergence of quantitative methods facilitates metabolic imaging or the calculation of approximated metabolite concentrations.

The theoretical description of NMR in this dissertation is based on [59] and [60].

3.1 The Basics of Nuclear Magnetic Resonance

Every atomic nucleus intrinsically possesses an atomic spin $\vec{I}$, which is based on the spins and orbital angular moments of all nuclear constituents. The atomic spin $\vec{I}$ is linked to an atomic magnetic moment $\vec{\mu} = \gamma \hbar \vec{I}$ with the isotope-specific gyromagnetic ratio γ.

Following the assumptions of the Zeeman effect, an external magnetic field B_0 polarizes the atomic spin $\vec{I}$ with the magnitude $|\vec{I}| = \hbar \sqrt{I(I+1)}$ according to the magnetic quantum

number $I_z = m_I \cdot \hbar$ ($m_I = -I, -I+1, ..., I-1, I$). The space quantization creates $2I+1$ energy levels E_m, which are defined by the z-component of the atomic spin $\vec{I}$. Consequentially, the energy levels E_m are calculated as $E_m = -\vec{\mu}\vec{B_0} = -\gamma\hbar\vec{I} \cdot \vec{B_0} = -\gamma\hbar m_I B_0$.

Fundamentally, a electromagnetic wave applied perpendicular to B_0 at resonance frequency ν could introduce transitions between neighboring energy levels:

$$\nu = \Delta E = \frac{\gamma}{2\pi}B_0 \tag{3.1}$$

Equation 3.1 is the fundamental relation describing the NMR effect. In principle, every atomic nucleus with one unpaired spin (e.g. 13C, 31P etc.) can be detected in the MRI. However, low relative biological abundance and low gyromagnetic ratios limit the accessibility of other nuclei in *in vivo* MRI. This work focuses on the NMR effect of protons (^{1}H). Fortunately, protons combine a high gyromagnetic ratio ($\gamma = 42.6$ MHz/T) and a high abundance ($\approx 10^{23}$ protons in a 1 mm^3 cubic volume (voxel)) in the human body. Additionally, protons possess only two energy levels according to $I_z = \pm 1/2$ leading to a single possible transition.

Regardless of the fact that MRI is based on a quantum mechanic effect, the superposition of a ensemble of spins in a cubic volume becomes apparent in a macroscopic magnetization, allowing the description of MRI without quantum mechanics.

3.2 Macroscopic Interpretation of Nuclear Magnetic Resonance

The ***macroscopic magnetization*** vector $\vec{M_0}$ is the vector sum of an ensemble of spins - e.g., in one voxel. By positioning a sample or patient in the static magnetic field B_0, which is created by the superconducting magnet of the tomograph, the distribution of protons over the two possible energy levels follows the ***Boltzmann distribution***. The samples used in MRI research are usually measured at room temperature or in case of *in vivo* measurements, at body temperature. Therefore, the so-called high-temperature-approximation can be used to describe the occupation of the N_α and N_β states:

$$\frac{N_\beta}{N_\alpha} = exp\left(-\frac{E_\beta - E_\alpha}{k_B T}\right) = exp\left(-\frac{\gamma\hbar B_0}{k_B T}\right) \approx 1 - \frac{2\gamma\hbar B_0}{k_B T} \tag{3.2}$$

with the Boltzmann constant k_B, and the number of protons N_α and N_β in the low and high energy state, respectively. N_α and N_β correspond to the number protons with the z-component

of their magnetic moment parallel or antiparallel to the static magnetic field B_0. The occupation number difference in both energy levels is very subtle at room temperature and is about $6.67 * 10^{-7}$ at 3 Tesla. Still, the vector sum over all protons creates macroscopic magnetization $\vec{M}_0$ in equilibrium, representing the main measurement parameter in MRI. The z-component M_z and the xy-components M_{xy} of $\vec{M}_0$ are named **longitudinal magnetization** and **transversal magnetization**, respectively. The coordinate system is defined by the direction of B_0, representing the z-axis. It is worth noting that M_{xy} is solely creating the detectable MRI signal.

A resonant electromagnetic wave can interact with the proton spins and alter the occupation of the energy levels. Immediately after applying a resonant radio frequency (RF) pulse $\vec{M}_0$ starts to precess around B_0. The precession of the individual spin equals the behavior of gyroscope in the gravitational field. Following a RF pulse, most of the spins are rotating with the same frequency and phase, while this **phase coherence** is lost over time. The precession frequency of $\vec{M}_0$ is the **Larmor frequency** and electromagnetic waves applied in resonance - the same frequency as the Larmor frequency of the target - can achieve state transitions and a manipulation of $\vec{M}_0$ (Equation 3.1).

In the tomograph, this is achieved by a transmit coil. This coil allows a resonant energy transfer in the sample by radiating RF waves with well-defined amplitudes and frequencies. Therefore, arbitrary orientations of $\vec{M}_0$ can be achieved. It is common to designate the name of the RF-pulse by its flip angle relative to B_0 - e.g., a $\pi/2$-pulse tilts $\vec{M}_0$ into the xy-plane by 90 degrees. $\pi/2$-pulses are commonly used for excitation in ^{1}H spectroscopy as the M_{xy} is maximal in this case, leading to the highest signals.

In the MRI scanner, the rotation of $\vec{M}_0$ is detected based on the induced voltage in a receive coil, which is placed close to the sample. Quadrature receive coils are arranged such that two signals with a phase of π are received, creating a complex-valued signal. As the signal is weak, it undergoes amplification before digital-to-analog conversion to create the final signal to be recorded.

In an NMR experiment, the magnetization vector $\vec{M}$ usually decays fast due to various relaxation processes. These processes affect the components of $\vec{M}$ differently, as $\vec{M}_{xy}$ evolves independently from $\vec{M}_z$. Following the natural motion of $\vec{M}$ the description of the relaxation processes is easier in a rotating frame.

3.3 Relaxation of the Magnetization Vector

3.3.1 Spin-Lattice Relaxation
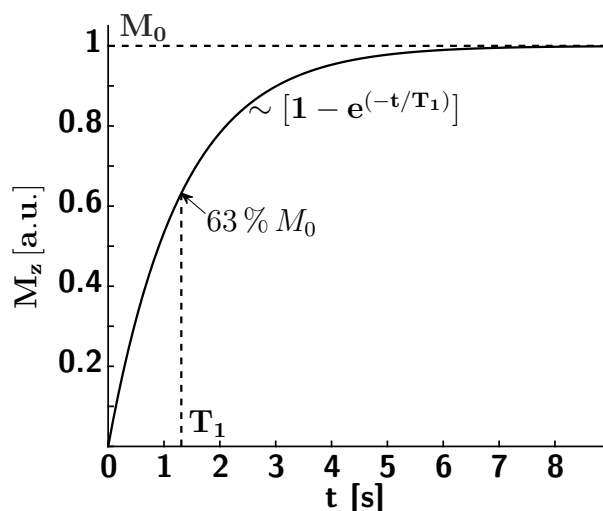
Figure 3.1 – Longitudinal relaxation process in NMR - T_1 relaxation after a $\pi/2$-pulse.

The **_longitudinal relaxation_** describes the process of inelastic interactions between the protons and their surroundings (Figure 3.1). The energy loss of the system through T_1 relaxation is unrecoverable, and describes the transfer of heat through rotation, collisions, and electromagnetic interactions.

During longitudinal relaxation, $\vec{M}_0$ regenerates into the equilibrium state parallel to $\vec{B}_0$. The z-component M_z of the magnetization vector at any time t and its relaxation is described by $M_z(t) = M_0 \left[1 - exp\left(-t/T_1 \right) \right]$ with T_1 being the **_longitudinal relaxation time_**. 63 % of M_0 is restored at $t = T_1$, and the equilibrium state is approximately reached for $t = 5 \cdot T_1$. T_1 is on the order of magnitude of seconds, and proportional to the magnetic field strength B_0 and the rigidity of the chemical bond of the protons. Large molecules representing more solid aggregations or bound states are associated with low mobility and high T_1 values. High mobility rates are found in small molecules behaving liquid-like or free. These states are also linked to high T_1 values, while the intermediate mobility region is characterized by lower T_1 values. For example, at 3 T, water or **_cerebro spinal fluid (CSF)_** has a T_1 of about 3800 ms [61], gray matter and white matter a T_1 of about 1300 ms and 800 ms [62], respectively. Ice (measured at 263 K at 2.9 T) possesses a T_1 of about 1.5 ms [63].

3.3.2 Spin-Spin Relaxation

Immediately after the deflection of $\vec{M}$ from the equilibrium state, another relaxation process takes place. This process appears at any flip angle. The spin-spin or **transversal relaxation** describes the loss of phase coherence through random (thermal) interactions between the spins. The name spin-spin relaxation derives from the fact, that this relaxation process is mediated through the interactions between two or more spins. T_2 relaxation mediated through spin-spin interactions is the major contributor to the decay of M_{xy}. The local magnetic field B_{loc} a spin experiences differs with the vicinity of every spin - e.g., a spin in a water molecule experiences a different B_{loc} in the vicinity of other water molecules than in the vicinity of iron atoms in hemoglobin. Consequently, the frequency at which the proton precesses is proportional to the combination of B_0 and B_{loc}. Thus, the phase coherence decreases over time, leading to signal decay.
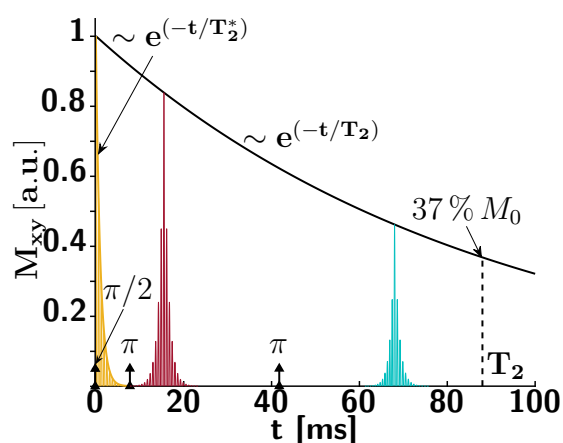
Figure 3.2 – Transversal relaxation process in NMR - T_2^* & T_2 relaxation after a $\pi/2$-pulse. Transversal relaxation (yellow: Free Induction Decay, red & cyan: spin echos) is observed via a spin echo with the combination of a $\pi/2$- and two π-pulses (black).

The T_2 relaxation following a spin echo is summarized in Figure 3.2. The transversal magnetization M_{xy} and its relaxation process at any time t are described by an exponential decay $M_{xy}(t) = M_0 \cdot exp\left(-t/T_2\right)$ with T_2 being the **spin-spin relaxation time** and time point at which 63 % of the M_0 has decayed. T_2 is usually on the order of magnitudes of milliseconds, and influenced by the rigidity of the chemical bond of the protons. The higher the mobility, the higher T_2. For example, at 3 T, water/CSF has a T_2 of about 500 ms [64], gray matter and white matter a T_2 of about 100 and 80 ms [62], respectively. Ice (measured at 263 K at 2.9 T) possesses a T_2 of about 150 μs [63].

The initial decay of the signal following a $\pi/2$-pulse, also called **Free Induction Decay**, happens much faster than expected by the processes described above. The visible decay is a combination of T_2 and the local, static (time-independent) imperfections and disturbances of the static magnetic field B_0. The combined relaxation rate is called $T_2^* = 1/T_2 + \gamma \Delta B_0$ with ΔB_0 being the local yet time-independent variations of the static magnetic field B_0. T_2^* is usually about a factor 3 smaller than T_2 for a specific tissue or molecule.

3.3.3 Spin echo

The T_2^* relaxation appears to be elastic and locally time-independent for protons in tissue. Therefore, T_2^* relaxation is reversible. The signal can be regenerated by a **spin echo**, which will only have decayed with T_2. To achieve this, a π-pulse is applied such that the spins are, for example, mirrored along the zy-plane. Immediately after the flip, the relative phase between the spins is inverted while the precession frequency is conserved. Therefore the phase differences between the spins will be reversed, and a spin echo can be measured. The ascent and decay are proportional to $exp\left(t/T_2^*\right)$ and $exp\left(-t/T_2^*\right)$, respectively. During acquisition a spin echo appears at the **echo time (TE)** inducing a signal in the receive coil. TE is usually chosen to be minimal to minimize signal loss due to T_2 relaxation. Theoretically, the spin echo can be recreated as long as the signal is not completely decayed through T_2 relaxation. A time period of **repetition time (TR)** $= 2$ s is commonly chosen prior to another excitation, which is the period between two $\pi/2$-pulses and accounts for the T_1 relaxation.

3.4 Magnetic Resonance Spectroscopy

MRS can be used to detect and distinguish *in vivo* metabolites and is based on the previously defined NMR effects. The investigated metabolite signal is usually by several orders of magnitude smaller than the signal from protons bound in water. Therefore, the requirements regarding the SNR are higher compared to normal MR imaging, which relies on the much stronger water signal. Early clinical applications include tumor differentiation [65] and schizophrenia investigations [66]. Furthermore, it has been used to investigate neurological, neuropsychiatric, and metabolic diseases, including ADHD [20], Tourette syndrome [67], ALS [68], and hepatic encephalopathy [16, 18, 19]. Additionally, healthy aging [69, 70, 71] and gender effects [72], as well as changes in metabolism due to genetic mutations in specific transporter proteins [73] or the consume of nicotine [74] and caffeine [75], can be investigated via MRS.

3.4.1 Volume selection with PRESS

The previously described MR processes are not spatially localized within the sample. Consecutive orthogonal **slice selection** can be used to generate a spatially localized spin echo known as ***Point RESolved Spectroscopy (PRESS)*** [76] (see Figure 3.3).
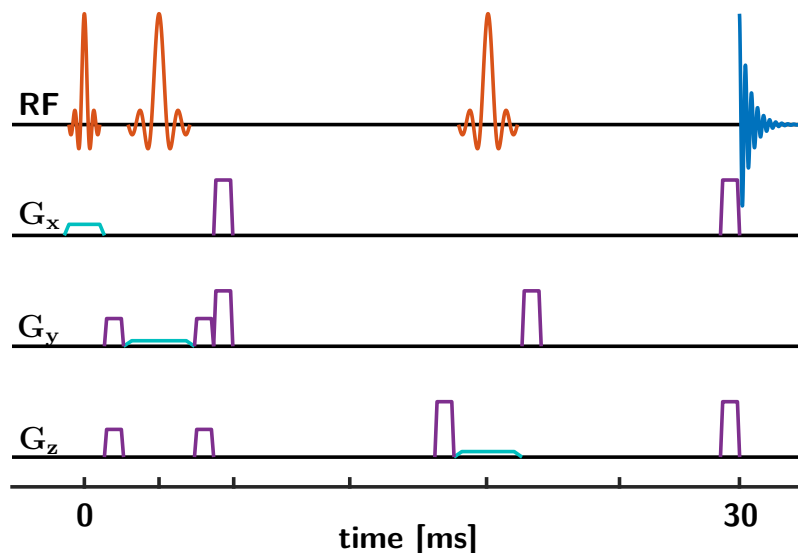
Figure 3.3 – **PRESS sequence diagram** - Excitation and refocusing RF pulses (orange) with slice selective gradients (cyan) to create a spin echo (blue). Crusher gradients (purple) are applied to dephase unwanted echos. Adapted from [76].

The volume selection achieved by superimposing magnetic gradients (G_x, G_y and G_z) with the static magnetic field B_0 leading for example in the z-direction to $B(z) = B_0 + G_z \cdot z$. The application of the gradient creates spatially varying precession frequencies $\nu(z) = \gamma(B_0 + G_z \cdot z)$. By combining a $\pi/2$-pulse and two π-pulses (orange) each simultaneously with their respective slice-selective gradient (cyan) in three orthogonal directions, a spatially localized spin echo (blue) is created.

After exciting a slice with the $\pi/2$-pulse, the first π-pulse generates an echo from a slab (the intersection of two perpendicular slices), and the second π-pulse refocuses the echo from a cubic volume (the intersection of three perpendicular slices). The final spin echo appears at t = TE, commonly chosen to be TE = 30 ms, which induces a signal in the receive coil. This complex valued signal is stored by the analog-to-digital converter, which represents a decaying echo in time domain. The frequency domain representation of the signal is created by transformation of the time domain signal with a **fast Fourier transformation (FFT)**. The integral over the real part of the resonance peak is proportional to the target concentration - e.g., water or a metabolite.

RF pulses are not perfectly rectangular in space, as a boxcar profile would require an infinitely long pulse in the time domain. The crusher gradients (purple) surrounding the slice selective gradients reduce unwanted signals from outside of the volume by artificially dephasing the out of volume signal.

The acquired signal is a superposition of the NMR signal and random noise. The noise originates from RF emission due to thermal motion in the sample and from the MRI scanner itself - e.g., the coils and other electronics in the measurement chain. The data quality of an MRI acquisition is often assessed by the *SNR*. SNR is proportional to the size of the spectroscopic volume or image voxel, and increases with $\sqrt{NEX}$ with **number of excitations (NEX)** being the number of acquired averages.

Parameters for sufficient SNR are typically in the order of magnitude of 10 ml and 100 NEX for PRESS with TE/TR = 30/2000 ms.

3.4.2 Chemical shift

Until here, we assumed all protons to be bound in water molecules, and therefore expected a single well-defined precession frequency. The precession frequency, however, depends on the local magnetic field B_{loc} at the position of an individual spin. B_{loc} is not only determined by the static external field B_0, but also modulated by neighboring protons and electrons. The electron clouds - located around the proton - introduce a **chemical shift** induced by the susceptibility of the electrons. The induced magnetic field B_{ind} is opposed to B_0 as it follows Lenz's law. Thus,

the proton is shielded from B_0 leading to $B_{loc} = B_0(1 - \sigma)$ with the shielding factor σ. Higher shielding σ leads to a lower B_{loc} and a lower precession frequency. The shielding of a particular proton is determined by the electronegativity of the adjacent atoms - e.g., an oxygen atom leads to a lower shielding for an adjacent proton than a carbon atom due to the higher electronegativity. Therefore, the electron density and the shielding is lower for a proton adjacent to a oxygen atom compared to a proton adjacent to a carbon atom. The chemical shift of a arbitrary proton is calculated by:

$$\delta = \frac{\nu_i - \nu_{ref}}{\nu_{ref}} \tag{3.3}$$

with a precession frequency ν_i and a reference substance resonance ν_{ref}. δ is independent of B_0 and commonly reported in **parts per million (ppm)** - which is a dimensionless constant - as ν_{ref} is often measured in MHz. ν_{ref} is defined as the Larmor frequency of the tetramethylsilane signal at which δ equals 0 ppm. For *in vivo* MRS in the brain t,he signal of N-acetylaspartate (NAA) at 2.01 ppm or the 3 ppm creatine signal are commonly used for referencing. The pattern of the spectrum is specific for the nucleus observed and the chemical structure containing the nucleus.
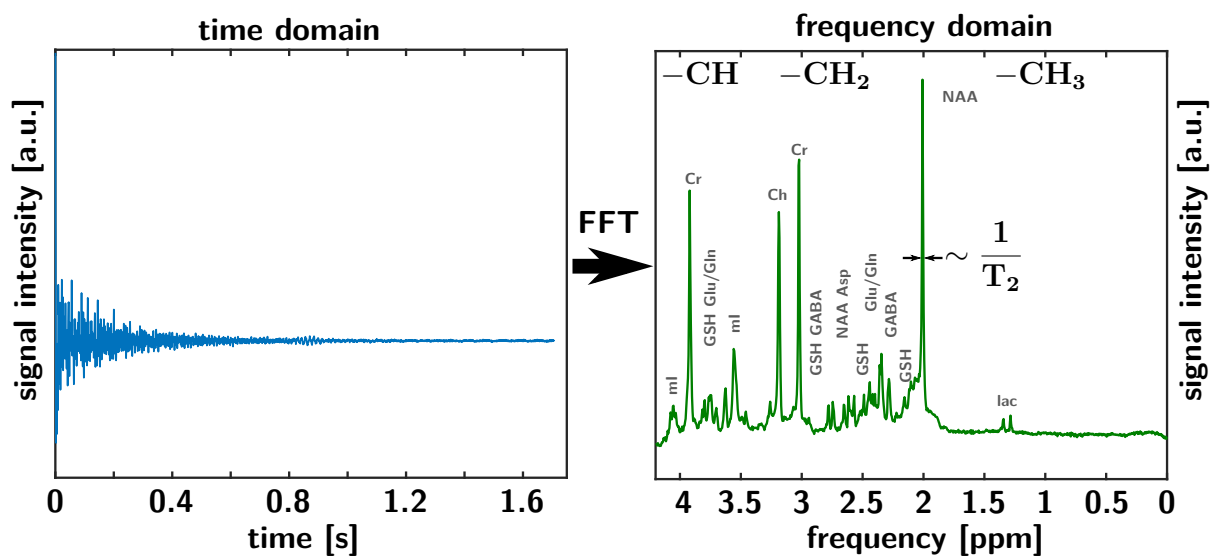
Figure 3.4 – Short TE PRESS spectrum - free induction decay (FID) and resulting ^{1}H MR spectrum of a phantom solution of typical brain metabolites (N-acetyl-aspartate (NAA), creatine (Cr), choline (Ch), aspartate (Asp), glutathione (GSH), GABA, myo-inositol (mI), glutamate (Glu), glutamine (Gln) & lactate (lac)). Measured with TE/TR = 30/2000 ms and 80 NEX at 3 T.

If the spectroscopic volume is placed in a sample which contains protons bound in different molecules, the resulting signal is a mixture of signals precessing various frequencies. The time-domain signal is transformed into the frequency domain using FFT. Figure 3.4 shows an echo from a solution containing typical metabolites of the human brain in the time domain, and its

FFT in the frequency domain. The FFT of an exponential decay in time domain represents a Lorentzian line shape in the frequency domain. As the echo in the time domain is approximately exponential, the shape of the spectral peak in frequency domain is Lorentzian. Consequently, the **full width at half maximum (FWHM)** of a spectral peak in the frequency domain is proportional to $1/(\pi T_2)$. This means that a highly homogeneous B_0 is necessary to achieve a suitable spectral resolution. In modern MRI scanners, B_0 homogenization is optimized during the shim process. The FWHM of creatine is used to define the linewidth of an *in vivo* spectrum, which is a quality criteria for B_0 homogeneity.

Figure 3.4 shows that only a few strong peaks are clearly distinguishable - e.g., NAA at 2.01 ppm, creatine (Cr) at 3.03 ppm and choline (Ch) choline at 3.19 ppm. The other resonances are split into doublets, triplets, or even higher-order multiplets as a consequence of **J-coupling**.

3.4.3 J-coupling

J-coupling is an electron-mediated interaction of two spins in one molecule based on the spin state of the valence electrons, affecting the spin state of the electrons of nearby nuclei. The splitting can be explained by the possible energy levels of the spin system, which are defined by the spin states of the involved nuclei. In a three spin system, the Larmor frequencies $\nu_{0,i}$ of the nuclei $i \in (1, 2, 3)$ can be defined as follows [60]:

$$\nu_{0,i} = -\frac{1}{2\pi}\gamma\left(1 + \delta_i\right)B_0, \ i \in (1, 2, 3) \tag{3.4}$$

with δ_i being the chemical shift of the resonances. There are eight possible combinations ($\alpha\alpha\alpha$, $\alpha\beta\alpha$, $\beta\alpha\alpha$, $\beta\beta\alpha$, $\alpha\alpha\beta$, $\alpha\beta\beta$, $\beta\alpha\beta$, and $\beta\beta\beta$) for the spin states in a three spin system with $m = \pm 1/2$.
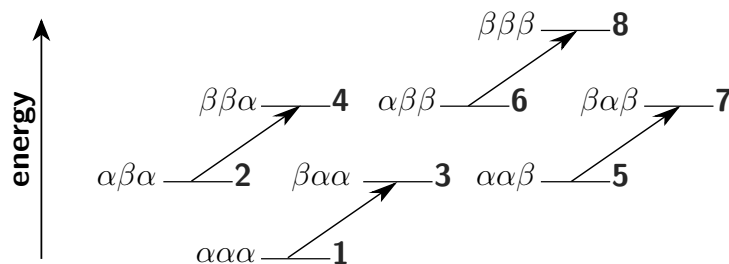
Figure 3.5 – Energy levels of spin 1 in a three spin system - Allowed transitions for spin 1 are marked with arrows. Adapted from [60].

The eight energy levels are depicted in Figure 3.5 and given by [60]:

$$E_{m_1 m_2 m_3} = m_1 \nu_{0,1} + m_2 \nu_{0,2} + m_3 \nu_{0,3} + m_1 m_2 J_{12} + m_3 m_3 J_{13} + m_2 m_3 J_{23} \qquad (3.5)$$

with J being the scalar coupling constants and m being the $m = \pm 1/2$ values of the spins. The J-coupling is independent of the static magnetic field B_0. Following the eight energy levels, the resulting frequencies of the resonances can be calculated by $\nu_{ij} = E_i - E_j$. There are four possible transitions allowed for spin 1. For example, the transition from $\beta\alpha\alpha$ to $\alpha\alpha\alpha$ leads to a frequency $\nu_{1,3} = -\nu_{0,1} - \frac{1}{2}J_{12} - \frac{1}{2}J_{13}$.

For $J_{12} \neq J_{13}$, the spectrum of spin 1 consists of a doublet of doublets around the Larmor frequency $-\nu_{0,1}$ of spin 1, corresponding to the four possible transitions. If $J_{12} = J_{13}$ spin 1 will show a 1:2:1 triplet around $\nu_{0,1}$ [60].
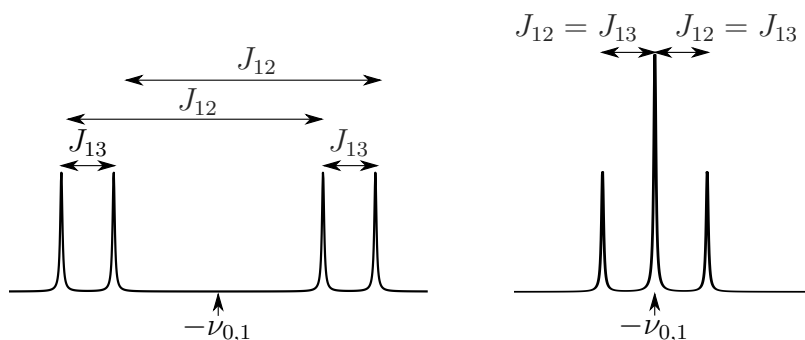
Figure 3.6 – **Multiplets of spin 1 in a three spin system** - Doublet of doublets of spin 1 around the Larmor frequency $-\nu_{0,1}$ with $J_{12} \neq J_{13}$ (left). 1:2:1 Triplet of spin 1 around the Larmor frequency $-\nu_{0,1}$ with $J_{12} = J_{13}$ (right). Adapted from [60].

This concept can be extended to any number of spins and the multiplet depends on the specific J value. The splitting can be predicted by the number of adjacent protons n in the system, creating a multiplicity of $n + 1$. Under the assumption of equal J values, the multiplett splitting follows the Pascal triangle and the amplitudes of the resonances can be calculated: doublet 1:1, triplet 1:2:1, and quartet 1:3:3:1 etc. The integral of the whole multiplet equals the area of the same resonance without J-coupling.

Figure 3.7, for example, illustrates the j-coupling of the GABA molecule and the corresponding resonances. The spin system of GABA can be approximated as an $A_2M_2X_2$ system (A being the protons at C_4 at 3.0 ppm, M being the protons at C_2 at 1.9 ppm, and X being the protons at C_3 at 2.3 ppm). Assuming $J_{AM} \approx J_{MX}$ and $J_{AX} \approx 0$ the spectrum of GABA consists of a quintet at 1.9 ppm and two triplets at 2.3 & 3.0 ppm, respectively [77].
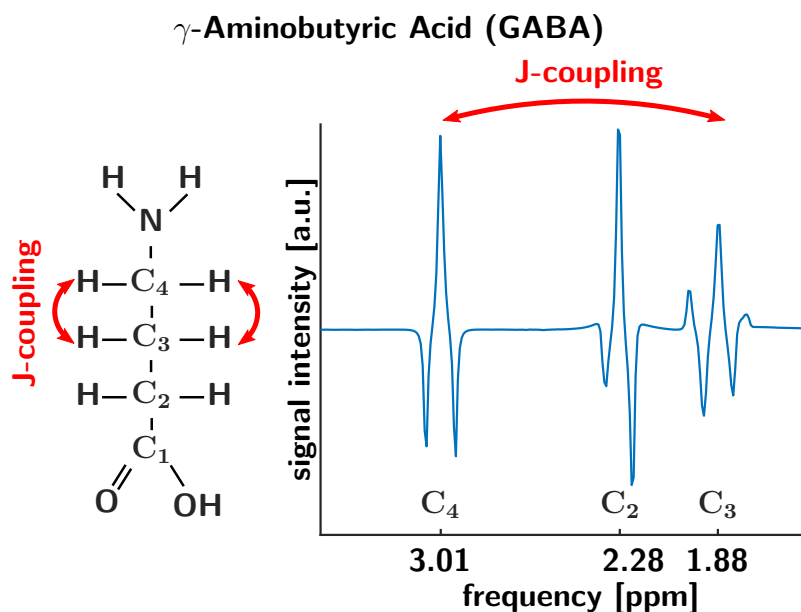
Figure 3.7 – GABA molecule and J-coupling - Structural formula of GABA (left) and 3 T ^{1}H MR spectrum with J-coupling connections. Adapted from [78, 79].

3.4.4 MEGA-PRESS

The **MEscher-GArwood Point RESolved Spectroscopy (MEGA-PRESS)** is an edited spectroscopy technique which exploits the phenomenon of J-coupling to resolve spectral overlapping resonances [80]. The following implementation is used in this dissertation: In comparison to a standard PRESS, additional frequency-selective Gaussian-shaped pulses are added symmetrically around the second π-pulse (Figure 3.8 in green) to manipulate the 3-ppm triplet.
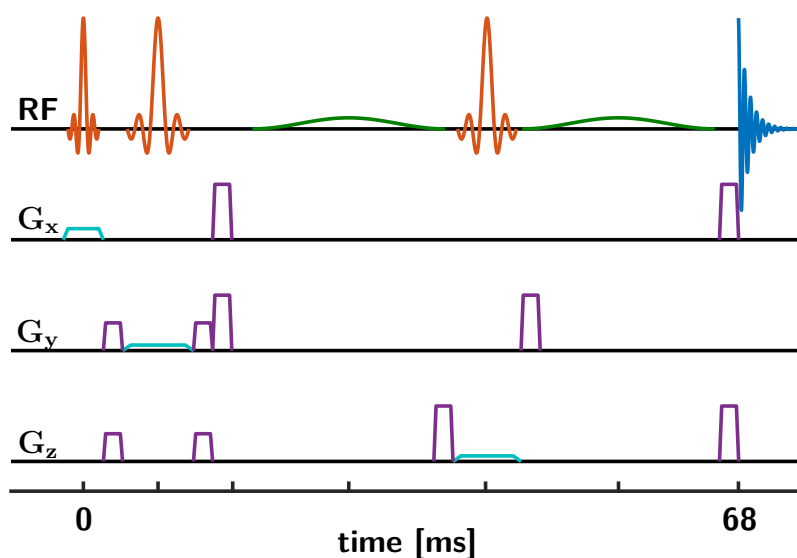
Figure 3.8 – **MEGA-PRESS sequence diagram** - Excitation and refocusing RF pulses (orange) with slice selective gradients (cyan) to create a spin echo (blue). Crusher gradients (purple) are applied to dephase unwanted echos. Gaussian-shaped MEGA pulses (green) are used for frequency-selective manipulation. Adapted from [76].

In the brain, the 3-ppm triplet of the low-concentration metabolite GABA is usually overlaid by the creatine resonance. The GABA-edited spectroscopy sequence (Figure 3.8) is adapted to resolve this issue. The MEGA experiment is divided into two sub-experiments differing in the frequency at which the editing pulse is applied (see Figure 3.9). In the OFF experiment, the editing pulses are applied off-resonance, typically at 7.5 ppm. At TE = 68 ms the 3-ppm triplet evolves such that the outer parts of the triplet are inverted compared to the center resonance. In the ON experiment, the editing pulses are applied at 1.9 ppm ($^3CH_2$) and the coupled $^2CH_2$ peaks of GABA evolve such that the outer parts of the 3-ppm triplet are upright compared to the center resonance. By subtracting the OFF spectrum from the ON spectrum, the 3-ppm GABA resonance is resolved into a pseudo-doublet, and all resonances not affected by the editing pulse are removed upon subtraction - e.g., the 3-ppm creatine resonance.
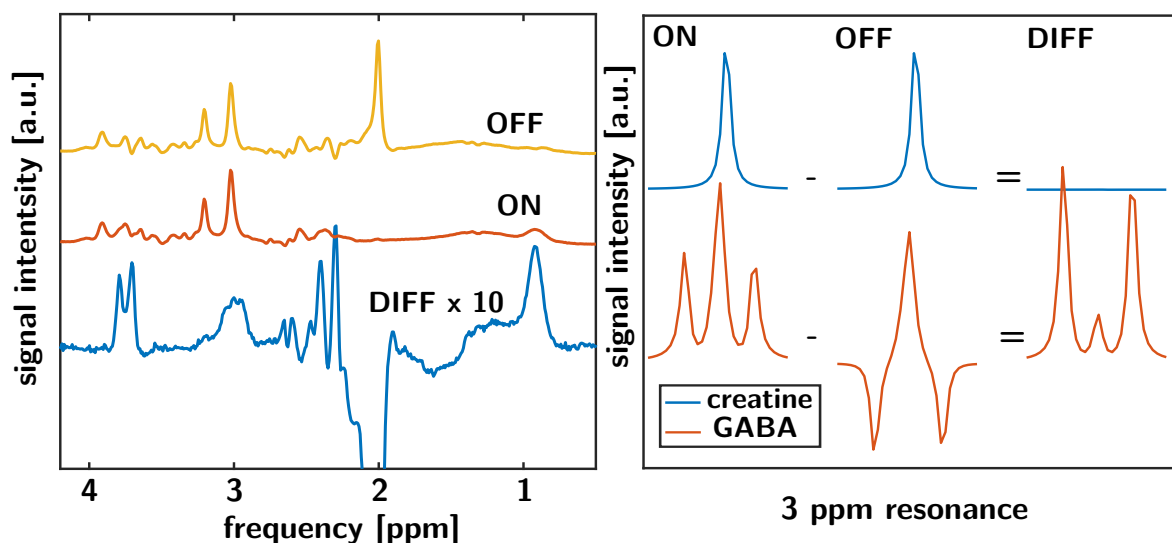
Figure 3.9 – GABA-edited MEGA-PRESS experiment - ^{1}H MRS spectra from each sub experiment (ON with editing pulse at 1.9 ppm; OFF with editing pulse at 7.5 ppm) and the difference (DIFF) spectrum (left). Detailed evolution of the 3-ppm GABA and the creatine resonance during the sub-experiments (right). Right figure adapted from [79].

Compared to conventional MRS, spectral editing tends to be more delicate and demanding for various reasons:

- Due to the low abundance of GABA and its coupled signals larger spectroscopy volumes than in standard PRESS have to be chosen to achieve sufficient SNR [81]. Commonly, these volumes are on the order of 25-30 ml [82, 83].

- Frequency and phase alignment between the two sub-experiments is crucial to avoid subtraction artifacts. Frequency drift can be introduced by gradient heating and subject motion [84]. Therefore, it is advisable to store the individual averages to correct for frequency-and-phase drift in the post-processing [85].

3.4.5 MRS quantification

It is an essential aim to calculate metabolite concentrations based on the integral over the real part of the resonance peak in the frequency domain or the FID amplitude of a certain frequency component in time domain. These metabolite concentrations can be used to investigate pathological alterations in specific brain regions. Unfortunately, the signal amplitudes depend on coil load - e.g., composition and size of the sample - and the induced signal during the MRS

acquisition. Therefore resonance amplitudes are not directly comparable between subjects as the amplitude estimates are influenced by external factors - e.g., the shape of the head and weight of the subject -, in addition to differences in metabolite levels. Relative quantification by normalizing each metabolite signal to the creatine signal is a convenient method to cancel out external factors and arrive at comparable metabolite estimates. It assumes creatine to be stable between subjects and unaltered by pathologies.

Prior to the quantification various pre-processing steps are included:

- Frequency-and-phase alignment of the individual transients to account for frequency drifts during the acquisition [85].

- Zero-filling of the time domain data. This process increases the apparent frequency resolution after applying the FFT without altering the line shape of the spectrum.

- Line broadening to increase SNR by applying a Gaussian filter in the time domain. The filter equals a multiplication with an exponentially decaying function with a certain line broadening constant. This filter attenuates the noise in the data, as this is mainly represented by the data points at the end of the echo. Additionally, the echo will decay faster which broadens the line shape of the resonances, as the a natural T_2 time is reduced.

- Residual water filtering by singular value decomposition (SVD).

- Frequency alignment of MEGA-PRESS sub-experiments before calculating the difference spectrum.

- Quantification of the metabolite, either in the time or frequency domain.

Several approaches to determine the contribution of different metabolites to the signal exist, and the ones used in the present work are revisited in the following:

- **Gannet 3.1** is a toolbox specifically developed to quantify GABA-edited spectroscopy [86]. It includes frequency-and-phase correction and rejection of corrupted averages, zero filling up to 32k datapoints, 3 Hz Gaussian line broadening, and calculation of the difference spectrum. Afterward, a 'GABAGlx' model is applied to the frequency domain spectrum. It models the 3-ppm GABA resonance with a single Gaussian peak at 3.0 ppm, the co-edited ***glutamate + glutamine (Glx)*** resonance at 3.75 ppm as a double Gaussian peak, and the baseline is described by a linear, a sine, and a cosine term. The area under both Gaussian peaks and a fitting error estimated by the ***standard deviation (SD)*** of the residual is reported.

- **LCModel** (Linear Combination Model) is an MRS quantification toolbox analyzing an *in vivo* spectrum in the frequency domain by a linear combination approach of simulated spectra (basis set) [87, 88]. In a linear combination model the spectrum $\hat{Y}(\nu_k)$ with k data points is modeled as [87]:

$$\hat{Y}(\nu_k) = exp\left[-i\left(\phi_0 + \nu_k\phi_1\right)\right] \left[\sum_{j=1}^{N_B} \beta_j B_j(\nu_k) + \sum_{l=1}^{N_M} C_l \sum_{j=N_S}^{N_S} S_n M_l(\nu_{k-n}, \gamma_l, \epsilon_l)\right] \quad (3.6)$$

with the constrains:

$$C_l \geq 0, \; \gamma_l \geq 0, \sum_{j=N_S}^{N_S} S_n = 1. \quad (3.7)$$

The metabolite concentrations C_l are calculated for the N_M metabolites, where the N_M metabolite spectra from the basis set $M_l(\nu; 0; 0)$, are line broadened by γ_l and shifted by ϵ_l, to account for shorter relaxation times *in vivo* and small frequency drifts. Additionally, S_n is a line shape coefficient to correct for field inhomogenities and eddy currents, or other confounders to the line shape. The N_B cubic B-spline, $B_j(\nu_k)$, is needed to approximate a baseline. The exponential term, corrects for zero- and first-order phase differences ϕ_0 and ϕ_1 [87].

A modified least-squares analysis is used to minimize the differences between the model $\hat{Y}(\nu_k)$ and the input signal $Y(\nu_k)$. It is performed iteratively in the predefined frequency range until a convergence is achieved and the metabolite concentrations C_l are determined [87].

The *in vitro* spectra from all individual metabolites which should be included in the analysis, are incorporated in the analysis to maximize the prior knowledge. This basis set can be simulated via density matrix simulations of each spin system with specific pulse shapes and timings of the underlying MR sequence. In contrast to Gannet 3.0, which models the individual resonances, LCModel models the metabolite based on the complete model spectrum (for example the complete GABA spectrum with all resonances).

The confidence levels of the metabolite concentrations are reported as **Cramér-Rao lower bounds (CRLB)** [88]. Usually, a CRLB cut-off of 20 % used to classify whether modeling of a metabolite is reliable.

- **Tarquin** is an MRS quantification toolbox which analyzes MRS data with a linear combination modeling approach [89] in the time domain. Comparable to LCModel, it employs a

non-negative least-squares fitting approach with soft constraints on the signal amplitudes to stabilize the solution of the nonlinear optimization problem.

When modeling MEGA-PRESS difference spectra, Tarquin includes 8 Gaussian resonances in the model (see Table 3.1). Metabolite concentrations and the confidence levels are reported similarly to LCModel.

metabolite	ppm
$GABA_A$	2.85
$GABA_B$	3.1
Glx_A	2.3
Glx_B	2.4
Glx_C	3.7
Glx_D	3.8
NAA	2.01
MM09	0.9

Table 3.1 – **Tarquin difference spectrum analysis** - Positions of Gaussian peaks in a MEGA-PRESS difference spectrum analysis with Tarquin. With MM09 being the macro-molecule at 0.9 ppm.

Similar to LCModel, a basis set can be incorporated in the quantification process, for example, for quantifying the OFF spectrum of a MEGA-PRESS experiment.

3.4.6 Further remarks on MRS

MRS is mostly limited by low SNR. Larger spectroscopic volumes, especially for GABA-edited spectroscopy - at the expense of anatomical specificity -, is one way to overcome this issue. More averages can partially recover lost SNR, but only at a rate of $\sqrt{NEX}$, introducing measurement times that prohibit its use in clinical settings. Additionally, the reported fitting error does not give any information about the real deviation from the actual concentration in the spectroscopic volume, as it only reflects the model accuracy. Therefore, it is of interest to investigate the influence of diminishing spectral quality on the real deviation of the estimated concentrations. These deviations can be calculated with a Monte-Carlo like approach, incorporating a known spectrum, which is manipulated by adding well-defined noise values and artificial line broadening, as well as frequency-and-phase drift. The concentrations estimated with different toolboxes can then be compared to the known concentration to judge the performance of GABA-edited spectroscopy at different levels of spectral quality. This Monte-Carlo like approach was used to design a simulation framework for MEGA-PRESS MRS in **Study 3**.

3.5 Magnetic Resonance Imaging

Apart from MRS, the creation of MR images represents the main application of MRI. The imaging process relies on the ability to localize the source of a particular FID, gradient or spin echo in the sample. Three general concepts are used to achieve spatial encoding: **slice selection**, **frequency encoding**, and **phase encoding**.

3.5.1 k-space and FFT

During the acquisition of an MRS signal, just one time-varying signal is measured from the whole spectroscopic volume. To create a 2-dimensional image, a signal space with 2 dimensions k_x and k_y has to be defined, representing the distribution of the signals introduced by the concepts of spatial encoding. This **k-space** can be extended to 3 dimensions k_x, k_y, and k_z with the signal $S(k_x, k_y, k_z)$ given by:

$$S(k_x, k_y, k_z) = \int_{-\infty}^{\infty} \int_{-\infty}^{\infty} \int_{-\infty}^{\infty} \rho\left(x, y, z\right) \cdot e^{-i \cdot 2 \cdot \pi \cdot (k_x \cdot x + k_y \cdot y + k_z \cdot z)} dx dy dz \qquad (3.8)$$

with the spin density distribution ρ at a certain coordinate. The transformation from k-space to the spin density distribution or **image space** is done via an inverse FFT. The definition of the coordinates is arbitrary and depends on the application. In the following example, a slab excitation is achieved via slice selection. k_y and k_z are defined by phase encoding, while k_x is defined by frequency encoding, which is the encoding scheme used in the **_Fast Low-Angle Shot (FLASH)_** sequence in this dissertation.

3.5.2 slice selection

Similar to MRS a selection of a specific slab can be achieved by superimposing the static magnetic field B_0 with a magnetic gradient G_{SS}, for example, in z-direction.

3.5.3 phase encoding

Phase encoding will be explained for the k_y-direction, but works similarly for the k_z-direction. The k_y-direction in k-space is defined by applying a gradient G_{PH} between the excitation and the readout. A spatial dependence of the phase of each voxel is created according to $\phi_p = -\gamma \cdot G_{PH} \cdot y \cdot t_y = -k_y \cdot y$. To sweep along the k_y-axes, different k_y-values are achieved

by $k_y = \gamma \cdot n \cdot \Delta G_{PH} \cdot t_{PH}$ with the step number n, the gradient step size ΔG_{PH} of the phase encoding gradient G_{PH}, and the phase encoding gradient duration t_{PH}. This process has to be repeated n times to get a full coverage along the k_y-direction. Thus, the k_y-axis is partitioned by a distinct phase of the signal from protons in a certain voxel, which is defined by $n \cdot G_{PH} \cdot t_{PH}$.

3.5.4 frequency encoding

In this example, frequency encoding is used to define the k_x-direction. By applying a gradient G_F during the readout, the signal is given by $S\left(t\right) = \int_{-\infty}^{\infty} \rho\left(x\right) \cdot e^{-i \cdot \gamma \cdot G_F \cdot x \cdot t} \cdot dx$. Therefore, each signal along the k_x-direction is given by $S\left(k_x\right) = \int_{-\infty}^{\infty} \rho\left(x\right) \cdot e^{-i \cdot 2 \cdot \pi \cdot k_x \cdot x} \cdot dx$ with $k_x = \frac{\gamma}{2 \cdot \pi} \cdot G_F \cdot t$ and the k_x-axis is defined by G_F and t.

3.5.5 gradient echo

In MRI, a signal echo can not only be created by a spin echo but also by a **gradient echo**. After excitation, the protons are artificially dephased by applying a gradient (dephasing lobe). By changing the polarity of the applied gradient (rephasing lobe), a gradient echo appears if the gradient moment $(G \cdot t)$ equals the gradient moment of the dephasing lobe. The rephasing lobe reverses the artificial dephasing of the spins affected by the dephasing lobe while T_2 and T_2^* relaxation remain unchanged. It is possible to create a gradient echo for any flip angle allowing the introduction of fast imaging sequences with low-flip angles to avoid limitations by T_1 relaxation.

3.5.6 3D FLASH

The FLASH sequence is a fast MR imaging sequence [90]. A major advantage over a spin echo sequence is the significantly lower acquisition duration, which allows the acquisition of high-resolution 3-dimensional MR images of complex anatomical structures in clinically feasible time. It is considered a significant breakthrough in MRI, paving the way for the success of MR in radiological imaging. It is based on the combination of a simple gradient echo combined with low flip angles for excitation and gradient spoiling, which artificially dephases remaining transversal magnetization prior to the next excitation, to allow fast repetition. A 3D FLASH sequence is depicted in Figure 3.10.
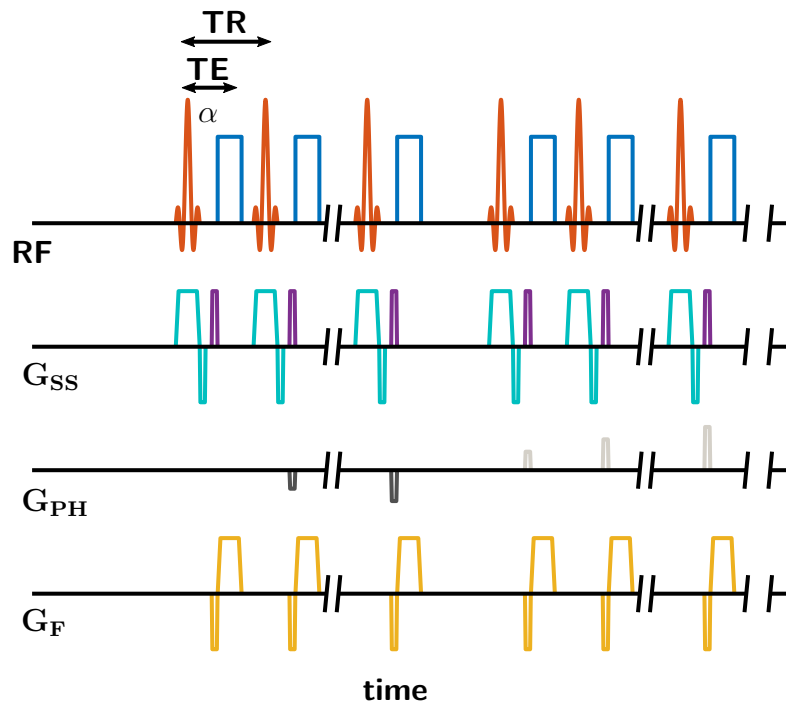
Figure 3.10 – 3D FLASH sequence diagram - The imaging contains an excitation pulse for a whole slab (Cyan: slice selective gradient) with flip angle α (orange), phase encoding in z- (purple) and -y-direction (grey), frequency encoding (yellow), and readout (blue)). Adapted from [91].

During the FLASH sequence, each gradient echo experiment is initiated by low flip-angle excitation ($\alpha \sim 5°$) of a whole slab usually including the whole 3D volume of interest (RF-pulse: orange gradient: cyan). The k_z- and k_y-axes are both defined through phase encoding (gradients: purple & gray), while k_x is frequency-encoded (yellow). The 3D k-space is filled with $n*m$ gradient echos with m & n phase encoding steps in the z- and y-direction, respectively. As the z-direction is phase-encoded, a 3D volume without gaps between the slices and with a high resolution ($\Delta z = 1$ mm) can be created. The first half of the k-space in k_y-direction is sampled from the center ($k_y = 0$) moving in the positive direction ($k_y > 0$), while the second half is sampled from the center moving in the negative direction ($k_y < 0$).

3.6 Magnetization Transfer in MRI

Magnetization transfer describes the exchange of magnetization between proton-containing species through various processes. They can broadly be divided in **_conventional magnetization transfer (MT)_**, **_chemical exchange saturation transfer (CEST)_**, and **_nuclear Overhauser enhancement (NOE)_**. These processes usually take place simultaneously, and are interfering with each other. The MT mechanism, as a contrast in MRI, was accidentally discovered by Balaban in 1998 [92, 93]. While attempting to perform a frequency-selective proton exchange experiment of urea in water, he observed a saturation frequency-independent reduction of the water signal in the MR image. Figure 3.11 summarizes the various magnetization transfer effects in tissue.
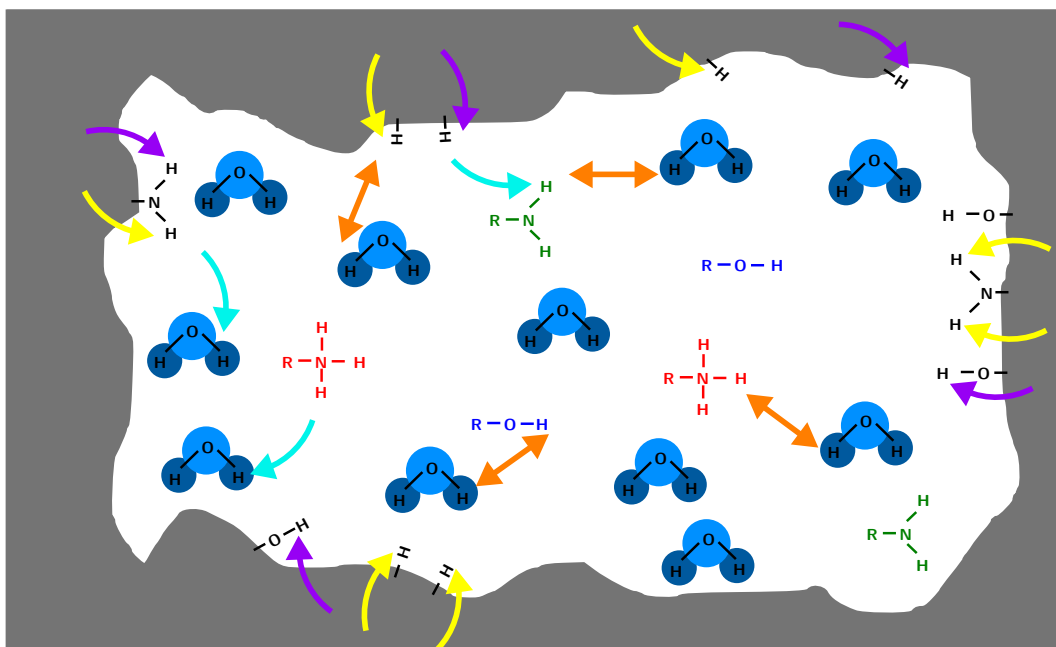
Figure 3.11 – **Magnetization transfer mechanisms** - _In vivo_ magnetization transfer processes in the vicinity of a macromolecule (gray). The model includes molecules in solution with hydroxyl (blue), amine (green), and amide (red) groups in the water pool. At the surface of the macromolecule, similar functional groups are presented. The magnetization transfer is divided into intramolecular Nuclear Overhauser Enhancement (NOE) (purple: direct; yellow: exchange-relayed), intermolecular NOE (cyan) and chemical proton exchange (orange). Conventional Magnetization Transfer is not depicted in the figure. Adapted from [94].

3.6.1 Conventional Magnetization Transfer

The conventional magnetization transfer (MT) effect is a common contrast mechanism in MRI, exploiting the magnetization transfer of bound protons. The ^1H image signal of non-fatty tissue contains contributions from three different but indistinguishable pools of proton-binding molecules. The **free water pool** contains rapidly rotating and freely diffusing water, and is characterized by a very narrow resonance peak and long T_1 and T_2 relaxation constants. It is the primary source of contrast in conventional MRI.

The **macromolecular pool** contains protons which are bound in macromolecules and therefore are highly movement-restricted. Consequently, protons in the macromolecular pool are characterized by a short T_2 relaxation time [95], causing a broad resonance. Macromolecular protons have a negligible contribution to the conventional MR contrast due to the fast relaxation.

The **bound water pool** contains protons in water molecules that are bound to the surface of macromolecules. These water molecules are commonly known as hydration layer. The magnetization of the bound water pool can be transferred to the macromolecules either via cross-relaxation or chemical exchange. Additionally, the bound water pool indirectly mediates the interaction between the macromolecules and the free water pool as it exchanges magnetization with both pools. As the macromolecular and the bound pool are closely associated, they can be grouped into the **bound pool**.

The MT contrast exploits interactions between the bound and the free water pools by applying a saturation pulse off-resonance from the water frequency prior to excitation - e.g., prior to an imaging or spectroscopy sequence. This MT pulse has a bandwidth of several hundred Hz and is shifted by 1 to 25 kHz relative to the water resonance [95]. Therefore, the magnetization of the protons in the bound pool is excited without affecting the protons of the free water pool. Through cross-relaxation and chemical exchange, the magnetization is transferred between the bound and the free water pool. Thus, the equilibrium magnetization M_0 of the free water pool is reduced prior to excitation of the image sequence, causing a signal suppression. The MT effect is part of every magnetization transfer experiment and is encountered over a wide frequency range. It introduces a broad saturation profile with a slightly stronger reduction down-field of the water resonance, which is an property of the MT [96].

The signal reduction can be expressed through the magnetization transfer ratio (MTR):

$$MTR = \frac{M_0 - M_{sat}}{M_0} \tag{3.9}$$

with M_0 and M_{sat} being the magnetization without and with the application of a saturation pulse, respectively.

3.6.2 Chemical Exchange Saturation Transfer (CEST)

The main effect observed in the present dissertation is based on the reversible physical exchange of protons between two molecules, A and B. The observed ^{1}H MRS spectrum of A and B is highly dependent on the frequency difference Δf and the exchange rate k (ranges from nanoseconds to seconds) between both molecules.

Under the assumption that the exchange rates ($k_{A \to B} = k_{B \to A} = k$) and T_2 relaxation times are equal, three different regimes exist: $k << \Delta f$ (slow exchange regime), $k \approx \Delta f$ (intermediate regime), and $k >> \Delta f$ (fast regime). In the slow regime, two separated peak with a difference of Δf are observed. For increasing exchange rates k the peaks broaden, as the T_2-relaxation is enhanced by the chemical exchange (transversal magnetization decreases when an excited spin 'leaves' the molecule), and the FWHM is inverse proportional to T_2. In the intermediate regime, one broad peak of both species occurs. In the fast regime, a single peak representing the average frequency of the relative populations of both species exists.

CEST describes a sub-process in the general picture of MT: the dynamic transfer of magnetization between different proton-containing species through chemical exchange. The term chemical exchange does not only include the physical exchange of two protons. It also includes changes in conformation, the movement of molecules in different tissue compartments, or the change from bound to free water.

CEST imaging exploits the chemical exchange of various molecules with water. The basic principle includes the frequency-selective saturation (**labeling**) of a target molecule - e.g., a protein - without affecting the water resonance, prior to an imaging sequence. The water signal is reduced by the chemical exchange between the free water pool and the labeled molecule (see Figure 3.12). As the saturation duration is long compared to the timescale at which the exchange happens, a sufficient reduction of the water signal can be achieved. Therefore, it is possible to resolve metabolites with a low abundance compared to the water signal, as the occurrence of several proton exchanges amplifies the reduction of the water signal.
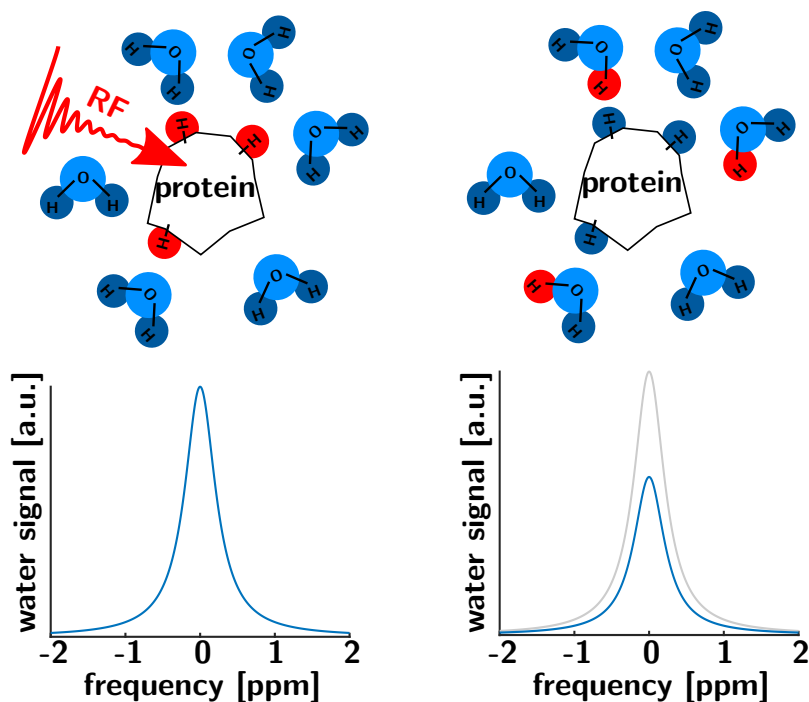
Figure 3.12 – CEST principles - The protons in the free water pool (dark blue) are indistinguishable from the protons in the labeled protein pool (red) (top left) until chemical exchange happens (top right). The chemical exchange results in a reduction (bottom right) of the measured water signal compared to an unsaturated state (bottom left). Adapted from [97].

Molecules in the slow and intermediate exchange regime are usually CEST-visible at $B_0 = 3$ T, while the fast exchange regime exhibits no visible CEST effect as the exchange happens too fast to achieve saturation. As the classification of the regime is based on the frequency difference Δf, CEST profits from higher magnetic field strength B_0 as the frequency difference Δf between water and a certain molecule increases with B_0. On the one hand, this allows a more specific saturation of the molecule, and on the other hand, it increases the range at which a CEST effect is detectable via MR. Additionally, it increases the SNR and the contrast-to-noise ratio of the CEST effect. As a necessity, the target molecule should resonate at a sufficient distance Δf from the water resonance to reduce the direct saturation of the water.

Another limiting factor to the visibility of the CEST effect is the exchange rate k of the target molecule. This rate is highly dependent on the surroundings of the target molecule. Several factors such as concentration, pH value, temperature, distribution across tissue compartments, or the conformational state of a molecule are known to affect k. There are several approaches to exploit the CEST effect to determine factors such as the pH value of a specific tissue [98] or the concentration of a particular metabolite [99]. These quantitative approaches are highly

sophisticated and require high saturation efficiency, high frequency selectivity, a homogeneous magnetic field, and excellent SNR, requiring long acquisition times. Therefore, these quantitative approaches are usually not feasible in a clinical environment. It is possible to calculate a semi-quantitative CEST effect at the cost of distinguishing between changes in one of the effects on k mentioned above.
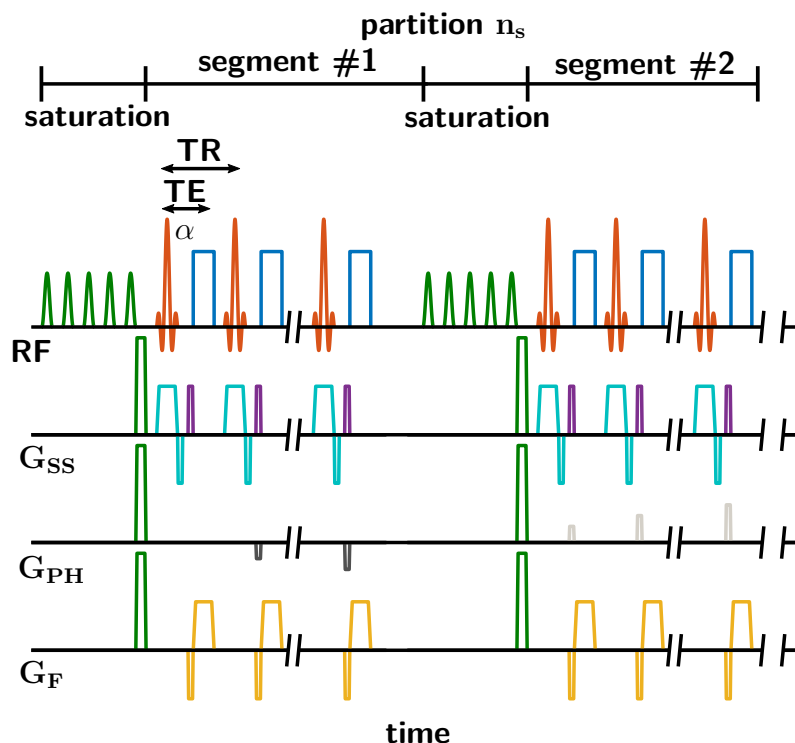
Figure 3.13 – **Segmented CEST 3D FLASH sequence diagram** - Saturation module (green) with Gaussian-shaped pulses and crusher gradients. The imaging contains an excitation pulse for a whole slab (Cyan: slice selective gradient) with flip angle α (orange), phase encoding in z- (purple) and -y-direction (grey), frequency encoding (yellow), and readout (blue)). The segmentation allows the application of another saturation module, for example, after half of the k-space of a certain slice is sampled. Adapted from [91].

The CEST effect depends on the parameters used during the saturation of the target molecules. A typical saturation module used in a clinical scanner is depicted in the CEST 3D FLASH sequence (see Figure 3.13 saturation module: green). It is formed by a train of $n = 5$ frequency-selective Gaussian-shaped RF pulses of a certain duration t_{sat} and amplitude B_1 as well as **_inter pulse delays (IPD)_**. A set of crusher gradients is applied to dephase unwanted magnetization prior to imaging. The CEST sequence allows a segmented acquisition. Therefore, a saturation module could be applied at different time points during the k-space, for example, after half k-space sam-

pling. The segmentation avoids reduction of the observed CEST effect through T_1 relaxation. The introduction of a pulsed saturation module is required as clinical MRI is constrained through SAR[1] limits.

The saturation parameters need to be optimized to maximize the visible CEST effect or a quantitative parameter of the target molecule. In the course of optimization, aqueous phantom solutions at several pH values with varying concentrations or conformational states of the target molecule are investigated with a large number of combinations of n, B_1, t_{sat}, and IPD values.

Typically the maximal values for t_{sat} and IPD are preferred, because they maximize the visible CEST effect. These values are constrained by the RF amplifier of the MR scanner. The number of pulses n determines the total saturation time. For total saturation times $> 5 \cdot T_{1w}$ steady-state saturation is achieved (T_{1w} being the T_1 relaxation value of water). In the steady-state, the loss of visible CEST effect during the signal acquisition is counteracted during the next saturation. Therefore, the CEST effect remains stable throughout the entire experiment. In this case, the CEST effect is only limited by the real chemical exchange rate, and not affected by T_1 relaxation during signal acquisition. For total saturation times $< 5 \cdot T_{1w}$, the measured CEST effect is reduced by T_1 relaxation. Even though steady-state acquisition is preferable, it requires longer measurements.

The amplitude B_1 has to be suited to the target molecule. Generally, the higher the exchange rate k, the higher the B_1 required needed for sufficient saturation. The CEST effect for typical metabolites in the human brain is visible down-field of water (> 4.7 ppm). It is generally grouped in hydroxyl (-OH), amine (-NH), and amide ($-NH_3$) groups with different resonance frequencies. Several applications are investigating the CEST effect of amide protons in proteins, peptides, and small lipids or brain metabolites such as glutamate, GABA or creatine, usually conducted at field strength > 3 T [100, 101].

3.6.3 Nuclear Overhauser Enhancement

The nuclear Overhauser enhancement (NOE) is a magnetization transfer effect typically occurring up-field from water (< 4.7 ppm) at the chemical shift of carbon bound protons, and non-exchangeable aliphatic and olefinic protons. It is caused by the bipolar interactions between protons. In contrast to J-coupling, which is mediated via bonds, it is mediated through space. Similar to J-coupling, with the spin state of a certain proton influencing nearby protons.

---

[1]SAR (Specific Absorption Rate) [W/kg]: Absorbed RF power per mass unit of a sample. In the brain it is limited to 3W/kg averaged over 10 minutes.

NOE can either take place within the molecule (intramolecular) or between different molecules (intermolecular). Mobile macromolecules such as proteins, peptides or lipids, as well as spatially restricted metabolites (e.g., metabolites in vesicles), are the source of intramolecular NOE in the brain. Apart from the described direct NOE, a exchange-relayed NOE, mediated through the magnetization transfer of fast exchanging groups (-OH and -NH$_2$) and the subsequent transfer of magnetization to the macromolecular backbone, exists. In contrast to the chemical exchange, both NOE effects build up in time as they are comparable to a relaxation process.

3.6.4 Quantification of CEST: The z-spectrum and MTR$_{asym}$
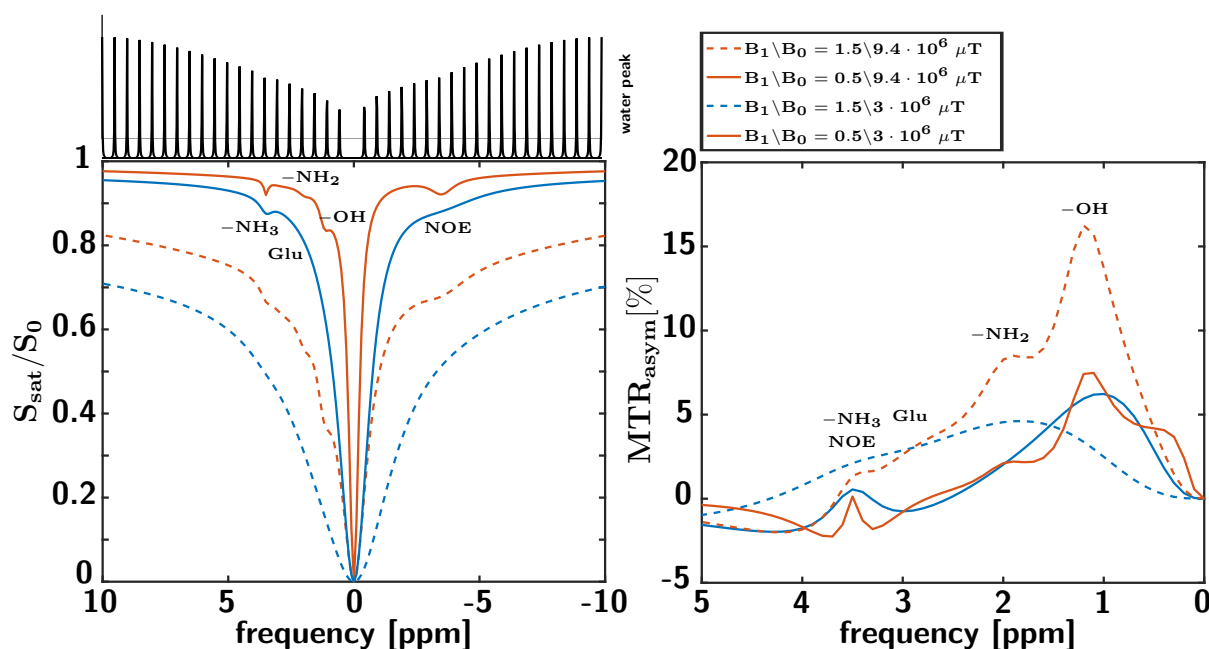
Figure 3.14 – z-spectrum and MTR$_{asym}$ - Simulated z-spectra (left) and corresponding MTR$_{asym}$ (right) at various B$_0$ strengths and B$_1$ amplitudes including conventional MT, amine, amide, glutamate, hydroxyl and NOE pools. The respective water signal (B$_1$\B$_0$ = 0.5\9.4 · 10^6 μT) is shown on top of the z-spectra.

Common CEST experiments consist of n_{Dyn} dynamics which differ in the frequency $\Delta\omega$ at which the saturation pulse is applied. The water frequency is typically defined as the center frequency with 0 ppm, and the dynamics are used to sample a range of frequencies - e.g., from 10 (down-field) to -10 (up-field) ppm. The measurement time increases linearly with the frequency resolution and bandwidth sampled in the CEST experiment.

A typical method to evaluate the CEST effect is the calculation of the z-spectrum [102] by plotting the signal ratio between the signal intensities S_{sat} (with an applied saturation pulse) and

S_0 (without a saturation pulse) against the frequency $\Delta\omega$ of the saturation pulse.

The left side of Figure 3.14 depicts a simulated z-spectra including chemical exchange of hydroxyl, amine, amide, and glutamate groups, as well as conventional MT and NOE effects with realistic *in vivo* exchange rates, relaxation constants and concentrations. The simulations include different field strengths B_0 (blue: 3 T; orange: 9.4 T) and saturation amplitudes B_1 (solid: 0.5 μT; dotted: 1.5 μT). The respective water peak is shown in the top row. As expected, SNR and frequency resolution increase with B_0. Higher saturation amplitudes B_1 increase the visible CEST effect at the cost of peak broadening. Besides, conventional MT increases with higher B_1, adding a broad asymmetric down-field saturation, which is an inherent property of MT. Finally, increasing B_1 amplify the direct water saturation, evidenced by the broadening of the peak around 0 ppm.

A straightforward approach to quantify the CEST effect of an exchanging resonance in the z-spectrum is the ***magnetization transfer ratio asymmetry (MTR$_{asym}$)*** analysis [98] (see right column Figure 3.14). Assuming the water frequency to be exactly centered at 0 ppm, the asymmetry is calculated as follows:

$$
\begin{aligned}
MTR_{asym} &= Z_{ref} - Z_{lab} \\
&= Z\left(\Delta\omega_{ref} = -\Delta\omega_{lab}\right) - Z\left(\Delta\omega_{lab}\right) \\
&= \frac{S\left(\Delta\omega_{ref} = -\Delta\omega_{lab}\right) - S\left(\Delta\omega_{lab}\right)}{S_0}
\end{aligned}
\tag{3.10}
$$

with the z-spectrum value of a labeled proton Z_{lab}, a reference z-spectrum at the opposite frequency Z_{ref}, and the signal intensity without a saturation pulse S_0. By calculating the MTR$_{asym}$ symmetrically around the water resonance, all balanced effects such as symmetric water saturation are canceled out. The resulting peak is a combination of down- and up-field magnetization transfer effects - e.g., MTR$_{asym}$(3.5 ppm) includes chemical exchange of down-field amide protons (3.5 ppm), up-field NOE (-3.5 ppm), and broad asymmetric MT. MTR$_{asym}$ describes a mixture of the above effects at a certain frequency, and is proportional to the concentration of the target molecule. It is sensitive to micro-environmental changes (e.g., pH and conformation). Accordingly, the semi-quantitative evaluation of CEST via MTR$_{asym}$ has to be interpreted with care. Contributing effects can be reduced or enhanced by optimizing the saturation parameters, which have to be adjusted for each application and metabolite individually.

3.6.5 Amide proton transfer (APT)-weighted imaging

The amide proton transfer-weighted (APT$_w$) imaging is a sub-field in CEST imaging focusing on the investigation of amide protons bound in the backbone of solute peptides, proteins, and small mobile lipids. These protons resonate at 3.5 ppm in the z-spectrum. It has been shown that APT$_w$ imaging is a valuable tool for tumor grading [103, 104] and it has been applied in the investigation of multiple sclerosis [105] and Parkinson's disease [15, 106].

Apart from the quantitative measurement of protein concentrations, APT$_w$ imaging is sensitive to micro-environmental changes in and around proteins. These include pH shifts, allowing APT$_w$ imaging to be used to generate *in vivo* pH maps [13], as well as monitor global protein folding states [107, 108], with potential applications in neurodegenerative diseases. As APT$_w$ imaging is subject to various confounders, the *in vivo* interpretation remains challenging.

Assuming a two-pool model with a small amide and a large water proton pool with full saturation of the amide protons, the **amide proton transfer ratio (APTR)** is given by [13]:

$$APTR = \frac{k_{sw} \cdot T_{1w} \cdot [amide\ proton]}{[water\ proton]} \cdot \left(1 - exp\left(-\frac{t_{sat}}{T_{1w}}\right)\right) \tag{3.11}$$

with $[amide \setminus water\ proton]$ indicating the proton concentrations of both species, the pH-dependent amide proton exchange rate k_{sw}, the water relaxation time T_{1w}, and the saturation time t_{sat} of the frequency-selective RF pulse. For rat brain tissue the amide proton exchange rate has been determined as $k_{sw} = 5.57 \times 10^{pH - 6.4}$ via CEST pH maps [13]. Subsequently, MTR$_{asym}$ contains a combination of the inherent asymmetry of conventional MT and APTR:

$$MTR_{asym}(\Delta\omega) = MT(\Delta\omega) + APTR(\Delta\omega) \tag{3.12}$$

The equations 3.11 and 3.12 are approximations of the observed chemical exchange, as the folding state of the proteins is not considered in the equations. In the present dissertation, only semi-quantitative analysis was performed using MTR$_{asym}$, as no steady-state saturation was applied in the *in vivo* measurements.

3.6.6 Further remarks on CEST

The CEST effect is highly susceptible to inhomogeneities of B$_0$ and B$_1$. B$_0$ inhomogeneities shift the water frequency, which defines the center frequency of the z-spectrum, leading to miscalculations of MTR$_{asym}$. During acquisition, B$_0$ inhomogeneities are reduced by optimizing the

shim. In addition, the **WAter Saturation Shift Referencing (WASSR)** technique [109] is used to evaluate the B_0 offset of the z-spectrum. WASSR is a high-resolution saturation experiment with saturation frequencies ranging between 1 and -1 ppm. By calculating the minimum of the WASSR z-spectrum, the B_0 offset is evaluated at each pixel position and can be used to correct the z-spectra of the CEST experiment by shifting them by the appropriate frequency offset.

B_1 inhomogeneities compromise the saturation efficiency of a CEST experiment. B_1 sensitivity can be minimized by B_1-corrections with an relative B_1-map in the post-processing [110, 111]. Furthermore, subject motion can introduce severe miscalculations in the CEST effect and require correction during the post-processing. A typical post-processing pipeline to evaluate *in vivo* data includes the following steps:

- Motion correction of the raw image data by co-registrating different dynamics of the CEST and WASSR experiment. It is effective to co-register all dynamics to the dynamic of the target molecule - e.g., all dynamics of CEST and WASSR to the 3.5 ppm dynamic of an APT_w CEST experiment [112].

- Image smoothing with Gaussian or non-local means (NLM) [113] image filters to increase SNR.

- Voxel-wise calculation of the z-spectra by interpolating the z-spectra to resolution of 0.05 ppm [98].

- Calculation of B_0 offset using a periodic maximum-symmetry center frequency (PMSCF) approach of the WASSR z-spectra [109], and applying this B_0 offset correction to the CEST z-spectra.

- Evaluation of MTR_{asym}, over the entire frequency range. Creation of an MTR_{asym} map averaging MTR_{asym} values in a range of 0.5 ppm around the target resonance.

- B_1-contrast correction of the MTR_{asym} images with a relative B_1 map [110]. Therefore, a linear interpolation between $MTR_{asym}(B_1 = 0) = 0$ and the measured MTR_{asym} map is performed with regard to the relative B_1 map. Afterwards, an interpolated MTR_{asym} map with a arbitrary nominal B_1 value can be calculated within the linear range.

- Optional T_1 normalization to account for T_1 relaxation effects on MTR_{asym} [114].

CEST imaging offers several advantages over spectroscopic imaging or single voxel MRS. The spatial resolution is much higher for CEST imaging, which allows resolving specific anatomical

structures. The in-plane resolution of CEST imaging is usually about 1 x 1 mm^2 with slice thicknesses of about 5 mm. In comparison, a cubic MRS volume of conventional MRS is usually about 8 ml large, while volumes for spectral editing of low-concentration coupled metabolites require even larger volumes (typically around 25 ml). Even the increased resolution of spectroscopic imaging is commonly limited to centimeter resolution.

CEST imaging further allows the detection of metabolites or functional groups that are hard to detect with MRS. For example, the amide group of a glycogen molecule resonating at about 6 ppm is undetectable with MRS, since it broadens with increasing temperature due to the accelerating exchange. On the other hand, the peak of the amide group at about 1.2 ppm in the z-spectra of a CEST experiment increases with temperature, and is therefore detectable under *in vivo* conditions [115].

CEST imaging allows the detection of metabolites with shorter relaxation times and higher exchange rates, including amide protons. However, the specificity of CEST is much lower than for MRS due to the stronger overlapping signal peaks of the chemical exchange.

4 Non-MRI approaches

4.1 Optical methods

Optical methods are based on the interaction of visible light (λ between 380 and 740 nm) with particles or tissue. These methods are a common research tool in biology, medicine, and analytical chemistry to determine various properties of the sample. Apart from classical microscopy, several advanced methods have been developed, for example, to study denaturation or aggregation of proteins [116, 117]. Several optical methods were used in this dissertation to substantiate the findings of APT$_w$ imaging, and to elucidate the mechanisms behind specific contrast changes in CEST imaging.

During the *in vitro* CEST optimization, the protein bovine serum albumin (BSA) with *in vivo* protein concentrations was used as a brain model. The denaturation process and the formation of aggregates were investigated by the optical methods described below.

4.1.1 Fluorescence Spectroscopy

Fluorescence spectroscopy is a spectroscopic method from analytic chemistry based on the effect of bio-fluorescence. In summary, fluorescence spectroscopy can be used to determine the denaturation of a protein, since the fluorescence of the protein changes with its conformation. Fluorescence spectroscopy describes the emission of light by a sample, shortly after the excitation by an electron transfer. Therefore, the process can be divided into two sub-processes: excitation $S_0 + h\nu_{ex} \rightarrow S_1$ with an electromagnetic pulse with the energy $h\nu_{ex}$, and fluorescence $S_1 \rightarrow S_0 + \nu_{em} + heat$ with the energy $h\nu_{em}$ of the emitted photon. Orbital electrons in the sample relax from an excited state S_1 into the ground state S_0, emitting a photon.

In this dissertation, fluorescence spectroscopy was used to investigate the fluorescence of the tryptophan residues of BSA to determine its denaturation. Tryptophan possesses the highest intrinsic fluorescence of the three possible fluorescent amino acids (tryptophan, tyrosine, and phenylalanine) in proteins. Tryptophan absorbs at $\lambda \approx 295\ nm$ and the fluorescence maximum is at $\lambda \approx 350\ nm$ [116]. Fluorescence properties such as fluorescence intensity and fluorescence maximum can be used to determine properties of the protein containing tryptophan. The fluorescence maximum is sensitive to changes in the polarity of the local environment and is correlated

with exposure of the tryptophan to the solvent [117]. The tryptophan is completely shielded from the solvent in a fully folded protein. Upon protein denaturation the tryptophan is exposed to the solvent and the polarity of the environment changes from non-polar to the polar, for example, through the dipole moment of water. These dipoles are aligned anti-parallel to the tryptophan, which also possesses a dipole moment. When the tryptophan is excited its dipole moment changes and further energy is lost during the realignment of the solvent dipoles. Therefore, the energy difference between the S_1 and the S_0 state is reduced by these interactions and the wavelength of the fluorescence maximum increases. Consequently, the exposure of tryptophan to a polar solvent shifts the fluorescence maximum.

Therefore, several BSA samples of the target peptide in different folding states have to be prepared by the addition of ammonia. A control sample has to be doped with guanidinium hydrochloride (GdnHCl), which introduces a completely unfolded state. Subsequently, the tryptophan residues of BSA at $\lambda = 295\ nm$ are excited with a laser. The fluorescence of each sample is measured between $\lambda = 310\ nm$ and $\lambda = 500\ nm$. To calculate the degree of denaturation, the ratio of the fluorescence intensities at $\lambda = 330\ nm$ (tryptophan in non-polar environment) and $\lambda = 360\ nm$ (maximum shift if tryptophan is in polar environment) is determined for each sample Ghisaidoobe2014. Finally, the pure protein sample is assumed to be folded entirely, while the GdnHCl-doped sample is defined as completely unfolded. This calibration of the fluorescence emission intensity ratios allows determining the dependency of the protein denaturation on the concentration of the added ammonia.

4.1.2 Dynamic Light Scattering

The following description is based on [118]. The dynamic light scattering (DLS) describes the scattering of light from particles which are in Brownian motion. Thus, DLS can be used to determine protein aggregation, since the formation of aggregate causes formation of proteins with varying hydrodynamic diameters in the sample. DLS measures the Brownian motion introduced by the continuous interaction of particles (for example BSA), with the solvent molecules (for example water). This random walk depends highly on the particle size, as well as the solvent properties such as viscosity and temperature. While the velocity of the Brownian motion is determined by the translational diffusion coefficient D, DLS measures the hydrodynamic diameter $d(H)$ defined by the Stokes-Einstein equation:

$$d(H) = \frac{k_B T}{3\pi\eta D} \tag{4.1}$$

with the absolute temperature T, the translational diffusion coefficient D, and the solvent viscosity η. D depends on the particle size, the surface structure of the particle, the types of ions in the medium, and the particle concentration.

DLS exploits dynamic changes in the light scattering during the Brownian motion of the particles in a dispersion. The sample is illuminated with a laser. With d being the particles diameter and λ the wavelength of the laser, the scattering of the particles is considered to be isotropic for $d = \lambda/10$. Using the Rayleigh approximation, the intensity I of the scattered light is given by $I \propto d^6$ and $I \propto 1/\lambda^4$. This implies that the intensity in polydisperse media (media with different sized particles) is dominated by larger particles.

The Mie theory describes the scattered intensity as a function of the illumination angle for particles with $d \approx \lambda$. For known illumination angles, laser wavelengths, and refractive indices, it is possible to calculate the number distribution of particles in the solvent from the intensity distribution.

Scattering patterns are highly dependent on the motion of the underlying particles. The smaller the particle, the faster the observed scattering intensities fluctuate. The Brownian motion of the particles can now be determined by auto-correlation analysis of the intensity fluctuations. Therefore, the intensity is measured over time (starting at t and subsequently δt). If the signal at the time t of particles underlying Brownian motion were to be compared to the signal at $\delta t \to \infty$, the randomly fluctuating signal would not allow any prediction of the signal intensity $I(\delta t \to \infty)$ from the initial signal $I(t)$. However, for very small intervals δt the intensities can be predicted as they are highly correlated with the intensity at the previous time point t. For small particles, the correlation will decay rapidly with time as they are moving fast. For larger particles, the auto-correlation will remain substantial over a longer period of time.

For samples with different particle sizes, the auto-correlation function is given by $G(\tau) = A[1 + Bg(\tau)^2]$ with the sum of the exponential decays $g(\tau)$ included in the auto-correlation function $G(\tau)$. The parameters A and B represent the baseline and the intersection of the auto-correlation function. These intensity-weighted distributions are highly dependent on particle size. Using Mie theory, it is possible to determine number-weighted distributions reflecting the actual number of particles with different diameters in the sample. The mean diameter and the particle size distribution of the sample can then be determined via single exponential fitting to the number-weighted function, and a non-negative least-squares fit of multiple exponential decays can be used to determine the distribution of different particle sizes in the sample.

4.2 Image Registration

Image registration describes the determination of a transformation T which allows a source image S to be aligned to a reference image R. To this end, a measure of similarity or disparity D is defined. The process of image registration requires optimization of D(T(S),R), which is either a minimization (D measuring the disparity) or maximization (D measuring the similarity). Image registration can be divided into four major steps: feature extraction, feature adaption, calculating the transformation, and application of the transformation.

Linear transformations include rotations, scaling, translations, and other affine transformations [119]. They are global as they alter the whole image, for example by scaling or moving. Local differences, which could be individual size and shape of a brain gyri, can not be accounted for by this transformations. They are suitable to perform intra-subject registrations, but can not be used to perform image registrations between subjects. Linear transformations are used to align different CEST dynamics to account for subject motion during the acquisition.

In contrast to linear transformations, elastic (non-rigid) transformation algorithms account for local structural differences between subjects by non-linearly warping the source image onto the reference image [120]. They can be used to co-register images from different subjects to create a standardized image template.

Image registration algorithms can also be divided into feature and intensity pattern-based algorithms. A feature-based algorithm determines the similarity between images from certain edges and regions in the images. An intensity pattern-based algorithm determines the similarity from the intensity distributions of both images. Feature-based algorithms are affected by saturation during the CEST experiment, which introduces very low pixel intensities for some dynamics. Therefore, certain image features might not be equally discernible in all dynamics. Intensity-based algorithms may likewise be affected by changing intensity patterns between the CEST dynamics and have to be considered with care.

4.2.1 Motion Correction

During CEST acquisition, subjects are likely to move due to the long acquisition time of about twenty minutes. To minimize the miscalculation of the CEST effect, it is necessary to account for subject motion. This is done by the co-registrating all dynamics (source images) to a certain dynamic (reference image). Additionally, all WASSR dynamics are registered to the same dynamic. In this work, this was done with the MATLAB toolbox SPM12 [121], a common tool in neuroscience research. SPM uses a mutual information algorithm to maximize agreement between

images. Mutal information is defined as the information two distributions A and B share [122]. It measures the predictability of B from knowing A. In other words, if A and B are independent, A contains no information about B and vice versa, so the mutual information is 0. Therefore, mutual information can be expressed as the ratio of the joint distribution $p(a, b)$ of A and B relative to the joint distributions $p(a)$ and $p(b)$ of A and B assuming full independence:

$$\log \left(\frac{p(a, b)}{p(a)p(b)} \right) \tag{4.2}$$

By maximizing the mutual information between two images, a transformation can be calculated that achieves maximal spatial alignment. If source and reference image are given in different resolutions, the source image has to be interpolated to match the reference image space. This is usually done by trilinear or higher-order spline interpolation.

4.2.2 Spatial Normalization

Spatial normalization means non-rigid transformations of images from different subjects into a shared coordinate space. This is a common approach in neuroscience, as it allows direct comparison between subjects, and additionally, only one set region of interest (ROI) has to be defined for an entire cohort. This reduces bias and errors introduced by defining individual ROIs for each subject. Cohort ROIs are defined on a standardized template. A commonly used reference space is the MNI-152 template, which is defined by 152 T1-weighted brain scans of healthy subjects containing their shared features [123]. It represents an 'averaged' brain of all these subjects.

In the present dissertation, a cohort template is created with the software Advanced Normalization Tools (ANTs) [124]. This template represents the shared feature space of the study cohort, accounting for structural changes that occur during the progression of HE. The key method for spatial normalization determines a diffeomorphism transformation ϕ. A diffeomorphism is a differentiable map $\phi : A \to B$ which is bijective and has a differentiable inverse $\phi^{-1} : B \to A$. This can be thought of as a deformation field to transform the source image into the reference image space. The existence of ϕ^{-1} allows to transform a source image into reference space and vice versa. Hence, a shared feature space of the cohort can be determined by iteratively updating a mean image of all subjects (reference) with the inverse diffeomorphism ϕ^{-1}, which is created subsequently to the calculation of the diffeomorphism ϕ to transform the individual subject into the reference space.

In ANTs, the diffeomorphism ϕ is generated by minimizing the norm of parameterized function of ϕ for the reference and the source image. This optimization problem is solved with a Greedy Syn [125] algorithm that locally minimizes the parametric function. After ϕ is calculated to normalize a high-resolution anatomical image into the shared feature space, it can be used to transform any image from the subject into the shared feature space - e.g., a low-resolution MTR_{asym} or T_1 map. After transformation, the quantitative maps can be directly compared between subjects with one set of ROI.

5 Aims

The present dissertation aimed to investigate the pathogenetic role of brain ammonia levels and their interplay with clinical parameters during the disease progression of hepatic encephalopathy. Furthermore, effects of SNR and linewidth on the quantification of the inhibitory neurotransmitter GABA were investigated in a simulation framework to evaluate and design a MEGA-PRESS study protocol to investigate GABA alterations in technically challenging regions. Finally, the neurometabolism in regions associated with the cerebello-thalamo-cortical pathway was investigated in HE patients.

The accumulation of ammonia in the brain is assumed to be crucial in the pathogenesis of HE. Human *in vivo* studies were so far limited by the non-invasive accessibility of ammonia in living brain tissue and have been conducted using PET. In **Study 1**, CEST contrasts were optimized with regard to ammonia sensitivity, and a deeper understanding of underlying mechanisms was established to facilitate the conduction of an ammonia-sensitive *in vivo* study.

Study 2 aimed to investigate brain ammonia levels based on an an ammonia-sensitive APT_w-CEST protocol in a clinically well-defined cohort of HE patients and controls. Based on prior findings, hyperammonemia was assumed to be a localized effect in distinct brain regions involved in motor and cognitive processing.

In **Study 3**, a simulation framework was designed to assess limitations in modeling of MR spectroscopy GABA signal due to SNR and linewidths constrains in deep brain structures. Both methodological studies (**Study 1 & Study 3**) improve the general understanding of APT_w imaging and GABA-edited spectroscopy, and are applicable to a broad range of issues.

Study 4 aimed to investigate the cerebello-thalamo-cortical neurometabolism in patients with HE, and to link potential neurometabolic alterations with behavioral changes.

The overarching objective of the dissertation was the methodical adaption of the metabolic MR techniques CEST and GABA-edited spectroscopy to investigate the pathogenesis of HE. It aimed to improve understanding of disease progression in terms of neurometabolic alterations and spatial distribution of ammonia accumulation in the brain.

6 Study 1:
Ammonia-weighted imaging by chemical exchange saturation transfer MRI at 3T

In **Study 1** (Zöllner et al. 2018 `https://doi.org/10.1002/nbm.3947`), the effects of ammonia on *in vitro* APT$_w$ CEST imaging were investigated. The goal was to develop a non-invasive brain imaging method to identify changes in ammonia levels in patients with hepatic encephalopathy. APT$_w$ imaging was performed in various model solutions, including pure ammonia solutions with varying pH, as well as BSA solutions, and pig brain tissue homogenate samples with varying ammonia concentrations. Finally, *in vivo* feasibility measurements were performed in one healthy control and two HE patients. The respective study can be found in Appendix C.
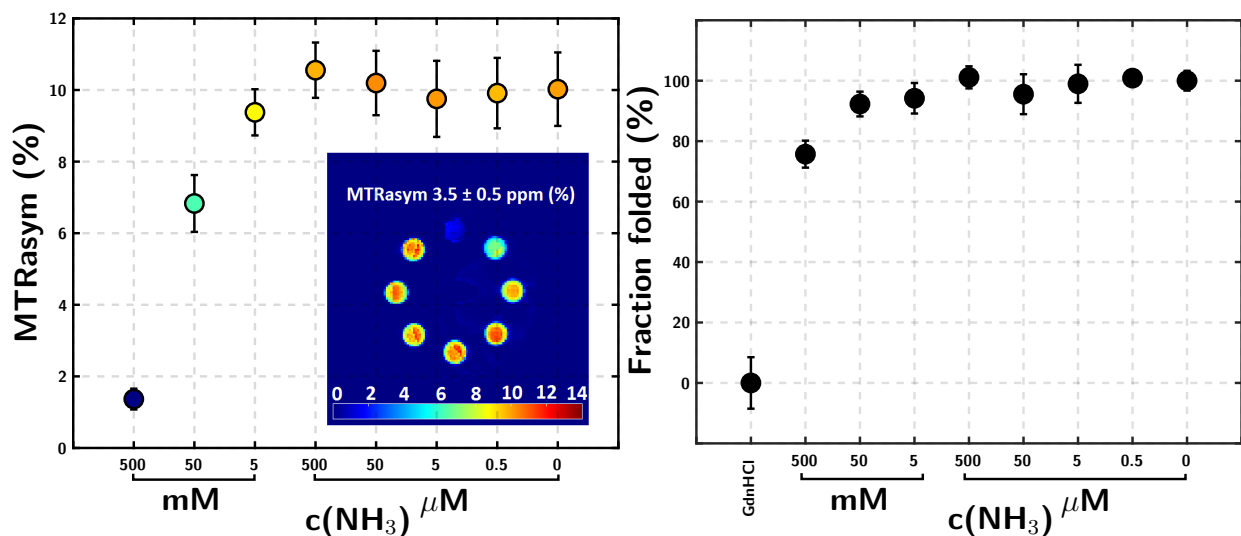
Figure 6.1 – Graphical Abstract Study 1 - Mean APT$_w$ imaging values of BSA sample solutions with varying ammonia concentrations (left), as well as APT$_w$ MTR$_{asym}$ map (inlay). The fraction of folded proteins in the corresponding solutions calculated with fluorescence spectroscopy (right).

6.1 Methods

In the present study, APT_w CEST imaging was optimized to be sensitive to ammonia concentration. Several model solutions with different levels of complexity were included in this *in vitro* study. In a first model solution, the relationship between pH and observable CEST effect was evaluated in a 500 mM pure ammonia solution. In a second model solution, the relationship between ammonia concentration and APT_w CEST effect was measured in a 10 % BSA solution (to model physiological protein content of the human brain) at varying ammonia concentration ([500, 50, 5] mM, [500, 50, 5, 0.5 0] μM). In a third model solution, an realistic *in vivo* model solution consisting of pig brain tissue homogenates was prepared with varying ammonia concentration, and doped with gadopentate dimeglumine to approximate *in vivo* T_1 relaxation times.

All phantoms were imaged with varying saturation amplitude B_1 in steady-state saturation and 66 dynamics to determine the optimal B_1 amplitude for observation of ammonia. Finally, the feasibility of a 3D whole-brain measurement was assessed in a healthy subject and two HE patients, using optimized saturation parameters. Measurement duration was reduced to 22 dynamics (20 minutes) to evaluate clinical feasibility. Patients underwent computer neuropsychometric testing, CFF measurement [52], and West-Haven grading [48, 50] by an experienced clinician.

Potential confounders to the contrast changes in the phantom solutions were assessed with T_1, T_2, and T_2^* mapping. Further changes in the micro-environment of the BSA solutions were determined with fluorescence spectroscopy and DLS experiments to account for protein denaturation and aggregation. The *in vivo* measurements included CEST imaging and T_1 mapping to determine the influence of longitudinal relaxation on the CESTeffect.

The CEST effect was determined via MTR_{asym} analysis with an in-house written MATLAB (MATrix LABoratory) script, including image smoothing with a 3 x 3 pixel Gaussian filter and z-spectra interpolation up to a spectral resolution of 0.05 ppm with a piecewise cubic Hermite interpolation algorithm. The MTR_{asym} (3.5 $\pm$ 0.5 ppm) contrast [98] was defined as the mean MTR_{asym} between 3 and 4 ppm to account for small frequency shifts.

All measurements were B_0- and B_1-corrected using WASSR [109] with a PMFC algorithm and a B_1-contrast correction method [110] based on relative B_1 power maps. These relative B_1 power maps were determined from a double-flip angle method [126] in the *in vitro* measurements and from a heavily smoothed low flip angle gradient echo image in the *in vivo* measurements [127]. Additionally, *in vivo* T_1 mapping was performed with two low flip angle gradient echo images [128]. A simple motion correction was performed by co-registering of all CEST dynamics to the first image volume. The brain tissue was segmented into white matter (WM), gray matter (GM) and CSF via SPM12. Group-wise comparisons (Student's t-test with Bonferroni correction) of

the MTR_{asym} and T_1 values in the *in vitro* and *in vivo* measurements were performed in MAT-LAB with an individual alpha level of 0.05. The correlation between the MTR_{asym} and T_1 was performed with a Pearson's correlation in MATLAB.

6.2 Results

6.2.1 Pure ammonia model solution

In the pure ammonia solution, a pH-dependent MTR_{asym} of ammonia (2.4 ± 0.5 ppm) was observed between pH 1.1 and 5.6, while the observable MTR_{asym} disappeared for pH > 5.6 (Appendix 112 **Figure 1**).

6.2.2 BSA + ammonia model solution

In the BSA + ammonia model solution, a decrease of MTR_{asym} of the amide group (3.5 ± 0.5 ppm) with increasing ammonia concentration was observed for B_1 amplitudes between 0.7 and 1.5 μT. At higher saturation amplitudes ($B_1 > 1.5$ μT) and ammonia concentrations smaller than 5 μM, the proportionality disappeared (Appendix C **Figure 2**). Therefore, a saturation amplitude $B_1 = 1.5$ μT was considered as optimal. A significant reduction of the B_1-contrast corrected MTR_{asym} (3.5 ± 0.5 ppm) was found for ammonia concentrations ≥ 5 mM (Appendix C **Figure 3**).

No correlation between T_2^* and MTR_{asym} (3.5 ± 0.5 ppm) was found. T_1 and T_2 correlated with MTR_{asym} (3.5 ± 0.5 ppm) in the BSA phantom (T_1, r = -0.96; p $<$ 0.05; T_2, r = 0.73; p $<$ 0.05), mainly driven by ammonia concentrations > 50 mM. In another analysis only including ammonia concentrations < 50 mM, no correlations between T_1 and T_2 and MTR_{asym} (3.5 ± 0.5 ppm) were found.

No denaturation of the BSA samples was observed with fluorescence spectroscopy for ammonia concentrations < 5 mM. Protein unfolding of 6, 8, and 25 % was observed for ammonia concentrations of 5, 50, and 500 mM, respectively (Appendix C **Figure 4**). DLS measurements revealed the same particle size distributions for the BSA sample with and without ammonia (c = 500 mM), suggesting that the protein did not aggregate substantially in the samples. The mean particle diameter was calculated to be 3.2 ± 5.3 nm for pure BSA and 3.0 ± 4.2 nm for BSA + 500 mM ammonia.

6.2.3 Tissue homogenate + ammonia model solution

The tissue homogenate + ammonia model solution showed a significant contrast reduction for all samples, except for 50 and 0.5 μM, compared to the tissue homogenate without ammonia (Appendix C **Figure 5**).

6.2.4 In vivo measurement

A whole-slice analysis of the B_1-corrected MTR_{asym} (3.5 ± 0.5 ppm) maps revealed a significant decrease between controls and HE I patients, as well as between both patients. T_1 was reduced in both patients compared to the control (Appendix C **Figure 6** & **Table 2**). The changes appeared to be stronger in GM, and were accompanied by a reduction in T_1. The GM/WM ratio (calculated from the numbers of segmented pixels in each tissue type) revealed no differences between subjects.

6.3 Discussion

APT_w imaging was found to be sensitive to ammonia concentration changes in several phantom measurements with different complexities. In an *in vivo* feasibility study, a reduction of MTR_{asym} (3.5 ± 0.5 ppm) was observed in a HE I patient compared to a healthy control and a mHE patient. In summary, APT_w imaging may serve as a potential tool to investigate *in vivo* brain ammonia levels in HE.

6.3.1 Pure ammonia model solution

The mean MTR_{asym} (2.4 ppm) was found to be base-catalyzed, showing a pH dependency of the observed CEST effect, which disappears above a certain pH (> 5.6) due to the transition from the slow to intermediate chemical exchange regime as previously demonstrated [129]. This suggests that ammonia is not directly observable at physiological conditions using CEST imaging at 3 T.

6.3.2 BSA + ammonia model solution

APT_w signal reductions with increasing ammonia concentrations ≥ 5 mM were observed in the model solutions. Micro-environmental changes in the immediate surrounding of the protein may be introduced by destabilizing effects of ammonia, which increases the hydrophobic behavior of the protein, and may mediate changes in the observed MTR_{asym} (3.5 ± 0.5 ppm) [98]. These suggested mechanisms were underlined by the results from fluorescence spectroscopy, reporting protein unfolding of about 6 % at an ammonia concentration of 5 mM. In addition, a reduction of water T_2 may be related to ammonia [130], introducing another potential pathway causing signal reduction in APT_w imaging.

The correlation between T_2 and MTR_{asym} (3.5 ± 0.5 ppm) may result from structural changes of the protein, as well as T_2-exchange mechanism alterations through the presence of ammonia. The absence of a correlation between T_2^* and MTR_{asym} (3.5 ± 0.5 ppm) could be explained by B_0 inhomogeneities obscuring exchange-related mechanisms in T_2^*.

Structural changes in the protein are the main contributor to the correlation observed between T_1 and MTR_{asym} (3.5 ± 0.5 ppm).

6.3.3 Tissue homogenate + ammonia model solution

In vitro CEST experiments are usually not directly transferable to *in vivo* observations due to the strong semi-solid MT in tissue, altered T_1, and the occurrence of multi-parametric effects, such as the increasing number of overlapping resonances [131]. The tissue homogenate model solution was designed to account for these effects. It exhibited the same signal reduction in APT_w imaging as the BSA phantom, as well as an increased semi-solid MT effect due to the presence of macromolecules in the brain tissue. Yet, the underlying mechanisms of the macromolecular changes introduced by ammonia remain unclear. In comparison to a real *in vivo* measurement, a slightly diluted protein solution was used. Therefore, amide proton concentrations differ between the tissue homogenate and living brain tissue. Additionally, no active metabolism was present in the model solution.

6.3.4 *In vivo* measurement

In vivo data suggested a global APT_w signal reduction with increasing HE severity. Regional differences mainly occur in the occipital cortex and the basal ganglia. Yet, these findings have to be considered preliminary due to the small sample size. Nevertheless, in combination with the phantom measurements, the findings are likely attributed to increasing ammonia concentrations.

6.3.5 Other *in vivo* confounders

Potential confounders in the *in vivo* measurement are mostly driven by micro-environmental changes in the vicinity of the proton. First, pH changes triggered by ammonia accumulation might alter the measured MTR_{asym} [13], even though intra- and extra-cellular pH are controlled in a homeostatic equilibrium. Second, small changes in water content - also related to the low edema hypothesis in HE [132] - may partially change the observed MTR_{asym}. Third, APT_w imaging has been shown to be sensitive to changes in protein content [133] and conformational changes in the protein [107, 108]. Thus, hepatocerebral degeneration [10, 36] may explain signal reduction in the HE brain.

As the number of overlapping resonances increases in the *in vivo* experiment, they have to be considered as possible confounders. Especially, glutamate and glutamine - both sharing amide groups resonating between 3 and 4 ppm [101] - are strongly altered in the pathogenesis of HE [38, 19, 40]. Further experiments have to be established to analyze the extent of MTR_{asym} alterations contributed by changes in brain metabolites.

6.3.6 Study limitations

The phantoms used in the present study should only be accounted for as raw models of pathological brain metabolism changes in HE as they only represented ammonia concentration changes. Changes in other neuro-metabolites - e.g., glutamate, glutamine, and GABA, which play an important role in the emergence of HE [38, 19, 40] - were not considered in the model. Additionally, it is unknown, if the denaturating process observed in the phantom occurs in living tissue. Furthermore, real ammonia concentrations in the human brain of HE patients were found to be 1 to 5 mM [134], which is at the lower limit of the sensitivity of the observed CEST effect.

MTR_{asym} represents a superposition of different magnetization transfer effects such as the CEST and NOE effects of proteins, and a broad conventional MT which is known to be altered in HE [135]. Additionally, T_1 is typically altered in HE [136], leading to further changes in the observed MTR_{asym}. Therefore, it will be necessary to include further corrections such as T_1 normalization [114] or more sophisticated models [137] to distinguish between the observed magnetization transfer effects in the analysis.

6.4 Summary

Study 1 observed a well-defined effect of ammonia load on APT_w CEST imaging in several phantom solutions by decreasing MTR_{asym} values of the amide protons. Yet, the underlying mechanisms in the *in vivo* conditions need to be further explored in future studies. The key finding of the study is the ammonia sensitivity of APT_w imaging, potentially allowing clinical monitoring and investigations of HE.

7 Study 2: Chemical exchange saturation transfer imaging in hepatic encephalopathy

Study 2 (Zöllner et al. 2019 `https://doi.org/10.1016/j.nicl.2019.101743`) aimed to apply the ammonia-sensitive APT_w CEST method established in **Study 1** to investigate CEST contrast changes in a clinically well-defined cohort of HE patients and controls. Whole-brain APT_w CEST imaging was performed to study potential ammonia load changes or the emergence of hepatocerebral degeneration during the disease progression of HE. The respective study can be found in Appendix D.
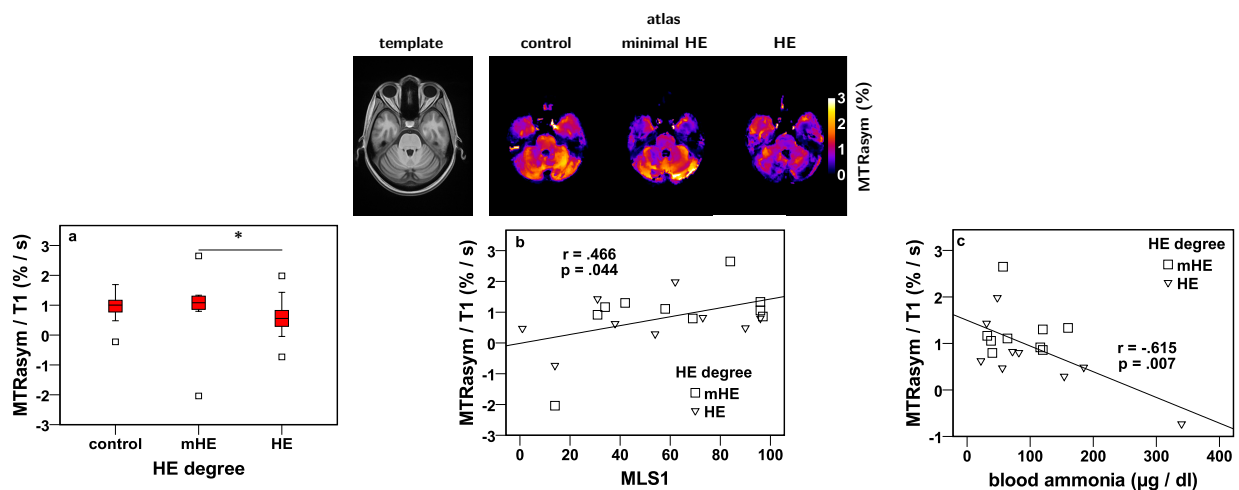
Figure 7.1 – Graphical Abstract Study 2 - Mean group atlases of APT_w imaging of the cerebellum in patients with hepatic encephalopathy (HE) (top row). Group boxplot with mean $APT_w{}^{T1}$ MTR_{asym} in the cerebellum showing a significant decrease in the HE I patients (a). Correlation between psychometric MLS1 score (hand steadiness/tremor) and mean $APT_w{}^{T1}$ MTR_{asym} in the cerebellum (b). Correlation between measured blood ammonia levels and $APT_w{}^{T1}$ MTR_{asym} in the cerebellum (c).

7.1 Methods

7.1.1 Study cohort and clinical assessment

The study cohort included 10 patients suffering from minimal HE and 10 patients with manifest HE, as well as 14 age-matched controls. HE severity grading was performed by an experienced clinician based on the West-Haven criteria [48, 50]. Additionally, computer neuropsychological testing and CFF [52] assessment with portable CFF goggles, and blood sample testing were performed. Exclusion criteria for the whole cohort included any medication acting on the central nervous system, severe intestinal diseases, peripheral/retinal neuropathy, and the diagnosis of neurological or psychiatric diseases other than HE for the patient group. Abstinence of $>= 4$ weeks prior to inclusion was required for patients with alcohol abuse as part of the medical history. Determination of minimal HE was performed with a computer-based neuropsychometric test, including five test batteries with 22 age-validated scores, which reflected motor and cognitive performance. Patients without clinical symptoms of manifest HE, but with >1 abnormal psychometric test were classified as mHE.

7.1.2 MR measurements

The MR protocol included a high-resolution anatomical T_1-weighted scan (1 mm isotropic resolution with 176 slices), a CEST and a WASSR experiment, and two gradient echo scans at different flip angles, each 3D volume covering the whole brain.

CEST experiments were performed with a prototype 3D gradient echo sequence (5 mm slice thickness; 1 mm gap; FoV = (230 x 230)mm^2; matrix size (192 x 192)) with 22 equidistant frequency offsets between -5 and 5 ppm using a pulse train of 5 Gaussian-shaped pulses (pulse duration 100 ms; inter-pulse delay 100 ms; $B_1 = 1.5$ μT) for saturation. An unsaturated S_0 image was acquired by turning off the saturation pulse. 22 equidistant frequency offsets between -1 and 1 ppm were recorded with the same imaging parameters for B_0 correction with WASSR [109].

The gradient echo scans were performed with a flip angle of $4°$ and $15°$ for T_1 mapping [128] and B_1-correction purposes [127].

7.1.3 Post-processing

The post-processing included several steps to create individual MTR$_{\text{asym}}$ maps:

- Motion correction was performed in MATLAB using the SPM12 co-registration function. The 3D volumes of each CEST dynamic were co-registered to the 3D volume of the 3.5 ppm dynamic [112] using a mutual information algorithm and trilinear interpolations. Subsequently, the WASSR dynamics were co-registered to the S_0 image. A brain mask was created by including pixels with relative tissue class probabilities > 0.8 for GM, WM, and CSF which were segmented with the newSegment function of SPM12.

- Firstly, all images were smoothed with an NLM filter to improve SNR, and to avoid image blurring [113].

- Z-spectra were calculated for all voxels with an in-house written MATLAB script. The z-spectra were interpolated to a 0.05 resolution with a piecewise cubic hermite interpolating polynomial algorithm.

- MTR$_{\text{asym}}$ curves were calculated over a frequency range between 0 and 5 ppm in the z-spectra. Subsequently, APT$_{\text{w}}$ MTR$_{\text{asym}}$ maps were calculated by averaging over a frequency range from 3 to 4 ppm.

- A relative B$_1$ map was created by heavily smoothing the $4°$ gradient echo scan. In addition, T$_1$ maps were calculated using the $4°$ and the $15°$ gradient echo volumes.

- B$_1$-one-point-contrast correction [110] was employed to account for B$_1$ inhomogeneities in the MTR$_{\text{asym}}$ maps.

Normalization of the anatomical images, as well as the MTR$_{\text{asym}}$ and T$_1$ maps, was implemented with the open-source software package Advanced Normalization Tools (ANTs) [124, 138]. A template of the current study cohort was created with a diffeomorphism approach applied to the anatomical images of each subject. First, 15 iterative steps of affine transformations were performed to align the images. Second, 15 diffeomorphism transformations were performed iteratively using a Greedy Syn algorithm [125] to create a template. The maximum iteration parameter, measuring the sparsity of the transformations, was increased in every iteration to increase the accuracy of the normalization. Third, the individual diffeomorphism ϕ to warp each anatomical image to the template was calculated, and subsequently the MTR$_{\text{asym}}$ and T$_1$ maps were transformed.

The Neuromorphometrics atlas [139, 140, 141] implemented in SPM12 was used to create 6 ROI - chosen based on prior studies - including both hemispheres. ROI included cerebellum, occipital cortex, putamen, thalamus, caudate, and white matter. In the ROI analysis, a T_1 normalized amide proton transfer - weighted (APT_w^{T1}) MTR_{asym} was calculated to account for T_1 relaxation. Group-level differences were assessed with a pairwise non-parametric Wilcoxon rank sum test. Relationships between CFF and APT_w^{T1} MTR_{asym}, blood ammonia levels and APT_w^{T1} MTR_{asym}, and between psychometric scores and APT_w^{T1} MTR_{asym} were assessed with a bivariate two-sided Pearson correlation test. All statistics were performed in IBM SPSS Statistics for Windows, Version 24.0 (IBM Corp. Armonk, NY, USA)

7.2 Results

The mean group atlases of the APT_w measurements revealed region-specific changes with increasing disease stage, especially in the cerebellum and the occipital region. Smaller changes were observed in the putamen, while the investigated white matter region, the caudate, and the thalamus did not show any group differences (Appendix D **Figure 1**).

7.2.1 Cerebellum

A reduction of mean APT_w^{T1} MTR_{asym} was found in HE patients compared to mHE patients, indicating higher ammonia concentrations or hepatocerebral degeneration in patients with manifest HE. A negative correlation between cerebellar APT_w MTR_{asym} and blood ammonia levels (r = -0.615; p = 0.13) was found. Positive correlations with cerebellar APT_w MTR_{asym} were found for MLS1 (hand steadiness /tremor r = 0.466; p = .044) and WRT2 (motor reaction time r = 0.523; p = .022) scores (Appendix D **Figure 2**).

7.2.2 Occipital Region

Reduced mean APT_w^{T1} MTR_{asym} were found in HE patients compared to control subjects. Additionally, a negative correlation of occipital APT_w MTR_{asym} and blood ammonia levels (r = -0.476; p = .045) and a negative correlation with the MLS2 score (arm/hand precision r = 0.544; p = .016) were observed. Finally, a positive correlation between APT_w^{T1} MTR_{asym} and LVT1 (time per item r = 0.541; p = .015) scores was found (Appendix D **Figure 3**).

7.2.3 Putamen

Increased putaminal APT_w^{T1} MTR_{asym} was found in minimal HE patients compared to healthy controls. Additionally, a negative correlation with the CFF (r = -0.423; p = .013) was found (Appendix D **Figure 4**).

7.2.4 Other regions of interest

No group differences were observed for caudate, thalamus, and the delineated white matter region. Nevertheless, a negative correlation between APT_w^{T1} MTR_{asym} and blood gamma-glutamyltransferase concentrations was found in the thalamus (Appendix D **Table 2**).

7.2.5 Psychometric scores

Motor reaction time (WRT2) and motor performance (MLS1) scores correlated positively with cerebellar APT_w^{T1} MTR_{asym}. APT_w^{T1} MTR_{asym} in the occipital cortex correlated positively with line following scores (LVT1; LVT2), motor scores (MLS1; MLS2), as well as motor reaction time (WRT2) (Appendix D **Table 3**).

7.3 Discussion

In the present study, CEST brain imaging was applied to investigate the link between hepatic encephalopathy, common HE disease markers, and APT_w imaging measures which are assumed to be sensitive to cerebral ammonia levels. Reduced APT_w measures were found in the cerebellum and the occipital region, additionally correlating with psychometric test scores and blood ammonia levels. APT_w MTR_{asym} values were found to be increased in mHE and correlated negatively with the individual CFF. Yet, the multifactorial nature of HE includes several changes in brain metabolism, which may interact with the APT_w contrast mechanisms. Several potential contributions are discussed in the study.

7.3.1 APTw imaging and clinical parameters in HE

During the continuous progression of HE, decreasing fine motor skills and hampered visual discrimination (as reflected by decreasing CFF) are typical subclinical signs of HE [52]. Decreasing

motor performance is reflected in the motor scores, which correlated with the APT_w values in the cerebellum, potentially caused by hyperammonemia or hepatocerebral degeneration. Cerebellar degeneration is coupled to sensorimotor deficits [142] and slowed upper limb movements [143], both tallied by decreasing finger movement frequencies and increased movements amplitudes in subclinical HE [144]. In conclusion, cerebellar involvement in the clinically overt signs of impaired motor performance is substantiated by the correlation with the motor reaction time (reaction time (WRT)2) score.

The mechanisms underlying the APT_w contrast changes in HE are diverse and discussed later on. Yet, the conducted *in vitro* measurements suggest changing protein structures as a primary contributor to the contrast changes. However, the chosen approach cannot discern whether these *in vivo* changes are driven by changes in the protein structure, potentially introduced by hepato-cerebral degeneration [145, 36], or by structural changes of the astrocytes into Alzheimer type II cells and general cell loss [35], or by indirect mechanisms induced by ammonia.

The visual system is assumed to be strongly impaired in HE. It includes worsening in visual perception, reflected in decreasing CFF [52], reduced visual GABA/Cr levels [18], and slowed brain oscillations [146, 53]. Increasing ammonia concentrations, reflected by decreasing APT_w values, may lead to a dysbalance in neurotransmitter homeostasis during the ammonia detoxification process.

Furthermore, putamen and thalamus displayed changes in APT_w measures during disease progression. These findings substantiate the hypothesis of an involvement of the basal ganglia in HE found in brain oscillation studies [147]. Yet, future CEST studies, including larger numbers of patients in higher disease stages, may help clarify the contribution of these regions.

7.3.2 Ammonia in HE

Ammonia is assumed to be a key player in the emergence of HE. As found in **Study 1**, ammonia remains undetectable to CEST imaging at a magnetic field strength of 3 T at physiological pH levels, but may be indirectly observed through its interaction with the APT_w protein signal. These changes are mainly driven by protein denaturation, leading to the assumption that decreasing APT_w signals in the present study are driven through the same mechanism as well. Our findings are in line with a $^{13}NH_3$-PET study [1], showing a link between blood ammonia and the metabolic flux of ammonia. The metabolic flux is defined as the net metabolic clearance rate of intracellular metabolites and arterial ammonia concentrations. This clearance via glutamine synthetase is located in the astrocytes. As APT_w signals predominantly reflect intracellular protein compounds, we assume the contrast changes in the present study to be mediated through ammonia in the

astrocytes. Similar correlations in cerebellum and visual cortex [1] allow the speculation that APT_w values reflect the metabolic flux of ammonia. At present, detailed kinetics of ammonia remain unresolved by CEST imaging, as it does not require a contrast agent and reflects an averaged metabolism of the acquisition interval.

7.3.3 CEST-sensitive confounders

Study 1 adapted APT_w imaging to maximize the contrast gained from changing ammonia concentrations and allowing whole-brain coverage in clinically feasible acquisition times. These changes were driven by protein denaturation *in vitro*, while the *in vivo* measurements include a higher number of possible confounders.

Firstly, changes in the glutamine/glutamate ratio through the clearance of ammonia [148, 10, 149] are frequently observed in HE. As both metabolites resonate between 3 and 4 ppm [131] they may contribute to the APT_w signal. However, we assumed the effect to be negligible, as we showed ammonia to dominate the contrast alterations in our *in vitro* measurement, and as the sensitivity of a 3 T system to changes in either glutamate or glutamine is comparably low [101]. The emergence of a low-grade edema is another pathophysiological mechanism in HE. Yet, the MR visibility remains a matter of discussion in literature, as one study reported changes up to 2 % [132], while another study reported an absence of changes [19]. These changes were assumed to be negligible as several studies at 4.7, and 7 T emphasized minor effects of water concentrations to the contrast formation of APT_w imaging [150, 151].

Lastly, T_1 relaxation changes, which are common findings in HE [136, 28, 152], were compensated by implementing T_1 normalization, which resolves in pure APT_w contrast mechanisms. Additionally, the used saturation parameters are assumed to be roughly insensitive to water T_1 [153].

7.3.4 Study Limitations

The low number of included patients, especially those at higher disease stages (HE II) which showed a substantial signal alteration in APT_w signals, is a limitation of the present study. For these patients, compliance to perform the psychometric testing and to achieve MR data with sufficient quality remains challenging. The number of participants also limited the number of regions in the analysis, and the statistical power. Therefore, the inclusion of a larger cohort would mitigate these power limitations and allow for the implementation of a non-parametric voxel-based analysis [154], which is not user-biased.

The low sensitivity of the CEST technique is a second limitation of the study. To resolve the interplay between APT_w contrast and neurometabolite concentration changes, single voxel CEST techniques [155] and J-edited MEGA-PRESS spectroscopy [80] may be combined in one region. These techniques would allow for a combined investigation of protein signal alterations and neurotransmitter metabolism (GABA, glutamate, glutamine), osmolytes (myo-inositol), and oxidative stress markers (glutathione).

The implementation of faster imaging or spectroscopy techniques would allow the coverage of the whole brain or a certain region with a higher number of CEST dynamics. Consequently, more advanced CEST techniques, such as AREX [133] or EMR [156] could be included. These techniques may reduce the possible impact of T_1 relaxation and MT. More advanced fitting routines could substantiate the findings and allow for differentiation of MT, CEST, and NOE, if an appropriate model is used. Especially, NOE quantification could shed further light on morphological changes which potentially underlie changes of MTR_{asym}.

7.4 Summary

Study 2 revealed a region-specific association between hepatic encephalopathy severity and APT_w signals. Ammonia is assumed to be the main contributor to the contrast reduction in the HE patients, especially in the cerebellum and the occipital region. These findings were linked to blood ammonia levels and several clinical scores. Therefore, APT_w imaging is a potential tool to further investigate the changes during the progression of HE.

8 Study 3:
In silico GABA+ MEGA-PRESS: Effects of signal-to-noise ratio and linewidth on modeling the 3-ppm GABA+ resonance

Study 3 aimed to investigate the modeling of the 3-ppm GABA resonance in a GABA-edited MEGA-PRESS spectrum at various combinations of GABA SNR and line broadening levels. These combinations were used to manipulate a noise-free template spectrum to simulate varying voxel size and B_0 homogeneity. After quantification with two different toolboxes, the estimation error was calculated as the relative difference to the ground truth 3-ppm GABA resonance from the template spectrum. Finally, two *in vivo* scenarios were compared to the simulated spectra to evaluate potential estimation errors in both scenarios. The respective study can be found in Appendix E.
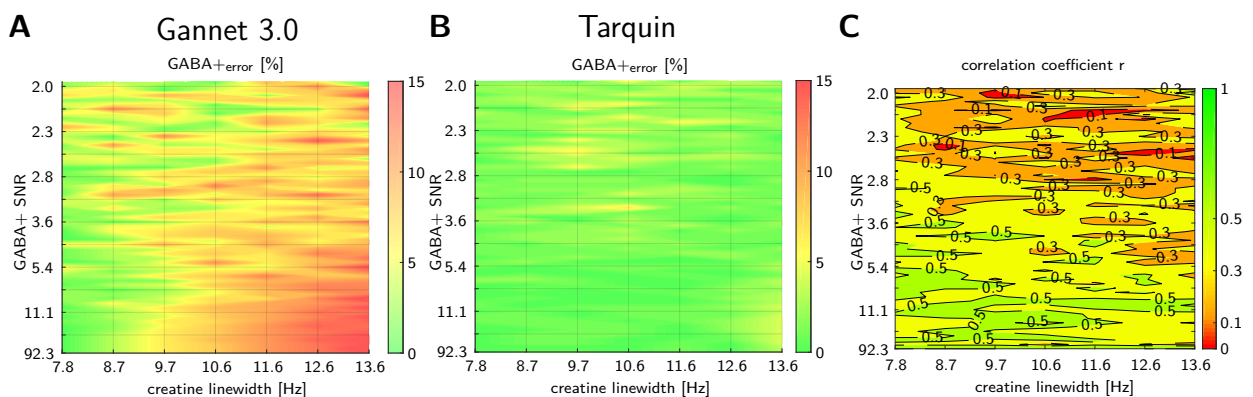
Figure 8.1 – **Graphical Abstract Study 3** - A) Mean deviation from the known GABA+ resonance in % (GABA+$_{error}$) for Gannet 3.0. B) Mean deviation from the known GABA+ resonance in % (GABA+$_{error}$) for Tarquin. C) Correlation coefficient r between model estimates of Gannet 3.0 and Tarquin. Each of the 427 conditions is simulated and analyzed 100 times, and the correlation analysis is performed between the 100 spectra. Areas with strong ($r > 0.5$), medium ($r > 0.3$), and ($r > 0.1$) correlation are highlighted.

8.1 Methods

8.1.1 MEGA-PRESS simulations

A template MEGA-PRESS spectrum with known GABA concentration was created in the following way: The template was created as the mean of the Siemens data sets of 48 volunteers which are available to the public as a NITRC data repository (http://www.nitrc.org/projects/biggaba) from a recent 'Big GABA' multi-site study [82]. The template ON and OFF spectra were calculated as the mean of the water-scaled and baseline-corrected ON and OFF spectra.

The template MEGA-PRESS spectrum was the ground truth for all subsequent SNR and line broadening manipulations. First, 7 different levels of exponential line broadening between 0 and 6 Hz were applied to the template spectrum to simulate variations in B_0 homogeneity. In a subsequent step, 61 SNR levels between 0 and 30 % were created by adding Gaussian-distributed noise to the data in the time domain. The target SNR level was measured as the height of the N-acetyl-aspartate signal at 2.01 ppm in the frequency domain relative to the noise standard deviation. In total, 100 spectra per combination were simulated.

8.1.2 MEGA-PRESS in vivo study

All *in vivo* data were acquired on a clinical whole-body 3T MRI (Siemens MAGNETOM Skyra A TIM System, Siemens Healthcare AG, Erlangen, Germany) using a 20-channel head coil for receive, and the body coil for transmitting. All fourteen healthy volunteers (5 female; age (mean ± SD) 26.3 ± 2.2 years) gave written informed consent prior to the examination. The *in vivo* study was focused on the thalamus, which is a challenging anatomical location regarding spectral quality and anatomical specificity of the MRS voxel. Two scenarios with different SNR levels based on voxel size and varying linewidths were investigated. A small voxel of 20 mm x 20 mm x 20 mm = 8 ml volume centered on the left thalamus and a larger voxel with 30 mm (AP) x 35 mm (LR) x 25 mm (HF) = 26.25 ml including the whole basal ganglia region were prescribed. The other parameters for both voxels were NEX = 256, TR/TE = 2050/68 ms, bandwidth = 1200 Hz, and 2048 datapoints. Automated Siemens *GRE Brain* and manual shimming was performed to achieve a water linewidth < 15 Hz for the small voxel, and < 20 Hz for the large voxel, respectively, as indicated by the inline interactive display on the scanner console.

8.1.3 Data processing, Quantification & Spectral Quality Metrics

Two modeling algorithms were used to quantify the 3-ppm GABA+ resonance of all difference spectra of the *in silico* and *in vivo* data. To reduce effects of user interaction and to process the large amount of data, fully automated processing was implemented for all quantifications. In the simulations, the estimation error (GABA+$_{error}$) of the model was defined as the rounded absolute value of the relative difference between the modeled GABA+ resonance in the template spectrum, i.e., the ground truth GABA+$_{GT}$, and the modeled GABA+ resonances of the manipulated spectra GABA+$_{Area}$ for each quantification tool:

$$GABA +_{error} (\%) = \left| \frac{GABA +_{Area} *100}{GABA +_{GT}} - 100 \right| \tag{8.1}$$

GABA+ areas, which were modeled to be outside of the range between $\pm$ 3 SD $=$ 36 % [82] from the ground truth GABA+ area were rejected. The two different data processing and quantification pipelines for Gannet 3.0 and Tarquin are described in chapter 3.4.5.

Briefly, the Gannet 3.0 [86] analysis included spectral registration for frequency and phase-correction of the individual transients, automated rejection of corrupted transients, zero-filling to 32768 data points, and 3-Hz exponential line broadening. The combined GABA-Glx model was used for quantification.

The toolbox FID-A [157] was used for individual frequency- and phase-correction of the individual transients of the *in vivo* data using spectral registration, and automated rejection of corrupted transients, both of which are not implemented in Tarquin [89] itself. No additional zero-filling or line broadening was applied.

Analysis with Tarquin included residual water removal, phasing, and referencing of the 2.01-ppm NAA signal. The internally calculated MEGA-PRESS basis set models GABA as two separate Gaussian peaks scales as 1 proton each, i.e., as a pseudo-doublet at 2.95 and 3.04 ppm. Additionally, a macromolecule correction factor of 0.5 was applied, and the GABA+ fit error was calculated analogously to Gannet 3.0.

Various spectral quality metrics were included in the analysis:

- The estimation error GABA+$_{error}$, which is usually unknown, to determine the reliability of the GABA+ modeling.

- The fit error GABA+$_{fit}$ as a common quality metric, some sort of which is usually provided by each tool.

- The standard deviation GABA+$_{SD}$ of the GABA+ quantification over the 100 simulated spectra per combination. GABA+$_{SD}$ reflects a measure of the variance of the modeling introduced by the underlying SNR and linewidth changes. Higher GABA+$_{SD}$ imply increased modeling susceptibility to SNR and linewidth changes.

- The number of rejected spectra was considered as a measure of severe outliers in the modeling.

8.2 Results

8.2.1 *In silico* quantification

The GABA+$_{error}$ remained lower than 5 % for creatine linewidths smaller than 9.7 Hz (Appendix E **Figure 4 A**) and is between 5 and 10 % for creatine linewidths between 9.7 and 10.6 Hz for Gannet 3.0. It exceeds 10 % for creatine linewidths larger than 10.6 Hz.
The fit error, GABA+$_{fit}$, and the standard deviation across the 100 simulated spectra, GABA+$_{SD}$, were mainly affected by GABA+ SNR (Appendix E **Figure 4 B & C**).
The rejection rate was less than 10 % for GABA+ SNR larger than 5.4, while for GABA+ SNR ranging from 5.3 to 3.2, the rejection rate was up to 30 %. For GABA+ SNR smaller than 3.2, up to 60 % of the data were rejected (Appendix E **Figure 4 D**).

The GABA+$_{error}$ was smaller than 5 % except for GABA+ SNR ranging from 3.6 to 3.2 with a creatine linewidth of 11.6 Hz for Tarquin (Appendix E **Figure 5 A**).
The GABA+$_{fit}$ ranged from 6 to 30 % for GABA+ SNR levels between 92.3 and 5.4. GABA+$_{fit}$ ranged from 30 to 104 % for GABA+ SNR smaller than 5.4. The fitting error increases approximately 5 % over the whole range of creatine linewidths for GABA+ SNR larger than 3.6, while it increased approximately 14 % for GABA+ SNR smaller than 5.4 (Appendix E **Figure 5 B**).
GABA+$_{SD}$ is smaller than 95 % for GABA+ SNR smaller than 5.4, while for GABA+ SNR it ranged between 5 and 19 %. GABA+$_{SD}$ ranged from 15 to 18 % for GABA+ SNR smaller than 2.1 (Appendix E **Figure 5 C**).
For GABA+ SNR larger than 2.5 less than 5 % of the data were rejected, while for GABA+ SNR smaller than 2.5 up to 17 % of the data met the rejection criteria (Appendix E **Figure 5 D**).

Clusters of combinations with strong ($r > 0.5$), medium ($r > 0.3$), and small ($r > 0.1$) correlation between the model estimates with Gannet 3.0 and Tarquin are observable. A strong correlation is observed for GABA+ SNR larger than 5.4 and creatine linewidth smaller than 11.6 Hz, while very weak correlations dominate for GABA+ SNR smaller than 2.5. The two modeling methods appear to have medium correlations for the remaining clusters (Appendix E **Figure 6**).

8.2.2 *In vivo* quantification

The mean spectra and their standard deviation show different characteristics for the two voxel scenarios (Appendix E **Figure 7 A & C**). The small voxel appears to have a smaller SD for Gannet 3.0, while the mean GABA+ models are comparable in amplitude for both tools. The SD appears to be higher for Tarquin due to the absence of line broadening (Appendix E **Figure 7 B**). Gannet 3.0 appears to have a smaller SD in the model than Tarquin for the larger voxel. The SD of the residuals is comparably low for both tools and does not appear to have a clear residual metabolite peak in the 3-ppm region (Appendix E **Figure 7 D**).

The estimated GABA+/Cr ratios are higher for Tarquin in both cases (Appendix E **Figure 8 A**). The coefficient of variance is lower for Gannet 3.0 than for Tarquin in the small voxel (gannet 3.0: 29 %; Tarquin: 30 %), while it is higher for Gannet 3.0 than for Tarquin in the large voxel (Gannet 3.0: 25 %; Tarquin: 14 %) (Appendix E **Figure 8 B**). Tarquin appears to have a higher SD for the fitting error than Gannet 3.0 for both voxels (Appendix E **Figure 8 B**). GABA+ SNR and creatine linewidth are higher in the larger voxel (Appendix E **Figure 8 C & D**).

No significant correlation was found between the GABA+/Cr ratios modeled by Gannet 3.0 and Tarquin ($r = .18$; $p = .65$) for the small voxel, while a significant correlation was found for the large voxel ($r = .54$; $p < .05$) (Appendix E **Figure 9 A & B**).

8.2.3 Comparing *in vivo* and *in silico* data

While the data distribution differs strongly between both datasets, the measures of fit error and rejects are largely congruent (Appendix E **Table 1**).

8.3 Discussion

Study 3 analyzed the influence of various SNR and linewidth combinations on the modeling of the 3-ppm GABA+ resonance in J-difference edited spectra obtained with MEGA-PRESS. In the first part, the effects of those parameters were mimicked by the manipulation of a near noise-free template spectrum. 427 combinations of noise and line broadening were added to the template prior to modeling with Gannet 3.0 and Tarquin. The GABA+$_{error}$ was calculated as the deviation from the known 3-ppm GABA+ resonance, and common quality metrics were determined.

Combining all evidence, acceptable GABA+ modeling is possible for GABA+ SNR > 3.2 and creatine linewidth < 9.7 Hz, which corresponds to only 14 % of the GABA+ SNR compared to the 27 ml / 10 min acquisition proposed in the literature [79]. The estimation error does not exceed 5 % for Gannet 3.0 and Tarquin for these combinations. However, GABA+ $_{SD}$ increases by 5 % for Gannet 3.0 and 11 % for Tarquin in the range from 5.4 to 2.5 for GABA+ SNR. Therefore, studies with lower GABA+ SNR are hampered by a loss of statistical power to detect small GABA+ changes with small effect sizes. Finally, the effect of creatine linewidth is negligible compared to the effects of GABA+ SNR.

Further conclusions could be drawn from the *in silico* modeling. First, the estimation error GABA+$_{error}$ differs between tools. Second, creatine linewidths only affect the modeling at very high GABA+ SNR levels. This implies that B$_0$ field homogeneity is, within commonly encountered ranges, not a critical criterion for accurate modeling of the 3-ppm GABA+ resonance. Third, GABA+$_{fit}$ is not related to GABA+$_{error}$. Consequently, the fit error does not give any information about the real deviation from the ground truth. Fourth, group variance of *in vivo* measurements - apart from biological variation within the cohort or variance by changes in the voxel positioning - depends on the used quantification algorithm. Nevertheless, the correlation reveals at least a medium agreement between the two modeling algorithms. Finally, the results illustrate that the commonly used quality metrics do not allow conclusions about the real estimation error.

In the second part, different *in vivo* scenarios were compared to the simulations, and an estimated GABA+$_{error}$ was determined. As the agreement between the *in vivo* and the *in silico* datasets was good, the simulation framework could be used as an indicator either to judge data quality of an already conducted study or to classify a voxel conducted in a pilot measurement during study design. Further investigations could clarify if the apparent differences in the data distribution between both datasets could be interpreted as a variation solely attributed to biological variance.

Additionally, a threshold noise level for significant differences could be determined by extending the simulation framework with different amplitudes of the GABA+ resonance.

Similar to a recent study on the design of GABA+-edited studies [81], our results indicate a high impact of GABA+ SNR on the modeling. Both studies indicate that GABA+-edited data reach a reliable quantification and reasonable group-level variance for 27-ml voxels with averages ranging from 128 to 210 compared to the recommended 320.

The results from the small *in vivo* voxel indicate that the coefficient of variance is considerably higher for low GABA+ SNR and depends on the quantification tool. Additionally, the number of rejected spectra - which are not reliably quantified - is higher. This must be considered in a study with small voxels. The present study indicates data with fitting errors GABA+$_{fit}$ larger than 15 % could still be reliably quantified. Therefore, data rejection criteria should not exclusively be defined by GABA+ SNR and fit error, but rather by considering the SD of the quantified GABA+ signal. Assuming GABA concentrations are relatively consistent within one group - considering biological variability and pathologies to be consistent within that group - GABA+$_{SD}$ should support data quality estimation and outlier rejection.

Aside from the general knowledge gained about the impact of diminishing spectral quality on GABA+-edited data, the present study provides insights on the performance of different quantification tools. The framework could serve as a benchmark for other quantification tools.

8.4 Summary

Study 3 suggests that GABA+-edited studies might be realized for voxels with low GABA+ SNR at the cost of higher group-level variance. The effect of B$_0$ field homogeneity is rather negligible compared to the effect of GABA+ SNR. Furthermore, no correlation between the estimation error GABA+$_{error}$ and the fit error GABA+$_{fit}$ was found. Additionally, group variance induced by different quantification tools introduces additionally unknown uncertainty, which might obscure small effect sizes in GABA+ levels.

9 Preliminary Results Study 4: J-edited MR Spectroscopy in Patients with Hepatic Encephalopathy

Study 4 aimed to investigate the cerebello-thalamo-cortical neurometabolism in patients with HE. Yet, the study is in its final part of the acquisition phase, and its results should be considered preliminary.

9.1 Methods

Up to this point, the study cohort included 14 patients with HE I, 2 patients classified as minimal HE and 16 age-matched controls. The grading was performed by an experienced clinician according to the West-Haven criteria [48, 50]. Additionally, CFF [52] assessment with portable CFF goggles, analysis of fine motor skills via Grooved PEG board testing [158] and blood sample tests were performed . Exclusion criteria were any medication acting on the central nervous system, severe intestinal diseases, peripheral/retinal neuropathy, and the diagnosis of neurological or psychiatric diseases other than HE for the patient group. Abstinence of $>= 4$ weeks was required for patients with alcohol abuse as part of the medical history prior to the inclusion.

9.1.1 MEGA-PRESS acquisition

The MR protocol included the acquisition of a high-resolution anatomical T_1-weighted scan (1 mm isotropic resolution with 176 slices) covering the whole brain to reconstruct all coronal and sagittal views for MRS voxel localization. MEGA-PRESS spectroscopy [80] (TE \TR = 68 \1750 ms; NEX = 256; bandwidth = 2400 Hz; 2080 datapoints) was performed in three voxels including the cerebellum (CER) (25 (AP) mm x 25 (LR) mm x 25 (HF) mm = 15.63 ml), the thalamus (THA) (30 (AP) mm x 35 (LR) mm x 25 (HF) mm = 26.25 ml), and the motor cortex (MOT) (30 (AP) x 30 (LR) x 30 (HF) = 27 ml). The voxels were designed in accordance with **Study 3**. The CER voxel was centered on the nucleus dentate and angulated parallel to the tentorium cerebelli. The THA voxel was angulated and placed such that it included the

whole thalamus, and the lateral ventricles were avoided [159]. The MOT voxel was placed on the sensorimotor cortex - e.g., centered on the hand knob landmark [160] - and angulated to avoid lipid contamination from the skull. The entire acquisition duration was about 40 minutes. Two HE I patients canceled the measurement after the CER and the THA voxel.

9.1.2 MEGA-PRESS data processing, quantification & statistics

GABA-to-creatine ratios were determined with Gannet 3.1 [86] as described in the previous chapter. OFF spectra were processed with FID-A [157] as previously described, and analyzed with LCModel v6.3 [88] using an online available basis set `http://purcell.healthsciences.purdue.edu/mrslab/basis_sets.html`. The basis set included alanine, aspartate, creatine, GABA, glutamine (Gln), glutamate, glutathione (GSH), glycerophosphorylcholine (GPC), lactate, myo-inositol (mI), N-acetyl-aspartate, N-acetylaspartylglutamate, scyllo-Inositol, and taurine. Due to excessive movement during scanning all spectra from 1 patient had to be excluded. Furthermore, 4 spectra from the cerebellum (2 controls and 2 HE I patients) and 4 spectra from the motor cortex (1 control and 3 HE I patients) had to be excluded due to poor spectral quality (low SNR) or substantial lipid contamination from the skull. Wilcoxon-Mann-Whitney-tests were used to assess metabolite level differences of six metabolites (GABA, glutamine, myo-inositol, aspartate, glutathione, and glycerophosphorylcholine) between the groups. Two-sided partial correlation analyses with CFF and PEG board scores were performed for all metabolite estimates with age as confounding variable (all significance levels alpha = 0.05). To this point, no multiple comparison correction was performed, and the group level analysis was restricted to the controls and the HE I patients due to the low number of mHE patients.
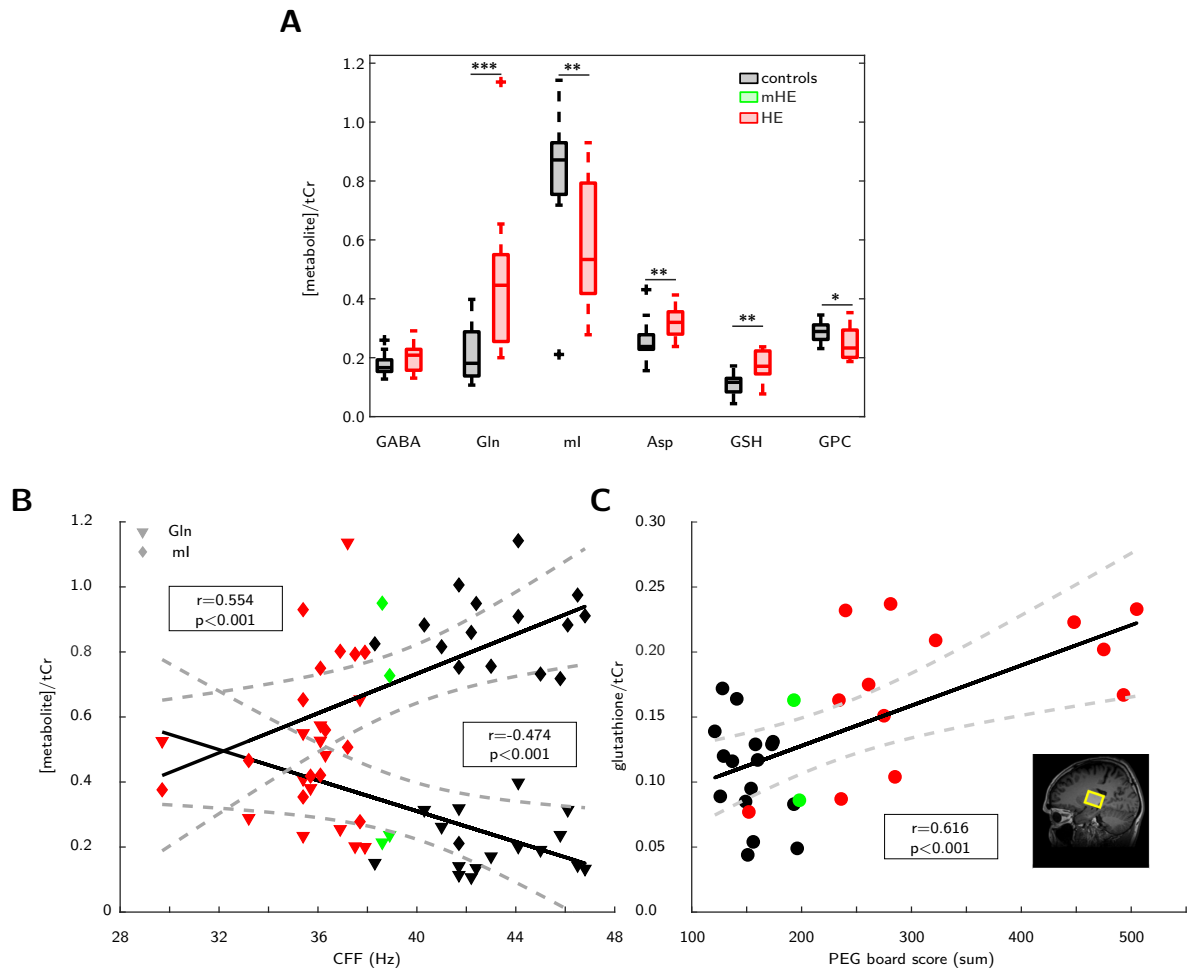
9.2 Results

9.2.1 Cerebellum
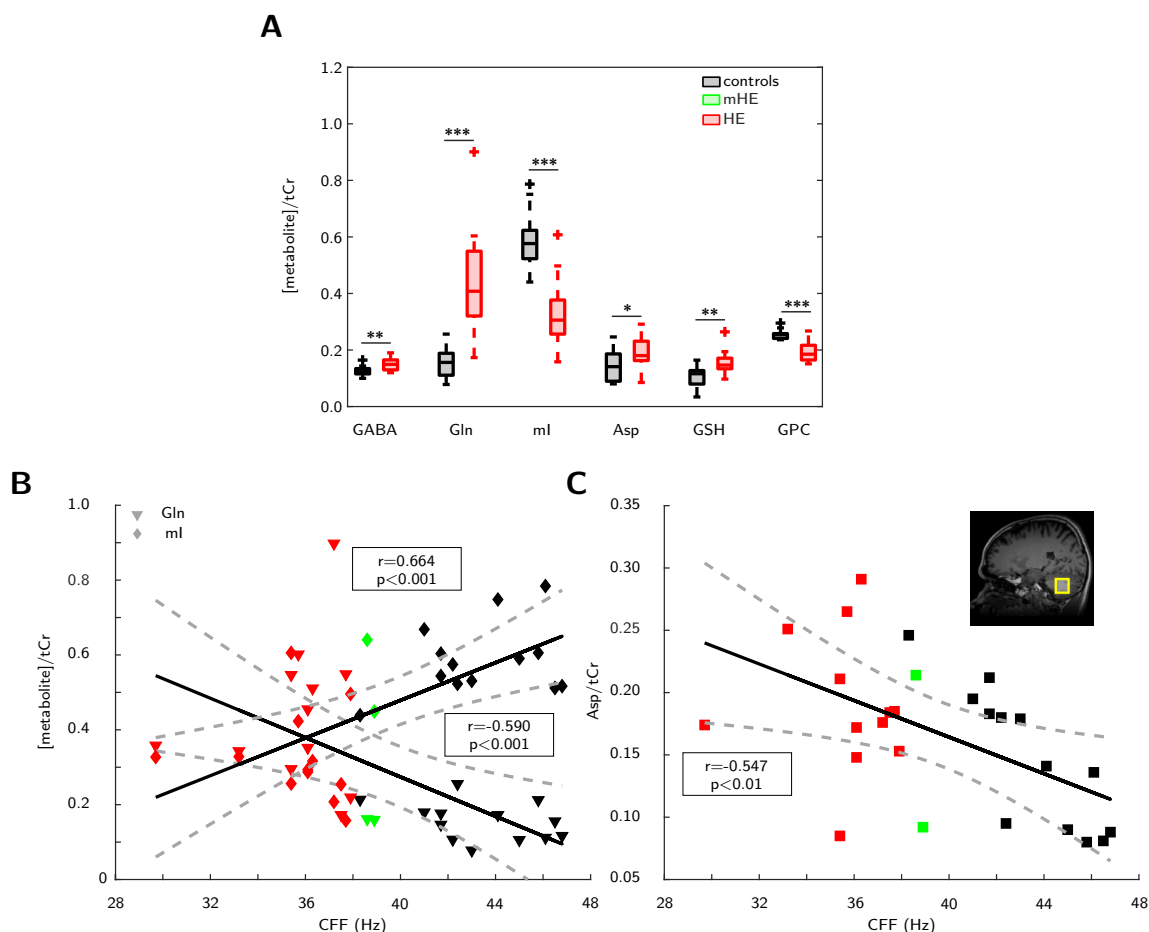
Figure 9.1 – MEGA-PRESS spectroscopy of the cerebellum - A) Boxplots of the metabolite-to-creatine ratios. Asterisks indicate significant group differences (* $\equiv$ p $<$ 0.05; ** $\equiv$ p $<$ 0.01; *** $\equiv$ p $<$ 0.001). B) Correlation analysis of glutamine (Gln) and myo-inositol (mI) levels with the CFF C) Correlation analysis of aspartate-to-creatine ratios with the CFF.

In the cerebellum increased GABA levels were accompanied by elevated glutamine, aspartate, and glutathione levels in HE I patients. In contrast, myo-inositol and glycerophosphorylcholine levels were decreased in HE I patients. GABA levels correlated significantly with CFF (r = -0.414; p < 0.05) and PEG board scores (r = 0.466; p < 0.05). Significant correlations with the CFF were found for glutamine (r = -0.590; p < 0.001), myo-inositol (r = 0.664; p < 0.001), aspartate (r = -0.547; p < 0.01), glutathione (r = -0.416; p < 0.01), and glycerophosphorylcholine (r

= 0.613; p < 0.001). For the PEG board scores, correlations with glutamine (r = 0.650; p < 0.001), myo-inositol (r = -0.740; p < 0.001), glutathione (r = 0.407; p < 0.05), and glycerophosphorylcholine (r = -0.646; p < 0.001) were found.

9.2.2 Thalamus

Figure 9.2 – **MEGA**-**PRESS** spectroscopy of the thalamus - A) Boxplots of the metabolite-to-creatine ratios. Asterisks indicate significant group differences (* ≡ p < 0.05; ** ≡ p < 0.01; *** ≡ p < 0.001). B) Correlation analysis of glutamine (Gln) and myo-inositol (mI) levels with the CFF C) Correlation analysis of glutathione-to-creatine ratios with the sum of the PEG board scores.

In the thalamus, GABA levels did not exhibit group differences between controls and HE I patients. Typical systemic effects on glutamine (increased), myo-inositol (decreased), and glutathione (increased) were found in HE I patients. Furthermore, decreased levels of glycerophosphorylcholine

and increased aspartate levels were found in these patients. The CFF correlated with glutamine (r = -0.474; p < 0.01), myo-inositol (r = 0.554; p < 0.01), aspartate (r = -0.403; p < 0.05), glutathione (r = -0.461; p < 0.01), as well as glycerophosphorylcholine (r = 0.418; p < 0.01). The motor performance (PEG board scores) correlated with glutamine (r = 0.761; p < 0.001), myo-inostiol (r = -0.506; p < 0.01), glutathione (r = 0.616; p < 0.001), and glycerophosphorylcholine (r = -0.565; p < 0.001).
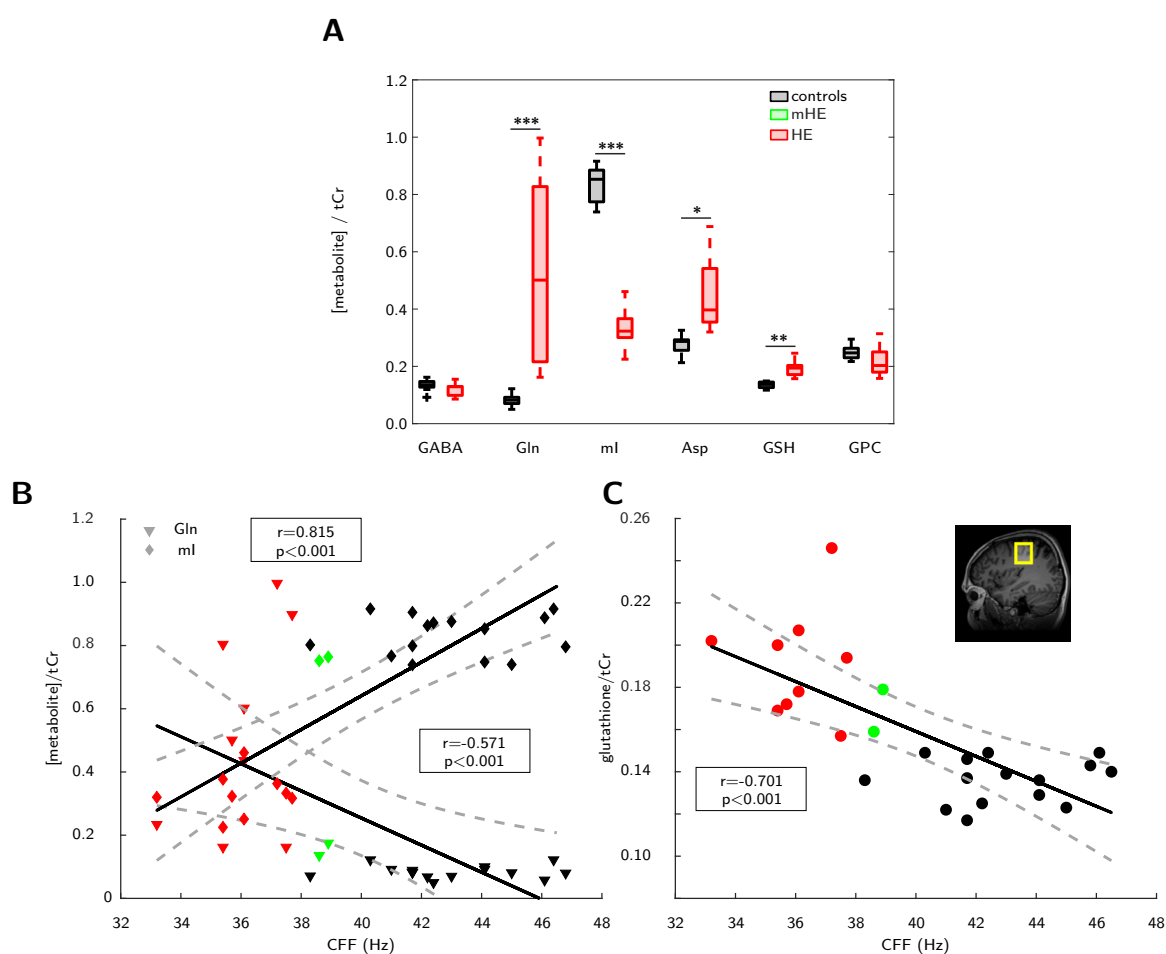
9.2.3 Motor cortex

Figure 9.3 – **MEGA**-**PRESS** spectroscopy of the motor cortex - A) Boxplots of the metabolite-to-creatine ratios. Asterisks indicate significant group differences (* ≡ p < 0.05; ** ≡ p < 0.01; *** ≡ p < 0.001). B) Correlation analysis of glutamine (Gln) and myo-inositol (mI) levels with the CFF C) Correlation analysis of glutathione-to-creatine ratios with the CFF.

In the motor cortex, GABA levels did not show significant group differences. HE-related systemic group differences (increased glutamine levels, decreased myo-inositol, and increased glutathione) were observed for the HE I patients. In addition, the aspartate levels showed a significant increase. Changes in glutamine ($r = -0.571$; $p < 0.01$), myo-inositol ($r = 0.815$; $p < 0.001$), aspartate ($r = -0.691$; $p < 0.001$) and glutathione ($r = -0.701$; $p < 0.001$) were linked to the CFF. PEG board scores were linked with glutamine ($r = 0.826$; $p < 0.001$), myo-inostiol ($r = -0.732$; $p < 0.001$), aspartate ($r = 0.444$; $p < 0.05$), glutathione ($r = 0.858$; $p < 0.001$), and glycerophosphorylcholine ($r = -0.392$; $p < 0.05$) were found.

9.3 Discussion

In **Study 4**, GABA-edited MEGA-PRESS spectroscopy was used to investigate changes in neurotransmitter levels in the cerebello-thalamo-cortical pathway. MEGA-PRESS spectroscopy was performed in the cerebellum, the thalamus, and the motor cortex in a cohort of 16 healthy controls and clinically well-defined 16 HE patients (2 mHE, 14 HE I). CFF testing, Grooved PEG board assessment, and blood sample tests were used for correlative analyses with the metabolite estimates.

Preliminary results indicate increased GABA-to-creatine levels in the cerebellum of patients with HE. Increased GABAergic neurotransmission in the cerebellum was reported in a study on hyperammonemic rats [161, 162] and reproduced in a recent transcranial magnetic stimulation study showing increased cerebellar inhibition [163]. Yet, the animal studies indicated reduced GABAergic tone in the motor cortex, which has not been observed in the preliminary results from this study. Furthermore, no changes in GABA levels were found in the thalamus. Increased GABA levels might provide an explanation for the reduced motor skills of HE patients [144] and could further substantiate the findings of cerebellar involvement found in **Study 2**.

Up to this point, the results indicate a systemic effect of HE on the whole brain, as increased glutamine levels and decreased myo-inositol levels were found in all regions. These findings are common to all regions due to the ammonia detoxification via glutamine synthetase, a subsequent counter-reaction on the increased osmotic gradient by myo-inositol depletion. The described changes are typical systemic effects in HE [10, 16, 38]. Additionally, increased levels of glutathione, which can be interpreted as an oxidative stress marker [10], were found in all regions. Increased glutathione levels under hyperammonemia conditions have also been found in various

cell studies using ammonium chloride solutions [164, 165] and animal studies [166, 167]. A recent human *in vivo* study reported increased glutathione levels in the visual and sensorimotor cortex of minimal HE patients measured with MRS [19]. MRS in the cerebellum further revealed decreasing choline levels, which is a typical finding in chronic HE [16].

Another striking result is the increase of aspartate in all regions, which has not been reported in a human *in vivo* MRS studies to date. Yet, changes in the high-affinity uptake of aspartate of rat hippocampal dendritic layers were found to be introduced by sera and CSF of patients with chronic liver disease [168].

At the current stage, all results have to be interpreted as preliminary. Final analyses should include cross-correlation between metabolites and regions, as well as multiple comparison corrections.

9.4 Summary

Study 4 revealed increased GABA-to-creatine levels in the cerebellum, while no changes were found in the thalamus and the motor cortex. Systemic effects on glutamine, myo-inositol, glutathione, and aspartate levels were closely linked to visual perception and motor performance. These findings suggest a systemic effect on the cerebello-thalamo-cortical pathway in HE, and increased GABAergic neurotransmission in the cerebellum.

10 General Discussion

The present dissertation aimed to improve metabolic investigations of *in vivo* magnetic resonance techniques. To this end, a brain ammonia- or HE-sensitive metabolic MR imaging method was established. The first two studies were focused on optimizing the metabolic MR method chemical exchange saturation transfer (CEST) for its ammonia-sensitivity and on assessing brain ammonia levels in a clinically well-defined cohort of HE patients. Underlying mechanisms were investigated with various phantom experiments, and relationships between clinical parameters and the CEST effect were established in the patient cohort. The third study aimed to design a simulation framework to investigate possible limitations in the modeling of GABA+ due to SNR or linewidth constraints during the acquisition of GABA-edited MRS. The relationship between the GABA+ estimation error and GABA+ SNR and linewidth were presented. The fourth study was conducted to investigate alterations in neurotransmitter levels in the cerebello-thalamo-cortical pathway in HE.

Study 1 relied on various phantom experiments with different levels of complexity to maximize the ammonia-sensitivity of the CEST method. Furthermore, optical methods were employed to investigate the mechanisms underlying the contrast changes in the phantom experiments. The phantom experiments implied that it is impossible to directly observe ammonia under physiological conditions. Yet contrast changes in the amide protons of proteins were linked to ammonia-induced denaturation in the phantom solutions. These findings were validated using fluorescence spectroscopy, and repeated in a complex phantom consisting of tissue homogenates of pig brain and with varying ammonia concentrations.

Study 2 applied the optimized CEST protocol to study a well-defined cohort of HE patients and healthy controls. A region-of-interest-based analysis of the data set, which was based on a normalized coordinate space, revealed a relationship between disease severity and CEST contrast in various brain regions. Apart from group differences, correlations between the CEST effect and several psychometric scores reflecting motor skills and reaction time, as well as blood ammonia levels, were found. Based on these findings, the CEST effect may be interpreted sensitive to brain ammonia levels, reflecting the continuous nature of HE.

Both studies found a reduced APT_w contrast with increasing ammonia concentrations. Signal changes are driven by protein denaturation, which is a known contributor to contrast changes in CEST imaging [107, 108]. These results support the interpretation of APT_w imaging as a multiparametric metabolic imaging technique [13, 107, 108], which reflects several tissue properties. Furthermore, findings from CEST pioneer papers were replicated during Study 1 [93].

The interpretation of the *in vivo* measurements in Study 2 is based on the observations of Study 1 and the pathophysiological concept of hyperammonemia in HE [21, 22, 23]. As the observed signal changes match observations from phantom experiments and are closely linked to blood ammonia levels and psychometric test scores reflecting HE severity, the interpretation of CEST as a brain ammonia level correlative stands to reason. Up to this date, $^{13}NH_3$-PET served as an imaging method to investigate brain ammonia levels in HE [44, 1]. The findings in the dissertation feature comparable correlations and patterns in the distribution of brain ammonia levels [1], which substantiates the interpretation presented above. In the $^{13}NH_3$-PET studies, the product of the net metabolic clearance in blood from intracellular metabolites and arterial ammonia concentrations, which was deduced from radioactively marked ammonia, was defined as metabolic flux. As glutamine synthetase is located in the astrocytes, and APT_w imaging predominantly reflects intracellular protein compounds, it can be speculated that APT_w imaging reflects metabolic flux. Considering the brain regions showing CEST contrast changes, the HE-sensitive interpretation is supported. Changes in fine motor skills are linked to cerebellar damage [142, 143], and hepatocerebral degeneration [145, 36] and the loss of astrocytes are common features in HE [35]. Altered visual perceptions reflected in reduced ability to recognize changes in visual stimuli [52], changes in neurotransmitter levels in the visual cortex [18], slowed brain oscillations [146, 53], and altered BOLD response [169] are known in HE. Therefore, increased ammonia levels are likely to contribute to CEST contrast changes. Finally, slowed brain oscillations in the thalamus point to an involvement of the thalamus in HE [147]. Thus, HE-related changes in the CEST contrast are reasonable.

Nevertheless, other confounders to the CEST contrast must be considered during the interpretation of the HE-related changes. APT_w imaging is confounded by changes in pH [13], water content and water T_1, as well as altered protein conformation of intracellular protein compounds [107, 108]. Based on the results of both conducted studies, the assumption of changes in protein conformation as a main contributor is reasonable. Thus, hepatocerebral degeneration [145, 36] and in particular, effects on the cerebellum in case of severe HE, could be a primary driver of the observed contrast changes [35]. Alcohol abuse is associated with a higher degree of severity in the loss of Purkinje cells, and higher HE prevalence [35].

The appearance of Alzheimer type II astrocytes is more likely in those patients and thus might alter APT_w imaging contrast by changing the number of exchangeable amide groups per volume. Furthermore, glutamine and glutamate are both CEST-sensitive and resonating between 3 and 4 ppm [131]. Therefore, changes in these metabolites, which are commonly elevated in HE [148, 10, 149], might contribute to the CEST contrast. Yet, phantom studies indicate that protein denaturation dominates the CEST contrast alterations, and 3 T systems might not reach the sensitivity to distinguish changes in glutamate or glutamine [101].

As various quantitative T_1 [136] and T_1-weighted [28, 152] imaging studies imply T_1 changes as a key finding in HE, T_1 normalization of the CEST effect was implemented. This normalization results in a pure APT_w contrast mechanism, which has recently been shown to be insensitive to water longitudinal relaxation for the saturation parameters used in the present study [153].

Another confounder featured in the pathophysiology of HE, is the emergence of a low-grade edema [132]. In terms of MR visibility of these alterations, one study reported water content changes of 2 % in various brain regions including putamen [132], whereas no MR visible water content changes in HE patients in less severe stages were reported in another study [19]. Water content changes are regarded as minor contributors to the formation of APT_w contrast at higher field strength in literature [150, 151] and may be neglected in our study.

In the context of neuroimaging studies of HE, the CEST contrast might open a more direct avenue to studying the pathophysiology of HE *in vivo*. Several neuroimaging studies were conducted in HE cohorts, which included T_1-weighted imaging [28, 152], quantitative T_1 mapping [136], MT imaging [170], diffusion-weighted imaging [170], and quantitative water content mapping [132, 19]. Yet, the CEST contrast as brain ammonia correlate could be interpreted as the most direct contrast mechanism reflecting HE severity. This is also reflected in the common finding implying the basal ganglia region as crucial in HE development. Water content studies revealed a correlation of occipital white matter water content and disease severity, which was absent in the gray matter of the occipital cortex, regardless of the strongly altered visual perception in HE [132]. In contrast, the present study linked APT_w contrast of the gray matter of the visual cortex to disease severity and additionally substantiated cerebellar involvement in HE [161, 169].

From the viewpoint of clinical research on HE, APT_w imaging can be a method to create a correlative measure of brain ammonia levels. Especially, the implementation of faster imaging sequences [171] allows the integration of a CEST experiment into an arbitrary neuroimaging protocol to assess brain ammonia levels in less than 8 minutes. Yet, the underlying mechanisms to the contrast changes have to be investigated in more detail. By implementing more advanced CEST methods [171], it may be possible to disentangle contributions of ammonia-induced changes

in the CEST effect from contributions of protein degeneration represented in NOE alterations. The clinical applicability of CEST in the diagnosis and monitoring of HE is limited through the high cost of a MR investigation compared to for example the CFF testing. Yet, it can be of interest to monitor alterations in the CEST effect of HE patients in a longitudinal study design, including various diseases stages. This approach can provide insight on the reversibility of the changes in the CEST effect. Under the assumption that the ammonia is cleared from the brain over time, the changes of the CEST effect should reach normal levels again, while CEST effect changes based on hepatocerebral degeneration should be irreversible.

Study 3 created a generally transferable simulation framework for GABA-edited MEGA-PRESS, which agrees well with recent literature findings [81], suggesting that GABA-edited studies may be conducted with lower GABA+ SNR levels than the recommended 27 ml with 320 averages. By reducing the MRS voxel size, the anatomical specificity could be increased significantly. Yet, these changes come at the cost of a higher intra-group variance, possibly covering subtle changes in GABA+ levels. Furthermore, GABA+ levels were found to be mostly insensitive to linewidth changes within the commonly encountered range.

The GABA level differences found in the cerebellum in Study 4 support the feasibility to perform GABA-edited spectroscopy in smaller volumes compared to the recommended 27 ml. Increased GABA levels might reflect increased GABAergic neurotransmission in the cerebellum, which has been found in hyperammonemia animal studies [161] and was supported by a recent transcranial magnetic stimulation study [163] in HE patients. No GABA level differences were found in the motor cortex, which contrasts the animal studies [161]. Study 4 provides further evidence of systemic effects due to the ammonia detoxification, especially on glutamine and myo-inositol, and an oxidative stress response reflected in increased glutathione levels.

Study 2 and Study 4 indicate that crucial changes in the cerebello-thalamo-cortical pathway might occur in the cerebellum. Increased GABA and glutamine levels, as well as CEST contrast attributed to ammonia level changes and hepatocerebral degeneration, were found primarily in this region. Up to this point, the study reports preliminary results, and a final conclusion is yet to be drawn.

In summary, this dissertation contributes important findings to neuroimaging and spectroscopy, and gives particular insight into the altered brain metabolism of HE. A novel image contrast - potentially reflecting brain ammonia levels - was developed. The interpretation of APT_w imaging as a biomarker for protein denaturation and the necessity of a multiparametric interpretation of the APT_w contrast were substantiated.

The subsequent *in vivo* study shows a direct link between HE severity and APT_w CEST contrast alterations, as well as correlations between behavioral measures - including motor performance and visual perception - and the APT_w CEST effect in various brain regions. Additionally, recommendations regarding a sufficient GABA+ SNR and linewidth were concluded from the simulation framework, which applies to GABA-edited MRS in general. Increased GABA levels, indicate a strong cerebellar involvement in the cerebello-thalamo-cortical pathway. Finally, this dissertation demonstrates the applicability of metabolic imaging and MRS to study the metabolism of the human brain under *in vivo* conditions.

11 Conclusion and Outlook

The present dissertation may serve to understand the relevance and spatial distribution of brain hyperammonemia in the disease progression of hepatic encephalopathy. The underlying APT_w MTR_{asym} contrast represents a imaging parameter sensitive to the severity of HE - in terms of ammonia levels and hepatocerebral degeneration. Furthermore, a simulation framework for GABA-edited spectroscopy was developed to investigate the impact of SNR and linewidth on the modeling of GABA. The results indicated that a reasonable quantification of GABA may be possible for smaller voxel sizes than commonly recommended. This knowledge was employed in the investigation of the cerebello-thalamo-cortical pathway using GABA-edited MEGA-PRESS spectroscopy, which revealed increased GABA levels in the cerebellum as a preliminary result.

First, this work facilitates the methodological development of CEST and especially of APT_w imaging. It underlines the multi-parametric nature of APT_w imaging and in particular, contrast changes by protein denaturation. It emphasizes the applicability of APT_w imaging as a neuro-scientific research method beyond tumor staging and the investigation of multiple sclerosis and Parkinson's disease. Furthermore, it demonstrates the integration of normalization approaches into a processing pipeline of a CEST study to reduce user input bias. This approach may open up new ways for non-parametric voxel-based statistics, which are unfortunately limited by the number of participants and therefore not implemented in the present dissertation.

Second, the discovery of the ammonia-sensitivity of APT_w MTR_{asym} imaging and its application to investigate HE represents a key outcome of the present work. This correlative parameter could be used in combination with other MR techniques to further investigate brain ammonia levels in HE. Yet the mechanisms underlying the contrast changes remain not fully explained, as hyperammonemia, as well as hepatocerebral degeneration, may confound the contrast.

Several approaches may be used to resolve these remaining uncertainties: The inclusion of an animal model of chronic HE while integrating a *post mortem* quantification of ammonia levels, protein denaturation, or morphological changes, may provide additional information. Beyond this, a three-step ammonia perfusion including a baseline, an ammonia-perfused, and a washout condition would allow identifying the direct effect of ammonia in an animal model. Similarly, single patients could undergo a protein challenge to artificially increase brain ammonia levels compared to baseline conditions, to shed light on the ammonia-induced contrast changes.

Furthermore, the combination of voxel-based CEST techniques with novel accelerated spectral editing sequences would allow identifying underlying contributions of glutamate and glutamine to the contrast changes. Additionally, these techniques would allow the quantification of several neurometabolites suggested to be part of the pathogenesis of HE, which have not yet been investigated in patients. Thus, the interplay between APT_w CEST effect as a brain ammonia correlative, neurotransmitter and osmolyte changes, oxidative stress responses, as well as alterations in aspartate and ascorbic acid could be investigated.

Third, the regional specificity of HE-related effects is substantiated by the present findings, especially by the CEST contrast changes and the differences in GABA levels. Furthermore, systemic effects due to the ammonia detoxification, which comprised glutamine and myo-inositol were found. Furthermore, the present dissertation indicates that several subsystems of the brain are differentially embedded in the pathogenesis of HE, as tactile and visual perception are altered in HE. Therefore, similar effects could be anticipated in the auditory system, which may be investigated in a multi-modal approach using MRS, voxel-based CEST, and MEG. Despite its advantages, MRS remains constrained by large cuboid volumes. The implementation of MRS Imaging (MRSI), in particular, edited MRSI may be used to identify the spatial extent of concentration changes of GABA as well as glutamate and glutamine. The MRSI technique may additionally be combined with fast CEST sequences to investigate links between the spatial distribution of glutamine and the CEST signal reductions.

Further integration of advanced edited MRS schemes could allow for the investigation of other low concentration metabolites - e.g., aspartate, ascorbic acid, and glutathione - using edited spectroscopy. These techniques might provide further insight into the pathogenesis of HE without suffering from prolonged measurements.

References

[1] S. Keiding, M. Sørensen, D. Bender, O. L. Munk, P. Ott, and H. Vilstrup. "Brain metabolism of13N-ammonia during acute hepatic encephalopathy in cirrhosis measured by positron emission tomography". eng. In: *Hepatology* 43.1 (2006), pp. 42–50. DOI: 10.1002/hep.21001.

[2] F. A. Azevedo, L. R. Carvalho, L. T. Grinberg, J. M. Farfel, R. E. Ferretti, R. E. Leite, W. J. Filho, R. Lent, and S. Herculano-Houzel. "Equal numbers of neuronal and nonneuronal cells make the human brain an isometrically scaled-up primate brain". In: *Journal of Comparative Neurology* 513.5 (2009), pp. 532–541. DOI: 10.1002/cne.21974.

[3] P. Reber. "Ask the Brains". In: *Scientific American Mind* 21.6 (2010), pp. 70–70. DOI: 10.1038/scientificamericanmind0111-70.

[4] M. F. Bear, B. W. Connors, and M. A. Paradiso. *Neuroscience: Exploring the brain, 3rd ed.* Philadelphia, PA, US: Lippincott Williams & Wilkins Publishers, 2007, pp. xxxviii, 857–xxxviii, 857.

[5] N. J. Priebe and D. Ferster. "Vision: Mechanisms of Orientation, Direction and Depth". In: *Encyclopedia of Neuroscience.* Academic Press, 2010, pp. 217–225. DOI: 10.1016/B978-008045046-9.00222-9.

[6] E. K. Miller, D. J. Freedman, and J. D. Wallis. "The prefrontal cortex: Categories, concepts and cognition". In: *Philosophical Transactions of the Royal Society B: Biological Sciences.* Ed. by A. Parker, A. Derrington, and C. Blakemore. Vol. 357. 1424. 2002, pp. 1123–1136. DOI: 10.1098/rstb.2002.1099.

[7] J. K. Mai and F. Forutan. "Thalamus". In: *The Human Nervous System.* Academic Press, 2012, pp. 618–677. DOI: 10.1016/B978-0-12-374236-0.10019-7.

[8] M. Bagnall, S. du Lac, and M. Mauk. "Cerebellum". In: *Fundamental Neuroscience.* Academic Press, 2013, pp. 677–696. DOI: 10.1016/B978-0-12-385870-2.00031-7.

[9] M. Blachier, H. Leleu, M. Peck-Radosavljevic, D. C. Valla, and F. Roudot-Thoraval. "The burden of liver disease in Europe: A review of available epidemiological data". In: *Journal of Hepatology* 58.3 (2013), pp. 593–608. DOI: 10.1016/j.jhep.2012.12.005. arXiv: 1801.04731.

[10] D. Häussinger and F Schliess. "Pathogenetic mechanisms of hepatic encephalopathy". eng. In: *Gut* 57.8 (2008), pp. 1156–1165. DOI: 10.1136/gut.2007.122176.

[11] S. Allampati and K. D. Mullen. "Hepatic encephalopathy". In: *Handbook of Liver Disease*. Vol. 5. 2. Oxford University Press, 2017, pp. 207–216. DOI: 10.1016/B978-0-323-47874-8.00015-8. arXiv: 504.

[12] K. Cai, M. Haris, A. Singh, F. Kogan, J. H. Greenberg, H. Hariharan, J. A. Detre, and R. Reddy. "Magnetic resonance imaging of glutamate". In: *Nature Medicine* 18.2 (2012), pp. 302–306. DOI: 10.1038/nm.2615.

[13] J. Zhou, J. F. Payen, D. A. Wilson, R. J. Traystman, and P. C. M. van Zijl. "Using the amide proton signals of intracellular proteins and peptides to detect pH effects in MRI". en. In: *Nature Medicine* 9.8 (2003), pp. 1085–1090. DOI: 10.1038/nm907.

[14] M. Haris, K. Cai, A. Singh, H. Hariharan, and R. Reddy. "In vivo mapping of brain myo-inositol". In: *NeuroImage* 54.3 (2011), pp. 2079–2085. DOI: 10.1016/j.neuroimage.2010.10.017. arXiv: NIHMS150003.

[15] C. Li, S. Peng, R. Wang, H. Chen, W. Su, X. Zhao, J. Zhou, and M. Chen. "Chemical exchange saturation transfer MR imaging of Parkinson's disease at 3 Tesla". In: *European Radiology* 24.10 (2014), pp. 2631–2639. DOI: 10.1007/s00330-014-3241-7. arXiv: 15334406.

[16] R. Kreis, N. Farrow, and B. D. Ross. "Localized 1H NMR spectroscopy in patients with chronic hepatic encephalopathy. Analysis of changes in cerebral glutamine, choline and inositols". In: *NMR in Biomedicine* 4.2 (1991), pp. 109–116. DOI: 10.1002/nbm.1940040214.

[17] B. D. Ross, S Jacobson, F Villamil, J Korula, R. Kreis, T Ernst, T Shonk, and R. A. Moats. "Subclinical hepatic encephalopathy: proton MR spectroscopic abnormalities." In: *Radiology* 193.2 (1994), pp. 457–463. DOI: 10.1148/radiology.193.2.7972763.

[18] G. Oeltzschner, M. Butz, T. J. Baumgarten, N. Hoogenboom, H.-J. Wittsack, and A. Schnitzler. "Low visual cortex GABA levels in hepatic encephalopathy: links to blood ammonia, critical flicker frequency, and brain osmolytes". eng. In: *Metabolic Brain Disease* 30.6 (2015), pp. 1429–1438. DOI: 10.1007/s11011-015-9729-2.

[19] G. Oeltzschner, M. Butz, F. Wickrath, H.-J. Wittsack, and A. Schnitzler. "Covert hepatic encephalopathy: elevated total glutathione and absence of brain water content changes". In: *Metabolic Brain Disease* 31.3 (2016), pp. 517–527. DOI: 10.1007/s11011-015-9760-3.

[20] S Bollmann, C Ghisleni, S. S. Poil, E Martin, J Ball, D Eich-Höchli, R. A. Edden, P Klaver, L Michels, D Brandeis, and R. L. O'Gorman. "Developmental changes in gamma-aminobutyric acid levels in attention-deficit/hyperactivity disorder". In: *Translational Psychiatry* 5.6 (2015), e589–e589. DOI: `10.1038/tp.2015.79`.

[21] M. D. Norenberg, L. Baker, L. O. Norenberg, J. Blicharska, J. H. Bruce-Gregorios, and J. T. Neary. "Ammonia-induced astrocyte swelling in primary culture". eng. In: *Neurochemical Research* 16.7 (1991), pp. 833–836. DOI: `10.1007/BF00965694`.

[22] M. D. Norenberg. *Astrocytic-ammonia interactions in hepatic encephalopathy*. 1996. DOI: `10.1055/s-2007-1007237`.

[23] A. H. Lockwood, E. W. H. Yap, and W.-H. Wong. "Cerebral Ammonia Metabolism in Patients with Severe Liver Disease and Minimal Hepatic Encephalopathy". eng. In: *Journal of Cerebral Blood Flow & Metabolism* 11.2 (1991), pp. 337–341. DOI: `10.1038/jcbfm.1991.67`.

[24] P. M. Harrison, J. A. Wendon, A. E. Gimson, G. J. Alexander, and R. Williams. "Improvement by acetylcysteine of hemodynamics and oxygen transport in fulminant hepatic failure". In: *N.Engl.J.Med* 324.0028-4793 (Print) (1991), pp. 1852–1857. DOI: `10.1056/NEJM199106273242604`.

[25] S. Sushma, S. Dasarathy, R. K. Tandon, S. Jain, S. Gupta, and M. S. Bhist. "Sodium benzoate in the treatment of acute hepatic encephalopathy: A double-blind randomized trial". In: *Hepatology* 16.1 (1992), pp. 138–144. DOI: `10.1002/hep.1840160123`.

[26] J. A. Wendon, P. M. Harrison, R. Keays, and R. Williams. "Cerebral blood flow and metabolism in fulminant liver failure". In: *Hepatology* 19.6 (1994), pp. 1407–1413. DOI: `10.1002/hep.1840190614`.

[27] M Baraldi, G Pinelli, P Ricci, and M. L. Zeneroli. "Toxins in hepatic encephalopathy: the role of the synergistic effect of ammonia, mercaptans and short chain fatty acids." In: *Archives of toxicology. Supplement. = Archiv fur Toxikologie. Supplement* 7 (1984), pp. 103–5.

[28] C Rose, R. F. Butterworth, J Zayed, L Normandin, K Todd, A Michalak, L Spahr, P. M. Huet, and G Pomier-Layrargues. "Manganese deposition in basal ganglia structures results from both portal-systemic shunting and liver dysfunction". In: *Gastroenterology* 117.3 (1999), pp. 640–644. DOI: `10.1016/S0016-5085(99)70457-9`.

[29] D. F. Schafer and E. Anthony Jones. "HEPATIC ENCEPHALOPATHY AND THE γ-AMINOBUTYRIC-ACID NEUROTRANSMITTER SYSTEM". In: *The Lancet* 319.8262 (1982), pp. 18–20. DOI: 10.1016/S0140-6736(82)92559-4.

[30] R Avallone, M. L. Zeneroli, I Venturini, L Corsi, P Schreier, M Kleinschnitz, C Ferrarese, F Farina, C Baraldi, N Pecora, M Frigo, and M Baraldi. "Endogenous benzodiazepine-like compounds and diazepam binding inhibitor in serum of patients with liver cirrhosis with and without overt encephalopathy." In: *Gut* 42.6 (1998), pp. 861–7.

[31] L. Grønbæk, H. Watson, H. Vilstrup, and P. Jepsen. "Benzodiazepines and risk for hepatic encephalopathy in patients with cirrhosis and ascites". In: *United European Gastroenterology Journal* 6.3 (2018), pp. 407–412. DOI: 10.1177/2050640617727179.

[32] E. A. Jones. "Ammonia, the GABA neurotransmitter system, and hepatic encephalopathy". In: *Metabolic Brain Disease*. Vol. 17. 4. 2002, pp. 275–281. DOI: 10.1023/A:1021949616422. arXiv: NIHMS150003.

[33] J. E. Fischer and R. J. Baldessarini. "FALSE NEUROTRANSMITTERS AND HEPATIC FAILURE". In: *The Lancet* 298.7715 (1971), pp. 75–80. DOI: 10.1016/S0140-6736(71)92048-4.

[34] M. D. Norenberg. "The role of astrocytes in hepatic encephalopathy". eng. In: *Neurochemical Pathology* 6.1-2 (1987), pp. 13–33. DOI: 10.1007/BF02833599.

[35] J. J. Kril, D. Flowers, and R. F. Butterworth. "Distinctive pattern of bergmann glial pathology in human hepatic encephalopathy". In: *Molecular and Chemical Neuropathology* 31.3 (1997), pp. 279–287. DOI: 10.1007/BF02815130.

[36] A. D. Yalçın, E. Oğuz-Akarsu, and H. M. Sökmen. "Acquired hepatocerebral degeneration". In: *Neurosciences* 21.2 (2016), pp. 164–167. DOI: 10.17712/nsj.2016.2.20150164.

[37] M. Romero-Gómez, S. Montagnese, and R. Jalan. "Hepatic encephalopathy in patients with acute decompensation of cirrhosis and acute-on-chronic liver failure". In: *Journal of Hepatology* 62.2 (2015), pp. 437–447. DOI: 10.1016/J.JHEP.2014.09.005.

[38] D. Häussinger, J. Laubenberger, S. Vom Dahl, T. Ernst, S. Bayer, M. Langer, W. Gerok, and J. Hennig. "Proton magnetic resonance spectroscopy studies on human brain Myo-inositol in hypo-osmolarity and hepatic encephalopathy". In: *Gastroenterology* 107.5 (1994), pp. 1475–1480. DOI: 10.1016/0016-5085(94)90552-5.

[39] M. Y. Morgan. "Cerebral magnetic resonance imaging in patients with chronic liver disease". In: *Metabolic Brain Disease*. Vol. 13. 4. 1998, pp. 273–290. DOI: 10.1023/A:1020680624084.

[40] N. Binesh, A. Huda, M. A. Thomas, N. Wyckoff, M. Bugbee, S. Han, N. Rasgon, P. Davanzo, J. Sayre, B. Guze, P. Martin, and F. Fawzy. "Hepatic encephalopathy: A neurochemical, neuroanatomical and neuropsychological study". In: *Journal of Applied Clinical Medical Physics* 7.1 (2006), pp. 86–96. DOI: 10.1120/jacmp.2027.25374.

[41] B. Görg, F. Schliess, and D. Häussinger. "Osmotic and oxidative/nitrosative stress in ammonia toxicity and hepatic encephalopathy". In: *Archives of Biochemistry and Biophysics* 536.2 (2013), pp. 158–163. DOI: 10.1016/j.abb.2013.03.010.

[42] J. Vaquero, C. Chung, M. E. Cahill, and A. T. Blei. *Pathogenesis of hepatic encephalopathy in acute liver failure*. 2003. DOI: 10.1055/s-2003-42644.

[43] B. Mínguez, J. C. García-Pagán, J. Bosch, J. Turnes, J. Alonso, A. Rovira, and J. Córdoba. "Noncirrhotic portal vein thrombosis exhibits neuropsychological and MR changes consistent with minimal hepatic encephalopathy". In: *Hepatology* 43.4 (2006), pp. 707–714. DOI: 10.1002/hep.21126.

[44] A. H. Lockwood, J. M. McDonald, R. E. Reiman, A. S. Gelbard, J. S. Laughlin, T. E. Duffy, and F. Plum. "The dynamics of ammonia metabolism in man. Effects of liver disease and hyperammonemia". In: *Journal of Clinical Investigation* 63.3 (1979), pp. 449–460. DOI: 10.1172/JCI109322.

[45] S. Schenker, D. W. McCandless, E. Brophy, and M. S. Lewis. "Studies on the intracerebral toxicity of ammonia." In: *The Journal of clinical investigation* 46.5 (1967), pp. 838–848. DOI: 10.1172/JCI105583.

[46] K. V. Rama Rao and M. D. Norenberg. *Brain energy metabolism and mitochondrial dysfunction in acute and chronic hepatic encephalopathy*. 2012. DOI: 10.1016/j.neuint.2011.09.007.

[47] D. Häussinger, G. Kircheis, R. Fischer, F. Schliess, and S. V. Dahl. *Hepatic encephalopathy in chronic liver disease: A clinical manifestation of astrocyte swelling and low-grade cerebral edema?* 2000. DOI: 10.1016/S0168-8278(00)80110-5.

[48] P. Ferenci, A. T. Blei, A. H. Lockwood, K. Mullen, R. Tarter, and K. Weissenborn. "Hepatic encephalopathy - Definition, nomenclature, diagnosis, and quantification: Final report of the Working Party at the 11th World Congresses of Gastroenterology, Vienna, 1998". In: *Hepatology* 35.3 (2002), pp. 716–721. DOI: 10.1053/jhep.2002.31250.

[49] J. S. Bajaj, J. Córdoba, K. D. Mullen, P. Amodio, D. L. Shawcross, R. F. Butterworth, and M. Y. Morgan. "Review article: the design of clinical trials in hepatic encephalopathy - an International Society for Hepatic Encephalopathy and Nitrogen Metabolism (ISHEN) consensus statement". In: *Alimentary Pharmacology & Therapeutics* 33.7 (2011), pp. 739–747. DOI: 10.1111/j.1365-2036.2011.04590.x.

[50] H. Vilstrup, P. Amodio, J. S. Bajaj, J. Córdoba, P. Ferenci, K. D. Mullen, K. Weissenborn, P. Wong, J. A. Talwalkar, H. S. Conjeevaram, M. Porayko, R. B. Merriman, P. L. Jansen, and F. Zoulim. *Hepatic Encephalopathy in Chronic Liver Disease: 2014 Practice Guideline by the European Association for the Study of the Liver and the American Association for the Study of Liver Diseases*. 2014. DOI: 10.1016/j.jhep.2014.05.042.

[51] G. Kircheis, D. Häussinger, M. Wettstein, A. Schnitzler, and L. Timmermann. "Critical flicker frequency for quantification of low-grade hepatic encephalopathy". In: *Hepatology* 35.2 (2002), pp. 357–366. DOI: 10.1053/jhep.2002.30957.

[52] G. Kircheis, N. Hilger, and D. Häussinger. "Value of Critical Flicker Frequency and psychometric hepatic encephalopathy score in diagnosis of low-grade hepatic encephalopathy". In: *Gastroenterology* 146.4 (2014), 961–969.e11. DOI: 10.1053/j.gastro.2013.12.026.

[53] T. J. Baumgarten, J. Neugebauer, G. Oeltzschner, N. D. Füllenbach, G. Kircheis, D. Häussinger, J. Lange, H. J. Wittsack, M. Butz, and A. Schnitzler. "Connecting occipital alpha band peak frequency, visual temporal resolution, and occipital GABA levels in healthy participants and hepatic encephalopathy patients". In: *NeuroImage: Clinical* 20 (2018), pp. 347–356. DOI: 10.1016/j.nicl.2018.08.013.

[54] W. Gerlach and O. Stern. "Der experimentelle Nachweis der Richtungsquantelung im Magnetfeld". In: *Zeitschrift für Physik* 9.1 (1922), pp. 349–352. DOI: 10.1007/BF01326983.

[55] P. Zeeman. "The effect of magnetisation on the nature of light emitted by a substance". In: *Nature* 55.1424 (1897), p. 347. DOI: 10.1038/055347a0.

[56] E. M. Purcell, H. C. Torrey, and R. V. Pound. *Resonance absorption by nuclear magnetic moments in a solid [7]*. 1946. DOI: 10.1103/PhysRev.69.37.

[57] F. Bloch. "Nuclear induction". In: *Physica* 17.3-4 (1951), pp. 272–281. DOI: 10.1016/0031-8914(51)90068-7. arXiv: arXiv:1011.1669v3.

[58] P. C. Lauterbur. "Image formation by induced local interactions: Examples employing nuclear magnetic resonance". In: *Nature* 242.5394 (1973), pp. 190–191. DOI: 10.1038/242190a0.

[59] M. H. Levitt. *Spin dynamics : basics of nuclear magnetic resonance*. Wiley, 2008, p. 714.

[60] J. Keeler. *Understanding NMR spectroscopy*. John Wiley and Sons, 2010, p. 511.

[61] H. Lu, L. M. Nagae-Poetscher, X. Golay, D. Lin, M. Pomper, and P. C. M. Van Zijl. "Routine clinical brain MRI sequences for use at 3.0 tesla". In: *Journal of Magnetic Resonance Imaging* 22.1 (2005), pp. 13–22. DOI: 10.1002/jmri.20356.

[62] J. P. Wansapura, S. K. Holland, R. S. Dunn, and W. S. Ball. "NMR relaxation times in the human brain at 3.0 Tesla". In: *Journal of Magnetic Resonance Imaging* 9.4 (1999), pp. 531–538. DOI: 10.1002/(SICI)1522-2586(199904)9:4<531::AID-JMRI4>3.0.CO;2-L.

[63] T. G. Nunes, E. W. Randall, and G. Guillot. "The first proton NMR imaging of ice: Stray-field imaging and relaxation studies". In: *Solid State Nuclear Magnetic Resonance* 32.2 (2007), pp. 59–65. DOI: 10.1016/j.ssnmr.2007.08.002.

[64] S. K. Piechnik, J. Evans, L. H. Bary, R. G. Wise, and P. Jezzard. "Functional changes in CSF volume estimated using measurement of water T2 relaxation". In: *Magnetic Resonance in Medicine* 61.3 (2009), pp. 579–586. DOI: 10.1002/mrm.21897.

[65] H Bruhn, J Frahm, M. L. Gyngell, K. D. Merboldt, W Hänicke, R Sauter, and C Hamburger. "Noninvasive differentiation of tumors with use of localized H-1 MR spectroscopy in vivo: initial experience in patients with cerebral tumors." In: *Radiology* 172.2 (1989), pp. 541–8. DOI: 10.1148/radiology.172.2.2748837.

[66] P. F. Buckley, C. Moore, H. Long, C. Larkin, P. Thompson, F. Mulvany, O. Redmond, J. P. Stack, J. T. Ennis, and J. L. Waddington. "1H-magnetic resonance spectroscopy of the left temporal and frontal lobes in schizophrenia: Clinical, neurodevelopmental, and cognitive correlates". In: *Biological Psychiatry* 36.12 (1994), pp. 792–800. DOI: 10.1016/0006-3223(94)90591-6.

[67] S. H. Mostofsky, N. A. J. Puts, M. Tommerdahl, R. A. E. Edden, H. S. Singer, A. D. Harris, C. Nettles, and D. Crocetti. "Reduced GABAergic inhibition and abnormal sensory symptoms in children with Tourette syndrome". In: *Journal of Neurophysiology* 114.2 (2015), pp. 808–817. DOI: 10.1152/jn.00060.2015.

[68] B. R. Foerster, M. Petrou, M. A. Mohamed, R. C. Carlos, R. C. Welsh, P. B. Barker, R. A. E. Edden, E. L. Feldman, M. G. Pomper, and B. C. Callaghan. "An Imbalance Between Excitatory and Inhibitory Neurotransmitters in Amyotrophic Lateral Sclerosis Revealed by Use of 3-T Proton Magnetic Resonance Spectroscopy". In: *JAMA Neurology* 70.8 (2013), p. 1009. DOI: 10.1001/jamaneurol.2013.234.

[69] E. C. Porges, A. J. Woods, R. A. Edden, N. A. Puts, A. D. Harris, H. Chen, A. M. Garcia, T. R. Seider, D. G. Lamb, J. B. Williamson, and R. A. Cohen. "Frontal Gamma-Aminobutyric Acid Concentrations Are Associated With Cognitive Performance in Older Adults". In: *Biological Psychiatry: Cognitive Neuroscience and Neuroimaging* 2.1 (2017), pp. 38–44. DOI: 10.1016/j.bpsc.2016.06.004.

[70] F. Gao, R. A. Edden, M. Li, N. A. Puts, G. Wang, C. Liu, B. Zhao, H. Wang, X. Bai, C. Zhao, X. Wang, and P. B. Barker. "Edited magnetic resonance spectroscopy detects an age-related decline in brain GABA levels". In: *NeuroImage* 78 (2013), pp. 75–82. DOI: 10.1016/j.neuroimage.2013.04.012.

[71] C. Maes, L. Hermans, L. Pauwels, S. Chalavi, I. Leunissen, O. Levin, K. Cuypers, R. Peeters, S. Sunaert, D. Mantini, N. A. Puts, R. A. Edden, and S. P. Swinnen. "Age-related differences in GABA levels are driven by bulk tissue changes". In: *Human Brain Mapping* 39.9 (2018), pp. 3652–3662. DOI: 10.1002/hbm.24201.

[72] R. L. O'Gorman, L. Michels, R. A. Edden, J. B. Murdoch, and E. Martin. "In vivo detection of GABA and glutamate with MEGA-PRESS: Reproducibility and gender effects". In: *Journal of Magnetic Resonance Imaging* 33.5 (2011), pp. 1262–1267. DOI: 10.1002/jmri.22520.

[73] M. N. Preising, B. Görg, C. Friedburg, N. Qvartskhava, B. S. Budde, M. Bonus, M. R. Toliat, C. Pfleger, J. Altmüller, D. Herebian, M. Beyer, H. J. Zöllner, H.-J. Wittsack, J. Schaper, D. Klee, U. Zechner, P. Nürnberg, J. Schipper, A. Schnitzler, H. Gohlke, B. Lorenz, D. Häussinger, and H. J. Bolz. "Biallelic mutation of human SLC6A6 encoding the taurine transporter TAUT is linked to early retinal degeneration". In: *The FASEB Journal* (2019), fj.201900914RR. DOI: 10.1096/fj.201900914RR.

[74] C. N. Epperson, S. O'Malley, K. A. Czarkowski, R. Gueorguieva, P. Jatlow, G. Sanacora, D. L. Rothman, J. H. Krystal, and G. F. Mason. "Sex, GABA, and nicotine: The impact of smoking on cortical GABA levels across the menstrual cycle as measured with proton magnetic resonance spectroscopy". eng. In: *Biological Psychiatry* 57.1 (2005), pp. 44–48. DOI: 10.1016/j.biopsych.2004.09.021. arXiv: NIHMS150003.

[75] G. Oeltzschner, H. J. Zöllner, M. Jonuscheit, R. S. Lanzman, A. Schnitzler, and H.-J. Wittsack. "J-difference-edited MRS measures of γ-aminobutyric acid before and after acute caffeine administration". In: *Magnetic Resonance in Medicine* (2018). DOI: 10.1002/mrm.27233.

[76] P. Bottomley. *Selective volume method for performing localized NMR spectroscopy*. 1985. DOI: 10.1016/0730-725X(85)90032-3.

[77] J. Near, C. J. Evans, N. A. Puts, P. B. Barker, and R. A. Edden. "J-difference editing of gamma-aminobutyric acid (GABA): Simulated and experimental multiplet patterns". In: *Magnetic Resonance in Medicine* 70.5 (2013), pp. 1183–1191. DOI: 10.1002/mrm.24572. arXiv: NIHMS150003.

[78] A. D. Harris, M. G. Saleh, and R. A. Edden. "Edited 1 H magnetic resonance spectroscopy in vivo: Methods and metabolites". In: *Magnetic Resonance in Medicine* 77.4 (2017), pp. 1377–1389. DOI: 10.1002/mrm.26619.

[79] P. G. Mullins, D. J. McGonigle, R. L. O'Gorman, N. A. Puts, R. Vidyasagar, C. J. Evans, R. A. Edden, M. J. Brookes, A. Garcia, B. R. Foerster, M. Petrou, D. Price, B. S. Solanky, I. R. Violante, S. Williams, and M. Wilson. "Current practice in the use of MEGA-PRESS spectroscopy for the detection of GABA". eng. In: *NeuroImage* 86 (2014), pp. 43–52. DOI: 10.1016/j.neuroimage.2012.12.004. arXiv: NIHMS150003.

[80] M. Mescher, H. Merkle, J. Kirsch, M. Garwood, and R. Gruetter. "Simultaneous in vivo spectral editing and water suppression". eng. In: *NMR in Biomedicine* 11.6 (1998), pp. 266–272. DOI: 10.1002/(SICI)1099-1492(199810)11:6<266::AID-NBM530>3.0.CO;2-J.

[81] M. Mikkelsen, R. S. Loo, N. A. Puts, R. A. Edden, and A. D. Harris. "Designing GABA-edited magnetic resonance spectroscopy studies: Considerations of scan duration, signal-to-noise ratio and sample size". In: *Journal of Neuroscience Methods* 303 (2018), pp. 86–94. DOI: 10.1016/J.JNEUMETH.2018.02.012.

[82] M. Mikkelsen, P. B. Barker, P. K. Bhattacharyya, M. K. Brix, P. F. Buur, K. M. Cecil, K. L. Chan, D. Y. Chen, A. R. Craven, K. Cuypers, M. Dacko, N. W. Duncan, U. Dydak, D. A. Edmondson, G. Ende, L. Ersland, F. Gao, I. Greenhouse, A. D. Harris, N. He, S. Heba, N. Hoggard, T. W. Hsu, J. F. Jansen, A. Kangarlu, T. Lange, R. M. Lebel, Y. Li, C. Y. E. Lin, J. K. Liou, J. F. Lirng, F. Liu, R. Ma, C. Maes, M. Moreno-Ortega, S. O. Murray, S. Noah, R. Noeske, M. D. Noseworthy, G. Oeltzschner, J. J. Prisciandaro, N. A. Puts, T. P. Roberts, M. Sack, N. Sailasuta, M. G. Saleh, M. P. Schallmo, N. Simard, S. P. Swinnen, M. Tegenthoff, P. Truong, G. Wang, I. D. Wilkinson, H.-J. Wittsack, H. Xu, F. Yan, C. Zhang, V. Zipunnikov, H. J. Zöllner, and R. A. Edden. "Big GABA: Edited MR spectroscopy at 24 research sites". In: *NeuroImage* 159 (2017), pp. 32–45. DOI: 10.1016/j.neuroimage.2017.07.021.

[83] M. Mikkelsen, D. L. Rimbault, P. B. Barker, P. K. Bhattacharyya, M. K. Brix, P. F. Buur, K. M. Cecil, K. L. Chan, D. Y.-T. Chen, A. R. Craven, K. Cuypers, M. Dacko, N. W. Duncan, U. Dydak, D. A. Edmondson, G. Ende, L. Ersland, M. A. Forbes, F. Gao, I. Greenhouse, A. D. Harris, N. He, S. Heba, N. Hoggard, T.-W. Hsu, J. F. Jansen, A. Kangarlu, T. Lange, R. M. Lebel, Y. Li, C.-Y. E. Lin, J.-K. Liou, J.-F. Lirng, F. Liu, J. R. Long, R. Ma, C. Maes, M. Moreno-Ortega, S. O. Murray, S. Noah, R. Noeske, M. D. Noseworthy, G. Oeltzschner, E. C. Porges, J. J. Prisciandaro, N. A. Puts, T. P. Roberts, M. Sack, N. Sailasuta, M. G. Saleh, M.-P. Schallmo, N. Simard, D. Stoffers, S. P. Swinnen, M. Tegenthoff, P. Truong, G. Wang, I. D. Wilkinson, H.-J. Wittsack, A. J. Woods, H. Xu, F. Yan, C. Zhang, V. Zipunnikov, H. J. Zöllner, and R. A. Edden. "Big GABA II: Water-referenced edited MR spectroscopy at 25 research sites". In: *NeuroImage* 191 (2019), pp. 537–548. DOI: 10.1016/J.NEUROIMAGE.2019.02.059.

[84] A. D. Harris, B. Glaubitz, J. Near, C. John Evans, N. A. Puts, T. Schmidt-Wilcke, M. Tegenthoff, P. B. Barker, and R. A. Edden. "Impact of frequency drift on gamma-aminobutyric acid-edited MR spectroscopy". In: *Magnetic Resonance in Medicine* 72.4 (2014), pp. 941–948. DOI: 10.1002/mrm.25009.

[85] J. Near, R. A. Edden, C. J. Evans, R. Paquin, A. D. Harris, and P. Jezzard. "Frequency and phase drift correction of magnetic resonance spectroscopy data by spectral registration in the time domain". eng. In: *Magnetic Resonance in Medicine* 73.1 (2015), pp. 44–50. DOI: 10.1002/mrm.25094.

[86] R. A. Edden, N. A. Puts, A. D. Harris, P. B. Barker, and C. J. Evans. "Gannet: A batch-processing tool for the quantitative analysis of gamma-aminobutyric acid-edited MR spectroscopy spectra". eng. In: *Journal of Magnetic Resonance Imaging* 40.6 (2014), pp. 1445–1452. DOI: 10.1002/jmri.24478. arXiv: NIHMS150003.

[87] S. W. Provencher. "Estimation of metabolite concentrations from localized in vivo proton NMR spectra". eng. In: *Magnetic Resonance in Medicine* 30.6 (1993), pp. 672–679. DOI: 10.1002/mrm.1910300604.

[88] S. W. Provencher. "Automatic quantitation of localized in vivo 1H spectra with LCModel". ENG. In: *NMR in Biomedicine* 14.4 (2001), pp. 260–264. DOI: 10.1002/nbm.698.

[89] M. Wilson, G. Reynolds, R. A. Kauppinen, T. N. Arvanitis, and A. C. Peet. "A constrained least-squares approach to the automated quantitation of in vivo 1 H magnetic resonance spectroscopy data". In: *Magnetic Resonance in Medicine* 65.1 (2011), pp. 1–12. DOI: 10.1002/mrm.22579.

[90] J. Frahm, A. Haase, and D. Matthaei. "Rapid three-dimensional MR imaging using the FLASH technique". In: *Journal of Computer Assisted Tomography* 10.2 (1986), pp. 363–368. DOI: 10.1097/00004728-198603000-00046.

[91] B. Schmitt. "Selective Magnetic Resonance Imaging in Humans by Means of Proton Exchange between Metabolites and Water". PhD thesis. Ruprecht-Karls-Universität Heidelberg, 2011.

[92] S. D. Wolff and R. S. Balaban. "Magnetization transfer contrast (MTC) and tissue water proton relaxation in vivo". eng. In: *Magnetic Resonance in Medicine* 10.1 (1989), pp. 135–144. DOI: 10.1002/mrm.1910100113.

[93] S. D. Wolff and R. S. Balaban. "NMR imaging of labile proton exchange". In: *Journal of Magnetic Resonance* 86.1 (1990), pp. 164–169. DOI: 10.1016/0022-2364(90)90220-4.

[94] M. Zaiss and P. Bachert. "Chemical exchange saturation transfer (CEST) and MR Z -spectroscopy in vivo : a review of theoretical approaches and methods". In: *Physics in Medicine and Biology* 58.22 (2013), R221–R269. DOI: 10.1088/0031-9155/58/22/R221.

[95] R. M. Henkelman, G. J. Stanisz, and S. J. Graham. "Magnetization transfer in MRI: A review". In: *NMR in Biomedicine* 14.2 (2001), pp. 57–64. DOI: 10.1002/nbm.683.

[96] J. Pekar, P. Jezzard, D. A. Roberts, J. S. Leigh, J. A. Frank, and A. C. McLaughlin. "Perfusion imaging with compensation for asymmetric magnetization transfer effects". In: *Magnetic Resonance in Medicine* 35.1 (1996), pp. 70–79. DOI: 10.1002/mrm.1910350110.

[97] Phillips. *Philipps APT Scheme*. 2019.

[98] J. Zhou and P. C. M. van Zijl. "Chemical exchange saturation transfer imaging and spectroscopy". In: *Progress in Nuclear Magnetic Resonance Spectroscopy* 48.2-3 (2006), pp. 109–136. DOI: 10.1016/j.pnmrs.2006.01.001.

[99] J.-E. Meissner, S. Goerke, E. Rerich, K. D. Klika, A. Radbruch, M. E. Ladd, P. Bachert, and M. Zaiss. "Quantitative pulsed CEST-MRI using Ω -plots". In: *NMR in Biomedicine* 28.10 (2015), pp. 1196–1208. DOI: 10.1002/nbm.3362.

[100] G. Yan, T. Zhang, Z. Dai, M. Yi, Y. Jia, T. Nie, H. Zhang, G. Xiao, and R. Wu. "A potential magnetic resonance imaging technique based on chemical exchange saturation transfer for in vivo γ-aminobutyric acid imaging". In: *PLoS ONE* 11.10 (2016). Ed. by Q. Jiang, e0163765. DOI: 10.1371/journal.pone.0163765.

[101] J. S. Lee, D. Xia, A. Jerschow, and R. R. Regatte. "In vitro study of endogenous CEST agents at 3T and 7T". In: *Contrast Media and Molecular Imaging* 11.1 (2016), pp. 4–14. DOI: 10.1002/cmmi.1652.

[102] R. G. Bryant. "The Dynamics of Water-Protein Interactions". In: *Annual Review of Biophysics and Biomolecular Structure* 25.1 (2002), pp. 29–52. DOI: 10.1146/annurev.biophys.25.1.29.

[103] C. K. Jones, M. J. Schlosser, P. C. M. van Zijl, M. G. Pomper, X. Golay, and J. Zhou. "Amide proton transfer imaging of human brain tumors at 3T". In: *Magnetic Resonance in Medicine* 56.3 (2006), pp. 585–592. DOI: 10.1002/mrm.20989.

[104] J. Zhou, H. Zhu, M. Lim, L. Blair, A. Quinones-Hinojosa, S. A. Messina, C. G. Eberhart, M. G. Pomper, J. Laterra, P. B. Barker, P. C. M. van Zijl, and J. Blakeley. "Three-dimensional amide proton transfer MR imaging of gliomas: Initial experience and comparison with gadolinium enhancement". In: *Journal of Magnetic Resonance Imaging* 38.5 (2013), pp. 1119–1128. DOI: 10.1002/jmri.24067. arXiv: NIHMS150003.

[105] S. By, R. L. Barry, A. K. Smith, B. D. Lyttle, B. A. Box, F. R. Bagnato, S. Pawate, and S. A. Smith. "Amide proton transfer CEST of the cervical spinal cord in multiple sclerosis patients at 3T". en. In: *Magnetic Resonance in Medicine* 79.2 (2018), pp. 806–814. DOI: 10.1002/mrm.26736.

[106] C. Li, M. Chen, X. Zhao, R. Wang, H. Chen, W. Su, S. Li, B. Lou, G. Song, S. Zhang, J. Zhang, and J. Zhou. "Chemical exchange saturation transfer MRI signal loss of the substantia Nigra as an imaging biomarker to evaluate the diagnosis and severity of Parkinson's disease". In: *Frontiers in Neuroscience* 11.AUG (2017), p. 489. DOI: 10.3389/fnins.2017.00489.

[107] S. Goerke, M. Zaiss, P. Kunz, K. D. Klika, J. D. Windschuh, A. Mogk, B. Bukau, M. E. Ladd, and P. Bachert. "Signature of protein unfolding in chemical exchange saturation transfer imaging". eng. In: *NMR in Biomedicine* 28.7 (2015), pp. 906–913. DOI: 10.1002/nbm.3317.

[108] S. Goerke, K. S. Milde, R. Bukowiecki, P. Kunz, K. D. Klika, T. Wiglenda, A. Mogk, E. E. Wanker, B. Bukau, M. E. Ladd, P. Bachert, and M. Zaiss. "Aggregation-induced changes in the chemical exchange saturation transfer (CEST) signals of proteins". eng. In: *NMR in Biomedicine* 30.1 (2017). DOI: 10.1002/nbm.3665.

[109] M. Kim, J. Gillen, B. A. Landman, J. Zhou, and P. C. M. van Zijl. "Water saturation shift referencing (WASSR) for chemical exchange saturation transfer (CEST) experiments". In: *Magnetic Resonance in Medicine* 61.6 (2009), pp. 1441–1450. DOI: 10.1002/mrm.21873.

[110] J. D. Windschuh, M. Zaiss, J. E. Meissner, D. Paech, A. Radbruch, M. E. Ladd, and P. Bachert. "Correction of B1-inhomogeneities for relaxation-compensated CEST imaging at 7T". eng. In: *NMR in Biomedicine* 28.5 (2015), pp. 529–537. DOI: 10.1002/nbm.3283.

[111] P. Schuenke, J. D. Windschuh, V. Roeloffs, M. E. Ladd, P. Bachert, and M. Zaiss. "Simultaneous mapping of water shift and B1(WASABI)—Application to field-Inhomogeneity correction of CEST MRI data". ENG. In: *Magnetic Resonance in Medicine* 77.2 (2017), pp. 571–580. DOI: 10.1002/mrm.26133.

[112] Y. Zhang, H.-Y. Heo, D.-H. Lee, X. Zhao, S. Jiang, K. Zhang, H. Li, and J. Zhou. "Selecting the reference image for registration of CEST series". In: *Journal of Magnetic Resonance Imaging* 43.3 (2016), pp. 756–761. DOI: 10.1002/jmri.25027.

[113] J. Yuan, G. Mok, Q. Zhang, Y.-X. Wang, and J. Zhou. "Improved quantification of chemical exchange saturation transfer (CEST) MRI using nonlocal means". In: *2014 IEEE Nuclear Science Symposium and Medical Imaging Conference, NSS/MIC 2014*. IEEE, 2016, pp. 1–5. DOI: 10.1109/NSSMIC.2014.7430844.

[114] I. Y. Zhou, D. Lu, Y. Ji, L. Wu, E. Wang, J. S. Cheung, X. A. Zhang, and P. Z. Sun. "Determination of multipool contributions to endogenous amide proton transfer effects in global ischemia with high spectral resolution in vivo chemical exchange saturation transfer MRI". In: *Magnetic Resonance in Medicine* 81.1 (2018), pp. 645–652. DOI: 10.1002/mrm.27385.

[115] P. C. M. van Zijl and N. N. Yadav. "Chemical exchange saturation transfer (CEST): What is in a name and what isn't?" eng. In: *Magnetic Resonance in Medicine* 65.4 (2011), pp. 927–948. DOI: 10.1002/mrm.22761. arXiv: NIHMS150003.

[116] A. Ghisaidoobe and S. Chung. "Intrinsic Tryptophan Fluorescence in the Detection and Analysis of Proteins: A Focus on Förster Resonance Energy Transfer Techniques". In: *International Journal of Molecular Sciences* 15.12 (2014), pp. 22518–22538. DOI: 10.3390/ijms151222518.

[117] J. T. Vivian and P. R. Callis. "Mechanisms of Tryptophan Fluorescence Shifts in Proteins". In: *Biophysical Journal* 80.5 (2001), pp. 2093–2109. DOI: 10.1016/S0006-3495(01)76183-8.

[118] J. Stetefeld, S. A. McKenna, and T. R. Patel. "Dynamic light scattering: a practical guide and applications in biomedical sciences." In: *Biophysical reviews* 8.4 (2016), pp. 409–427. DOI: 10.1007/s12551-016-0218-6.

[119] L. G. Brown and L. Gottesfeld. "A survey of image registration techniques". In: *ACM Computing Surveys* 24.4 (1992), pp. 325–376. DOI: 10.1145/146370.146374.

[120] A. Sotiras, C. Davatzikos, and N. Paragios. "Deformable Medical Image Registration: A Survey". In: *IEEE Transactions on Medical Imaging* 32.7 (2013), pp. 1153–1190. DOI: 10.1109/TMI.2013.2265603.

[121] K Friston. *Statistical Parametric Mapping: The Analysis of Functional Brain Images*. Academic Press, 2007.

[122] M. Hutter. "Distribution of Mutual Information". In: *NIPS Proceedings*. 2002.

[123] G. Grabner, A. L. Janke, M. M. Budge, D. Smith, J. Pruessner, and D. L. Collins. "Symmetric atlasing and model based segmentation: an application to the hippocampus in older adults." In: *Medical image computing and computer-assisted intervention : MICCAI ... International Conference on Medical Image Computing and Computer-Assisted Intervention* 9.Pt 2 (2006), pp. 58–66. DOI: 10.1007/11866763_8.

[124] B. Avants, N. J. Tustison, G. Song, P. A. Cook, A. Klein, and J. C. Gee. "A reproducible evaluation of ANTs similarity metric performance in brain image registration". In: *NeuroImage* 54.3 (2011), pp. 2033–2044. DOI: 10.1016/j.neuroimage.2010.09.025.

[125] A. Klein, J. Andersson, B. A. Ardekani, J. Ashburner, B. Avants, M.-C. Chiang, G. E. Christensen, D. L. Collins, J. Gee, P. Hellier, J. H. Song, M. Jenkinson, C. Lepage, D. Rueckert, P. Thompson, T. Vercauteren, R. P. Woods, J. J. Mann, and R. V. Parsey. "Evaluation of 14 nonlinear deformation algorithms applied to human brain MRI registration". In: *NeuroImage* 46.3 (2009), pp. 786–802. DOI: 10.1016/J.NEUROIMAGE.2008.12.037.

[126] C. H. Cunningham, J. M. Pauly, and K. S. Nayak. "Saturated double-angle method for rapid B1+ mapping". In: *Magnetic Resonance in Medicine* 55.6 (2006), pp. 1326–1333. DOI: 10.1002/mrm.20896.

[127] M. Sabati and A. A. Maudsley. "Fast and high-resolution quantitative mapping of tissue water content with full brain coverage for clinically-driven studies". In: *Magnetic Resonance Imaging* 31.10 (2013), pp. 1752–1759. DOI: 10.1016/j.mri.2013.08.001. arXiv: NIHMS150003.

[128] K. A. Christensen, D. M. Grant, E. M. Schulman, and C. Walling. "Optimal determination of relaxation times of fourier transform nuclear magnetic resonance. Determination of spin-lattice relaxation times in chemically polarized species". In: *The Journal of Physical Chemistry* 78.19 (1974), pp. 1971–1977. DOI: 10.1021/j100612a022.

[129] V. Guivel-Scharen, T. Sinnwell, S. D. Wolff, and R. S. Balaban. "Detection of Proton Chemical Exchange between Metabolites and Water in Biological Tissues". eng. In: *Journal of Magnetic Resonance* 133.1 (1998), pp. 36–45. DOI: 10.1006/jmre.1998.1440.

[130] D. L. Rabenstein and S. Fan. "Proton Nuclear Magnetic Resonance Spectroscopy of Aqueous Solutions: Complete Elimination of the Water Resonance by Spin-Spin Relaxation". In: *Analytical Chemistry* 58.14 (1986), pp. 3178–3184. DOI: 10.1021/ac00127a057.

[131] H. Schmidt, N. F. Schwenzer, S. Gatidis, T. Küstner, K. Nikolaou, F. Schick, and P. Martirosian. "Systematic Evaluation of Amide Proton Chemical Exchange Saturation Transfer at 3 T". In: *Investigative Radiology* 51.10 (2016), pp. 635–646. DOI: 10.1097/RLI.0000000000000292.

[132] N. J. Shah, H. Neeb, G. Kircheis, P. Engels, D. Häussinger, and K. Zilles. "Quantitative cerebral water content mapping in hepatic encephalopathy". eng. In: *NeuroImage* 41.3 (2008), pp. 706–717. DOI: 10.1016/j.neuroimage.2008.02.057.

[133] M. Zaiss, J. D. Windschuh, D. Paech, J. E. Meissner, S. Burth, B. Schmitt, P. Kickingereder, B. Wiestler, W. Wick, M. Bendszus, H. P. Schlemmer, M. E. Ladd, P. Bachert, and A. Radbruch. "Relaxation-compensated CEST-MRI of the human brain at 7T: Unbiased insight into NOE and amide signal changes in human glioblastoma". eng. In: *NeuroImage* 112 (2015), pp. 180–188. DOI: 10.1016/j.neuroimage.2015.02.040.

[134] C. R. Bosoi and C. F. Rose. "Identifying the direct effects of ammonia on the brain". In: *Metabolic Brain Disease* 24.1 (2009), pp. 95–102. DOI: 10.1007/s11011-008-9112-7.

[135] F. R. Miese, H.-J. Wittsack, G. Kircheis, A. Holstein, C. Mathys, U. Mödder, and M. Cohnen. "Voxel-based analyses of magnetization transfer imaging ofthe brain in hepatic encephalopathy". eng. In: *World Journal of Gastroenterology* 15.41 (2009), p. 5157. DOI: 10.3748/wjg.15.5157.

[136] N. J. Shah, H. Neeb, M. Zaitsev, S. Steinhoff, G. Kircheis, K. Amunts, D. Häussinger, and K. Zilles. "Quantitative T1Mapping of Hepatic Encephalopathy Using Magnetic Resonance Imaging". In: *Hepatology* 38.5 (2003), pp. 1219–1226. DOI: 10.1053/jhep.2003.50477.

[137] M. Zaiss, B. Schmitt, and P. Bachert. "Quantitative separation of CEST effect from magnetization transfer and spillover effects by Lorentzian-line-fit analysis of z-spectra". In: *Journal of Magnetic Resonance* 211.2 (2011), pp. 149–155. DOI: 10.1016/j.jmr.2011.05.001.

[138] B. Avants, N. Tustison, G. Song, and J. Gee. *ANTS: Advanced Open-Source Normalization Tools for Neuroanatomy, Penn IMage Computing and Science Laboratory*. 2009.

[139] Neuromorphometrics. *Neuromorphometrics, Inc. | Building a Model of the Living Human Brain*. 2012.

[140] R. L. Buckner, D. Head, J. Parker, A. F. Fotenos, D. Marcus, J. C. Morris, and A. Z. Snyder. "A unified approach for morphometric and functional data analysis in young, old, and demented adults using automated atlas-based head size normalization: Reliability and validation against manual measurement of total intracranial volume". In: *NeuroImage* 23.2 (2004), pp. 724–738. DOI: 10.1016/j.neuroimage.2004.06.018.

[141] Y. Zhang, M. Brady, and S. Smith. "Segmentation of brain MR images through a hidden Markov random field model and the expectation-maximization algorithm". In: *IEEE Transactions on Medical Imaging* 20.1 (2001), pp. 45–57. DOI: 10.1109/42.906424.

[142] R. C. Miall, L. O. D. Christensen, O. Cain, and J. Stanley. "Disruption of State Estimation in the Human Lateral Cerebellum". In: *PLoS Biology* 5.11 (2007), e316. DOI: 10.1371/journal.pbio.0050316.

[143] M. Manto, J. M. Bower, A. B. Conforto, J. M. Delgado-García, S. N. F. Da Guarda, M. Gerwig, C. Habas, N. Hagura, R. B. Ivry, P. Marien, M. Molinari, E. Naito, D. A. Nowak, N. O. Ben Taib, D. Pelisson, C. D. Tesche, C. Tilikete, and D. Timmann. "Consensus paper: Roles of the cerebellum in motor control-the diversity of ideas on cerebellar involvement in movement". In: *Cerebellum* 11.2 (2012), pp. 457–487. DOI: 10.1007/s12311-011-0331-9.

[144] M. Butz, L. Timmermann, M. Braun, S. J. Groiss, L. Wojtecki, S. Ostrowski, H. Krause, B. Pollok, J. Gross, M. Südmeyer, G. Kircheis, D. Häussinger, and A. Schnitzler. "Motor impairment in liver cirrhosis without and with minimal hepatic encephalopathy". In: *Acta Neurologica Scandinavica* 122.1 (2010), pp. 27–35. DOI: 10.1111/j.1600-0404.2009.01246.x.

[145] M. Victor, R. D. Adams, and M. Cole. "The acquired (non-wilsonian) type of chronic hepatocerebral degeneration". eng. In: *Medicine (United States)* 44.5 (1965), pp. 345–396. DOI: 10.1097/00005792-196509000-00001.

[146] N. Kahlbrock, M. Butz, E. S. May, M. Brenner, G. Kircheis, D. Häussinger, and A. Schnitzler. "Lowered frequency and impaired modulation of gamma band oscillations in a bimodal attention task are associated with reduced critical flicker frequency". In: *NeuroImage* 61.1 (2012), pp. 216–227. DOI: 10.1016/j.neuroimage.2012.02.063.

[147] L. Timmermann, M. Butz, J. Gross, M. Ploner, M. Südmeyer, G. Kircheis, D. Häussinger, and A. Schnitzler. "Impaired cerebral oscillatory processing in hepatic encephalopathy". In: *Clinical Neurophysiology* 119.2 (2008), pp. 265–272. DOI: 10.1016/j.clinph.2007.09.138.

[148] V. Felipo. "Hepatic encephalopathy: Effects of liver failure on brain function". In: *Nature Reviews Neuroscience* 14.12 (2013), pp. 851–858. DOI: 10.1038/nrn3587.

[149] R. Prakash and K. D. Mullen. "Mechanisms, diagnosis and management of hepatic encephalopathy". In: *Nature Reviews Gastroenterology & Hepatology* 7.9 (2010), pp. 515–525. DOI: 10.1038/nrgastro.2010.116.

[150] V. Khlebnikov, J. C. Siero, J. P. Wijnen, F. Visser, P. R. Luijten, D. W. Klomp, and H. J. Hoogduin. "Is there any difference in Amide and NOE CEST effects between white and gray matter at 7 T?" In: *Journal of Magnetic Resonance* 272 (2016), pp. 82–86. DOI: 10.1016/j.jmr.2016.09.010.

[151] D.-H. Lee, H.-Y. Heo, K. Zhang, Y. Zhang, S. Jiang, X. Zhao, and J. Zhou. "Quantitative assessment of the effects of water proton concentration and water T_1 changes on amide proton transfer (APT) and nuclear overhauser enhancement (NOE) MRI: The origin of the APT imaging signal in brain tumor". eng. In: *Magnetic Resonance in Medicine* 77.2 (2017), pp. 855–863. DOI: 10.1002/mrm.26131.

[152] A. Rovira, J. Alonso, and J. Córdoba. "MR Imaging Findings in Hepatic Encephalopathy". In: *American Journal of Neuroradiology* 29.9 (2008), pp. 1612–1621. DOI: 10.3174/ajnr.A1139.

[153] Z. Zu. "Towards the complex dependence of MTR asym on T_{1w} in amide proton transfer (APT) imaging". In: *NMR in Biomedicine* 31.7 (2018), e3934. DOI: 10.1002/nbm.3934.

[154] A. P. Holmes, R. C. Blair, J. D. Watson, and I. Ford. "Nonparametric analysis of statistic images from functional mapping experiments". In: *Journal of Cerebral Blood Flow and Metabolism* 16.1 (1996), pp. 7–22. DOI: 10.1097/00004647-199601000-00002.

[155] S. Walker-Samuel, S. P. Johnson, B. Pedley, M. F. Lythgoe, and X. Golay. "Extracranial measurements of amide proton transfer using exchange-modulated point-resolved spectroscopy (EXPRESS)". en. In: *NMR in Biomedicine* 25.6 (2012), pp. 829–834. DOI: 10.1002/nbm.1798.

[156] H.-Y. Heo, Y. Zhang, S. Jiang, D.-H. Lee, and J. Zhou. "Quantitative assessment of amide proton transfer (APT) and nuclear overhauser enhancement (NOE) imaging with extrapolated semisolid magnetization transfer reference (EMR) signals: II. Comparison of three EMR models and application to human brain glioma at". In: *Magnetic Resonance in Medicine* 75.4 (2016), pp. 1630–1639. DOI: 10.1002/mrm.25795.

[157] R. Simpson, G. A. Devenyi, P. Jezzard, T. J. Hennessy, and J. Near. "Advanced processing and simulation of MRS data using the FID appliance (FID-A)—An open source, MATLAB-based toolkit". en. In: *Magnetic Resonance in Medicine* 77.1 (2017), pp. 23–33. DOI: 10.1002/mrm.26091.

[158] J. Tiffin and E. J. Asher. "The Purdue Pegboard: norms and studies of reliability and validity." In: *Journal of Applied Psychology* 32.3 (1948), pp. 234–247. DOI: 10.1037/h0061266.

[159] U. Dydak, Y. M. Jiang, L. L. Long, H. Zhu, J. Chen, W. M. Li, R. A. Edden, S. Hu, X. Fu, Z. Long, X. A. Mo, D. Meier, J. Harezlak, M. Aschner, J. B. Murdoch, and W. Zheng. "In vivo measurement of brain GABA concentrations by magnetic resonance spectroscopy in smelters occupationally exposed to manganese". eng. In: *Environmental Health Perspectives* 119.2 (2011), pp. 219–224. DOI: 10.1289/ehp.1002192.

[160] T. Yousry, U. D. Schmid, H Alkadhi, D Schmidt, A Peraud, A Buettner, and P Winkler. "Localization of the motor hand area to a knob on the precentral gyrus. A new landmark". In: *Brain* 120.1 (1997), pp. 141–157. DOI: 10.1093/brain/120.1.141.

[161] O. Cauli, M. T. Mansouri, A. Agustí, and V. Felipo. "Hyperammonemia Increases GABAergic Tone in the Cerebellum but Decreases It in the Rat Cortex". English. In: *Gastroenterology* 136.4 (2009), 1359–1367.e2. DOI: 10.1053/j.gastro.2008.12.057.

[162] O. Cauli, R. Rodrigo, M. Llansola, C. Montoliu, P. Monfort, B. Piedrafita, N. El Mlili, J. Boix, A. Agustí, and V. Felipo. "Glutamatergic and gabaergic neurotransmission and neuronal circuits in hepatic encephalopathy". In: *Metabolic Brain Disease* 24.1 (2009), pp. 69–80. DOI: 10.1007/s11011-008-9115-4.

[163] S. S. Hassan, T. J. Baumgarten, A. M. Ali, N.-D. Füllenbach, M. S. Jördens, D. Häussinger, M. Butz, A. Schnitzler, and S. J. Groiss. "Cerebellar inhibition in hepatic encephalopathy". In: *Clinical Neurophysiology* 130.6 (2019), pp. 886–892. DOI: 10.1016/J.CLINPH.2019.02.020.

[164] C. R. Murthy, A. S. Bender, R. S. Dombro, G. Bai, and M. D. Norenberg. "Elevation of glutathione levels by ammonium ions in primary cultures of rat astrocytes". In: *Neurochemistry International* 37.2-3 (2000), pp. 255–268. DOI: 10.1016/S0197-0186(00)00028-0.

[165] M. Węgrzynowicz, W. Hilgier, A. Dybel, S. S. Oja, P. Saransaari, and J. Albrecht. "Up-regulation of cerebral cortical glutathione synthesis by ammonia in vivo and in cultured glial cells: The role of cystine uptake". In: *Neurochemistry International* 50.7-8 (2007), pp. 883–889. DOI: 10.1016/J.NEUINT.2006.12.003.

[166] K. V. Sathyasaikumar, I. Swapna, P. V. B. Reddy, C. R. K. Murthy, A. Dutta Gupta, B. Senthilkumaran, and P. Reddanna. "Fulminant Hepatic Failure in Rats Induces Oxidative Stress Differentially in Cerebral Cortex, Cerebellum and Pons Medulla". In: *Neurochemical Research* 32.3 (2007), pp. 517–524. DOI: 10.1007/s11064-006-9265-x.

[167] W. Hilgier, M. Węgrzynowicz, J. Ruszkiewicz, S. S. Oja, P. Saransaari, and J. Albrecht. "Direct Exposure to Ammonia and Hyperammonemia Increase the Extracellular Accumulation and Degradation of Astroglia-Derived Glutathione in the Rat Prefrontal Cortex". In: *Toxicological Sciences* 117.1 (2010), pp. 163–168. DOI: 10.1093/toxsci/kfq171.

[168] W Schmidt, G Wolf, K Grüngreiff, M Meier, and T Reum. "Hepatic encephalopathy influences high-affinity uptake of transmitter glutamate and aspartate into the hippocampal formation." In: *Metabolic brain disease* 5.1 (1990), pp. 19–31.

[169] H. J. Chen, X. Q. Zhu, Y. Jiao, P. C. Li, Y. Wang, and G. J. Teng. "Abnormal baseline brain activity in low-grade hepatic encephalopathy: A resting-state fMRI study". In: *Journal of the Neurological Sciences* 318.1-2 (2012), pp. 140–145. DOI: 10.1016/j.jns.2012.02.019.

[170] F. Miese, G. Kircheis, H.-J. Wittsack, F. Wenserski, J. Hemker, U. Mödder, D. Häussinger, and M. Cohnen. "1H-MR spectroscopy, magnetization transfer, and diffusion-weighted imaging in alcoholic and nonalcoholic patients with cirrhosis with hepatic encephalopathy". eng. In: *American Journal of Neuroradiology* 27.5 (2006), pp. 1019–1026. DOI: 27/5/1019[pii].

[171] A. Deshmane, M. Zaiss, T. Lindig, K. Herz, M. Schuppert, C. Gandhi, B. Bender, U. Ernemann, and K. Scheffler. "3D gradient echo snapshot CEST MRI with low power saturation for human studies at 3T". In: *Magnetic Resonance in Medicine* 81.4 (2019), pp. 2412–2423. DOI: 10.1002/mrm.27569.

[172] G. Oeltzschner, A. Schnitzler, F. Wickrath, H. J. Zöllner, and H.-J. Wittsack. "Use of quantitative brain water imaging as concentration reference for J-edited MR spectroscopy of GABA". In: *Magnetic Resonance Imaging* 34.8 (2016), pp. 1057–1063. DOI: 10.1016/j.mri.2016.04.013.

[173] M. Povazan, M. Mikkelsen, D. L. Rimbault, P. K. Bhattacharyya, M. K. Brix, P. F. Buur, K. M. Cecil, K. L. Chan, D. Y.-T. Chen, A. R. Craven, K. Cuypers, M. Dacko, N. W. Duncan, U. Dydak, D. A. Edmondson, G. Ende, L. Ersland, M. A. Forbes, F. Gao, I. Greenhouse, A. D. Harris, N. He, S. Heba, N. Hoggard, T.-W. Hsu, J. F. Jansen, A. Kangarlu, T. Lange, R. M. Lebel, Y. Li, C.-Y. E. Lin, J.-K. Liou, J.-F. Lirng, F. Liu, J. R. Long, R. Ma, C. Maes, M. Moreno-Ortega, S. O. Murray, S. Noah, R. Noeske, M. D. Noseworthy, G. Oeltzschner, E. C. Porges, J. J. Prisciandaro, N. A. Puts, T. P. Roberts, M. Sack, N. Sailasuta, M. G. Saleh, M.-P. Schallmo, N. Simard, D. Stoffers, S. P. Swinnen, M. Tegenthoff, P. Truong, G. Wang, I. D. Wilkinson, H.-J. Wittsack, A. J. Woods, H. Xu, F. Yan, C. Zhang, V. Zipunnikov, H. J. Zöllner, R. A. Edden, and P. B. Barker. "Comparison of multi-vendor, single-voxel MRS data acquired at 26 sites". In: *Radiology, under revision* (2019).

Appendices

A Abbreviations

ANTs Advanced Normalization Tools

APT amide proton transfer

APTR amide proton transfer ratio

APT$_w$ amide proton transfer-weighted

APT$_w$^{T1} T_1 normalized amide proton transfer - weighted

BBB blood brain barrier

BSA bovine serum albumin

CEST chemical exchange saturation transfer

CER cerebellum

CFF critical flicker frequency

Ch choline

Cr creatine

CRLB Cramér-Rao lower bounds

CSF cerebro spinal fluid

DLS dynamic light scattering

FFT fast Fourier transformation

FID free induction decay

FLASH Fast Low-Angle Shot

FWHM full width at half maximum

GABA γ-aminobutyric acid

GdnHCl guanidinium hydrochloride

Glx glutamate + glutamine

GM gray matter

HE hepatic encephalopathy

HSVD Hankel single value decomposition

HLSVD Hankel Lanczos single value decomposition

IPD inter pulse delays

LVT line tracking test

MEGA-PRESS MEscher-GArwood Point RESolved Spectroscopy

mHE minimal HE

MLS motoric performance series

MOT motor cortex

MR magnetic resonance

MRI magnetic resonance imaging

MRS magnetic resonance spectroscopy

MRSI MRS Imaging

MT magnetization transfer

MTR magnetization transfer ratio

MTR$_{asym}$ magnetization transfer ratio asymmetry

NAA N-acetylaspartate

NEX number of excitations

NLM non-local means

NMR nuclear magnetic resonance

NOE nuclear Overhauser enhancement

PET positron emission tomography

ppm parts per million

PRESS Point RESolved Spectroscopy

RF radio frequency

ROI region of interest

SD standard deviation

SNR signal-to-noise ratio

SVD singular value decomposition

TE echo time

THA thalamus

TR repetition time

WM white matter

WASSR WAter Saturation Shift Referencing

WRT reaction time

B Publications

The dissertation at hand is based on:

Study 1:

H. J. Zöllner, M. Butz, G. Kircheis, S. Klinker, D. Häussinger, B. Schmitt, A. Schnitzler, and H.-J. Wittsack. "Ammonia-weighted imaging by chemical exchange saturation transfer MRI at 3 T". in: *NMR in Biomedicine* 31.9 (2018), e3947. DOI: 10.1002/nbm.3947.

Reprint from NMR in Biomedicine can be found in Appendix C with permission from John Wiley and Sons. The original paper is available online at https://doi.org/10.1002/nbm.3947.

Impact factor (2018): 3.414

Personal contribution: 80% (Data acquisition, data analysis, data interpretation, manuscript drafting)

Study 2:

H. J. Zöllner, M. Butz, M. Jördens, N.-D. Füllenbach, D. Häussinger, B. Schmitt, H.-J. Wittsack, and A. Schnitzler. "Chemical exchange saturation transfer imaging in hepatic encephalopathy". In: *NeuroImage: Clinical* 22 (2019), p. 101743. DOI: 10.1016/j.nicl.2019.101743.

Reprint from NeuroImage: Clinical can be found in Appendix D. The original paper is published under CC BY-NC-ND 4.0 open access license and available online at https://doi.org/10.1016/j.nicl.2019.101743.

Impact factor (2018): 3.943

Personal contribution: 80% (Data acquisition, data analysis, data interpretation, manuscript drafting)

Study 3:

H. J. Zöllner, G. Oeltzschner, A. Schnitzler, and H.-J. Wittsack. "In silico GABA+ MEGA-PRESS: Effects of signal-to-noise ratio and linewidth on modeling the 3-ppm GABA+ resonance". In: *NMR in Biomedicine, under review* (2019).

Manuscript under revision in NMR in Biomedicine can be found in Appendix E.

Impact factor (2018): 3.414

Personal contribution: 80% (Data acquisition, data analysis, data interpretation, manuscript drafting)

Other aspects are taken from:

1)

G. Oeltzschner, A. Schnitzler, F. Wickrath, H. J. Zöllner, and H.-J. Wittsack. "Use of quantitative brain water imaging as concentration reference for J-edited MR spectroscopy of GABA". in: *Magnetic Resonance Imaging* 34.8 (2016), pp. 1057–1063. DOI: 10.1016/j.mri.2016.04.013.

Impact factor (2016): 2.225

Personal contribution: $< 5\%$ (Data acquisition during revision)

2)

G. Oeltzschner, H. J. Zöllner, M. Jonuscheit, R. S. Lanzman, A. Schnitzler, and H.-J. Wittsack. "J-difference-edited MRS measures of γ-aminobutyric acid before and after acute caffeine administration". In: *Magnetic Resonance in Medicine* (2018). DOI: 10.1002/mrm.27233.

Impact factor (2018): 3.858

Personal contribution: 50% (Equal contribution: Supervision data acquisition, data analysis, manuscript revision)

3)

M. Mikkelsen, P. B. Barker, P. K. Bhattacharyya, M. K. Brix, P. F. Buur, K. M. Cecil, K. L. Chan, D. Y. Chen, A. R. Craven, K. Cuypers, M. Dacko, N. W. Duncan, U. Dydak, D. A. Edmondson, G. Ende, L. Ersland, F. Gao, I. Greenhouse, A. D. Harris, N. He, S. Heba, N. Hoggard, T. W. Hsu, J. F. Jansen, A. Kangarlu, T. Lange, R. M. Lebel, Y. Li, C. Y. E. Lin, J. K. Liou, J. F. Lirng, F. Liu, R. Ma, C. Maes, M. Moreno-Ortega, S. O. Murray, S. Noah, R. Noeske, M. D. Noseworthy, G. Oeltzschner, J. J. Prisciandaro, N. A. Puts, T. P. Roberts, M. Sack, N. Sailasuta, M. G. Saleh, M. P. Schallmo, N. Simard, S. P. Swinnen, M. Tegenthoff, P. Truong, G. Wang, I. D. Wilkinson, H.-J. Wittsack, H. Xu, F. Yan, C. Zhang, V. Zipunnikov, H. J. Zöllner, and R. A. Edden. "Big

GABA: Edited MR spectroscopy at 24 research sites". In: *NeuroImage* 159 (2017), pp. 32–45. DOI: 10.1016/j.neuroimage.2017.07.021.

Impact factor (2017): 5.426

Personal contribution: $< 5\%$ (Data acquisition, manuscript revision)

4)

M. Mikkelsen, D. L. Rimbault, P. B. Barker, P. K. Bhattacharyya, M. K. Brix, P. F. Buur, K. M. Cecil, K. L. Chan, D. Y.-T. Chen, A. R. Craven, K. Cuypers, M. Dacko, N. W. Duncan, U. Dydak, D. A. Edmondson, G. Ende, L. Ersland, M. A. Forbes, F. Gao, I. Greenhouse, A. D. Harris, N. He, S. Heba, N. Hoggard, T.-W. Hsu, J. F. Jansen, A. Kangarlu, T. Lange, R. M. Lebel, Y. Li, C.-Y. E. Lin, J.-K. Liou, J.-F. Lirng, F. Liu, J. R. Long, R. Ma, C. Maes, M. Moreno-Ortega, S. O. Murray, S. Noah, R. Noeske, M. D. Noseworthy, G. Oeltzschner, E. C. Porges, J. J. Prisciandaro, N. A. Puts, T. P. Roberts, M. Sack, N. Sailasuta, M. G. Saleh, M.-P. Schallmo, N. Simard, D. Stoffers, S. P. Swinnen, M. Tegenthoff, P. Truong, G. Wang, I. D. Wilkinson, H.-J. Wittsack, A. J. Woods, H. Xu, F. Yan, C. Zhang, V. Zipunnikov, H. J. Zöllner, and R. A. Edden. "Big GABA II: Water-referenced edited MR spectroscopy at 25 research sites". In: *NeuroImage* 191 (2019), pp. 537–548. DOI: 10.1016/J.NEUROIMAGE.2019.02.059.

Impact factor (2018): 5.812

Personal contribution: $< 5\%$ (Data acquisition, manuscript revision)

5)

M. N. Preising, B. Görg, C. Friedburg, N. Qvartskhava, B. S. Budde, M. Bonus, M. R. Toliat, C. Pfleger, J. Altmüller, D. Herebian, M. Beyer, H. J. Zöllner, H.-J. Wittsack, J. Schaper, D. Klee, U. Zechner, P. Nürnberg, J. Schipper, A. Schnitzler, H. Gohlke, B. Lorenz, D. Häussinger, and H. J. Bolz. "Biallelic mutation of human SLC6A6 encoding the taurine transporter TAUT is linked to early retinal degeneration". In: *The FASEB Journal* (2019), fj.201900914RR. DOI: 10.1096/fj.201900914RR.

Impact factor (2018): 5.391

Personal contribution: 5% (Data acquisition, data analysis)

6)

M. Povazan, M. Mikkelsen, D. L. Rimbault, P. K. Bhattacharyya, M. K. Brix, P. F. Buur, K. M. Cecil, K. L. Chan, D. Y.-T. Chen, A. R. Craven, K. Cuypers, M. Dacko, N. W. Duncan, U. Dydak, D. A. Edmondson, G. Ende, L. Ersland, M. A. Forbes, F. Gao, I. Greenhouse, A. D. Harris, N. He, S. Heba, N. Hoggard, T.-W. Hsu, J. F. Jansen, A. Kangarlu, T. Lange, R. M. Lebel, Y. Li, C.-Y. E. Lin, J.-K. Liou, J.-F. Lirng, F. Liu, J. R. Long, R. Ma, C. Maes, M. Moreno-Ortega, S. O. Murray, S. Noah, R. Noeske, M. D. Noseworthy, G. Oeltzschner, E. C. Porges, J. J. Prisciandaro, N. A. Puts, T. P. Roberts, M. Sack, N. Sailasuta, M. G. Saleh, M.-P. Schallmo, N. Simard, D. Stoffers, S. P. Swinnen, M. Tegenthoff, P. Truong, G. Wang, I. D. Wilkinson, H.-J. Wittsack, A. J. Woods, H. Xu, F. Yan, C. Zhang, V. Zipunnikov, H. J. Zöllner, R. A. Edden, and P. B. Barker. "Comparison of multi-vendor, single-voxel MRS data acquired at 26 sites". In: *Radiology, under revision* (2019).

Impact factor (2018): 7.608

Personal contribution: $< 5\%$ (Data acquisition, manuscript revision)

RESEARCH ARTICLE

WILEY **NMR IN BIOMEDICINE**

Ammonia-weighted imaging by chemical exchange saturation transfer MRI at 3 T

Helge Jörn Zöllner[1,2] | Markus Butz[1] | Gerald Kircheis[3] | Stefan Klinker[4] | Dieter Häussinger[3] | Benjamin Schmitt[5] | Alfons Schnitzler[1] | Hans-Jörg Wittsack[2]

[1] Institute of Clinical Neuroscience and Medical Psychology, Medical Faculty, Heinrich Heine University Düsseldorf, Germany

[2] Department of Diagnostic and Interventional Radiology, Medical Faculty, Heinrich Heine University Düsseldorf, Germany

[3] Department of Gastroenterology, Hepatology and Infectiology, Medical Faculty, Heinrich Heine University Düsseldorf, Germany

[4] Institute of Physical Biology, Heinrich Heine University Düsseldorf, Germany

[5] Siemens Ltd. Australia, Healthcare Sector, MacquariePark, NSW, Australia

Correspondence
Helge Jörn Zöllner, Universitätsstraße 1, 40225 Düsseldorf, Germany.
Email: helge.zoellner@med.uni-duesseldorf.de

Funding information
Deutsche Forschungsgemeinschaft, Grant/Award Number: SFB 974 TP B07

Hepatic encephalopathy (HE) is triggered by liver cirrhosis and is associated with an increased ammonia level within the brain tissue. The goal of this study was to investigate effects of ammonia on in vitro amide proton transfer (APT)-weighted chemical exchange saturation transfer (CEST) imaging in order to develop an ammonia-sensitive brain imaging method.

APT-weighted CEST imaging was performed on phantom solutions including pure ammonia, bovine serum albumin (BSA), and tissue homogenate samples doped with various ammonia concentrations. All CEST data were assessed by magnetization transfer ratio asymmetry. In addition, optical methods were used to determine possible structural changes of the proteins in the BSA phantom. In vivo feasibility measurements were acquired in one healthy participant and two patients suffering from HE, a disease associated with increased brain ammonia levels.

The CEST effect of pure ammonia showed a base-catalyzed behavior. At pH values greater than 5.6 no CEST effect was observed. The APT-weighted signal was significantly reduced for ammonia concentrations of 5mM or more at fixed pH values within the different protein phantom solutions. The optical methods revealed no protein aggregation or denaturation for ammonia concentrations less than 5mM. The in vivo measurements showed tissue specific and global reduction of the observed CEST signal in patients with HE, possibly linked to pathologically increased ammonia levels.

APT-weighted CEST imaging is sensitive to changes in ammonia concentrations. Thus, it seems useful for the investigation of pathologies with altered tissue ammonia concentrations such as HE. However, the underlying mechanism needs to be explored in more detail in future in vitro and in vivo investigations.

KEYWORDS

amide proton, ammonia, APT, CEST, HE, hepatic encephalopathy

1 | INTRODUCTION

Hepatic encephalopathy (HE) is a common complication in patients with liver cirrhosis. It comprises a variety of neuropsychiatric and motor symptoms,[1] and is assumed to be largely mediated by an increase of ammonia within the brain.[2,3] In vitro, ammonia accumulation has been linked to cell swelling.[4] In vivo, HE causes a variety of changes in advanced MR contrasts, suggesting the appearance of a low-grade edema due to ammonia accumulation. Shah et al. reported region-dependent increases of quantitative measurements of MR-visible brain water in HE patients,[5] while an absence of such changes in lower-grade HE was found by Oeltzschner et al.[6] Other studies investigating semi-solid magnetization transfer (MT) reported a signal loss with increasing HE severity, with potential causes being water content changes, mild alterations in myelin structure, or cell inflammation.[7-9] To fully improve the understanding of increased ammonia levels on brain microstructure or physiology, it is desirable to study ammonia as a primary source of contrast, rather than to observe the secondary effects of increased brain ammonia levels on other imaging contrasts.

Chemical exchange saturation transfer (CEST) imaging is a potential tool for the assessment of ammonia levels. CEST provides an advanced MRI contrast depending on diluted labile protons, which are undetectable in conventional MRI. Common MRI contrast is generated by the bulk water signal. The CEST contrast is based on the change of the bulk water signal due to the MT between the bulk water protons and frequency selective saturated labile protons.[10] Chemical exchange between ammonia and bulk water studied with 11.7 T MRI microscope systems showed a strong pH dependence of the MT of ammonia[11] and was investigated in a former pioneer study by Wolff and Balaban.[12] Based on the fact that ammonia cannot be detected directly with CEST MRI at physiological conditions, possible effects of ammonia on CEST-sensitive amide protons were investigated.

CEST MRI is sensitive to changes in the environment of the saturated protons, e.g. changes of pH or temperature. Apart from amide proton quantification, amide proton transfer (APT)-weighted imaging allows for the detection of pH changes in the environment of the labelled protons[13] located in proteins. It includes global measurements of in vitro protein unfolding[14,15] leading to possible applications in neurodegenerative diseases.

The aim of the present study was to assess the potential of APT-CEST to create an ammonia-sensitive imaging method which could benefit studies of the pathophysiological basis of HE. The influence of ammonia on APT-weighted CEST contrast was investigated with phantom measurements of amide proton solutions with varying pH, levels of ammonia, and levels of APT contrast agents. Finally, the method was tested in vivo in three participants, including two patients with HE and one healthy control.

2 | MATERIALS AND METHODS

2.1 | Model solution: pure ammonia

In the first phantom, 16 samples with different pH values (post-MR acquisition: pH = 1.1, 1.3, 2.3, 2.5, 3.0, 3.7, 5.3, 5.6, 6.7, 7.1, 7.8, 8.3, 8.9, 10.0, 10.3, and 11.2) were titrated with hydrochloric acid and sodium hydroxide based on a 500mM ammonia stock solution. The pH values were measured before and after the MR acquisition using a Mettler Toledo (Columbus, OH, USA) FE 20 with a LE407 pH electrode. This phantom was designed to measure the behavior of ammonia over a broad range of pH values. Small changes in pH were negligible, so no buffer was used.

2.2 | Model solution: BSA + ammonia

The solution in the second phantom was prepared using a 50mM phosphate-based sodium-hydrogen (PBS) buffer at pH 7.1. Albumin from bovine serum (BSA) ($\geq$98%, Carl Roth, Karlsruhe, Germany) was used as APT-CEST contrast agent. Eight 20 ml tubes with PBS buffer solution containing increasing ammonia concentrations ([0, 0.5, 5, 50, 500] µM, [5, 50, 500] mM) were prepared with 10% BSA, and incubated at room temperature for 4 h to allow a potential unfolding reaction. The concentration was chosen as the physiological total protein content is about 10% in the human brain.[16] Another sample with 500mM ammonia was used as reference.

2.3 | Model solution: tissue homogenate + ammonia

In the third phantom, tissue homogenates were created as described by Zaiss and colleagues.[17] Homogeneous tissue was extracted from a pig brain, homogenized using a hollow needle and pestle, and the volume was diluted (1:2) with distilled water. Eight 20 ml tubes were used to prepare solutions containing this tissue homogenate and buffered ammonia solution (with the same ammonia concentrations as the second phantom) at a volume ratio of 1:2. T_1 relaxation times of each sample were reduced with 20 µM gadopentetate dimeglumine (Magnevist™, Schering, Berlin, Germany).

2.4 | Fluorescence spectroscopy experiments

To determine the protein denaturation of the BSA, fluorescence experiments were performed on 1 ml of each sample of the second phantom 2 h before the MR experiments. An additional BSA sample with 6 M guanidine hydrochloride (GdnHCl) was used as control sample with completely unfolded protein. Fluorescence was measured with a Jasco (Easton, MD, USA) FP-6500 spectrofluorometer by exciting the tryptophan residues of

BSA at $\lambda = 295$ nm (bandwidth 5 nm). Fluorescence emission of each sample was measured three times between $\lambda = 310$ nm and $\lambda = 500$ nm with 1 nm data pitch, and averaged afterwards. The ratio of the fluorescence emission intensities at $\lambda = 330$ nm and $\lambda = 360$ nm of each sample was calculated. Subsequently, the 0mM ammonia BSA sample was assumed to be natively folded and the GdnHCl-doped sample was assumed to be completely unfolded. This normalization of the fluorescence emission intensity ratios was used to determine the dependence of protein denaturation on ammonia concentration.

2.5 | Dynamic light scattering experiments

To determine possible protein aggregation of the BSA, dynamic light scattering (DLS) experiments were performed on 1 ml of the 0 and 500mM ammonia concentration samples of the second phantom. A PSS-380Nicomp (Particle Sizing System, Santa Barbara, CA, USA) DLS device was used to measure the particle size distribution. Number-weighted Gaussian distributions were calculated for both samples to determine the mean particle diameter.

2.6 | MR experiments

MR experiments were performed at room temperature on a clinical whole-body 3 T MRI (Siemens MAGNETOM Trio A TIM System, Siemens Healthcare, Erlangen, Germany) using a 12-channel head matrix coil to receive, and the body coil to transmit. 16 ml of each sample was transferred into a phantom containing eight tubes. The phantoms were placed inside a large water-filled container to reduce B_0 inhomogeneities. The first phantom was measured twice with eight samples in each measurement. In the second phantom, an ammonia reference tube with 500mM ammonia at pH = 7.1 was added. In vitro CEST data were acquired using a prototype two-dimensional gradient echo sequence. The acquisition parameters were as follows: $T_E = 3.06$ ms; $T_R = 10000$ ms; flip angle = 10°; FoV = (180 × 180) mm^2; matrix size 128 × 128; slice thickness 8 mm. Saturation was performed with a pulse train of 48 Gaussian-shaped pulses with pulse duration (PD) = 100 ms and inter-pulse delay (IPD) = 100 ms. 44 equidistant frequency offsets between −4 and 4 ppm were sampled for the first phantom, whereas data were sampled with 66 equidistant frequency offsets between −5 and 5 ppm for the other phantoms. The unsaturated S_0 image was acquired by turning the saturation pulse off within the sequence. The first phantom was investigated with eight different B_1 power amplitudes ($B_1 = 0.6, 0.8, 1, 1.2, 1.4, 1.7, 2, 2.2$ μT), and the other phantoms using nine different B_1 saturation power amplitudes ($B_1 = 0.4, 0.7, 1, 1.3, 1.4, 1.5, 1.6, 1.7, 2$ μT). Relative B_1 maps were calculated with the double-flip-angle method[18] using flip angles of 45° and 90°. B_0 inhomogeneities were corrected using a water saturation shift referencing (WASSR) map.[19] T_1 maps were measured with an inversion recovery sequence with 15 inversion times ($T_I = 50, 75, 100, 125, 150, 200, 250, 400, 600, 800, 1000, 1300, 1900, 2400, 3500$ ms) and $T_R = 10\,980$ ms. T_1 maps were calculated using Stroketool (Digital Image Solution, Frechen, Germany). T_2 measurements were made using a multi-spin-echo sequence with 32 echoes between $T_E = 50$ ms and 1600 ms with $T_R = 10\,000$ ms. T_2^* was measured with a multi-gradient echo sequence with 12 echoes between $T_E = 4.80$ ms and 75.37 ms. The spatial dimensions were the same as described in the CEST sequence. T_2 and T_2^* maps were calculated on an external workstation (syngoMMWP, VE23A, Siemens, Berlin, Germany).

2.7 | MTR$_{asym}$ evaluation

Finally, averaged z-spectra and magnetization transfer ratio asymmetry (MTR$_{asym}$) images were calculated within the regions of interest using an in-house written MATLAB script (MathWorks, Natick, MA, USA). All images were smoothed using a 3 × 3 pixel Gaussian filter. The z-spectra were interpolated using the *interp1* MATLAB function with a piecewise cubic Hermite interpolating polynomial (*pchip*) algorithm in steps of 0.05 ppm. Asymmetry analysis[20] was calculated as follows: MTR$_{asym}$ = Z_{ref} − Z_{lab}, with labelled proton scan $Z_{lab} = Z (\Delta\omega_{lab}) = S (\Delta\omega_{lab})/S_0$ and reference at the opposite frequency $Z_{ref} = Z (\Delta\omega_{ref} = -\Delta\omega_{lab}) = S (\Delta\omega_{ref} = -\Delta\omega_{lab})/S_0$. In accordance with Guivel-Scharen and colleagues,[11] the peak of pure ammonia was investigated with $Z_{lab} = Z(2.4$ ppm$)$ and $Z_{ref} = Z(-2.4$ ppm$)$ within the first phantom. The asymmetry is subsequently referred to as MTR$_{asym}$ (2.4 ppm). For the other phantoms and the in vivo measurements, the MTR$_{asym}$ curves were calculated over a frequency range between 0 and 5 ppm within the z-spectra. Subsequently, the APT-weighted signal within the MTR$_{asym}$ maps was calculated by averaging MTR$_{asym}$ over a frequency range from 3 to 4 ppm. This will be referred to as MTR$_{asym}$ (3.5 ± 0.5 ppm) in the following. B_1-contrast correction was performed for the second and third phantoms as described by Windschuh and colleagues[21] with a nominal saturation power of $B_{1,nom} = 1.5$ μT. Statistical analysis was performed within each tube using a region of interest analysis by applying a binary mask.

2.8 | In vivo measurements

All investigations were approved by the local ethics committee (5179R) and performed in agreement with the Declaration of Helsinki. Two patients (one male, one female) with clinically confirmed HE, graded as minimal HE (mHE) and HE I, as well as one female age-matched control, were examined after giving prior written informed consent. The minimal HE was determined by neuropsychometric testing[1,22] and assessment of the critical flicker frequency (CFF). In vivo CEST images were acquired using a prototype three-dimensional gradient echo sequence. The acquisition parameters were adapted as follows: $T_E = 3.06$ ms; $T_R = 1390$ ms; flip angle = 10°; FoV = (230 × 230) mm^2; matrix size 192 × 192; 24 slices; slice thickness 5mm; gap 1 mm. Saturation was performed with a pulse train of five Gaussian-shaped pulses with PD = 100 ms and IPD = 100 ms. 22 equidistant frequency offsets were sampled between −5 and 5 ppm with $B_1 = 1.5$ μT. Four three-dimensional gradient echo scans with different flip angles

(4°, 15°, 23°, 27°) were acquired with the same spatial dimensions as the CEST sequence. A relative B_1 map was obtained by heavily smoothing the low flip angle (4°) three-dimensional gradient echo sequence.[23] In addition, a T_1 map was calculated using two of the images above (4°, 15°).[23]

Post-processing included motion correction with the co-registration method of the MATLAB toolbox SPM12.[24] The 3D volumes of the CEST and WASSR datasets of each saturation frequency were co-registered to the 3D volume of the first saturation frequency of the CEST dataset (S_0). B_1-contrast correction was performed as described by Windschuh et al.[21] with a nominal saturation power of $B_{1,nom}$ = 1.4 µT. Tissue compounds and cerebrospinal fluid (CSF) were segmented with the SPM newSegment function, and tissue masks were created with tissue probabilities greater than 0.99 for gray (GM) and white matter (WM). The CSF cut-out mask included only pixels with probabilities greater than 0.8 for GM and WM. GM/WM tissue fraction ratios were calculated from the number of pixels of each specific tissue class. Mean z-spectra and MTR$_{asym}$ curves were calculated for each specific tissue class.

2.9 | Statistical analysis

The MATLAB *corrcoef* function was used to calculate Pearsons's correlation coefficients for the relaxation times and MTR$_{asym}$ values. The in vitro and in vivo measurements were assessed with MATLAB *ttest2* function to perform Student's *t*-test. Bonferroni correction for multiple comparisons was applied to determine significant effects at an individual alpha level of 0.05.

3 | RESULTS

3.1 | MR experiments model solution: pure ammonia

Figure 1A,B shows the calculated mean z-spectra and MTR$_{asym}$ curves within the tubes of the first phantom containing pure ammonia solutions with different pH values at B_1 = 0.6 µT. Figure 1C shows the MTR$_{asym}$ effect at 2.4 ppm for different B_1 values. Between pH 1.1 and 5.6, the measured MTR$_{asym}$ (2.4 ppm) value is proportional to pH (Figure 1A), whereas at pH > 5.6 the visible asymmetry vanishes (Figure 1B). There is no apparent MTR$_{asym}$ (2.4 ppm) effect of ammonia at physiological pH values. The measured MTR$_{asym}$ (2.4 ppm) is based on the real chemical exchange between ammonia and the bulk water at pH values less than 5.64.

3.2 | MR experiments model solution: BSA + ammonia

The mean MTR$_{asym}$ (3.5 ± 0.5 ppm) values within the tubes containing 10% BSA solutions at different ammonia concentrations and the ammonia reference at various B_1 power amplitudes are depicted in Figure 2. Between B_1 = 0.7 and 1.5 µT, MTR$_{asym}$ (3.5 ± 0.5 ppm) decreases with increasing concentrations of ammonia. The reduction in MTRasym (3.5 ± 0.5 ppm) is mainly visible for ammonia concentrations of 5mM or greater. For higher saturation powers (B_1 > 1.5 µT) and ammonia concentrations smaller than 5 µM, the proportionality vanishes, which is also the case for low saturation powers (B_1 = 0.4 µT). Therefore, B_1 = 1.5 µT was used for the in vivo measurements. In addition, a negative MTR$_{asym}$ occurs within the
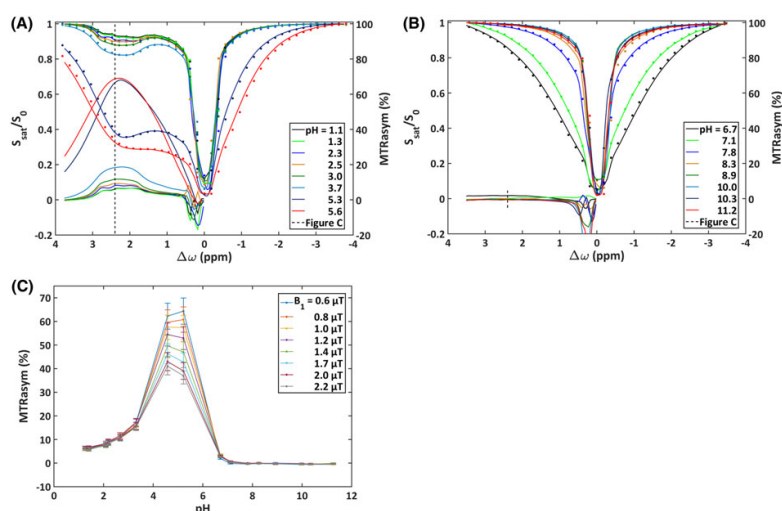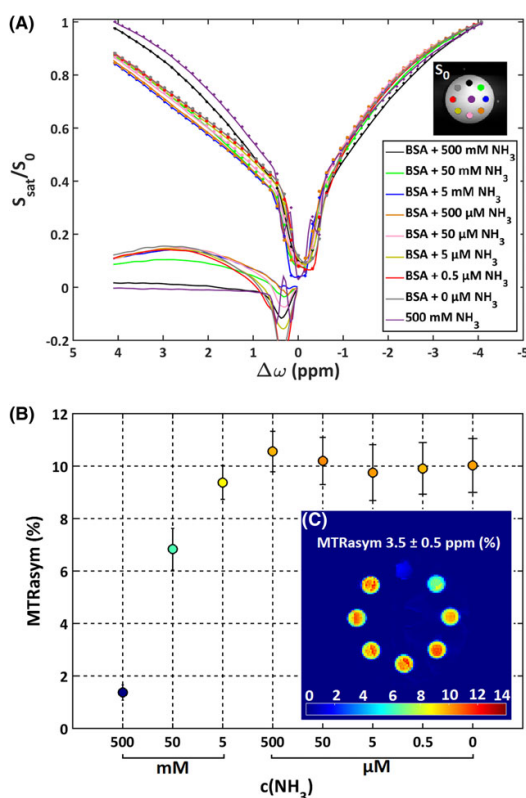

FIGURE 1 A, Mean z-spectra and MTR$_{asym}$ curves of the tubes within the ammonia phantom at different pH levels between 1.1 and 5.6 measured with B_1 = 0.6 µT. B, Mean z-spectra and MTR$_{asym}$ curves of the tubes within the ammonia phantom at different pH levels between 6.7 and 11.2 measured with B_1 = 0.6 µT. C, Measured pH dependence of the mean MTR$_{asym}$ at 2.4 ppm at different B_1 saturation powers. The dotted line in A and B indicates the position of the calculated MTR$_{asym}$ (2.4 ppm) values
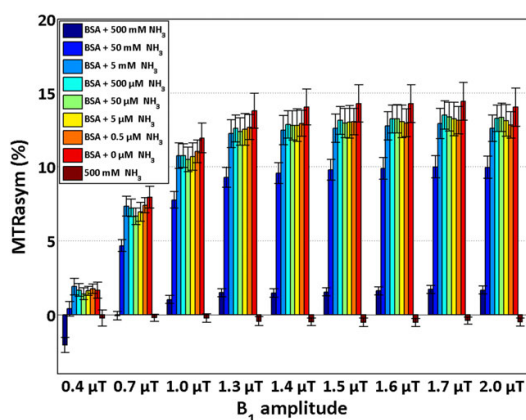
FIGURE 2 Mean MTR_{asym} (3.5 ± 0.5 ppm) values within the tubes of 10% BSA model solutions with different ammonia concentrations and a 500mM ammonia reference at various B_1 saturation powers. The pH was kept at 7.1

BSA + 500mM NH_3 sample at low saturation powers. The ammonia reference shows a small negative MTR_{asym} of approximately -0.5% throughout all saturation powers, which is comparable to the measured values in the first phantom at the same pH value.

The mean z-spectra and MTR_{asym} curves within the tubes of the BSA phantom are displayed in Figure 3A. MTR_{asym} between 1.5 and 4 ppm decreases with increased ammonia concentration. MTR_{asym} between 1.5 and 4 ppm increases notably in the BSA + 500mM NH_3 compared with

FIGURE 3 A, Mean z-spectra and MTR_{asym} curves within the tubes of 10% BSA model solutions with different ammonia concentrations and a 500mM ammonia reference measured with $B_1 = 1.6$ µT. An S_0 image with the colors corresponding to the legend is added as guidance. B, Concentration dependence plot of the B_1-contrast-corrected mean MTR_{asym} (3.5 ± 0.5 ppm) values within the tubes. C, B_1-contrast-corrected MTR_{asym} (3.5 ± 0.5 ppm) map of 10% BSA solution with different ammonia concentrations. The B_1-contrast correction was performed with a nominal $B_{1,nom} = 1.5$ µT

the ammonia reference. The dependence of the mean MTR_{asym} (3.5 ± 0.5 ppm) with a nominal saturation power of $B_{1,nom}$ = 1.5 µT within the tubes of the BSA samples with different ammonia concentrations is depicted in Figure 3B, including an MTR_{asym} (3.5 ± 0.5 ppm) map of the phantom (Figure 3C). Strong signal reduction occurs at ammonia concentrations between 5 and 500mM. Concentrations less than 5mM were associated with lower effects on MTR_{asym} (3.5 ± 0.5 ppm).

Table 1 summarizes the statistics of the measured T_1, T_2, and T_2* values as well as mean MTR_{asym} (3.5 ± 0.5 ppm) with a nominal saturation power $B_{1,nom}$ = 1.5 µT in dependence on the ammonia concentrations in the regions of interest. Ammonia concentrations higher than 500 µM introduce a significant difference in comparison with the pure BSA sample. Measured T_2* values reveal no correlation with the calculated MTR_{asym} (3.5 ± 0.5 ppm) within the phantom solutions (r = 0.69; p = 0.62). T_1 and T_2 values correlate with MTR_{asym} (3.5 ± 0.5 ppm) (T_1, r = −0.96; p < 0.05; T_2, r = 0.73; p < 0.05), which is mainly driven by ammonia concentrations higher than 50mM. For ammonia concentrations lower than 50mM, the measured T_1 and T_2 values do not correlate with MTR_{asym} (3.5 ± 0.5 ppm) values (T_1, r = −0.71; p = 0.50; T_2, r = 0.10; p = 0.82).

3.3 | Fluorescence spectroscopy experiments

The fluorescence spectroscopy measurements of the BSA + ammonia phantom are summarized in Figure 4. The overlaid normalized intensity plots (Figure 4A) and the corresponding denaturation function (Figure 4B) do not reveal denaturation for concentrations below 5mM. For higher ammonia concentrations (≥5mM), changes in the denaturation curve appear with around 6, 8, and 25% protein unfolding for 5, 50, and 500mM, respectively.

3.4 | DLS experiments

The DLS measurements of the BSA sample without and with ammonia showed the same particle size distribution. Although the presence of ammonia influences protein folding, the size distribution and dispersity of BSA were not changed. The mean particle diameter was calculated as 3.2 ± 5.3 nm for pure BSA and 3.0 ± 4.2 nm for BSA + 500mM NH_3, which is in accordance with the calculations of Axelsson.[25]

3.5 | MR experiment model solution: tissue homogenate + ammonia

Figure 5 demonstrates the MTR_{asym} (3.5 ± 0.5 ppm) map with nominal $B_{1,nom}$ = 1.5 µT of the tissue homogenate. Possible direct water saturation effects, inducing a symmetric broadening around the water peak, should be cancelled out by asymmetry analysis (Figure 5A). The signal reduction becomes apparent even for low concentrations less than 5mM. All samples except the 50 and 0.5 µM show significant signal reduction compared with the tissue homogenate without ammonia.

3.6 | In vivo measurements

The in vivo measurements are depicted in Figure 6, including mean z-spectra and MTRasym curves of all subjects and segmented tissue types (Figure 6A,B). The MTR_{asym} (3.5 ± 0.5 ppm) map calculated with a nominal saturation power of $B_{1,nom}$ = 1.4 µT is shown with corresponding anatomical pictures of each subject in Figure 6C. MTR_{asym} (3.5 ± 0.5 ppm) is reduced globally within the whole slice with increasing severity of HE. Regional dependences appear within the occipital brain regions and around the basal ganglia. Tissue specific statistics are summarized in Table 2. Within the whole slice, mean MTR_{asym} (3.5 ± 0.5 ppm) is reduced by 0.47 percentage points between patients with mHE and HE I (p < 0.01), whereas reduction between the healthy control and the mHE patient is much lower at 0.03 percentage points (p = 0.94). Tissue specific differences are higher for GM, where mean MTR_{asym} (3.5 ± 0.5 ppm) is reduced by 0.23 percentage points between the healthy control and the mHE patient. In WM the mean MTR_{asym} (3.5 ± 0.5 ppm) is slightly increased between mHE patients and controls (0.1%). Between the mHE

TABLE 1 In vitro investigations of several MR parameters (with B_1-contrast-corrected MTR_{asym} (3.5 ± 0.5 ppm) with a nominal saturation power of $B_{1,nom}$ = 1.5 µT) in 10% BSA phantoms with different ammonia concentrations. The statistics were performed within each tube and t-tests were performed in comparison with 10% BSA solution (asterisks indicates significant difference: *P < 0.007, **P < 0.0014, Bonferroni-adjusted significance level)

10% BSA + c (NH_3)	MTR_{asym} (%)	T_2 (ms)	T_2* (ms)	T_1 (ms)
500mM	1.37 ± 0.3**	301 ± 82	36 ± 2	1941 ± 45
50mM	6.83 ± 0.8**	336 ± 75	36 ± 1	1883 ± 45
5 mM	9.38 ± 0.6**	314 ± 83	36 ± 1	1889 ± 29
500 µM	10.55 ± 0.8*	333 ± 81	35 ± 2	1875 ± 32
50 µM	10.20 ± 0.9	346 ± 67	32 ± 1	1915 ± 29
5 µM	9.80 ± 1.1	329 ± 58	34 ± 2	1896 ± 30
0.5 µM	9.91 ± 1.0	335 ± 79	36 ± 1	1894 ± 43
0 µM	10.02 ± 1.0	345 ± 84	35 ± 1	1910 ± 54
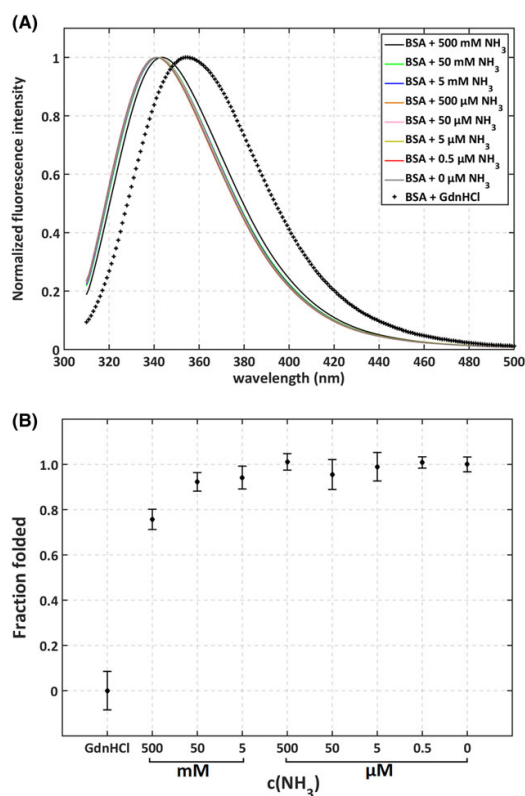
FIGURE 4 Fluorescence spectroscopy measurements of BSA model solutions with different ammonia concentrations and GdnHCl reference. A, Mean normalized fluorescence intensity measured between λ = 310 nm and λ = 500 nm. B, Denaturation function calculated from fluorescence emission ratio of λ = 330 nm and λ = 360 nm, assuming complete or no unfolding within the GdnHCl reference or 0mM ammonia BSA sample respectively. The mean and standard deviation of the three repeated measurements are included

and the HEI patients, mean MTR_{asym} (3.5 ± 0.5 ppm) is reduced by 0.53 percentage points in GM and 0.37 percentage points. Median MTR_{asym} (3.5 ± 0.5 ppm) is reduced by 0.38 percentage points between the two patients, while the difference in MTR_{asym} (3.5 ± 0.5 ppm) between the healthy control and the mHE patient is relatively small (0.05%). The standard deviation of MTR_{asym} (3.5 ± 0.5 ppm) is comparable for all measurements at around one percentage point. Mean T_1 values within the slices were reduced in the mHE patient compared with the healthy control (difference of 154 ms), and slightly increased in the HE I patient compared with the mHE patient (difference of 13 ms).

4 | DISCUSSION

The influence of ammonia on APT CEST imaging was investigated in model solutions of ammonia and BSA as well as in pig brain homogenates with ammonia. The measurements revealed a clear decrease of the APT CEST signal with increasing concentration of ammonia within the phantom. In the in vivo measurements in patients with HE, a decrease in the MTR_{asym} (3.5 ± 0.5 ppm) signal occurred when compared with a healthy control. As a pathological increase of ammonia in the brain of HE patients is a well-known finding, the presented method may be a suitable ammonia-sensitive imaging method to study ammonia levels in the HE brain in vivo.

4.1 | Pure ammonia model solution

The mean MTR_{asym} (2.4 ppm) of pure ammonia was found to be proportional to pH. For pH > 5.6, the exchange rate reaches the fast exchange regime, leading to an apparent reduction in MTR_{asym}. This base-catalyzed behavior (as shown in Figure 1C) has previously been demonstrated by Guivel-Scharen and colleagues.[11] Above pH = 5.6, the chemical exchange exceeds the range of slow to intermediate proton exchange, leading to a strong reduction of the MTR_{asym} (2.4 ppm) value. Therefore, ammonia is not directly observable at physiological conditions using CEST imaging methods at a magnetic field strength of 3 T.
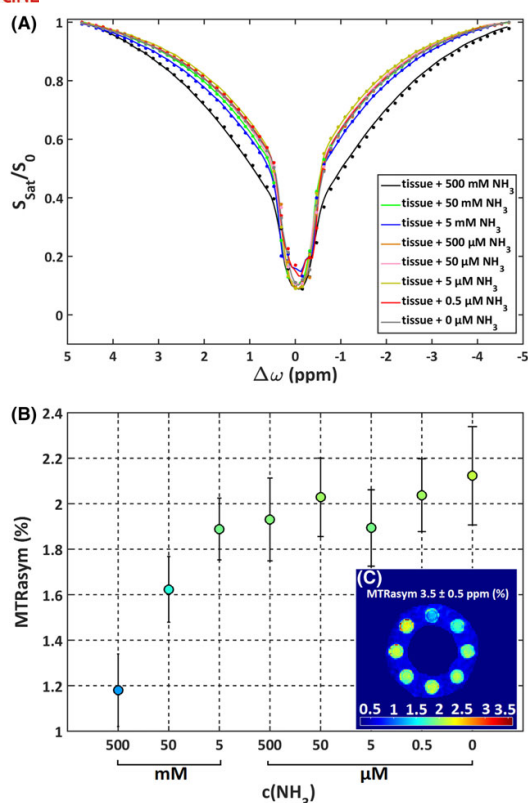
FIGURE 5 A, Mean z-spectra within the tubes of pig brain tissue homogenates with different ammonia concentrations measured with $B_1 = 1.6$ μT. B, Concentration dependence plot of the B_1-contrast-corrected mean MTR_{asym} (3.5 ± 0.5 ppm) values of the pig brain tissue homogenates. C, Calculated B_1-contrast-corrected MTR_{asym} (3.5 ± 0.5 ppm) map. The B_1-contrast correction was performed with a nominal $B_{1,nom} = 1.5$ μT

4.2 | BSA + ammonia model solution

Ammonia is known to destabilize proteins by increasing their hydrophobic behavior, inducing aggregation which may lead to precipitation of proteins in solution.[26] It is also known to reduce water T_2 values. At 5 M NH_4Cl, full water suppression was achieved by spin–spin relaxation in MR spectroscopy.[27] The effects mentioned above may reduce the APT-weighted signal with increasing ammonia concentrations (shown in Figures 2 and 3). Ammonia concentrations less than 5mM did not induce aggregation or denaturation, as confirmed with optical methods (see Figure 4B). For concentrations of 5mM or higher, ammonia induced protein unfolding in up to 25% of BSA proteins. About 6% protein unfolding was observed at a concentration of 5mM ammonia, which could be assumed as in vivo concentration measured in animal models.[28]

The correlation between the measured T_2 values and MTR_{asym} (3.5 ± 0.5 ppm) could be explained by different pathways. One pathway is an alteration in T_2-exchange mechanism through the presence of ammonia reported by Rabenstein and Fan,[27] which may induce a reduction of the water T_2 values. The second pathway is driven by structural changes within the proteins, which are leading to T_2 alterations. The fact that T_2^* did not correlate with MTR_{asym} (3.5 ± 0.5 ppm) may originate in B_0 inhomogeneities, which covers the exchange-related mechanism in T_2^*.

The correlation between T_1 and MTR_{asym} (3.5 ± 0.5 ppm) is likely driven by the structural changes within the BSA + 500mM NH_3 sample, as the correlation vanishes after exclusion of this sample. In addition, high ammonia concentrations introduce an increasing semi-solid MT leading to a negative MTR_{asym} (3.5 ± 0.5 ppm) within the BSA + 500mM NH_3 sample.

Possible effects of B_1 inhomogeneities, which have a large impact on the observed chemical exchange in CEST imaging,[21] are reduced by the applied B_1 correction method including a large number of different B_1 amplitudes measured in the phantom.

As the in-plane resolution was approximately 1.4 mm/pixel for the phantom measurements, partial volume effects within the 1.4 cm tube may introduce further variation in the pixel intensities. Therefore, the rim of the tubes was avoided in the regions of interest. Through-plane partial volume effects are assumed to be small, as the slice was placed in the middle of the symmetric phantom, and no concentration gradient should appear within the tubes.
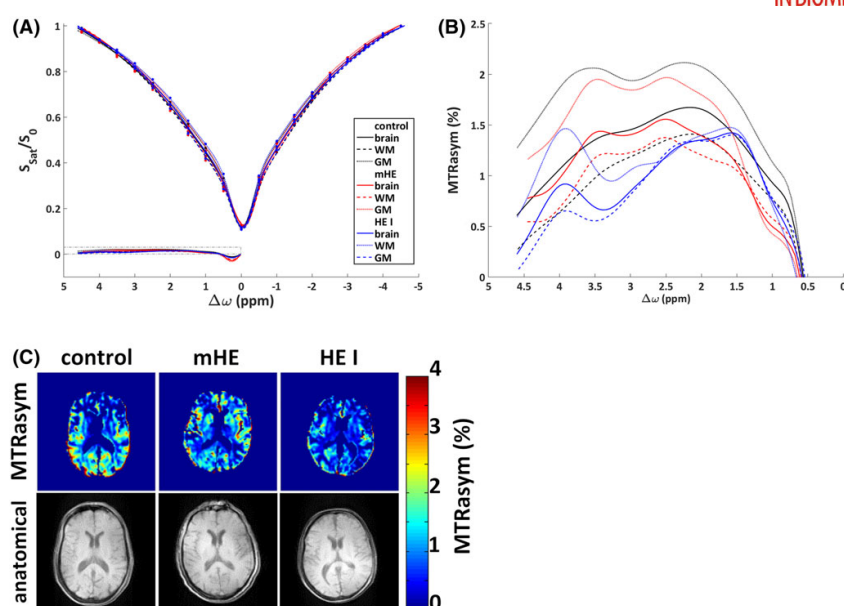
FIGURE 6 A, In vivo mean z-spectra and MTR_{asym} curves of the segmented tissue (whole slice, WM, and GM) within different subjects measured with B_1 = 1.5 µT. B, Enlarged mean MTR_{asym} curves. C, In vivo measurements with corresponding anatomical images (second row). B_1-contrast-corrected MTR_{asym} (3.5 ± 0.5 ppm) map with nominal $B_{1,nom}$ = 1.4 µT of patients with different severities of HE and one healthy control (first row). The subclinical patient is graded using CFF and psychometric testing, while the HE I patient is rated according to West Haven criteria. The disease severity and assumed ammonia accumulation increases from left to right

TABLE 2 In vivo investigations of B_1-corrected MTR_{asym} (3.5 ± 0.5 ppm) with a nominal $B_{1,nom}$ = 1.5 µT and T_1 values within the depicted slices (see Figure 6) and segmented tissues (GM and WM). The GMWM ratio is the ratio of the number of pixels of each specific tissue. The statistics were performed within the whole depicted slice and the segmented tissue

	Healthy control		mHE		HE I	
Age (y)	60		62		61	
GMWM ratio	0.45		0.49		0.41	
	MTR_{asym} (%)	T_1 (ms)	MTR_{asym} (%)	T_1 (ms)	MTR_{asym} (%)	T_1 (ms)
Whole slice						
mean ± SD	1.2 ± 1.2	1531 ± 361	1.1 ± 0.9	1386 ± 387	0.7 ± 1.1	1399 ± 704
median	1.1	1421	1.0	1282	0.6	1197
GM						
mean ± SD	1.9 ± 1.4	1908 ± 376	1.6 ± 1.1	1758 ± 344	1.1 ± 1.4	1913 ± 852
median	1.8	1856	1.6	1749	1.1	1854
WM						
mean ± SD	0.8 ± 0.8	1478 ± 240	0.9 ± 0.7	1306 ± 250	0.5 ± 0.6	1273 ± 438
median	0.8	1443	0.8	1252	0.5	1186

4.3 | Tissue homogenate ammonia model solution

Regarding the in vivo measurements, it has been shown that in vitro CEST measurements are not directly transferable to in vivo measurements.[29] This can be explained by the strong effects of semi-solid MT[30] in tissue and the appearance of multi-parametric effects on the measured spectra, such as increased numbers of resonances overlapping with the observed APT signal.[29] The more advanced brain sample aimed for a better modelling of in vivo conditions than the BSA model solutions. The reduction in the observed saturation transfer with increasing ammonia concentration was also found in this tissue measurement. Furthermore, an increasing semi-solid MT occurred in the phantom measurements with increasing ammonia concentration. In comparison with the BSA phantom, the tissue homogenate contains macromolecules, which are influenced by the presence of ammonia. Miese et al. reported alterations in semi-solid MT of patients with HE, which were interpreted as a demyelination process or water content changes.[9] Our data suggest an influence of ammonia on the MT of water, but could not identify the underlying mechanisms, which

could be any changes in the macromolecular structure. However, it is not directly comparable to in vivo measurements, where protein concentrations are higher and water concentrations are lower than in the diluted tissue samples. In addition, there is no active metabolism in vitro, and pathological changes in metabolite ratios could not be modeled by this approach.

Further potential confounders to the different CEST effect are the unknown composition of the tissue homogenates, and higher water concentration, compared with the in vivo condition. T_1 relaxation times within the phantom (data not shown) were comparable to GM relaxation times in the in vivo measurements. The overall decrease in MTR$_{asym}$ (3.5 ± 0.5 ppm) in comparison with the BSA phantom seems mainly driven by T_1 reduction through gadopentetate dimeglumine. In addition, the concentration of the amide protons may differ between the BSA and the tissue homogenate phantom.

4.4 | In vivo measurements

The in vivo data were acquired from patients with different gradings of HE, showing global signal reduction within the depicted slices. Regional differences appeared mainly within occipital regions and in basal ganglia. Changes in basal ganglia may be driven by T_1 value alterations due to pallidal manganese deposition.[31] Reduction was stronger in cortical regions, as MTR$_{asym}$ (3.5 ± 0.5 ppm) decreases more strongly within the GM. These regional effects should be carefully interpreted, given the low sample size and small differences relative to the signal variance. The signal variance in the in vivo measurement could be mainly driven by partial volume effects due to the slice thickness of 5mm. Partial volume effects, particularly at the border between tissue and CSF, will affect the calculated MTR$_{asym}$ and the tissue segmentation. The impact of partial volume effects in the in-plane dimension should be lower as the resolution was much higher (~1.2 mm/pixel) compared with the through-plane dimensions. In addition, flow artefacts may increase the variability at the border of tissue and CSF. Based on the phantom measurements, it can be assumed that the signal reduction is associated with increasing ammonia concentrations. As all slices have roughly the same GM/WM ratio, differences in tissue composition could be neglected.

4.5 | Other in vivo confounders

In healthy tissue, homeostasis determines intra- and extracellular pH to a tissue specific equilibrium value. Nevertheless, even small changes in pH may contribute to alterations of MTR$_{asym}$ in the brain. pH may change in different pathologies between 6.9 and 7.2.[32] Thus, increased ammonia concentrations may shift pH to higher values and affect the base-catalyzed amide proton exchange. Zhou and colleagues demonstrated that amide MTR$_{asym}$ is proportional to pH in ischemic rat brains,[13] which was also reproduced in later work.[33] Transferring these findings to the assumption of a possible increase due to the presence of ammonia, one would assume an increase in the amide MTR$_{asym}$ of HE patients. APT-weighted contrast may be decreased by the increasing water content of the investigated patients, which was measured in WM from 70.9% in controls up to 72.9% in patients with overt HE.[6]

Numerical simulations revealed an increasing amide CEST effect with increasing pH, while amine CEST (~2.85 ppm) decreases, because the exchange rate of amine protons changes in the fast exchange regime.[34] Although the in vivo MTR$_{asym}$ effect was calculated as the mean between 3 and 4 ppm in the present study, possible changes of the amine CEST effect may contribute to the results.

In vivo measurements may further be influenced by other metabolites, as the ratio of glutamine and glutamate are strongly altered in patients with HE,[1,9,35] and both metabolites resonate between 3 and 4 ppm[29] in the z-spectra. Therefore, an increased Glx/Cr ratio,[9] which would be mainly driven by Gln,[28] may increase the in vivo MTR$_{asym}$ between 3 and 4 ppm. As the in vivo APT-weighted signal showed a decreasing trend, the effect of glutamine and glutamate ratio changes seemed not to affect the APT-weighted signal. Hence, regional dependences of ammonia accumulation[3] in HE may account for regional dependences of the observed APT-weighted signal. In the three in vivo measurements, regional dependences remain unclear, as changes of the CEST effect between the different groups are small. Consequently, larger populations need to be investigated to evaluate regional dependences of APT-weighted imaging in groups of patients with varying grades of HE severity.

APT-weighted imaging is used as a marker for protein content and is altered by conformational changes within intracellular protein compounds.[15,36] Thus, hepatocerebral degeneration[37,38] may explain signal reduction in APT-weighted images with increased concentration of ammonia.

4.6 | Study limitations

Differences between in vitro and in vivo APT measurements have been previously observed in healthy individuals.[29] Hence, a phantom consisting of BSA or tissue samples modified with ammonia can only be seen as a very raw model for HE. As the real concentration of ammonia in human brain tissue of HE patients is yet unknown, it remains elusive whether the reduced APT-weighted CEST signal is exclusively driven by an increased ammonia level. However, the phantom results provide a clear indication of the ammonia sensitivity of the APT-weighted CEST signal, if ammonia is higher than 5mM.

Additionally, water content changes are proposed to alter the semi-solid MT, which is also impacted by demyelination processes in HE.[7] To reduce the impact of T_1, T_2, and MT, different correction methods have been proposed.[30,39,40] These correction methods require steady-state measurements or additional T_1 and T_2 maps, leading to increased measurement time. As we aimed for full-brain coverage in the in vivo measurements, saturation did not reach steady state within feasible acquisition times. Hence, the measured chemical exchange is confounded by semi-solid magnetization and possibly increased water content due to HE. As T_1 also reflects tissue water content, a T_1 relaxation compensation of

the MTR$_{asym}$ values should decrease the impact of water content alterations in the in vivo imaging. Longer T_1 relaxation times and higher water concentrations led to higher APT signals within the phantom and may increase the sensitivity to small ammonia concentration differences compared with the in vivo condition. For this reason, relaxation compensation should be applied in follow-up studies.

As B_1 differs for the in vivo and in vitro measurements (in vitro, eight or nine B_1 amplitudes; in vivo, one B_1 amplitude), the impact of B_1 may be stronger in the in vivo measurement. In addition, all measurements demonstrated B_0 inhomogeneities within the depicted z-spectra, which may affect the measured MTR$_{asym}$ values. Furthermore, the reduced number of CEST saturation frequencies that were necessary to reach feasible acquisition times may affect the sensitivity of the reduction of APT signal within the HE patients. In vitro MTR$_{asym}$ changes are mainly driven by APT changes. To further assess whether the in vivo changes are driven by nuclear Overhauser effect (NOE) or amide proton exchange differences, imaging contrasts from both sides of the z-spectra could be analyzed.[41] This approach would disentangle the contributions of NOE and amide proton exchange, which are mixed within the MTR$_{asym}$ and might increase the NOE-free APT signal as described by Heo et al.[42]

As a key limitation, the small sample size of preliminary in vivo acquisitions must be mentioned, which does not allow any final judgement of CEST imaging in HE. However, the present study was primarily focused on establishing an ammonia contrast in vitro, which showed clear evidence of the ammonia sensitivity of APT-weighted CEST imaging.

5 | CONCLUSION

The current study shows a well-defined effect of ammonia load on APT-weighted CEST imaging in phantoms by decreased amide MTR$_{asym}$. The decreased amide MTR$_{asym}$ in HE patients is likely due to ammonia accumulation. However, the underlying mechanism in the in vivo measurements needs to be explored in more detail in future investigations. Nevertheless, ammonia-weighted CEST imaging may be useful for the investigation and clinical monitoring of HE.

ORCID

Helge Jörn Zöllner http://orcid.org/0000-0002-7148-292X

REFERENCES

1. Häussinger D, Blei AT. Hepatic encephalopathy. In: *Textbook of Hepatology: From Basic Science to Clinical Practice*. 3rd ed. Hoboken, New Jersey: Wiley-Blackwell; 2007:728-760.

2. Lockwood AH, Yap EW, Wong WH. Cerebral ammonia metabolism in patients with severe liver disease and minimal hepatic encephalopathy. *J Cereb Blood Flow Metab*. 1991;11(2):337-341. https://doi.org/10.1038/jcbfm.1991.67

3. Keiding S, Sørensen M, Bender D, Munk OL, Ott P, Vilstrup H. Brain metabolism of ^{13}N-ammonia during acute hepatic encephalopathy in cirrhosis measured by positron emission tomography. *Hepatology*. 2006;43(1):42-50. https://doi.org/10.1002/hep.21001

4. Norenberg MD, Rao KVR, Jayakumar AR. Mechanisms of ammonia-induced astrocyte swelling. *Metab Brain Dis*. 2005;20(4):303-318. https://doi.org/10.1007/s11011-005-7911-7

5. Shah NJ, Neeb H, Kircheis G, Engels P, Häussinger D, Zilles K. Quantitative cerebral water content mapping in hepatic encephalopathy. *Neuroimage*. 2008;41(3):706-717. https://doi.org/10.1016/j.neuroimage.2008.02.057

6. Oeltzschner G, Butz M, Wickrath F, Wittsack HJ, Schnitzler A. Covert hepatic encephalopathy: elevated total glutathione and absence of brain water content changes. *Metab Brain Dis*. 2016;31(3):517-527. https://doi.org/10.1007/s11011-015-9760-3

7. Miese F-R, Wittsack H-J, Kircheis G, et al. Voxel-based analyses of magnetization transfer imaging of the brain in hepatic encephalopathy. *World J Gastroenterol*. 2009;15(41):5157-5164.

8. Rovira A, Alonso J, Córdoba J. MR imaging findings in hepatic encephalopathy. *Am J Neuroradiol*. 2008;29(9):1612-1621. https://doi.org/10.3174/ajnr.A1139

9. Miese F, Kircheis G, Wittsack HJ, et al. ^{1}H-MR spectroscopy, magnetization transfer, and diffusion-weighted imaging in alcoholic and nonalcoholic patients with cirrhosis with hepatic encephalopathy. *Am J Neuroradiol*. 2006;27(5):1019-1026.

10. Wolff SD, Balaban RS. Magnetization transfer contrast (MTC) and tissue water proton relaxation in vivo. *Magn Reson Med*. 1989;10(1):135-144.

11. Guivel-Scharen V, Sinnwell T, Wolff SD, Balaban RS. Detection of proton chemical exchange between metabolites and water in biological tissues. *J Magn Reson*. 1998;133(1):36-45. https://doi.org/10.1006/jmre.1998.1440

12. Wolff SD, Balaban RS. NMR imaging of labile proton exchange. *J Magn Reson*. 1990;86(1):164-169.

13. Zhou J, Payen J-F, Wilson DA, Traystman RJ, van Zijl PCM. Using the amide proton signals of intracellular proteins and peptides to detect pH effects in MRI. *Nat Med*. 2003;9(8):1085-1090. https://doi.org/10.1038/nm907

14. Goerke S, Milde KS, Bukowiecki R, et al. Aggregation-induced changes in the chemical exchange saturation transfer (CEST) signals of proteins. *NMR Biomed*. 2017;30(1). https://doi.org/10.1002/nbm.3665

15. Goerke S, Zaiss M, Kunz P, et al. Signature of protein unfolding in chemical exchange saturation transfer imaging. *NMR Biomed*. 2015;28(7):906-913. https://doi.org/10.1002/nbm.3317

16. Banay-Schwartz M, Kenessey A, DeGuzman T, Lajtha A, Palkovits M. Protein content of various regions of rat brain and adult and aging human brain. *Age*. 1992;15(2):51-54. https://doi.org/10.1007/BF02435024

17. Zaiss M, Windschuh J, Goerke S, et al. Downfield-NOE-suppressed amide-CEST-MRI at 7 Tesla provides a unique contrast in human glioblastoma. *Magn Reson Med*. 2016. https://doi.org/10.1002/mrm.26100

18. Stollberger R, Wach P. Imaging of the active B_1 field *in vivo*. *Magn Reson Med*. 1996;35(2):246-251. https://doi.org/10.1002/mrm.1910350217

19. Kim M, Gillen J, Landman BA, Zhou J, van Zijl PCM. WAter Saturation Shift Referencing (WASSR) for chemical exchange saturation transfer experiments. *Magn Reson Med*. 2009;61(6):1441-1450. https://doi.org/10.1002/mrm.21873

20. Zhou J, van Zijl PCM. Chemical exchange saturation transfer imaging and spectroscopy. *Prog Nucl Magn Reson Spectrosc* 2006;48 (2/3):109–136. https://doi.org/10.1016/j.pnmrs.2006.01.001.

21. Windschuh J, Zaiss M, Meissner J-E, et al. Correction of $B1$-inhomogeneities for relaxation-compensated CEST imaging at 7 T. *NMR Biomed*. 2015;28(5):529-537. https://doi.org/10.1002/nbm.3283

22. Ferenci P, Lockwood A, Mullen K, Tarter R, Weissenborn K, Blei AT. Hepatic encephalopathy—Definition, nomenclature, diagnosis, and quantification: Final report of the Working Party at the 11th World Congresses of Gastroenterology, Vienna, 1998. *Hepatology*. 2002;35(3):716-721. https://doi.org/10.1053/jhep.2002.31250

23. Sabati M, Maudsley AA. Fast and high-resolution quantitative mapping of tissue water content with full brain coverage for clinically-driven studies. *Magn Reson Imaging*. 2013;31(10):1752-1759. https://doi.org/10.1016/j.mri.2013.08.001

24. Penny W, Friston K, Ashburner J, Kiebel S, Nichols T. *Statistical Parametric Mapping: the Analysis of Functional Brain Images*. London, UK: Academic; 2007.

25. Axelsson I. Characterization of proteins and other macromolecules by aagarose gel chromatography. *J Chromatogr*. 1978;152(10). https://ac.els-cdn.com/S0021967300853303/1-s2.0-S0021967300853303-main.pdf?_tid=af03288e-db4f-11e7-bd5e-00000aab0f26&acdnat=1512652274_d375df3fe14baa4b935f98ce679e5387. Accessed December 7, 2017

26. Hofmeister F. Zur Lehre von der Wirkung der Salze. *Arch für Exp Pathol Pharmakol*. 1888;24(4/5):247-260. https://doi.org/10.1007/BF01918191

27. Rabenstein DL, Fan S. Proton nuclear magnetic resonance spectroscopy of aqueous solutions: complete elimination of the water resonance by spin-spin relaxation. *Anal Chem*. 1986;58(14):3178-3184. https://doi.org/10.1021/ac00127a057

28. Swain M, Butterworth RF, Blei AT. Ammonia and related amino acids in the pathogenesis of brain edema in acute ischemic liver failure in rats. *Hepatology*. 1992;15(3):449-453. https://doi.org/10.1002/hep.1840150316

29. Schmidt H, Schwenzer NF, Gatidis S, et al. Systematic evaluation of amide proton chemical exchange saturation transfer at 3 T: effects of protein concentration, pH, and acquisition parameters. *Invest Radiol*. 2016;51(10):635-646.

30. Zaiss M, Xu J, Goerke S, et al. Inverse Z-spectrum analysis for spillover-, MT-, and T_1-corrected steady-state pulsed CEST-MRI—application to pH-weighted MRI of acute stroke. *NMR Biomed*. 2014;27(3):240-252. https://doi.org/10.1002/nbm.3054

31. Spahr L, Butterworth RF, Fontaine S, et al. Increased blood manganese in cirrhotic patients: relationship to pallidal magnetic resonance signal hyperintensity and neurological symptoms. *Hepatology*. 1996;24(5):1116-1120. https://doi.org/10.1002/hep.510240523

32. Magnotta VA, Heo H-Y, Dlouhy BJ, et al. Detecting activity-evoked pH changes in human brain. *Proc Natl Acad Sci U S A*. 2012;109(21):8270-8273. https://doi.org/10.1073/pnas.1205902109

33. Sun PZ, Zhou J, Sun W, Huang J, van Zijl PC. Detection of the ischemic penumbra using pH-weighted MRI. *J Cereb Blood Flow Metab*. 2007;27(6):1129-1136. https://doi.org/10.1038/sj.jcbfm.9600424

34. McVicar N, Li AX, Gonçalves DF, et al. Quantitative tissue pH measurement during cerebral ischemia using amine and amide concentration-independent detection (AACID) with MRI. *J Cereb Blood Flow Metab*. 2014;34(4):690-698. https://doi.org/10.1038/jcbfm.2014.12

35. Oeltzschner G, Butz M, Baumgarten TJ, Hoogenboom N, Wittsack H-J, Schnitzler A. Low visual cortex GABA levels in hepatic encephalopathy: links to blood ammonia, critical flicker frequency, and brain osmolytes. *Metab Brain Dis*. 2015;30(6):1429-1438. https://doi.org/10.1007/s11011-015-9729-2

36. Zaiss M, Windschuh J, Paech D, et al. Relaxation-compensated CEST-MRI of the human brain at 7T: unbiased insight into NOE and amide signal changes in human glioblastoma. *Neuroimage*. 2015;112:180-188. https://doi.org/10.1016/j.neuroimage.2015.02.040

37. Victor M, Adams RD, Cole M. The acquired (non-Wilsonian) type of chronic hepatocerebral degeneration. *Medicine*. 1965;44(5):345-396.

38. Yalçın D, Oğuz-Akarsu E, Sökmen M. Acquired hepatocerebral degeneration. *Neurosciences*. 2016;21(2):164-167. https://doi.org/10.17712/nsj.2016.2.20150164

39. Jin T, Wang P, Zong X, Kim S-G. Magnetic resonance imaging of the Amine-Proton EXchange (APEX) dependent contrast. *Neuroimage*. 2012;59(2):1218-1227. https://doi.org/10.1016/j.neuroimage.2011.08.014

40. Sun PZ, Murata Y, Lu J, Wang X, Lo EH, Sorensen AG. Relaxation-compensated fast multislice amide proton transfer (APT) imaging of acute ischemic stroke. *Magn Reson Med*. 2008;59(5):1175-1182. https://doi.org/10.1002/mrm.21591

41. Jin T, Wang P, Zong X, Kim S-G. MR imaging of the amide-proton transfer effect and the pH-insensitive nuclear Overhauser effect at 9.4 T. *Magn Reson Med*. 2013;69(3):760-770. https://doi.org/10.1002/mrm.24315

42. Heo H-Y, Zhang Y, Burton TM, et al. Improving the detection sensitivity of pH-weighted amide proton transfer MRI in acute stroke patients using extrapolated semisolid magnetization transfer reference signals. *Magn Reson Med*. 2017;78(3):871-880. https://doi.org/10.1002/mrm.26799
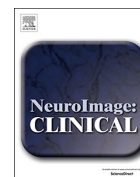
Chemical exchange saturation transfer imaging in hepatic encephalopathy

Helge Jörn Zöllner[a,b,*], Markus Butz[a], Markus Jördens[c], Nur-Deniz Füllenbach[c],
Dieter Häussinger[c], Benjamin Schmitt[d], Hans-Jörg Wittsack[b], Alfons Schnitzler[a]

[a] Institute of Clinical Neuroscience and Medical Psychology, Medical Faculty, Heinrich Heine University Düsseldorf, Germany
[b] Department of Diagnostic and Interventional Radiology, Medical Faculty, Heinrich Heine University Düsseldorf, Germany
[c] Department of Gastroenterology, Hepatology and Infectiology, Medical Faculty, Heinrich Heine University Düsseldorf, Germany
[d] Siemens Ltd. Australia, Healthcare Sector, 160 Herring Road, Macquarie Park, NSW 2113, Australia

ARTICLE INFO

ABSTRACT

Hepatic encephalopathy (HE) is a common complication in liver cirrhosis and associated with an invasion of ammonia into the brain through the blood-brain barrier. Resulting higher ammonia concentrations in the brain are suggested to lead to a dose-dependent gradual increase of HE severity and an associated impairment of brain function. Amide proton transfer-weighted (APT_w) chemical exchange saturation transfer (CEST) imaging has been found to be sensitive to ammonia concentration. The aim of this work was to study APT_w CEST imaging in patients with HE and to investigate the relationship between disease severity, critical flicker frequency (CFF), psychometric test scores, blood ammonia, and APT_w signals in different brain regions.

Whole-brain APT_w CEST images were acquired in 34 participants (14 controls, 20 patients (10 minimal HE, 10 manifest HE)) on a 3 T clinical MRI system accompanied by T_1 mapping and structural images. T_1 normalized magnetization transfer ratio asymmetry analysis was performed around 3 ppm after B_0 and B_1 correction to create APT_w images. All APT_w images were spatially normalized into a cohort space to allow direct comparison. APT_w images in 6 brain regions (cerebellum, occipital cortex, putamen, thalamus, caudate, white matter) were tested for group differences as well as the link to CFF, psychometric test scores, and blood ammonia.

A decrease in APT_w intensities was found in the cerebellum and the occipital cortex of manifest HE patients. In addition, APT_w intensities in the cerebellum correlated positively with several psychometric scores, such as the fine motor performance scores MLS1 for hand steadiness / tremor ($r = 0.466$; $p = .044$) and WRT2 for motor reaction time ($r = 0.523$; $p = .022$). Moreover, a negative correlation between APT_w intensities and blood ammonia was found for the cerebellum ($r = -0.615$; $p = .007$) and the occipital cortex ($r = -0.478$; $p = .045$). An increase of APT_w intensities was observed in the putamen of patients with minimal HE and correlated negatively with the CFF ($r = -0.423$; $p = .013$).

Our findings demonstrate that HE is associated with regional differential alterations in APT_w signals. These variations are most likely a consequence of hyperammonemia or hepatocerebral degeneration processes, and develop in parallel with disease severity.

1. Introduction

Liver cirrhosis is known to manifest in systemic effects. In particular, the most common neurological manifestation of liver cirrhosis is hepatic encephalopathy (HE), which comprises a variety of symptoms. Patients suffering from HE exhibit alterations in cognitive and motor function as well as behavioral changes. The clinical symptoms of HE vary with disease severity, starting with mild attentional deficits and disorientation, cognitive deterioration, and disturbed motor control. They may develop into somnolence and stupor and in the most severe case hepatic coma (Butterworth, 2000; Felipo, 2013; Ferenci et al., 2002; Prakash and Mullen, 2010).

The pathophysiology of HE is not finally understood, but is assumed to be multifactorial (Cichoz-Lach and Michalak, 2013; Felipo, 2013;

Häussinger and Sies, 2013). A key element in the pathophysiology is the invasion of ammonia into the brain through the blood-brain barrier. Previous studies using $^{13}NH_3$-PET imaging have revealed an increased uptake of circulating ammonia into the brain of cirrhosis patients (Keiding et al., 2006; Lockwood et al., 1991).

In addition to increased oxidative stress caused by ammonia accumulation (Norenberg et al., 2005), an excess of glutamine is produced in the astrocytes as a result of ammonia detoxification by glutamine synthetase. The increased glutamine concentration in the astrocytes triggers cell swelling *via* osmotic imbalance, finally leading to alteration of brain water homeostasis and emergence of a low-grade edema (Detry et al., 2006; Häussinger and Schliess, 2008). The emergence of a low-grade edema was further investigated by different studies using advanced MR imaging: Quantitative T_1 mapping and semi-solid magnetization transfer (MTC) imaging studies attributed increased T_1 values (Shah et al., 2003) and alterations in the calculated MTC effect (Miese et al., 2006) to increased water content in HE patients. Additionally, a quantitative water mapping approach has demonstrated a small increase of water content in white matter areas (Shah et al., 2008), while these findings remained absent in another quantitative water mapping study including patients with low-grade HE (Oeltzschner et al., 2016). In general, T_1-weighted (Butterworth et al., 1995; Klos et al., 2006; Pujol et al., 1993; Rovira et al., 2008) or quantitative T_1 (Shah et al., 2003) imaging may be altered by increased water content. However, T_1 changes especially within the basal ganglia are more likely to be mediated by manganese deposition, which is a common neurotoxin in HE (Rose et al., 1999).

All MR visible effects described above are based on the notion of ammonia accumulation in the patients' brains. Therefore, it is of paramount interest to measure ammonia in a most direct way, without the use of radiation, and with increased resolution compared to $^{13}NH_3$-PET imaging.

Chemical exchange saturation transfer (CEST) represents a suitable tool for the assessment of changes of *in vivo* ammonia levels. CEST provides an advanced MRI contrast depending on diluted labile protons, which are usually undetectable by conventional MRI. The CEST contrast is based on the mitigation of the bulk water signal due to magnetization transfer between the bulk water and frequency-selectively saturated labile protons (Wolff and Balaban, 1989). Amide proton transfer-weighted (APT$_w$) imaging, which is based on magnetization transfer from exchangeable amide protons of mobile tissue proteins and peptides (Jones et al., 2012), is an emerging field in CEST imaging. It allows several applications, such as amide proton quantification, detection of pH changes in the amide proton environment (Mori et al., 1998; van Zijl et al., 2003; Zhou et al., 2003a), and measurement of global *in vitro* protein folding (Goerke et al., 2017, 2015) with possible applications in neurodegenerative diseases. Additionally, CEST depends on non-exchange-related factors, such as direct water saturation, MTC, and water longitudinal relaxation time (Zu, 2018). Thus, these factors have to be included in the interpretation of possible HE related changes in APT$_w$ imaging.

In our recent *in vitro* study, we were able to link increasing ammonia concentrations to a decreasing APT$_w$ CEST signal through protein denaturation (Zöllner et al., 2018). We could also apply this finding to example cases of HE patients. The present study aimed to systematically investigate the sensitivity of APT$_w$ imaging to HE-related brain ammonia levels, and to gauge its potential to monitor disease severity and progression *via* the HE-related signal alteration in APT$_w$ imaging. To this end, APT$_w$ imaging was performed in a cohort of clinically well-characterized HE patients in different grades of severity, as well as healthy age-matched controls. To investigate the relationship between disease severity and APT$_w$ imaging, the critical flicker frequency (CFF), psychometric testing scores, and blood ammonia levels were assessed. In addition, T_1 maps were acquired to control for T_1 effects on the measured MTR$_{asym}$ values by T_1 normalization in the region-of-interest analysis.

2. Material and methods

2.1. Participants and HE grading

The study was performed in accordance with the Declaration of Helsinki in its current version ("*World Medical Association declaration of Helsinki: Ethical principles for medical research involving human subjects*", 2013), and was approved by the local institutional review board (study number 5179R). All participants gave written informed consent prior to the examination. 15 controls and 20 patients with clinically confirmed HE, graded as minimal HE (mHE) and manifest HE (HE), were examined. Exclusion criteria for both patients and controls included neurological or psychiatric diseases excluding the diagnosis of HE for the patient group, severe intestinal diseases, the use of any medication acting on the central nervous system and diagnosed peripheral/retinal neuropathy. If alcohol abuse was part of the medical history, the patient had to remain abstinent for ≥ 4 weeks prior to examination. The grading was performed in line with the *West-Haven* criteria (Ferenci et al., 2002; Kircheis et al., 2002). In addition, neuropsychological testing, critical flicker frequency (CFF) assessment with portable CFF goggles (NEVOlab, Maierhöfen, Germany), and blood sample tests were carried out. In the CFF test, the tested individual has to indicate with a button press when the impression of a virtual light source in 12 m distance changes from a fused light source to a flickering one. After a short training session, the CFF is assessed eight times, and the mean and standard deviation are calculated for further analysis. The CFF was included as it has been shown to be a reliable clinical parameter for HE monitoring, and accounts for the continuous nature of symptom severity (Kircheis et al., 2014, 2002). One control had to be excluded due to a CFF value < 39 Hz, which is the cut-off frequency for mHE. The remaining study population is summarized in Table 1.

HE severity was determined by an experienced clinician and included a clinical assessment regarding the mental state and consciousness of the patients and neuropsychometric testing. Computer-based neuropsychometric tests from the Vienna Test System (Dr. Schuhfried GmbH, Mödling, Austria) consisted of five test batteries and reported 22 age-validated scores (percentile rank values in comparison to an age-matched control cohort) reflecting motor and cognitive performance. Better performance was graded with higher scores. The parameter values were considered as abnormal in case of a percentile rank lower than 15.9 compared to the control cohort implemented in the test system. Patients without clinical symptoms of manifest HE, but with > 1 abnormal psychometric test result were classified as mHE (Kircheis et al., 2002). Selected scores were incorporated for further analysis, including cognitive (COG1: time to reject a geometric shape not matching control shapes; COG2: time to confirm a geometric shape matching a control shape), fine motor performance (line following test: LVT1: time per item; LVT2: overall score), motor/precision/speed (MLS1: hand steadiness/tremor; MLS2: arm/hand precision; MLS3: arm/hand speed; MLS4: finger tapping speed), and reaction

Table 1
Remaining study cohort.

	N	Sex [M/F]	Age [years] Mean ± SD	CFF [Hz] Mean ± SD	Etiology of liver cirrhosis
Controls	14	8/6	60.1 ± 5.3	44.2 ± 3.4	–
mHE	10	7/3	55.1 ± 10.4	41.0 ± 3.2*	5 ALC, 1 HCV, 1 NASH, 1 OS, 2 U
HE	10	6/4	59.5 ± 6.7	36.4 ± 2.3**	5 ALC, 2 HCV, 2 NASH, 1 OS

* Significantly different from controls ($p < .05$) with non-parametric Wilcoxon rank sum test.

** Significantly different from controls ($p < .01$) and mHE ($p < .01$) with non-parametric Wilcoxon rank sum test (*ALC* alcoholic, *HCV* hepatitis C virus, *NASH* non-alcoholic steatohepatitis, *OS* overlap syndrome, *U* unknown).

performance (WRT1: reaction time; WRT2: motor reaction time) scores.

2.2. MR measurements

All MR investigations were performed on a clinical whole-body 3 T MRI (Siemens MAGNETOM Trio A TIM System, Siemens Healthcare AG, Erlangen, Germany) using a 12-channel head coil for receive, and the internal body coil for transmit.

2.2.1. Structural MRI

Following a scout scan, a high-resolution 3D anatomical transversal T_1-weighted magnetization prepared gradient echo (MP-RAGE) scan (TR/TE = 1950/4.6 ms; isotropic resolution of 1 mm; 176 slices) was performed aligned to the AC-PC line.

2.2.2. CEST MRI

The CEST images were acquired using a prototype transversal 3-dimensional gradient echo sequence (TR/TE = 1390/3.06 ms; flip angle = 10°; FoV = (230×230) mm^2; matrix size 192×192; 24 slices; slice thickness 5 mm; gap 1 mm) to obtain full brain coverage. 22 equidistant frequency offsets were sampled between -5 and 5 ppm using a pulse train of 5 Gaussian shaped pulses (pulse duration 100 ms; inter pulse delay 100 ms, B_1 = 1.5 µT) for saturation.

The unsaturated S_0 image was acquired by turning off the saturation pulse. Additionally, data for B_0 inhomogeneity correction with a water saturation reference map (WASSR) (Kim et al., 2009) were recorded.

2.2.3. GRE MRI

Two 3-dimensional gradient echo scans with different flip angles (FA = 4°, 15) were acquired with the same spatial dimensions as the CEST images. Relative B_1 maps were created by heavily smoothing the low flip angle (FA = 4°) volume (Sabati and Maudsley, 2013). In addition, T_1 maps were calculated using the volumes (FA = 4°, 15°) (Sabati and Maudsley, 2013) leading to a measurement time of 25 min in total.

2.3. Data processing

2.3.1. Motion correction and brain masking

Motion correction was performed using the co-registration method of the MATLAB (MathWorks Inc., Natrick, MA, USA) toolbox SPM12 (Friston, 2007). The 3D volumes of the CEST datasets of each saturation frequency were co-registered to the 3D volume of the 3.5 ppm saturation frequency, as described by Zhang et al. (Zhang et al., 2016). Subsequently, all WASSR datasets were co-registered to the S_0 volume. Tissue compounds and cerebrospinal fluid (CSF) were segmented with the SPM *newSegment* function, and a brain mask was created, which included all pixels with probabilities > 0.8 for grey matter (GM), white matter (WM), and CSF.

2.3.2. MTR$_{asym}$ evaluation

Z-spectra and magnetization transfer ratio asymmetry (MTR$_{asym}$) images were calculated for all pixels within the brain mask using an in-house written MATLAB script. All images were smoothed using a non-local means (NLM) filter to improve the signal-to-noise ratio, and to avoid blurring of the images (Yuan et al., 2016). The used filter is a MATLAB reimplementation (https://de.mathworks.com/matlabcentral/fileexchange/52018-simple-non-local-means-nlm-filter) of the NLM filter described by Manjón et al. (Manjón et al., 2008). The filtered pixel value is calculated by the weighted average of all pixels in the image. The weights originate from the similarity between the user-defined neighborhood of the filtered pixel and are defined by an exponential decay control parameter h and the Gaussian weighted Euclidian distance of the pixels in the neighborhood. The parameters within the MATLAB toolbox were chosen as follows: search window $t = 3$, similarity window f = 2, standard deviation of the Gaussian low-

pass h1 = 0.01, decay control parameter h2 = 18 = 1.18σ with σ being estimated from the noise standard deviation of the background of all images. The factor 1.18 is suggested in the original publication to be optimal for proton-density weighted images. More details are described in Manjón et al. (Manjón et al., 2008).

The *Piecewise Cubic Hermite Interpolating Polynomial* (pchip) algorithm was chosen in the *interp1* MATLAB to interpolate the spectra in steps of 0.05 ppm. Asymmetry analysis (Zhou and van Zijl, 2006) was calculated as follows:

$$MTR_{asym} = Z_{ref} - Z_{lab}$$
$$= Z(\Delta\omega_{ref} = -\Delta\omega_{lab}) - Z(\Delta\omega_{lab})$$
$$= \frac{S(\Delta\omega_{ref} = -\Delta\omega_{lab}) - S(\Delta\omega_{lab})}{S_0}$$

With labelled proton scan Z_{lab}, a reference scan at the opposite frequency Z_{ref} and the unsaturated image S_0.

MTR_{asym} curves were calculated over a frequency range between 0 and 5 ppm within the z-spectra. Subsequently, the APT-weighted MTR_{asym} maps were calculated by averaging over a frequency range from 3 to 4 ppm and it will be referred to as APT$_w$ imaging. B_1-one-point-contrast correction is performed as described in detail by Windschuh et al. (Windschuh et al., 2015). Additionally, T_1 normalization of the MTR_{asym} was performed in the region-of-interest (ROI) analysis to correct for a T_1 relaxation effects (Zhou et al., 2018). It will be referred to as APT$_w^{T1}$ MTR$_{asym}$.

2.3.3. Normalization

Data normalization was performed with the open-source software package *Advanced Normalization Tools* (ANTs) (Avants et al., 2009). The package includes algorithms for bias correction, template construction, and image normalization. A template from the current study population was created with the ANTSNormTemp.sh script using the structural images (Avants et al., 2011). The script uses an iterative approach including two steps: At first, all individual structural images are spatially transformed onto one reference image. Initially, an average of all structural images was used as reference and 15 iterative steps of affine transformations were performed to align the volumes. In the second step, the inverse transformation matrix is applied to the reference image to update its shape. These two steps are applied iteratively, starting with the updated reference image of the previous iteration. Subsequently, 15 diffeomorphism transformations were performed iteratively with a *Greedy Syn* algorithm to create the template. The maximum iterations (parameter -m) within the registrations were as followed: Iterations 1 to 5 with *-m 30 × 90 × 40*, iterations 5 to 10 with *-m 60 × 180 × 80 × 45* and iteration 10 to 15 with *-m 120 × 360 × 160 × 90*. The step size of the image registrations in every sub iteration ($-m$) decreased with each level. Afterwards, all individual scans were normalized to the template using the diffeomorphism transformation, and the transformation matrix was applied to the CEST and T_1 maps. Thus, all individual CEST and T_1 maps could be assessed with an atlas-based statistical analysis.

2.4. Statistical evaluations

2.4.1. Atlas-based analysis

The APT$_w$ images and T_1 maps were analyzed by an atlas-based approach, using the Neuromorphometrics atlas integrated in SPM12 (Friston, 2007). The atlas was co-registered to the cohorts template obtained from ANTs. A set of 6 regions including both hemispheres at once was included in the analysis. The regions are summarized in Table 2 and the selection was based on their suggested involvement in HE pathophysiology as referenced in previous studies (Cauli et al., 2009; Kril et al., 1997; Oeltzschner et al., 2016; Rovira et al., 2008; Shah et al., 2003, 2008). Group level differences (control, mHE, HE) in APT$_w^{T1}$ MTR$_{asym}$ were investigated with a pairwise non-parametric Wilcoxon rank sum test. Group differences were considered significant

Table 2
Atlas based statistics of APT_w^{T1} MTR_{asym} in HE (minimal HE (mHE), manifest HE (HE)).

	T_1 normalized MTR_{asym} (%) Mean (± SD)			Correlation with		
	Control	Patients		CFF	Blood ammonia	GGT
		mHE	HE	r p	r p	r p
Cerebellum	0.94 (0.48)	0.92 (1.16)	**0.61**[#] **(0.75)**	0.043 0.807	**−0.615** **0.007**	−0.251 0.300
Occipital cortex	0.82 (0.60)	0.88 (0.50)	**0.39**[*] **(0.50)**	0.102 0.564	**−0.478** **0.045**	−0.267 0.269
Putamen	0.61 (0.11)	**0.76**[*] **(0.09)**	0.81 (0.24)	**−0.423** **0.013**	−0.285 0.252	−0.393 0.096
Thalamus	0.43 (0.08)	0.45 (0.08)	0.48 (0.18)	−0.323 0.062	−0.365 0.137	**−0.454** **0.049**
Caudate	0.35 (0.12)	0.37 (0.13)	0.42 (0.16)	−0.200 0.257	−0.221 0.379	−0.008 0.975
White matter	0.49 (0.08)	0.51 (0.12)	0.57 (0.14)	−0.231 0.190	−0.409 0.137	−0.048 0.847

Asterisks indicate significant differences from controls (* = $p < .05$). Pound signs indicate significant differences between patient groups (# = $p < .05$). Bold numbers indicate significant correlations over all participants. Reduced APT_w^{T1} MTR_{asym} and its correlation with blood ammonia in cerebellar and occipital regions indicate either increased ammonia accumulation or hepatocerebral degeneration. Increased putaminal APT_w^{T1} MTR_{asym} are related to other contrast mechanisms, such as strong alterations in metabolite concentrations.

for $p < .05$.

Relationships between CFF and APT_w^{T1} MTR_{asym}, blood ammonia and APT_w^{T1} MTR_{asym}, and between psychometric scores and APT_w^{T1} MTR_{asym} were compared with a bivariate two-sided Pearson correlation test. Correlations were considered significant in case $p < .05$. No multiple comparison correction was employed in the analysis.

All statistical analyses were performed using IBM SPSS Statistics for Windows, Version 24.0 (IBM Corp., Armonk, NY, USA).

3. Results

All 34 MRI datasets (14 controls, 10 mHE, 10 HE) remained in the final analysis. The manifest HE group included 9 HE I patients and one patient graded as HE II. One HE I patient did not undergo psychometric testing, and two patients did not undergo blood testing (1 mHE, 1 HE).

3.1. APT_w atlases

Mean group APT_w atlases are depicted in Fig. 1. The atlases indicate decreasing APT_w MTR_{asym} in the cerebellum and the occipital region of the manifest HE patients. In addition, slight alterations in deep grey matter regions are occurring, as APT_w MTR_{asym} increases within the Putamen. An absence of changes is visible for caudate, thalamus, and the selected white matter region.

Supplementary Fig. 1 represents the mean APT_w atlases, as well as the corresponding slices of mean T1 atlases. To avoid any contamination of APT_w effects by water longitudinal relaxation, a T_1 normalization was performed in the ROI based analysis. Group results and correlations with critical flicker frequency (CFF), blood ammonia, and gamma-glutamyltransferase (GGT) concentration are summarized in Table 2. The ROI based analysis is summarized in the following sections. The figures are focused on the ROI with significant differences in the measured APT_w^{T1} MTR_{asym}.

3.2. Cerebellum

Mean cerebellar APT_w^{T1} MTR_{asym} values were reduced in HE patients compared to mHE patients ($p < .05$; Fig. 2a) indicating higher levels of ammonia or hepatocerebral degeneration in the patients with manifest HE compared to minimal HE. No differences were found between controls compared to both patient groups. A negative correlation of cerebellar APT_w imaging blood ammonia levels ($r = -0.615$; $p = .013$; Fig. 2b) and a positive correlation with the psychometric MLS1 (hand steadiness / tremor) score ($r = 0.466$; $p = .044$; Fig. 2c) were found. Furthermore, a positive correlation of the psychometric WRT2 score and mean APT_w^{T1} MTR_{asym} could be observed ($r = 0.523$; $p = .022$; Fig. 2d).

3.3. Occipital cortex

A decrease in mean APT_w^{T1} MTR_{asym} was observed between controls and HE patients ($p < .05$), whereas no significant differences were detected between controls and mHE patients and between both patient groups (Fig. 3a). A negative correlation of occipital APT_w imaging and blood ammonia levels ($r = -0.476$; $p = .045$; Fig. 3b) and a positive correlation with the psychometric MLS2 (arm/hand precision) score ($r = 0.544$; $p = .016$; Fig. 3c) were present. A positive correlation of occipital APT_w imaging and psychometric MLS2 (arm/hand precision) score ($r = 0.544$; $p = .016$; Fig. 3c) and a negative correlation with blood ammonia levels ($r = -0.476$; $p = .045$; Fig. 3b) were present. Additionally, a positive correlation between the psychometric LVT1 score and the mean APT_w^{T1} MTR_{asym} was found (Fig. 3d).

3.4. Putamen

Mean putaminal APT_w^{T1} MTR_{asym} were increased in mHE patients compared to controls ($p < .05$), whereas no differences were found between controls and HE patients and between the two patient groups (Fig. 4a). Additionally, the mean values in the HE patient group showed a greater variability. A negative correlation of CFF and APT_w^{T1} MTR_{asym} was observed (Fig. 4b). In contrast to the cerebellar and occipital region, the increased putaminal APT_w^{T1} MTR_{asym} suggests the domination of other contrast mechanism, such as increased glutamine concentrations, in this region. Alterations through increased water or the accumulation of manganese were ruled out by T_1 normalization.

3.5. Psychometric testing

Results of the correlation analysis of the psychometric tests are summarized in Table 3. The motor score MLS1 and the motor reaction time score WRT2 correlated positively with the APT_w^{T1} intensities in the cerebellum. This indicates a connection between motor deficits of HE patients and reduced APT_w^{T1} MTR_{asym} in the cerebellum. The line following scores LVT1 and LVT2, the motor scores MLS2 and MLS3, as well as the motor reaction time WRT2 correlated positively with the observed APT_w^{T1} intensities in the occipital cortex.

4. Discussion

In the present *in vivo* CEST study, we applied chemical exchange saturation transfer imaging to investigate the link between hepatic encephalopathy, blood ammonia levels, and APT_w measures which reflect cerebral ammonia levels. Our results reveal reduced APT_w^{T1} MTR_{asym} within the cerebellum and occipital regions correlating both with blood ammonia and psychometric scores. Additionally, APT_w intensities are increased within the putamen of mHE patients. Furthermore, putaminal APT_w^{T1} MTR_{asym} correlates negatively with CFF.
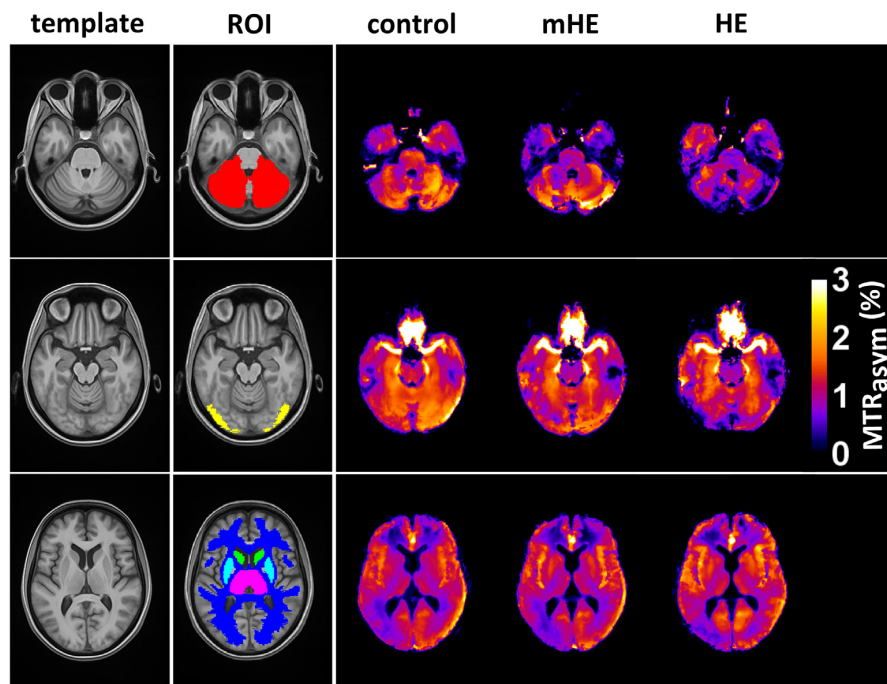
4

Fig. 1. Mean group atlases of APT_w MTR_{asym} in healthy controls and HE patients. The rows depict three representative slices including the six selected regions of interests (ROI) (Red: Cerebellum; Yellow: Occipital cortex; Cyan: Putamen; Magenta: Thalamus; Green: Caudate; Blue: White matter). The template of the current study population is depicted in the first column. ROI are illustrated in the second column. The last three columns display the mean atlases of the APT_w imaging of each group (control, minimal HE (mHE), manifest HE (HE)). The signal reduction could either be linked to increased ammonia accumulation or hepatocerebral degeneration.

4.1. CEST and clinical parameters in HE

Psychometric testing, CFF, and blood ammonia are common clinical parameters to assess the severity of HE, especially in cases of minimal HE, when no clinical overt signs of HE are apparent (Kircheis et al., 2014). Decreased fine motor abilities in HE patients are reflected in decreased MLS1 score, which correlate with APT_w^{T1} MTR_{asym} in the cerebellum in the present work. Increased ammonia accumulation or hepatocerebral degeneration, reflected in decreasing APT_w^{T1} MTR_{asym}, might be associated with these findings. This notion tallies previous findings demonstrating that cerebellar damage is linked to sensorimotor deficits (Miall et al., 2007) and slower upper limb movements (Manto et al., 2012). In minimal HE, motor impairments manifest in decreasing finger movement frequency and increasing movement amplitudes even prior to alterations in psychometric test scores (Butz et al., 2010). Therefore, APT_w^{T1} MTR_{asym} could shed light on cerebellar alterations leading to impaired motor performance in HE. An additional hint to this interpretation is the correlation with the motor reaction time (WRT2) score.

The contrast mechanisms behind APT_w imaging are assumed to be multifactorial and are a matter of debate in the literature today. Possible confounders are changes in pH (Zhou et al., 2003b), water content and water T1 (Lee et al., 2017), and concentration changes in metabolites and proteins (Zaiss et al., 2015), as well as altered protein conformation within intracellular protein compounds (Goerke et al., 2015), to mention a few. These factors are discussed further in 4.3. Based on our previous study and the supplementary data (Supplementary Fig. 2) we assume changes in the protein structure to be the main contributor to the observed contrast change in our study. Whether these changes are mediated through direct conformational changes in the protein structure or indirect mechanisms of ammonia, however, cannot be disentangled with the present findings. Thus, hepatocerebral degeneration (Victor et al., 1965; Yalçin et al., 2016) might contribute to the signal reduction in APT_w images in more severe HE affecting the cerebellum specifically (Butterworth, 2007). Cerebellar degeneration in HE is characterized by loss of Purkinje cells, and alcoholic abuse is associated with a greater degree of severity of loss of these cells, and a

higher HE prevalence (Kril et al., 1997). In light of the etiology of our patient cohort (50% alcoholic liver cirrhosis, 50% non-alcoholic etiology), APT_w^{T1} MTR_{asym} may be altered by an alcohol-induced high degree of cell loss in the cerebellum. Moreover, the appearance of Alzheimer type II astrocytes is likely in those patients (Kril et al., 1997). These cells undergo morphological changes and thus, might alter the APT_w^{T1} MTR_{asym} by changing the number of exchangeable amide groups within the measurement volume. Further *in vitro* CEST studies including different cell types with HE-related morphological changes might unravel their specific contribution to our findings at hand.

Previous studies reported an involvement of the visual cortex in HE. This includes worse performance in CFF tests (Kircheis et al., 2014), reduced visual GABA/Cr levels (Oeltzschner et al., 2015), abnormal neuronal activity in resting-state fMRI of the visual cortex (Chen et al., 2012), slowed frequency of of alpha and gamma band oscillations recorded with MEG (Baumgarten et al., 2018; Kahlbrock et al., 2012), and alterations in visual evoked potentials (Zeneroli et al., 1984). This involvement is reflected in significant reduction of APT_w signals within the occipital cortex and its correlation with the psychometric scores. Increased ammonia accumulation, reflected by decreasing APT_w^{T1} MTR_{asym}, could lead to an impairment of visual perception through neurotransmitter imbalance by ammonia detoxification. A link to CFF was only found within the putamen. This could be due to the fact of relatively large dispersion of the measured APT_w MTR_{asym} signals. The strong correlation of blood ammonia levels with APT_w signals in cerebellum and occipital cortex substantiates our findings as markers for HE severity.

Further liver disease related markers from the blood test, such as gamma-glutamyltransferase (GGT) concentrations displayed significant correlation with APT_w^{T1} signals in the thalamus. Future CEST studies including larger number of patients and especially patients at higher diseases stage (HE II) may help better clarifying links between clinical parameters and APT_w signals in different brain regions.

4.2. Ammonia in HE

The multifactorial nature of the pathophysiology of HE includes

5
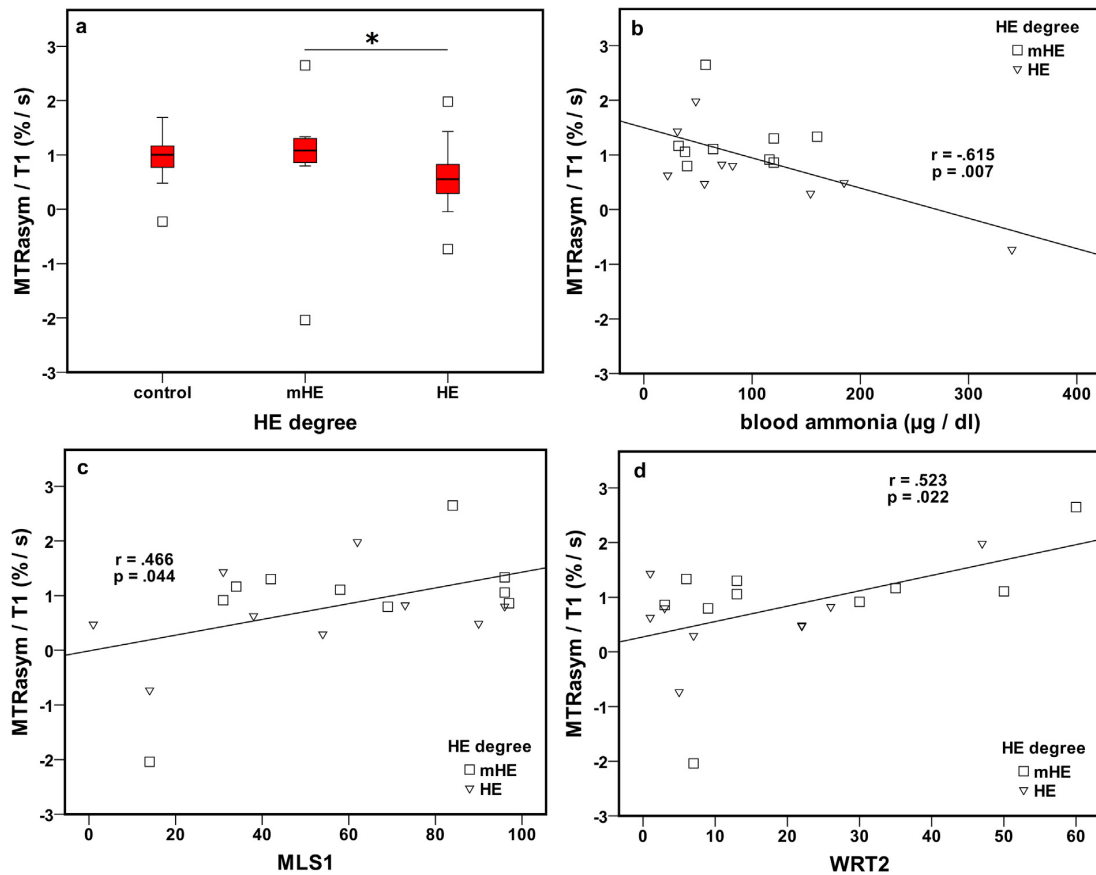
Fig. 2. APT$_w$ imaging of the cerebellum in healthy controls and HE patients (minimal HE (mHE), manifest HE (HE)). (a) Group boxplots including mean APT$_w$^{T1} MTR$_{asym}$ values. Asterisks indicate significant differences between groups ($p < .05$). Correlations between blood ammonia levels (b), psychometric MLS1 score (hand steadiness/tremor) (c), psychometric WRT2 score (motor reaction time) (d), and mean APT$_w$^{T1} MTR$_{asym}$. The data suggests a strong cerebellar involvement in HE explaining poor motor performance of HE patients, which could possibly be linked to ammonia accumulation or hepatocerebral degeneration.

several alterations in brain metabolism, which interact with the APT$_w$ imaging contrast. A key role in the pathophysiology is attributed to the invasion of ammonia in the patients' brains (Cichoz-Lach and Michalak, 2013; Häussinger and Sies, 2013). At physiological pH levels, ammonia remains invisible to the classical CEST approach, due to its high exchange rate. Nevertheless, our recent study could demonstrate a link between ammonia concentration and APT$_w$ MTR$_{asym}$ protein signal (Zöllner et al., 2018).

In vitro, the contrast mechanisms were mainly driven by an induced protein denaturation through ammonia, while contrast mechanisms remained unclear in the *in vivo* cases (Zöllner et al., 2018). Our data describes APT$_w$ signal reductions in the cerebellum and the occipital cortex of HE patients, including correlations with blood ammonia levels and psychometric test scores. A possible interpretation is to link this reduction to an increased ammonia load in these regions, as we already assumed in our *in vitro* experiments.

Our findings are in line with an earlier ^{13}NH$_3$-PET study (Keiding et al., 2006) depicting a correlation between blood ammonia and the metabolic flux of ammonia. In this work, the metabolic flux was defined as the product of the netto metabolic clearance in blood from intracellular metabolites and arterial ammonia concentration, which was deduced from radioactively marked ammonia. Intracellular glutamine is linked to ammonia removal through glutamine synthase within the brain. As APT$_w$ signal predominantly reflects intracellular protein compounds we assume the contrast changes in our study to be mediated through ammonia within the astrocytes, which is underlined by

comparable correlations in cerebellum and cortex (Keiding et al., 2006). Therefore, we speculate APT$_w$ signal to reflect the metabolic flux of ammonia. At present, a more elaborate differentiation of ammonia kinetic remains inaccessible with APT$_w$ imaging as it is measured without contrast agents and reflects an averaged metabolism during the whole acquisition. In the present study, we found an increased APT$_w$ signal in the putamen and a negative correlation with the CFF, which is in contrast to the findings reported by Keiding et al. for the basal ganglia (Keiding et al., 2006). This result indicates the potentially larger contribution of another contrast mechanism in this region. Such changes might be driven by increased manganese levels within the basal ganglia (Felipo, 2013; Häussinger and Sies, 2013; Prakash and Mullen, 2010; Rose et al., 1999; Rovira et al., 2008).

Earlier PET studies (Keiding et al., 2006; Lockwood et al., 1991) also reported increased cerebral metabolic rates and radioactivity of ammonia in the thalamus, respectively. Additionally, thalamic volume changes were found *via* voxel-based morphometry studies in HE (Lu et al., 2018). In the present study, thalamic APT$_w$ signals only correlated with GGT concentrations. Firstly, increased glutamine concentrations could interfere with the effect of ammonia, which is complementary to our additional phantom experiments (Supplementary Fig. 2). Secondly, the changes in thalamic volume could alter the APT$_w$ signal due to changes in the protein concentration. Thirdly, the changes in APT$_w$ signal could be dominated by hepatocerebral degeneration, which possibly differs between various regions. Yet, these explanations need to remain speculative.

6
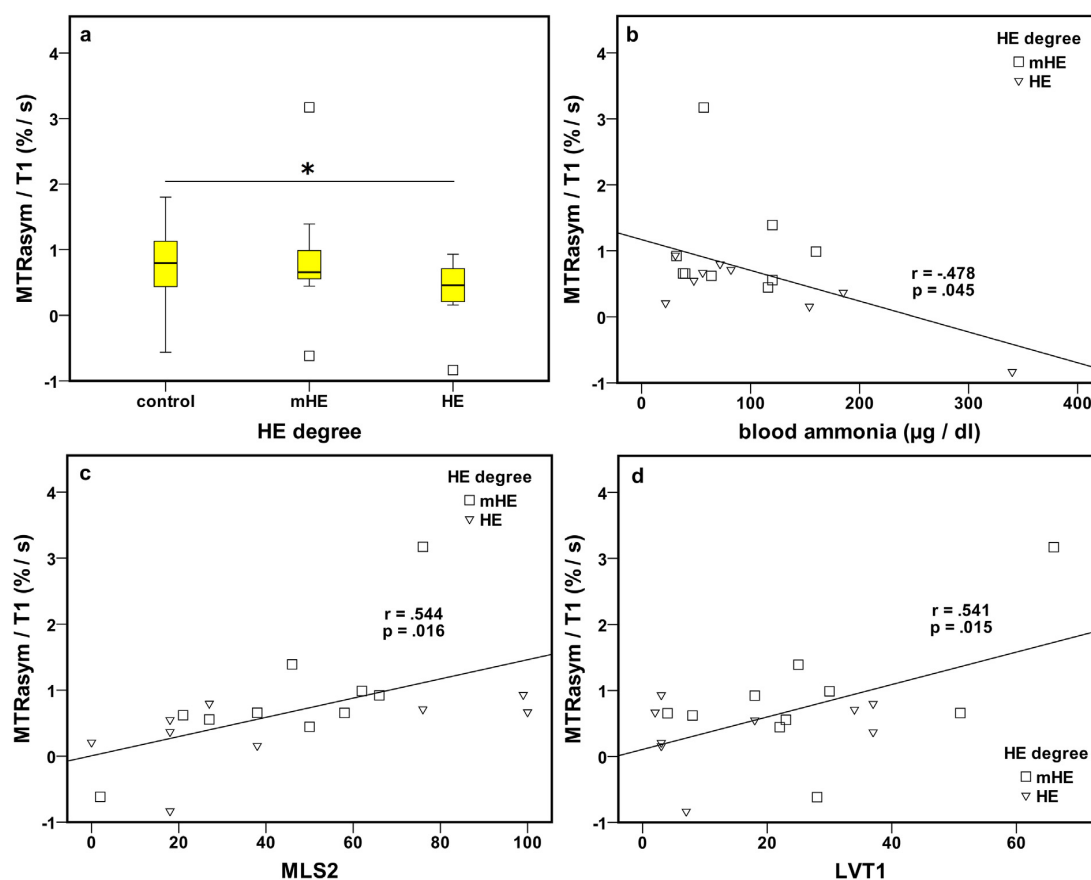
Fig. 3. APT$_w$ imaging of the occipital cortex in healthy controls and HE patients (minimal HE (mHE), manifest HE (HE)). (a) Group boxplots including mean APT$_w^{T1}$ MTR$_{asym}$ values. Asterisks indicate significant differences between groups ($p < .05$). Correlations between blood ammonia levels (b), psychometric MLS2 score (arm/hand precision) (c), psychometric LVT1 score (time per item) (d), and mean APT$_w^{T1}$ MTR$_{asym}$ values. This might explain alterations in visual perception of HE patients with increasing diseases severity due to ammonia accumulation.

Ammonia detoxification by glutamine synthase triggers the accumulation of glutamine within astrocytes (Felipo, 2013; Häussinger and Sies, 2013; Prakash and Mullen, 2010). Several studies reported disturbance in glutamate/glutamine balance, such as increasing glutamine concentrations after chronic liver failure in rat models (Swain et al., 1992), and elevated glutamine concentrations in basal ganglia (Miese et al., 2006) and cortical brain regions of HE patients (Häussinger et al., 1994; Kreis et al., 1991; Oeltzschner et al., 2015). Glutamine and glutamate are both CEST-sensitive, and resonate between 3 and 4 ppm (Schmidt et al., 2016).

As a result, signal contributions of both metabolites might interact with the APT$_w$ mechanism used in this study. In this case, the increasing APT$_w$ signal and the negative correlation with the CFF in the putamen could be interpreted as increased glutamate + glutamine (Glx) ratios. In additional phantom experiments (Supplementary Fig. 2), we found that ammonia dominates the contrast mechanism with its presence, by adding *in vivo* realistic glutamate, glutamine (control and HE concentrations), and ammonia concentrations in one solution.

Besides, a 3 T system does not have a high sensitivity to depict changes in either glutamate or glutamine (Lee et al., 2016), but showed sensitivity to ammonia load in protein based solutions (Zöllner et al., 2018). Hence, the underlying mechanisms in the putamen remain unclear, but are likely to be linked to HE disease severity.

4.3. CEST-sensitive confounders

Starting from APT$_w$ imaging, we adapted our saturation parameters in two ways (Zöllner et al., 2018). In *in vitro* experiments, the saturation parameters were selected to maximize the contrast gained from the effect of ammonia on the protein signal. Then, these saturation parameters were used to create full brain coverage within the *in vivo* measurements. *In vitro,* we were able to link the alterations in APT$_w$ signals directly to ammonia, but *in vivo,* ammonia could only be one of a few contributors to the alterations. Another physiological change described for HE is the osmotic imbalance, which is triggered through the ammonia depletion. Finally, alterations in brain water homeostasis and the emergence of a low-grade edema are reported (Häussinger and Schliess, 2008). Regarding the MR visibility of these changes, one study reported water content changes of about 2% in several brain regions including the putamen (Shah et al., 2008), whereas an absence of MR visible water content changes was reported in another study in HE patients in less severe stages (Oeltzschner et al., 2016).

Several APT$_w$ CEST studies at 4.7 T and 7 T emphasize that water content plays a minor role in the contrast formation of APT only (Khlebnikov et al., 2016; Lee et al., 2017). However, as the APT$_w$ values were normalized by the T1 relaxation time, any possible T1 effect can be neglected.

Quantitative T$_1$ (Shah et al., 2003) and T$_1$-weighted (Butterworth et al., 1995; Klos et al., 2006; Pujol et al., 1993; Rovira et al., 2008)
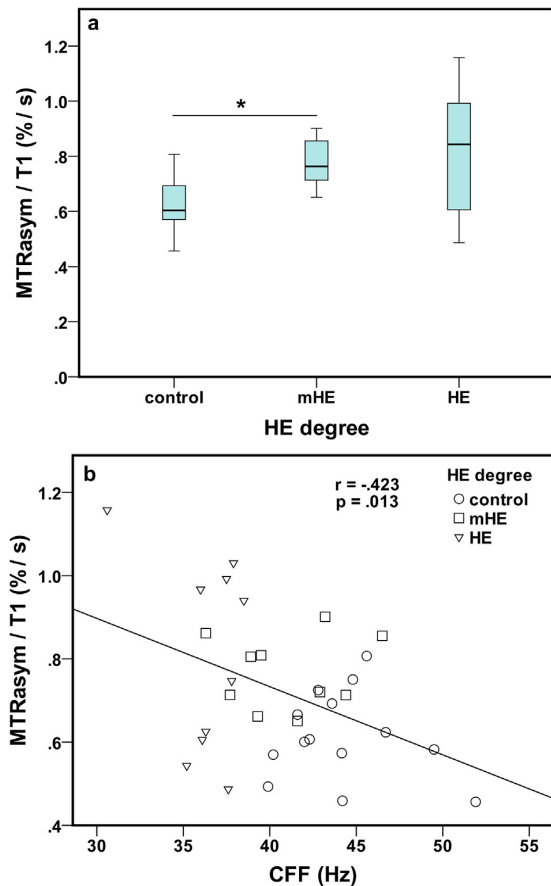
Fig. 4. APT_w imaging of the putamen in healthy controls and HE patients (minimal HE (mHE), manifest HE (HE)). (a) Group boxplots including mean APT_w^{T1} MTR_{asym}. Asterisks indicate significant differences between groups ($p < .05$). (b) Correlation between critical flicker frequency (CFF) and mean APT_w^{T1} MTR_{asym} values. The data suggests the domination of other contrast mechanisms, such as metabolite concertation changes.

changes are known to be a key finding in MR imaging of hepatic encephalopathy. To rule out the contamination of our MTR_{asym} we employed a T_1 normalization, which resolves in pure APT_w contrast

mechanisms. In addition, a recent study claimed that MTR_{asym} of amide protons at the saturation parameters (B_1, t_{sat}) used in the present study is roughly insensitive to water longitudinal relaxation time (Zu, 2018).

4.4. Limitations

One limitation of the present study is the number of included patients. As our data suggests that the APT_w signals are strongly altered in manifest HE, the inclusion of more patients in the higher HE grade could have strengthened our findings. However, the inclusion of patients in higher disease stages is hard to achieve, as patient compliance is needed both to perform psychometric testing and to achieve sufficient quality of MR data without a substantial amount of movement artifacts.

Another limitation is the number of analyzed ROIs, which included prior knowledge and assumptions within the analysis and led to the fact that some effects might be missed in other brain regions. Thus, all interpretations remain descriptive in the first place and final conclusions about affected brain regions and APT_w imaging as marker for HE severity have to be confirmed in future larger studies. In addition, the inclusion of larger cohorts would allow the implementation of non-parametric voxel based analysis (Holmes et al., 1996). This technique excludes user-biased ROI analysis and could give further insight in the disease progression and spatial distribution of HE-related changes. Nevertheless, the present study indicates that APT_w imaging is a possible marker for HE, as correlations with HE-related clinical markers were evident.

The sensitivity of the CEST technique is another limitation and a possible explanation for the absence of thalamic alterations in the present study. As discussed above, several confounders to the APT_w signal remain elusive, which could lead to increasing type II error rates. In future studies, a combination of MRS with the CEST technique could shed light on the underlying contrast mechanisms. By using the voxel-based acquisition technique EXPRESS (Walker-Samuel et al., 2012) in combination with J-difference-edited MEGA-PRESS spectroscopy (Mescher et al., 1998) or a novel accelerated spectral editing sequence allowing the measurement of multiple compounds at the same time in the same brain region (Saleh et al., 2016), the interplay between neurotransmitter metabolism (GABA, glutamate, glutamine), osmolytes (myo-inositol), oxidative stress markers (glutathione), and changes in the protein signals could be investigated. These studies may focus on alterations in cerebellum and thalamus, as the interplay of metabolism and HE is yet unclear in these regions. Additional acquisition of water references would further allow drawing conclusions about water content.

To reach sufficient acquisition times and full brain coverage, relatively short saturation times, small numbers of saturation frequencies,

Table 3
Correlations of psychometric test scores and mean APT_w^{T1} MTR_{asym} (COG1: time to reject a geometric shape not matching control shapes; COG2: time to confirm a geometric shape matching a control shape; line following: LVT1: time per item; LVT2: overall score; MLS1: hand steadiness/tremor; MLS2: arm/hand precision; MLS3: arm/hand speed; MLS4: finger tapping speed; WRT1: reaction time; WRT2: motor reaction time). Bold numbers indicate significant correlations.

	COG1	COG2	LVT1	LVT2	MLS1	MLS2	MLS3	MLS4	WRT1	WRT2
	r	r	r	r	r	r	r	r	r	r
	p	p	p	p	p	p	p	p	p	p
Cerebellum	0.164	0.162	0.299	0.277	**0.466**	0.443	0.357	0.156	0.282	**0.523**
	0.503	0.508	0.213	0.250	**0.044**	0.058	0.133	0.525	0.243	**0.022**
Occipital cortex	0.378	0.400	**0.547**	**0.469**	0.399	**0.544**	**0.526**	−0.092	0.356	**0.531**
	0.110	0.089	**0.015**	**0.043**	0.091	**0.016**	**0.021**	0.708	0.019	**0.019**
Putamen	−0.093	−0.105	0.318	0.391	0.314	−0.034	−0.013	0.258	−0.139	0.285
	0.704	0.668	0.184	0.098	0.191	0.890	0.958	0.286	0.569	0.237
Thalamus	−0.070	−0.102	0.124	0.185	0.181	0.272	0.181	0.038	−0.056	0.188
	0.776	0.678	0.614	0.449	0.458	0.260	0.458	0.876	0.821	0.441
Caudate	−0.335	−0.381	−0.150	−0.146	0.151	−0.174	−0.301	0.384	−0.373	0.005
	0.161	0.108	0.539	0.552	0.538	0.476	0.210	0.104	0.116	0.985
White matter	−0.140	−0.170	0.038	0.114	0.236	0.356	0.108	−0.021	0.002	0.099
	0.567	0.488	0.876	0.643	0.330	0.135	0.659	0.930	0.994	0.688

and a non-steady state acquisition were chosen in the present study. Faster imaging sequences would allow improving those parameters, which could even include steady-state CEST measurements within the acquisition. As a result, further correction of the CEST signal could be implemented, such as AREX (Zaiss et al., 2015) or EMR (Heo et al., 2016). More advanced quantification approaches like Lorentzian fitting (Zaiss et al., 2011) could also improve data quality and strengthen the findings. Additionally, a Lorentzian fitting model could be able to distinguish between APT, Nuclear Overhauser effect (NOE), and MTC, if a suitable model is chosen. Apart from the fact that ammonia only affects the APT exchange in *in vitro* experiments (Zöllner et al., 2018), some *in vivo* studies reported MTC to be altered in HE patients (Miese et al., 2006). Moreover, morphological changes might affect the NOE, thus Lorentzian fitting could give further insight to the underlying contrast mechanisms in HE. It was not implemented in the current study, as it requires a large number of saturation frequencies leading to long total acquisition times. The implemented MTR_{asym} analysis combined with the full brain coverage already permits the distinction between controls and patients, based on APT_w signal alterations in several brain regions.

5. Conclusions

Hepatic encephalopathy is associated with a region-specific decrease of APT_w signals, in particularly in the cerebellum and the occipital cortex. These signal changes are linked to increased blood ammonia concentrations, and clinical scores of cognitive and motor function. These variations are most likely a consequence of hyperammonemia or hepatocerebral degeneration processes and develop in parallel with disease severity. Therefore, APT_w CEST imaging could be a possible tool to investigate HE and advance the understanding of region-specific alterations in HE and its clinical equivalents. By including additional methods to quantify metabolite levels and water content, the interplay between metabolism and protein signal alterations in HE could be assessed in more detail in future studies.

Conflict of interest

D.H. belongs to a group of patent holders for the bedside measurement device determining the critical flicker frequency.

Appendix A. Supplementary data

Supplementary data to this article can be found online at https://doi.org/10.1016/j.nicl.2019.101743.

References

Avants, B.B., Tustison, N.J., Song, G., Gee, J.C., 2009. ANTS: Advanced Open-Source Normalization Tools for Neuroanatomy. Penn IMage Computing and Science Laboratory.

Avants, B.B., Tustison, N.J., Song, G., Cook, P.A., Klein, A., Gee, J.C., 2011. A reproducible evaluation of ANTs similarity metric performance in brain image registration. Neuroimage 54, 2033–2044. https://doi.org/10.1016/j.neuroimage.2010.09.025.

Baumgarten, T.J., Neugebauer, J., Oeltzschner, G., Füllenbach, N.D., Kircheis, G., Häussinger, D., Lange, J., Wittsack, H.J., Butz, M., Schnitzler, A., 2018. Connecting occipital alpha band peak frequency, visual temporal resolution, and occipital GABA levels in healthy participants and hepatic encephalopathy patients. NeuroImage Clin. 20, 347–356. https://doi.org/10.1016/j.nicl.2018.08.013.

Butterworth, R.F., 2000. Complications of cirrhosis III. Hepatic encephalopathy. J. Hepatol. 32, 171–180. https://doi.org/10.1016/S0168-8278(00)80424-9.

Butterworth, R.F., 2007. Neuronal cell death in hepatic encephalopathy. Metab. Brain Dis. 22, 309–320. https://doi.org/10.1007/s11011-007-9072-3.

Butterworth, R.F., Spahr, L., Fontaine, S., Layrargues, G.P., 1995. Manganese toxicity, dopaminergic dysfunction and hepatic encephalopathy. Metab. Brain Dis. 10, 259–267. https://doi.org/10.1007/BF02109357.

Butz, M., Timmermann, L., Braun, M., Groiss, S.J., Wojtecki, L., Ostrowski, S., Krause, H., Pollok, B., Gross, J., Südmeyer, M., Kircheis, G., Häussinger, D., Schnitzler, A., 2010. Motor impairment in liver cirrhosis without and with minimal hepatic encephalopathy. Acta Neurol. Scand. 122, 27–35. https://doi.org/10.1111/j.1600-0404.2009.01246.x.

Cauli, O., Rodrigo, R., Llansola, M., Montoliu, C., Monfort, P., Piedrafita, B., El Mlili, N., Boix, J., Agustí, A., Felipo, V., 2009. Glutamatergic and gabaergic neurotransmission and neuronal circuits in hepatic encephalopathy. Metab. Brain Dis. 24, 69–80. https://doi.org/10.1007/s11011-008-9115-4.

Chen, H.J., Zhu, X.Q., Jiao, Y., Li, P.C., Wang, Y., Teng, G.J., 2012. Abnormal baseline brain activity in low-grade hepatic encephalopathy: a resting-state fMRI study. J. Neurol. Sci. 318, 140–145. https://doi.org/10.1016/j.jns.2012.02.019.

Cichoz-Lach, H., Michalak, A., 2013. Current pathogenetic aspects of hepatic encephalopathy and noncirrhotic hyperammonemic encephalopathy. World J. Gastroenterol. https://doi.org/10.3748/wjg.v19.i1.26.

Detry, O., De Roover, A., Honoré, P., Meurisse, M., 2006. Brain edema and intracranial hypertension in fulminant hepatic failure: pathophysiology and management. World J. Gastroenterol. 12, 7405–7412. https://doi.org/10.3748/wjg.v12.i46.7405.

Felipo, V., 2013. Hepatic encephalopathy: effects of liver failure on brain function. Nat. Rev. Neurosci. 14, 851–858. https://doi.org/10.1038/nrn3587.

Ferenci, P., Blei, A.T., Lockwood, A.H., Mullen, K., Tarter, R., Weissenborn, K., 2002. Hepatic encephalopathy - definition, nomenclature, diagnosis, and quantification: final report of the working party at the 11th world congresses of gastroenterology, Vienna, 1998. Hepatology 35, 716–721. https://doi.org/10.1053/jhep.2002.31250.

Friston, K., 2007. Statistical Parametric Mapping: The Analysis of Functional Brain Images. Academic Press.

Goerke, S., Zaiss, M., Kunz, P., Klika, K.D., Windschuh, J.D., Mogk, A., Bukau, B., Ladd, M.E., Bachert, P., 2015. Signature of protein unfolding in chemical exchange saturation transfer imaging. NMR Biomed. 28, 906–913. https://doi.org/10.1002/nbm.3317.

Goerke, S., Milde, K.S., Bukowiecki, R., Kunz, P., Klika, K.D., Wiglenda, T., Mogk, A., Wanker, E.E., Bukau, B., Ladd, M.E., Bachert, P., Zaiss, M., 2017. Aggregation-induced changes in the chemical exchange saturation transfer (CEST) signals of proteins. NMR Biomed. 30. https://doi.org/10.1002/nbm.3665.

Häussinger, D., Schliess, F., 2008. Pathogenetic mechanisms of hepatic encephalopathy. Gut 57, 1156–1165. https://doi.org/10.1136/gut.2007.122176.

Häussinger, D., Sies, H., 2013. Editorial: hepatic encephalopathy: clinical aspects and pathogenetic concept. Arch. Biochem. Biophys. 536, 97–100. https://doi.org/10.1016/j.abb.2013.04.013.

Häussinger, D., Laubenberger, J., Vom Dahl, S., Ernst, T., Bayer, S., Langer, M., Gerok, W., Hennig, J., 1994. Proton magnetic resonance spectroscopy studies on human brain Myo-inositol in hypo-osmolarity and hepatic encephalopathy. Gastroenterology 107, 1475–1480. https://doi.org/10.1016/0016-5085(94)90552-5.

Heo, H.-Y., Zhang, Y., Jiang, S., Lee, D.-H., Zhou, J., 2016. Quantitative assessment of amide proton transfer (APT) and nuclear overhauser enhancement (NOE) imaging with extrapolated semisolid magnetization transfer reference (EMR) signals: II. Comparison of three EMR models and application to human brain glioma at 3 Tesla. Magn. Reson. Med. 75, 1630–1639. https://doi.org/10.1002/mrm.25795.

Holmes, A.P., Blair, R.C., Watson, J.D.G., Ford, I., 1996. Nonparametric analysis of statistic images from functional mapping experiments. J. Cereb. Blood Flow Metab. 16, 7–22. https://doi.org/10.1097/00004647-199601000-00002.

Jones, C.K., Polders, D., Hua, J., Zhu, H., Hoogduin, H.J., Zhou, J., Luijten, P.R., van Zijl, P.C.M., 2012. In vivo three-dimensional whole-brain pulsed steady-state chemical exchange saturation transfer at 7 T. Magn. Reson. Med. 67, 1579–1589. https://doi.org/10.1002/mrm.23141.

Kahlbrock, N., Butz, M., May, E.S., Brenner, M., Kircheis, G., Häussinger, D., Schnitzler, A., 2012. Lowered frequency and impaired modulation of gamma band oscillations in a bimodal attention task are associated with reduced critical flicker frequency. Neuroimage 61, 216–227. https://doi.org/10.1016/j.neuroimage.2012.02.063.

Keiding, S., Sørensen, M., Bender, D., Munk, O.L., Ott, P., Vilstrup, H., 2006. Brain metabolism of 13N-ammonia during acute hepatic encephalopathy in cirrhosis measured by positron emission tomography. Hepatology 43, 42–50. https://doi.org/10.1002/hep.21001.

Khlebnikov, V., Siero, J.C.W., Wijnen, J.P., Visser, F., Luijten, P.R., Klomp, D.W.J., Hoogduin, H.J., 2016. Is there any difference in Amide and NOE CEST effects between white and gray matter at 7 T? J. Magn. Reson. 272, 82–86. https://doi.org/10.1016/j.jmr.2016.09.010.

Kim, M., Gillen, J., Landman, B.A., Zhou, J., van Zijl, P.C.M., 2009. Water saturation shift referencing (WASSR) for chemical exchange saturation transfer (CEST) experiments. Magn. Reson. Med. 61, 1441–1450. https://doi.org/10.1002/mrm.21873.

Kircheis, G., Häussinger, D., Wettstein, M., Schnitzler, A., Timmermann, L., 2002. Critical flicker frequency for quantification of low-grade hepatic encephalopathy. Hepatology 35, 357–366. https://doi.org/10.1053/jhep.2002.30957.

Kircheis, G., Hilger, N., Häussinger, D., 2014. Value of Critical Flicker Frequency and psychometric hepatic encephalopathy score in diagnosis of low-grade hepatic encephalopathy. Gastroenterology 146, 961–969. e11. https://doi.org/10.1053/j.gastro.2013.12.026.

Klos, K.J., Ahlskog, J.E., Kumar, N., Cambern, S., Butz, J., Burritt, M., Fealey, R.D., Cowl, C.T., Parisi, J.E., Josephs, K.A., 2006. Brain metal concentrations in chronic liver failure patients with pallidal T1 MRI hyperintensity. Neurology 67, 1984–1989. https://doi.org/10.1212/01.wnl.0000247037.37807.76.

Kreis, R., Farrow, N., Ross, B.D., 1991. Localized 1H NMR spectroscopy in patients with chronic hepatic encephalopathy. Analysis of changes in cerebral glutamine, choline and inositols. NMR Biomed. 4, 109–116. https://doi.org/10.1002/nbm.1940040214.

Kril, J.J., Flowers, D., Butterworth, R.F., 1997. Distinctive pattern of bergmann glial pathology in human hepatic encephalopathy. Mol. Chem. Neuropathol. 31, 279–287. https://doi.org/10.1007/BF02815130.

Lee, J.S., Xia, D., Jerschow, A., Regatte, R.R., 2016. In vitro study of endogenous CEST agents at 3T and 7T. Contrast Media Mol. Imaging 11, 4–14. https://doi.org/10.1002/cmmi.1652.

Lee, D.-H., Heo, H.-Y., Zhang, K., Zhang, Y., Jiang, S., Zhao, X., Zhou, J., 2017. Quantitative assessment of the effects of water proton concentration and water T_1 changes on amide proton transfer (APT) and nuclear overhauser enhancement (NOE) MRI: the origin of the APT imaging signal in brain tumor. Magn. Reson. Med. 77, 855–863. https://doi.org/10.1002/mrm.26131.

Lockwood, A.H., Yap, E.W.H., Wong, W.-H., 1991. Cerebral ammonia metabolism in patients with severe liver disease and minimal hepatic encephalopathy. J. Cereb. Blood Flow Metab. 11, 337–341. https://doi.org/10.1038/jcbfm.1991.67.

Lu, C.-Q., Jiao, Y., Meng, X.-P., Cai, Y., Luan, Y., Xu, X.-M., Ju, S., 2018. Structural change of thalamus in cirrhotic patients with or without minimal hepatic encephalopathy and the relationship between thalamus volume and clinical indexes related to cirrhosis. NeuroImage Clin. https://doi.org/10.1016/J.NICL.2018.09.015.

Manjón, J.V., Carbonell-Caballero, J., Lull, J.J., García-Martí, G., Martí-Bonmatí, L., Robles, M., 2008. MRI denoising using non-local means. Med. Image Anal. 12, 514–523. https://doi.org/10.1016/j.media.2008.02.004.

Manto, M., Bower, J.M., Conforto, A.B., Delgado-García, J.M., Da Guarda, S.N.F., Gerwig, M., Habas, C., Hagura, N., Ivry, R.B., Marien, P., Molinari, M., Naito, E., Nowak, D.A., Ben Taib, N.O., Pelisson, D., Tesche, C.D., Tilikete, C., Timmann, D., 2012. Consensus paper: roles of the cerebellum in motor control-the diversity of ideas on cerebellar involvement in movement. Cerebellum 11, 457–487. https://doi.org/10.1007/s12311-011-0331-9.

Mescher, M., Merkle, H., Kirsch, J., Garwood, M., Gruetter, R., 1998. Simultaneous in vivo spectral editing and water suppression. NMR Biomed. 11, 266–272. https://doi.org/10.1002/(SICI)1099-1492(199810)11:6<266::AID-NBM530>3.0.CO;2-J.

Miall, R.C., Christensen, L.O.D., Cain, O., Stanley, J., 2007. Disruption of state estimation in the human lateral cerebellum. PLoS Biol. 5, e316. https://doi.org/10.1371/journal.pbio.0050316.

Miese, F., Kircheis, G., Wittsack, H.-J., Wenserski, F., Hemker, J., Mödder, U., Häussinger, D., Cohnen, M., 2006. 1H-MR spectroscopy, magnetization transfer, and diffusion-weighted imaging in alcoholic and nonalcoholic patients with cirrhosis with hepatic encephalopathy. Am. J. Neuroradiol. 27, 1019–1026 (doi:27/5/1019 [pii]).

Mori, S., Eleff, S.M., Pilatus, U., Mori, N., van Zijl, P.C.M., 1998. Proton NMR spectroscopy of solvent-saturable resonances: a new approach to study pH effects in situ. Magn. Reson. Med. 40, 36–42. https://doi.org/10.1002/mrm.1910400105.

Norenberg, M.D., Rama Rao, K.V., Jayakumar, A.R., 2005. Mechanisms of ammonia-induced astrocyte swelling. Metab. Brain Dis. 20, 303–318. https://doi.org/10.1007/s11011-005-7911-7.

Oeltzschner, G., Butz, M., Baumgarten, T.J., Hoogenboom, N., Wittsack, H.-J., Schnitzler, A., 2015. Low visual cortex GABA levels in hepatic encephalopathy: links to blood ammonia, critical flicker frequency, and brain osmolytes. Metab. Brain Dis. 30, 1429–1438. https://doi.org/10.1007/s11011-015-9729-2.

Oeltzschner, G., Butz, M., Wickrath, F., Wittsack, H.-J., Schnitzler, A., 2016. Covert hepatic encephalopathy: elevated total glutathione and absence of brain water content changes. Metab. Brain Dis. 31, 517–527. https://doi.org/10.1007/s11011-015-9760-3.

Prakash, R., Mullen, K.D., 2010. Mechanisms, diagnosis and management of hepatic encephalopathy. Nat. Rev. Gastroenterol. Hepatol. 7, 515–525. https://doi.org/10.1038/nrgastro.2010.116.

Pujol, A., Pujol, J., Graus, F., Rimola, A., Peri, J., Mercader, J.M., Garcia-Pagan, J.C., Bosch, J., Rodes, J., Tolosa, E., 1993. Hyperintense globus pallidus on T1-weighted MRI in cirrhotic patients is associated with severity of liver failure. Neurology 43, 65. https://doi.org/10.1212/WNL.43.1_Part_1.65.

Rose, C., Butterworth, R.F., Zayed, J., Normandin, L., Todd, K., Michalak, A., Spahr, L., Huet, P.M., Pomier-Layrargues, G., 1999. Manganese deposition in basal ganglia structures results from both portal-systemic shunting and liver dysfunction. Gastroenterology 117, 640–644. https://doi.org/10.1016/S0016-5085(99)70457-9.

Rovira, A., Alonso, J., Córdoba, J., 2008. MR imaging findings in hepatic encephalopathy. Am. J. Neuroradiol. 29, 1612–1621. https://doi.org/10.3174/ajnr.A1139.

Sabati, M., Maudsley, A.A., 2013. Fast and high-resolution quantitative mapping of tissue water content with full brain coverage for clinically-driven studies. Magn. Reson. Imaging 31, 1752–1759. https://doi.org/10.1016/j.mri.2013.08.001.

Saleh, M.G., Oeltzschner, G., Chan, K.L., Puts, N.A.J., Mikkelsen, M., Schär, M., Harris, A.D., Edden, R.A.E., 2016. Simultaneous edited MRS of GABA and glutathione. Neuroimage 142, 576–582. https://doi.org/10.1016/j.neuroimage.2016.07.056.

Schmidt, H., Schwenzer, N.F., Gatidis, S., Küstner, T., Nikolaou, K., Schick, F., Martirosian, P., 2016. Systematic evaluation of amide proton chemical exchange saturation transfer at 3 T. Investig. Radiol. 51, 635–646. https://doi.org/10.1097/RLI.0000000000000292.

Shah, N.J., Neeb, H., Zaitsev, M., Steinhoff, S., Kircheis, G., Amunts, K., Häussinger, D., Zilles, K., 2003. Quantitative T1Mapping of hepatic encephalopathy using magnetic resonance imaging. Hepatology 38, 1219–1226. https://doi.org/10.1053/jhep.2003.50477.

Shah, N.J., Neeb, H., Kircheis, G., Engels, P., Häussinger, D., Zilles, K., 2008. Quantitative cerebral water content mapping in hepatic encephalopathy. Neuroimage 41, 706–717. https://doi.org/10.1016/j.neuroimage.2008.02.057.

Swain, M., Butterworth, R.F., Blei, A.T., 1992. Ammonia and related amino acids in the pathogenesis of brain edema in acute ischemic liver failure in rats. Hepatology 15, 449–453. https://doi.org/10.1002/hep.1840150316.

van Zijl, P.C.M., Zhou, J., Mori, N., Payen, J.F., Wilson, D.A., Mori, S., 2003. Mechanism of magnetization transfer during on-resonance water saturation. A new approach to detect mobile proteins, peptides, and lipids. Magn. Reson. Med. 49, 440–449. https://doi.org/10.1002/mrm.10398.

Victor, M., Adams, R.D., Cole, M., 1965. The acquired (non-wilsonian) type of chronic hepatocerebral degeneration. Med. (United States) 44, 345–396. https://doi.org/10.1097/00005792-196509000-00001.

Walker-Samuel, S., Johnson, S.P., Pedley, B., Lythgoe, M.F., Golay, X., 2012. Extracranial measurements of amide proton transfer using exchange-modulated point-resolved spectroscopy (EXPRESS). NMR Biomed. 25, 829–834. https://doi.org/10.1002/nbm.1798.

Windschuh, J.D., Zaiss, M., Meissner, J.E., Paech, D., Radbruch, A., Ladd, M.E., Bachert, P., 2015. Correction of B1-inhomogeneities for relaxation-compensated CEST imaging at 7T. NMR Biomed. 28, 529–537. https://doi.org/10.1002/nbm.3283.

Wolff, S.D., Balaban, R.S., 1989. Magnetization transfer contrast (MTC) and tissue water proton relaxation in vivo. Magn. Reson. Med. 10, 135–144. https://doi.org/10.1002/mrm.1910100113.

World Medical Association declaration of Helsinki: Ethical principles for medical research involving human subjects, 2013. J. Am. Med. Assoc. 310, 2191–2194. https://doi.org/10.1001/jama.2013.281053.

Yalçın, A.D., Oğuz-Akarsu, E., Sökmen, H.M., 2016. Acquired hepatocerebral degeneration. Neurosciences 21, 164–167. https://doi.org/10.17712/nsj.2016.2.20150164.

Yuan, J., Mok, G.S.P., Zhang, Q., Wang, Y.-X., Zhou, J., 2016. Improved quantification of chemical exchange saturation transfer (CEST) MRI using nonlocal means. In: 2014 IEEE Nuclear Science Symposium and Medical Imaging Conference, NSS/MIC 2014. IEEE, pp. 1–5. https://doi.org/10.1109/NSSMIC.2014.7430844.

Zaiss, M., Schmitt, B., Bachert, P., 2011. Quantitative separation of CEST effect from magnetization transfer and spillover effects by Lorentzian-line-fit analysis of z-spectra. J. Magn. Reson. 211, 149–155. https://doi.org/10.1016/j.jmr.2011.05.001.

Zaiss, M., Windschuh, J.D., Paech, D., Meissner, J.E., Burth, S., Schmitt, B., Kickingereder, P., Wiestler, B., Wick, W., Bendszus, M., Schlemmer, H.P., Ladd, M.E., Bachert, P., Radbruch, A., 2015. Relaxation-compensated CEST-MRI of the human brain at 7T: unbiased insight into NOE and amide signal changes in human glioblastoma. Neuroimage 112, 180–188. https://doi.org/10.1016/j.neuroimage.2015.02.040.

Zeneroli, M.L., Pinelli, G., Gollini, G., Penne, A., Messori, E., Zani, G., Ventura, E., 1984. Visual evoked potential: a diagnostic tool for the assessment of hepatic encephalopathy. Gut 25, 291–299. https://doi.org/10.1136/gut.25.3.291.

Zhang, Y., Heo, H.-Y., Lee, D.-H., Zhao, X., Jiang, S., Zhang, K., Li, H., Zhou, J., 2016. Selecting the reference image for registration of CEST series. J. Magn. Reson. Imaging 43, 756–761. https://doi.org/10.1002/jmri.25027.

Zhou, J., van Zijl, P.C.M., 2006. Chemical exchange saturation transfer imaging and spectroscopy. Prog. Nucl. Magn. Reson. Spectrosc. 48, 109–136. https://doi.org/10.1016/j.pnmrs.2006.01.001.

Zhou, J., Lal, B., Wilson, D.A., Laterra, J., van Zijl, P.C.M., 2003a. Amide proton transfer (APT) contrast for imaging of brain tumors. Magn. Reson. Med. 50, 1120–1126. https://doi.org/10.1002/mrm.10651.

Zhou, J., Payen, J.F., Wilson, D.A., Traystman, R.J., van Zijl, P.C.M., 2003b. Using the amide proton signals of intracellular proteins and peptides to detect pH effects in MRI. Nat. Med. 9, 1085–1090. https://doi.org/10.1038/nm907.

Zhou, I.Y., Lu, D., Ji, Y., Wu, L., Wang, E., Cheung, J.S., Zhang, X.A., Sun, P.Z., 2018. Determination of multipool contributions to endogenous amide proton transfer effects in global ischemia with high spectral resolution in vivo chemical exchange saturation transfer MRI. Magn. Reson. Med. 81, 645–652. https://doi.org/10.1002/mrm.27385.

Zöllner, H.J., Butz, M., Kircheis, G., Klinker, S., Häussinger, D., Schmitt, B., Schnitzler, A., Wittsack, H.-J., 2018. Ammonia-weighted imaging by chemical exchange saturation transfer MRI at 3 T. NMR Biomed. e3947. https://doi.org/10.1002/nbm.3947.

Zu, Z., 2018. Towards the complex dependence of MTR_{asym} on T_{1w} in amide proton transfer (APT) imaging. NMR Biomed. 31, e3934. https://doi.org/10.1002/nbm.3934.

NMR in Biomedicine

In silico GABA+ MEGA-PRESS: Effects of signal-to-noise ratio and linewidth on modeling the 3-ppm GABA+ resonance

Journal:	*NMR in Biomedicine*
Manuscript ID	Draft
Wiley - Manuscript type:	Research Article
Date Submitted by the Author:	n/a
Complete List of Authors:	Zöllner, Helge; Heinrich-Heine-Universität Düsseldorf, Institute for Clinical Neuroscience and Medical Psychology, Medical Faculty; Heinrich-Heine-Universität Düsseldorf, Department of Diagnostic and Interventional Radiology, Medical Faculty Oeltzschner, Georg; Johns Hopkins University, Russell H. Morgan Department of Radiology and Radiological Science; Johns Hopkins University, F. M. Kirby Research Center for Functional Brain Imaging Schnitzler, Alfons; Heinrich-Heine-Universität Düsseldorf, Institute for Clinical Neuroscience and Medical Psychology, Medical Faculty Wittsack, Hans-Jörg; Heinrich-Heine-Universität Düsseldorf, Department of Diagnostic and Interventional Radiology, Medical Faculty
Keywords:	MR Spectroscopy (MRS) and Spectroscopic Imaging (MRSI) Methods < Methods and Engineering, Spectroscopic quantitation < MR Spectroscopy (MRS) and Spectroscopic Imaging (MRSI) Methods < Methods and Engineering, Normal brain < Neurological < Applications

SCHOLARONE™
Manuscripts

1

In silico GABA+ MEGA-PRESS:
Effects of signal-to-noise ratio and linewidth
on modeling the 3-ppm GABA+ resonance

Helge Jörn Zöllner[1,2], Georg Oeltzschner[3,4],
Alfons Schnitzler[1], Hans-Jörg Wittsack[2]

1. Institute of Clinical Neuroscience and Medical Psychology, Medical Faculty,
   Heinrich Heine University Düsseldorf, Germany.
2. Department of Diagnostic and Interventional Radiology, Medical Faculty,
   Heinrich Heine University Düsseldorf, Germany.
3. Russell H. Morgan Department of Radiology and Radiological Science,
   The Johns Hopkins University School of Medicine, Baltimore, MD, United States.
4. F. M. Kirby Research Center for Functional Brain Imaging,
   Kennedy Krieger Institute, Baltimore, MD, United States.

Corresponding author: Helge Jörn Zöllner, Moorenstrasse 5, 40225 Düsseldorf,
Germany, +49 (0)211-81-08609,
helge.zoellner@uni-duesseldorf.de

Running title: In silico GABA+ MEGA-PRESS

Word count: 4774

Key words: MRS, MEGA-PRESS, GABA, SNR, linewidth, simulations, fitting accuracy

Abbreviations: MEGA-PRESS – Mescher-Garwood PRESS; GABA – γ-Aminobutyric acid; SNR - signal-to-noise ratio; CRLB – Cramer-Rao-lower-bounds; SD – standard deviation; NEX – number of excitations; GABA+$_{error}$ – GABA+ estimation error; GABA+$_{fit}$ – GABA+ fit error; GABA+$_{SD}$ – GABA+ standard deviation; CoV – coefficient of variance;

2

Abstract

To generate recommendations for the design of edited magnetic resonance spectroscopy studies, the influence of varying signal-to-noise ratio (SNR) and linewidth on modeling of GABA+ using MEGA-PRESS was investigated.

MEGA-PRESS data from 48 volunteers were averaged to generate a template MEGA-PRESS spectrum, which was modeled and quantified to generate a GABA+ level ground truth. This spectrum was then manipulated by adding 427 combinations of varying artificial noise levels and line broadening, mimicking variations in GABA+ SNR, and B0 homogeneity. GABA+ modeling and quantification was performed with 100 simulated spectra per condition using automated routines both in Gannet 3.0 and Tarquin. The GABA+ estimation error was calculated as the relative deviation to the quantified GABA+ ground truth levels to assess the accuracy of GABA+ modeling. Finally, the accordance between the simulations and different *in vivo* scenarios was assessed.

The GABA+ estimation error was smaller than 5% over the entire range of GABA+ SNR for creatine linewidths lower than 9.7Hz (Gannet 3.0) or unequal 10.6Hz (Tarquin). The standard deviation of the GABA+ amplitude over 100 spectra per condition varied between 3.1 and 17% (Gannet 3.0) and between 1 and 11% (Tarquin) over the *in vivo* relevant GABA+ SNR range between 2.6 and 3.5.

GABA+ edited studies might be realized for voxels with low GABA+ SNR at the cost of higher group-level variance. The accuracy of GABA+ modeling had no relation to commonly used quality metrics. Time domain fitting was found to be more robust against linewidth changes than frequency domain fitting.

Introduction

At 3T, *J*-difference-edited ^{1}H MRS has become a common tool to investigate the major inhibitory neurotransmitter γ-Aminobutyric acid (GABA) noninvasively [1]. To this end, the Mescher-Garwood PRESS [2] (MEGA-PRESS) is increasingly used. A *J*-difference-edited MRS experiment usually consists of two sub-acquisitions ('ON' and 'OFF'), which differ in the frequency of an editing pulse which is applied to differentiate signals from different spin systems according to their coupling networks. In a GABA-edited experiment, the 'ON' pulse editing frequency is set to 1.9 ppm to refocus the evolution of the 3-ppm (GABA) signal, whereas 7.5 ppm is chosen in the 'OFF' experiment to let the coupling evolve freely. These experiments are usually repeated several hundred times to increase the signal-to-noise ratio (SNR). After averaging, the difference spectrum between ON and OFF experiments is calculated. Since the signals from Cr are identical in both halves of the experiment, they cancel out upon subtraction, rendering the underlying 3-ppm GABA resonance visible. The described editing scheme is co-editing homocarnosine and macromolecules [3]; therefore, the quantified 3-ppm signal is commonly termed GABA+.

GABA+-edited MEGA-PRESS has been frequently applied both in clinical and in behavioral studies. Measured GABA+ concentrations correlate with functional tasks/imaging [4,5]. Altered GABA+ concentrations are observed in healthy aging [6–8] as well as in various diseases including ADHD [9] and Tourette syndrome[10]. Further changes measured via GABA+-edited spectroscopy were reported for ALS [11] and hepatic encephalopathy [12].

Due to low concentrations of GABA (1-2 mmol/l) in the brain, strong signal overlap and the effort to implement difference editing, the *in vivo* quantification remains technically challenging. Various sources of variance have been identified, including hardware influences, e.g. scanner drift [13,14] or differences in sequence implementations between vendors [15,16]. Therefore, limitations exist regarding the minimal spectroscopic voxel size, the number of acquired transients and the required statistical power for the analysis [17]. In neurophysiological diseases showing regional specific effects, it remains challenging

4

to create suitable voxel dimensions to reach sufficient SNR within acceptable scanning durations. Large voxel volumes up to 27 ml are the default recommendation for obtaining sufficient SNR [1]. This approach sacrifices much needed anatomical specificity for measurement reliability and increases the risk of unknown partial volume effects. In some studies the voxel size was reduced to the target area [18], but this resulted in substantially higher inter-subject variance as compared to usually ~12 % in typical GABA+-edited investigations [15]. Another relevant parameter in MRS is the shim quality, as broad lines hinder the resolution of neighboring resonances and frequency precision is elementary for spectral editing. B0 field homogenization is of particular concern when investigating frontal or deep brain structures, as these tend to be close to areas of strong susceptibility gradients.

Unknown errors resulting from data modeling are another challenge in MRS. Usually, Cramer-Rao-lower-bounds (CRLB) [19] or the GABA+ amplitude normalized standard deviation of the fit residual, as implemented in Gannet[20], are used to provide a measure of uncertainty of the metabolite modeling. Outlier criteria based on CRLB, SNR, or linewidth, may also be used to judge whether the data has been modeled reliably [8,12,21]. The major effect of SNR on the reliability of the fitting is commonly known and has been investigated in various studies [22–24]. Yet, the deviation of the model from real metabolite levels remains unclear. To judge the reliability of a MRS method, several approaches have been proposed: measuring the reproducibility via a test-retest approach [25,26], manipulation of simulated datasets to create various spectral qualities [27,28], and most recently a correlation analysis of specific metabolites between different spectroscopy techniques acquired in the same voxel [29].

The aim of this study was to investigate the impact of varying SNR and linewidth on modeling of GABA+. To this end, a MEGA-PRESS spectrum with a ground truth GABA+ peak area was manipulated to achieve various SNR levels and linewidths. Afterwards, spectra were quantified with two quantification tools for GABA+-edited MRS. The deviations of the modeled GABA+ area from the ground truth GABA+ area were calculated to determine minimal requirements of SNR and linewidth. Finally, the accordance in terms of GABA+ fit error, group variance, and number of rejected spectra between the simulations and two *in vivo* GABA+-edited scenarios was assessed.

138

5

1
2
3
4
5
6
7
8
9
10
11
12
13
14
15
16
17
18
19
20
21
22
23
24
25
26
27
28
29
30
31
32
33
34
35
36
37
38
39
40
41
42
43
44
45
46
47
48
49
50
51
52
53
54
55
56
57
58
59
60

Material and Methods

In a first part, different SNR levels and linewidths were added to a template MEGA-PRESS spectrum, and GABA+ levels were derived by modeling the spectra with two different analysis software tools. In a second part, different *in vivo* scenarios were analyzed to assess the accordance between the simulations and the *in vivo* GABA+ modeling.

MEGA-PRESS simulations

Creation of the template MEGA-PRESS spectrum

A template MEGA-PRESS spectrum with known metabolite concentrations was created as follows: A template MEGA-PRESS spectrum (number of excitations (NEX) = 256, TR\TE = 2000\68 ms, bandwidth = 4000 Hz, V = 27 ml, 4096 datapoints) was created as mean Siemens datasets of 48 volunteers. This dataset is the outcome of a recent 'Big GABA' multi-site study [15], which is available to the public from the NITRC data repository (http://www.nitrc.org/projects/biggaba) as. For each individual dataset, all 256 averages were frequency-and-phase corrected via spectral registration [30] using the MATLAB-based (MathWorks Inc., Natick, MA, USA) toolbox Gannet 3.0 [20], without applying zero-filling. Two datasets were excluded after visual inspection due to severe frequency drift. The template ON and OFF spectra for the simulations were baseline corrected and normalized with the individual water references to account for differences between each acquisition (**Figure 1 A**). This approach was chosen over a fully simulated approach to achieve a more *in vivo* realistic template spectrum. The creatine linewidth of the template spectrum was 7.9 Hz. The models of each quantification tool of the 3-ppm GABA+ resonance of the template are depicted in **Figure 1 B**. Both individual models were used as the ground truth GABA+ levels.

In silico manipulation of the template spectrum

The template MEGA-PRESS spectrum was the basis for all subsequent SNR and line broadening manipulations, which were performed with MATLAB-based toolbox FID-A [31]. In a first step, 7 different levels of exponential line broadening between 0 and 6 Hz were applied to the template spectrum to mimic differences in B_0 homogeneity. Subsequently,

6

61 different SNR levels between 0 and 30 times the to the height of the N-acetyl-aspartate signal at 2.01 ppm, determined between 1.9 and 2.1 ppm in the frequency domain were created. Therefore, Gaussian-distributed noise was multiplied with the factor determined by the NAA height and added to the real and imaginary parts of the template in the time domain.

For visualization and unrelated to the used quantification tools, the creatine linewidth (**Figure 1 C**) and GABA+ SNR (**Figure 1 D**) were calculated with FID-A for each combination. The creatine linewidth was determined as the FWHM of the lorentzian fit between 2.85 and 3.1 ppm. The GABA+ SNR was defined as the ratio of the maximum height of the GABA+ peak between 2.7 and 3.2 ppm and the noise SD between 9 and 10 ppm. The axis indicates the mean value of the calculated creatine linewidth or GABA+ SNR for a specific spectral manipulation, which are additionally visualized in the color map. These calculations allow a direct comparison with literature as creatine linewidth and GABA+ SNR are usually reported. In total, 100 spectra were simulated for each of the combinations of noise and line broadening levels.

Exemplary raw 3-ppm GABA+ resonances for different combinations are depicted in **Figure 2**. As expected the line broadening broadens the GABA+ resonance and increases the GABA+ SNR in the template spectrum (first column). In an *in vivo* measurement poor B0 field homogeneity would lead to broad linewidth and poor SNR at once. Yet the parameter in the simulations were chosen such that constant GABA+ SNR and linewidth for easier data interpretation. By intentionally applying the SNR level changes in the second step, all spectra preserve the broadened linewidth (mimicking a poor B0 field homogeneity) (**Figure 1 C; Figure 2**) and possess roughly the same GABA+ SNR (**Figure 1 D; Figure 2**).

MEGA-PRESS in vivo study

All *in vivo* data were acquired on a clinical whole-body 3T MRI (Siemens MAGNETOM Skyra A TIM System, Siemens Healthcare AG, Erlangen, Germany) using a 20-channel head coil for receive, and the body coil for transmit. Fourteen healthy volunteers (5 female; age (mean ± standard deviation) 26.3 ± 2.2 years) were recruited. The study was performed in accordance with the Declaration of Helsinki in its current version [32]

140

7

and approved by the local internal review board (517R). All participants gave written informed consent prior to the examination. The *in vivo* study was focused on the thalamus, which is a challenging anatomical location regarding spectral quality and anatomical specificity of the MRS voxel.

Structural image

In each participant, a high-resolution 3D anatomical T_1-weighted magnetization prepared gradient echo (MP-RAGE) scan (TR/TE = 1950/4.6 ms; isotropic resolution of 1 mm; 176 transversal slices) was performed aligned to the anterior commissure – posterior commissure line after a scout scan. Sagittal and coronal images were reconstructed online for optimal localization of the spectroscopic voxels.

MEGA-PRESS acquisition

Two voxels with different SNR levels based on the voxel size and varying creatine linewidths were investigated. A small voxel of 2 mm x 2 mm x 2 mm = 8 ml volume centered on the left thalamus and a larger voxel with 30 mm (AP) x 35 mm (LR) x 25 mm (HF) = 26.25 ml including the whole basal ganglia region are depicted in **Figure 3**. The other parameters for both voxels were NEX = 256, TR\TE = 2050\68 ms, bandwidth = 1200 Hz, and 2048 datapoints. In comparison to the *in vivo* spectrum used for the artificial spectrum, TR was slightly reduced to shorten the acquisition duration. Siemens *GRE Brain* shim procedure followed by manual shimming was performed to achieve a water linewidth < 15 Hz for the small voxel, and < 20 Hz for the large voxel, respectively, as indicated by the inline interactive display on the console.

Data processing, Quantification & Spectral Quality Metrics

Two different modeling algorithms were used to quantify the 3-ppm GABA+ resonance of all difference spectra of the *in silico* and *in vivo* data. Both quantification tools are commonly used for GABA+ quantification. Additionally, both tools are freely available and allow fully automated processing to reduce effects of user interaction. Furthermore possible differences in frequency and time domain fitting could be determined by choosing those quantification tools. In the simulations, the estimation error (GABA+$_{error}$) of the model was defined as the rounded absolute value of the relative difference between the modeled GABA+ resonance in the template spectrum for each

141

8

quantification tool, i.e. the ground truth GABA+$_{GT}$, and the modeled GABA+ resonances of the manipulated spectra GABA+$_{Area}$ for each quantification tool:

$$GABA +_{error}(\%) = \left| \frac{GABA +_{Area} * 100}{GABA +_{GT}} - 100 \right|$$

GABA+ areas that were calculated to be outside of a range between ± 3 SD = 36 % [15] from the ground truth GABA+ area were rejected. *In vivo* spectra were quantified using GABA+/Creatine ratios. The two different data processing and quantification pipelines for Gannet 3.0 and Tarquin are described in detail below.

Gannet 3.0

The analysis with the MATLAB-based toolbox Gannet 3.0 [20], which is specifically developed for GABA+ quantification, included by default spectral registration for frequency- and phase-correction of the individual transients, automated rejection of corrupted transients, zero-filling to 32,768 data points and 3-Hz exponential line broadening. The combined GABA-Glx model included parameters to model a single Gaussian peak for the 3-ppm GABA+, a double Gaussian peak for the co-edited 3.75 ppm Glx resonances, as well as baseline parameters with linear, sine, and cosine terms in the difference spectrum. GABA+ fit errors as a measurement of the quality of the individual fit are given (in percent) as the ratio of the standard deviation of the residual over the fitting range (2.79 – 3.55 ppm) and the GABA+ peak area.

Tarquin

Data pre-processing with FID-A

The MATLAB-based toolbox FID-A was used for individual frequency- and phase-correction of the individual transients of the *in vivo* data using the spectral registration algorithm [30], and automated rejection of corrupted transients, both of which are not implemented in Tarquin itself. Alignment and rejection parameters were chosen analogously to the Gannet 3.0 implementation. No additional zero-filling or line broadening was applied. No separate frequency- and phase-correction was applied for the *in silico* data, as the ON and OFF sub-spectra were assumed to be aligned. The processed spectra were analyzed with Tarquin [33] as described in the following.

142

9

Fitting with Tarquin

Analysis with Tarquin [33] included residual water removal by HSVD, automatic phasing and referencing of the 2.01-ppm NAA signal. The quantification is performed with an internally calculated MEGA-PRESS basis set via non-linear least squares fitting in the time domain. This basis set models the GABA+ resonance as two separate Gaussian peaks scaled as 1 proton each, i.e. as a pseudo-doublet at 2.95 and 3.04 ppm. The first 10 points of the time domain data are truncated during the initial fitting, as suggested in the documentation of Tarquin. Afterwards, the differences between metabolite signal of the fit which is extrapolated to t = 0 and the full data is used to estimate the baseline. To allow a direct comparison of the modeling, a GABA+ fit error was calculated analogously to Gannet 3.0. Additionally, a macromolecule correction factor of 0.5 was applied.

Spectral Quality Metrics

To analyze the results of the simulations, several spectral quality metrics were included in the analysis: (i) the mean of the estimation error (GABA+$_{error}$) calculated over the 100 simulated spectra per combination as difference from the known GABA+ model amplitude was examined as a unique characteristic of the present study – which is usually unknown –, to determine the reliability of the GABA+ modeling; (ii) the fit error (GABA+$_{fit}$) as a common quality metric, some sort of which is usually provided by each tool; (iii) the standard deviation (GABA+$_{SD}$) of the GABA+ quantification of the 100 simulated spectra per combination. GABA+$_{SD}$ reflects a measure of variance of the modeling introduced by the underlying SNR and linewidth changes. Higher GABA+$_{SD}$ imply increasing susceptibility to SNR and linewidth changes of the modeling approach. Finally, the number of rejected spectra was considered as a measure of severe outliers in the modeling due to SNR and linewidth changes. GABA+ areas that were calculated to be outside of a range between ± 3 SD = 36 % [15] from the ground truth GABA+ area were rejected. Within *in vivo* studies, these outliers are not exclusively driven by the factors mentioned above, but also by patient movement or frequency drift, as well as biological GABA variance and voxel placement inconsistencies not considered in this study. Additionally, the Pearson correlation coefficient r between the quantified 3-ppm GABA+ amplitudes for Gannet 3.0 and Tarquin was calculated across all parameter combinations.

143

10

1
2
3
4
5
6
7
8
9
10
11
12
13
14
15
16
17
18
19
20
21
22
23
24
25
26
27
28
29
30
31
32
33
34
35
36
37
38
39
40
41
42
43
44
45
46
47
48
49
50
51
52
53
54
55
56
57
58
59
60

The diagrams (**Figure 4 - 6**) are designed as follows: The y axis represents the 61 possible GABA+ SNR levels, the x axis shows the seven possible creatine linewidth values in Hz, and the color map displays the analyzed spectral quality metric.

Results

In silico quantification

The four analyzed quality metrics for the modeling via Gannet 3.0 are depicted in **Figure 4**. Nearly over the entire GABA+ SNR range, the estimation error GABA+$_{error}$ is lower than 5 % for creatine linewidths smaller than 9.7 Hz (**Figure 4 A**), and remains between 5 and 10 % for creatine linewidths between 9.7 to 10.6 Hz. For creatine linewidths larger than 10.6 Hz, GABA+$_{error}$ exceeds 10 %. The fit error, GABA+$_{fit,}$ and the standard deviation across all 100 simulated spectra, GABA+$_{SD,}$ are mainly affected by changes in GABA+ SNR (**Figure 4 B** & **Figure 4 C**). GABA+$_{fit}$ is smaller than 5 % for GABA+ SNR smaller than 7.2, and remains between 5 and 15 % for GABA+ SNR in the range of 7.2 to 2.5. For GABA+ SNR smaller than 2.5, the fitting error is between 15 and 20 %, which is only exceeded for creatine linewidths larger than 12.6 Hz. For GABA+ SNR larger than 4.3 the fitting error increases approximately 1 % over the whole range of creatine linewidths, while for GABA+ SNR smaller than 4.3 it increases approximately 2 % over the whole range of creatine linewidths. GABA+$_{SD}$ smaller than 5 % is observed for GABA+ SNR larger than 11.1, while it ranges between 5 and 15 % for GABA+ SNR in the range of 11.1 to 5.4. For GABA+ SNR smaller than 5.4 a standard deviation ranging from 15 to 22 % is visible (**Figure 4 D**). Less than 10 % of the data were rejected for GABA+ SNR larger than 5.4, while up to 30 % of the data were rejected for GABA+ SNR ranging from 5.3 to 3.2. Up to 60 % of the data were rejected for GABA+ SNR smaller than 3.2.

Figure 5 illustrates the four analyzed quality metrics for the modeling via Tarquin. Over the whole GABA+ SNR range GABA+$_{error}$ smaller than 5 % is observed (**Figure 5 A**). A deviation of larger than 5 % is observed for creatine linewidth = 11.6 Hz and GABA+ SNR between 3.6 and 3.2. As with Gannet 3.0 GABA+$_{fit}$ and GABA+$_{SD}$ are mainly affected by changes in GABA+ SNR (**Figure 5 B** & **Figure 5 C**). GABA+$_{fit}$ ranges from 6 to 30 % for GABA+ SNR levels between 92.3 and 5.4. For GABA+ SNR smaller than 5.4 it has a range from 30 to 104 %. For GABA+ SNR larger than 3.6 the fitting error increases approximately 5 % over the whole range of creatine linewidths, while for GABA+ SNR smaller than 5.4 it increases approximately 14 % over the whole range of creatine linewidths. For GABA+ SNR larger than 5.4 GABA+$_{SD}$ smaller than 95 % is

12

observed, while it ranges between 5 and 19 % for GABA+ SNR smaller than 5.4. For GABA+ SNR smaller than 2.1 GABA+$_{SD}$ ranges from 15 to 18 %. Less than 5 % of the data were rejected for GABA+ SNR larger than 2.5, while up to 17 % of the data were rejected for GABA+ SNR smaller than 2.5 (**Figure 5 D**).

The correlation coefficient r between the model estimates with Gannet 3.0 and Tarquin are presented in **Figure 6**. Clusters of combinations with strong (r > 0.5), medium (r > 0.3), and small (r > 0.1) correlation are observable. For GABA+ SNR larger than 5.4 and creatine linewidth smaller than 11.6 Hz a strong correlation can be observed, while only very weak correlations between the two methods result for GABA+ SNR smaller than 2.5. The remaining clusters appear to have a medium correlation.

In vivo quantification
Based on the defined outlier criteria, data from the small voxels were excluded in three participants, while all data from the large voxels remained in the analysis. In the Big GABA dataset, three participants were excluded for the modeling with Gannet, and one was excluded for the modeling with Tarquin.

Figure 7 illustrates the mean spectra and their standard deviation (SD) of the small (**Figure 7 A**) and the large *in vivo* voxel (**Figure 7 C**). The mean and SD of the fits and the residual of both quantification tools are depicted in **Figure 7 B** and **D** for the small and the large voxel, respectively. The lower SNR of the small voxel becomes apparent in a higher SD of the mean spectra, fits, and residue.

In the small voxel, the following characteristics become apparent: Gannet 3.0 appears to have a smaller SD within the fits, while the mean GABA+ fits are comparable in the height. The model of the GABA+ is notably broader for Tarquin due to the double Gaussian model. The SD of the residual is higher for Tarquin as no line broadening was applied.

For the large voxel, Gannet 3.0 has a smaller SD for the fits than Tarquin. The SD of the residual is low for both quantification tools and does not feature clear residual metabolite peaks in the 3-ppm GABA+ peak area.

13

Figure 8 shows the quantification results and quality metrics of the *in vivo* measurements. The estimated GABA+/Cr values were systematically higher with Tarquin (**Figure 8 A**). The coefficient of variance (CoV) is lower for Gannet than for Tarquin in the small voxel (Gannet 3.0: 29 %; Tarquin: 30 %), while it is higher for Gannet than for Tarquin in the large voxel (Gannet 3.0: 25 %; Tarquin: 14 %). For both voxels, the fitting error and its standard deviation are higher for Tarquin than for Gannet 3.0 (**Figure 8 B**). GABA+ SNR (**Figure 8 C**) and creatine linewidth (**Figure 8 D**) are higher within the larger voxel.

For the small voxel, no significant correlation was found between the GABA+/Cr ratios determined by Gannet 3.0 and Tarquin (r = .18; p = .65) (**Figure 9 A**), while a significant correlation was found for the large voxel (r = .54; p < .05) (**Figure 9 B**).

Comparing in vivo and in silico data

Both datasets are largely congruent in the measures of fit error and rejects; however, the precise numbers are only comparable in the order of a magnitude. The data distribution differs strongly between the *in silico* and the *in vivo* results. An estimation error for the different in vivo voxels was predicted by reading out the estimation error for a specific creatine linewidth and GABA+ SNR from the simulations. **Table 1** compares the simulations to the *in vivo* measurements.

Discussion

This study analyzed the influence of different SNR and linewidths of MEGA-PRESS spectra in order to identify recommendations for GABA spectroscopy studies.

In the first part, the effect of diminishing spectral quality on MEGA-PRESS spectroscopy, mimicked by artificial SNR and line broadening manipulations, was investigated in 427 different noise and creatine linewidth combinations with 100 simulated spectra for each possible combination. The GABA+ peaks of the difference spectra were modeled with two commonly used quantification tools (Gannet 3.0 and Tarquin). The GABA+$_{error}$ was calculated as the deviation from the known 3-ppm GABA+ resonance, and common quality metrics (fit error, standard deviation, and rejects) were determined.

All evidence combined, reliable GABA+ modeling is possible for GABA+ SNR > 3.2 and creatine linewidth < 9.7 Hz, which possess 14 % of the GABA+ SNR compared to the 27 ml / 10 min acquisition proposed in literature [34]. The estimation error (i.e. the deviation from the known GABA+ amplitude) does not exceed 5 % for Gannet 3.0 and Tarquin for these scenarios. However, for GABA+ SNR in the range of 5.4 to 2.5, GABA+$_{SD}$ increases by 5 % for Gannet 3.0 and 11 % for Tarquin. Therefore, studies with lower GABA+ SNR are hampered by a loss of statistical power to detect small GABA+ changes with low effect sizes. Finally, GABA+ SNR changes at constant creatine linewidths are more critical to the GABA+ quantification than changes in the creatine linewidth at constant GABA+ SNR. For Tarquin, an estimation error of < 5 % was measured for creatine linewidths < 11.6 Hz, while it ranges from 5 to 10 % for Gannet 3.0 for the same scenarios. This implies time domain fitting to be less susceptible to linewidth change than frequency domain fitting. Thus, the choice of the quantification algorithm should especially considered during investigation of regions which are susceptible to linewidth changes – e.g. the frontal cortices and thalamus.

Firstly, GABA+$_{fit}$ is not related to GABA+$_{error}$. Therefore, the real deviation from the ground truth cannot be judged by the fit quality [29] or other commonly used quality metrics for MRS. This fact should be considered carefully during the determination of the best algorithm to use for fitting the GABA+ resonance. Secondly, reliable GABA+

15

modeling is highly dependent on the quantification tool. The estimation error $GABA+_{error}$ exhibits differences between tools. $GABA+_{error}$ <5% was rarely exceeded for Tarquin, while it is passed by Gannet 3.0 for creatine linewidths > 10.6 Hz. Thirdly, creatine linewidths affected $GABA+_{error}$ only for very high GABA+ SNR values, while the effects on the fit error $GABA+_{fit}$, the standard deviation of GABA+ estimates $GABA+_{SD}$, and the number of rejects were negligible. This implies that B0 field homogeneity is, within commonly encountered ranges, not that critical criterion for accurate modeling of the GABA+ resonance. SNR needs to be considered more carefully, which is in agreement with literature [17]. Fourthly, $GABA+_{SD}$ differs between the quantification tools, with Tarquin presenting lower $GABA+_{SD}$ than Gannet 3.0. This implies that the group variance of *in vivo* measurements – apart from biological variation within an *in vivo* cohort or variance introduced by changes in the voxel positioning – depends on the used quantification algorithm. Therefore, comparably small effect sizes could be obscured by variations introduced by the quantification tool. Despite the differences in the quality metrics, a strong correlation was found between the GABA+ model estimates of both quantification tools for reasonable GABA SNR > 4.3 and creatine linewidth < 11.6 Hz. A medium correlation was found over a relatively broad range of conditions. This indicates a good agreement between the different model algorithms. Finally, the results illustrate that the commonly used quality metrics do not allow conclusions about the real estimation error $GABA+_{error}$.

In the second part of this study, 14 *in vivo* datasets were acquired in two thalamic voxels of different sizes as this region is known to be complex for MRS. Afterwards, these spectra, as well as the data from the multi-site study [15], on which the template spectrum was based, were compared with the simulations. Additionally, an estimated $GABA+_{error}$ was determined. As there is a good agreement between the *in vivo* and the simulation dataset, the simulation may be used as an indicator either to judge the data quality of an already conducted study, or to classify a voxel conducted in a pilot measurement during study design. Future investigations should be executed to clarify, if the apparent differences in the data distribution between the *in silico* and the *in vivo* datasets could be interpreted as a variation solely attributed to biological variation. Additionally, it would be of interest to investigate the threshold noise level where significant differences remain

16

visible. Therefore, the simulation space could be extended with different amplitudes of the GABA+ peak in the template spectrum. This approach would require a more sophisticated template spectrum as proposed here.

Our results regarding the impact of GABA+ SNR on the group-level variance tally with a recent study on the design of GABA+-edited studies [17]. Both studies indicate a reduction in quality gain, in terms of lower GABA+$_{SD}$, for higher GABA+ SNR levels. The GABA+ SNR of the large voxel in the present study is comparable to a 27-ml voxel with 320 averages, while the small voxel is comparable to 27-ml with 96 averages. As a conclusion of the *in silico* and *in vivo* measurements, GABA+-edited data reaches reliable quantification and reasonable group-level variance for 27-ml voxels with averages ranging from 128 and 210 compared to the commonly used 320.

By comparing the results of the small *in vivo* voxel and the simulations with similar GABA+ SNR values, further conclusions can be drawn. The CoV is considerably higher for low GABA+ SNR and depends on the quantification tool. Finally, the number of rejected spectra increases for lower GABA+ SNR, which must be considered in studies with small voxels. Our results indicate that GABA+-edited data exhibiting a fit error larger than 15 % lead to reliable spectra. Data rejection criteria should not exclusively be defined by GABA+ SNR or fit errors, but rather by considering the standard deviation of the quantified GABA signal. Assuming GABA concentrations to be similar within one group – considering biological variability and pathologies to be consistent within that group – data quality estimation and outlier detection should be supported by GABA+$_{SD}$.

Aside from the general knowledge gained about the impact of SNR and linewidth on GABA+-edited data, the present study provides insights on the performance of different quantification tools. The simulation approach presented within the work at hand could be used to determine the performance of other quantification tools. Further studies on the performance of the common quantification tools are needed to fully understand the differences between the analytic methods, which could be achieved by using benchmark datasets collected in the 'Big GABA' multi-site studies [15].

17

Conclusion

This study suggests that GABA+-edited studies might be realized for voxels with low
GABA+ SNR at the cost of a higher group-level variance. Within the tested range the
effect of decreasing GABA+ SNR at constant linewidth is more critical than the effect of
increasing linewidth at constant GABA+ SNR. This is dependency occurs especially for
time domain fitting. Additionally, no relation between commonly reported quality metrics
and GABA+ modeling accuracy was found. Group variance induced by different
quantification tools introduces additional unknown uncertainty, which might obscure
group differences with small effect sizes in GABA+.

18

Acknowledgement

152

References

1. Puts NAJ, Edden RAE. In vivo magnetic resonance spectroscopy of GABA: a methodological review. *Prog Nucl Magn Reson Spectrosc*. 2012;60:29-41. doi:10.1016/j.pnmrs.2011.06.001

2. Mescher M, Merkle H, Kirsch J, Garwood M, Gruetter R. Simultaneous in vivo spectral editing and water suppression. *NMR Biomed*. 1998;11(6):266-272. doi:10.1002/(SICI)1099-1492(199810)11:6<266::AID-NBM530>3.0.CO;2-J

3. Henry PG, Dautry C, Hantraye P, Bloch G. Brain gaba editing without macromolecule contamination. *Magn Reson Med*. 2001;45(3):517-520. doi:10.1002/1522-2594(200103)45:3<517::AID-MRM1068>3.0.CO;2-6

4. Puts NAJ, Edden RAE, Evans CJ, McGlone F, McGonigle DJ. Regionally specific human GABA concentration correlates with tactile discrimination thresholds. *J Neurosci*. 2011;31(46):16556-16560. doi:10.1523/JNEUROSCI.4489-11.2011

5. Muthukumaraswamy SD, Edden RAE, Jones DK, Swettenham JB, Singh KD. Resting GABA concentration predicts peak gamma frequency and fMRI amplitude in response to visual stimulation in humans. *Proc Natl Acad Sci U S A*. 2009;106(20):8356-8361. doi:10.1073/pnas.0900728106

6. Gao F, Edden RAE, Li M, et al. Edited magnetic resonance spectroscopy detects an age-related decline in brain GABA levels. *Neuroimage*. 2013;78:75-82. doi:10.1016/j.neuroimage.2013.04.012

7. Porges EC, Woods AJ, Edden RAE, et al. Frontal Gamma-Aminobutyric Acid Concentrations Are Associated With Cognitive Performance in Older Adults. *Biol Psychiatry Cogn Neurosci Neuroimaging*. 2017;2(1):38-44. doi:10.1016/j.bpsc.2016.06.004

8. Maes C, Hermans L, Pauwels L, et al. Age-related differences in GABA levels are driven by bulk tissue changes. *Hum Brain Mapp*. 2018;39(9):3652-3662. doi:10.1002/hbm.24201

9. Bollmann S, Ghisleni C, Poil SS, et al. Developmental changes in gamma-aminobutyric acid levels in attention-deficit/hyperactivity disorder. *Transl Psychiatry*. 2015;5(6):e589-e589. doi:10.1038/tp.2015.79

10. Mostofsky SH, Puts NAJ, Tommerdahl M, et al. Reduced GABAergic inhibition and abnormal sensory symptoms in children with Tourette syndrome. *J Neurophysiol*. 2015;114(2):808-817. doi:10.1152/jn.00060.2015

11. Foerster BR, Petrou M, Mohamed MA, et al. An Imbalance Between Excitatory and Inhibitory Neurotransmitters in Amyotrophic Lateral Sclerosis Revealed by Use of 3-T Proton Magnetic Resonance Spectroscopy. *JAMA Neurol*. 2013;70(8):1009. doi:10.1001/jamaneurol.2013.234

12. Oeltzschner G, Zöllner HJ, Jonuscheit M, Lanzman RS, Schnitzler A, Wittsack H-J. J-difference-edited MRS measures of γ-aminobutyric acid before and after acute caffeine administration. *Magn Reson Med*. 2018. doi:10.1002/mrm.27233

20

13. Edden RAE, Oeltzschner G, Harris AD, et al. Prospective frequency correction for macromolecule-suppressed GABA editing at 3T. *J Magn Reson Imaging*. 2016;44(6):1474-1482. doi:10.1002/jmri.25304

14. Harris AD, Glaubitz B, Near J, et al. Impact of frequency drift on gamma-aminobutyric acid-edited MR spectroscopy. *Magn Reson Med*. 2014;72(4):941-948. doi:10.1002/mrm.25009

15. Mikkelsen M, Barker PB, Bhattacharyya PK, et al. Big GABA: Edited MR spectroscopy at 24 research sites. *Neuroimage*. 2017;159:32-45. doi:10.1016/j.neuroimage.2017.07.021

16. Mikkelsen M, Rimbault DL, Barker PB, et al. Big GABA II: Water-referenced edited MR spectroscopy at 25 research sites. *Neuroimage*. 2019;191:537-548. doi:10.1016/J.NEUROIMAGE.2019.02.059

17. Mikkelsen M, Loo RS, Puts NAJ, Edden RAE, Harris AD. Designing GABA-edited magnetic resonance spectroscopy studies: Considerations of scan duration, signal-to-noise ratio and sample size. *J Neurosci Methods*. 2018;303:86-94. doi:10.1016/J.JNEUMETH.2018.02.012

18. Yasen AL, Smith J, Christie AD. Glutamate and GABA concentrations following mild traumatic brain injury: a pilot study. *J Neurophysiol*. 2018;120(3):1318-1322. doi:10.1152/jn.00896.2017

19. Provencher SW. Automatic quantitation of localized in vivo1H spectra with LCModel. *NMR Biomed*. 2001;14(4):260-264. doi:10.1002/nbm.698

20. Edden RAE, Puts NAJ, Harris AD, Barker PB, Evans CJ. Gannet: A batch-processing tool for the quantitative analysis of gamma-aminobutyric acid-edited MR spectroscopy spectra. *J Magn Reson Imaging*. 2014;40(6):1445-1452. doi:10.1002/jmri.24478

21. Slotboom J, Nirkko A, Brekenfeld C, Van Ormondt D. Reliability testing of in vivo magnetic resonance spectroscopy (MRS) signals and signal artifact reduction by order statistic filtering. *Meas Sci Technol*. 2009;20(10):104030. doi:10.1088/0957-0233/20/10/104030

22. Bartha R. The Effect of Signal to Noise Ratio and Linewidth On 4T Short Echo Time 1H MRS Metabolite Quantification. *Proc 13th Sci Meet Int Soc Magn Reson Med*. 2005;216(1):2459-2459. https://cds.ismrm.org/ismrm-2005/Files/02459.pdf. Accessed July 31, 2019.

23. Wijtenburg S, Knight-Scott J. *The Impact of SNR on the Reliability of LCModel and QUEST Quantitation in 1H-MRS*. Vol Honolulu.; 2009. /MyPathway2009/2401. Accessed August 6, 2019.

24. Otazo R, Mueller B, Ugurbil K, Wald L, Posse S. Signal-to-noise ratio and spectral linewidth improvements between 1.5 and 7 Tesla in proton echo-planar spectroscopic imaging. *Magn Reson Med*. 2006;56(6):1200-1210. doi:10.1002/mrm.21067

25. Geramita M, van der Veen JW, Barnett AS, et al. Reproducibility of prefrontal γ-aminobutyric acid measurements with J-edited spectroscopy. *NMR Biomed*.

154

2011;24(9):1089-1098. doi:10.1002/nbm.1662

26.   O'Gorman RL, Michels L, Edden RAE, Murdoch JB, Martin E. In vivo detection of
       GABA and glutamate with MEGA-PRESS: Reproducibility and gender effects. *J
       Magn Reson Imaging*. 2011;33(5):1262-1267. doi:10.1002/jmri.22520

27.   Near J, Andersson J, Maron E, et al. Unedited in vivo detection and quantification
       of γ-aminobutyric acid in the occipital cortex using short-TE MRS at 3T. *NMR
       Biomed*. 2013;26(11):1353-1362. doi:10.1002/nbm.2960

28.   Hancu I, Port J. The case of the missing glutamine. *NMR Biomed*. 2011;24(5):529-
       535. doi:10.1002/nbm.1620

29.   Dhamala E, Abdelkefi I, Nguyen M, Hennessy TJ, Nadeau H, Near J. Validation of
       in vivo MRS measures of metabolite concentrations in the human brain. *NMR
       Biomed*. January 2019:e4058. doi:10.1002/nbm.4058

30.   Near J, Edden RAE, Evans CJ, Paquin R, Harris AD, Jezzard P. Frequency and
       phase drift correction of magnetic resonance spectroscopy data by spectral
       registration in the time domain. *Magn Reson Med*. 2015;73(1):44-50.
       doi:10.1002/mrm.25094

31.   Simpson R, Devenyi GA, Jezzard P, Hennessy TJ, Near J. Advanced processing
       and simulation of MRS data using the FID appliance (FID-A)—An open source,
       MATLAB-based toolkit. *Magn Reson Med*. 2017;77(1):23-33.
       doi:10.1002/mrm.26091

32.   World Medical Association declaration of Helsinki: Ethical principles for medical
       research involving human subjects. *JAMA - J Am Med Assoc*. 2013;310(20):2191-
       2194. doi:10.1001/jama.2013.281053

33.   Wilson M, Reynolds G, Kauppinen RA, Arvanitis TN, Peet AC. A constrained
       least-squares approach to the automated quantitation of in vivo 1 H magnetic
       resonance spectroscopy data. *Magn Reson Med*. 2011;65(1):1-12.
       doi:10.1002/mrm.22579

34.   Mullins PG, McGonigle DJ, O'Gorman RL, et al. Current practice in the use of
       MEGA-PRESS spectroscopy for the detection of GABA. *Neuroimage*. 2014;86:43-
       52. doi:10.1016/j.neuroimage.2012.12.004

Tables

	creatine linewidth [Hz]	GABA+ SNR	estimation error [%]		fit error [%]		distribution [%]		rejects [%]	
			in silico	*in vivo*	*in silico*	*in vivo*	*in silico* (SD)	*in vivo* (CoV)	*in silico*	*in vivo*
Big GABA	7.9	24.4								
Gannet	-	-	0.3	-	3.1	4.0	2.7	10.4	9	6.25
Tarquin	-	-	0.1	-	6.0	5.7	1.4	14.7	0	2
Small voxel	9.5	3.6								
Gannet	-	-	7.3	-	11.8	19.3	19.8	29.9	27	21
Tarquin	-	-	0.1	-	11.5	14.9	10.8	31.6	0	21
Large voxel	10.4	8.4								
Gannet	-	-	7.1	-	5.6	8.6	11.4	25.2	7	0
Tarquin	-	-	3.6	-	7.7	5.7	4.1	15.1	0	0

Table 1 – Comparison between the GABA+ quantification of the simulations (in silico) and the in vivo measurements including the Big GABA data as well as the data measured in the present study. The data distribution is reported as standard deviation (SD) for the simulations and as coefficient of variance (CoV) for the in vivo measurements The estimation error from the different voxels were predicted from the estimation error of the simulations for a specific creatine linewidth and GABA+ SNR.

Figure captions

Figure 1 – Template spectrum and spectral manipulation. A) Template ON/OFF spectra and resulting difference spectrum (magnified by a factor of 10) B). Quantified 3-ppm GABA+ resonance of the artificial difference spectrum without noise or line broadening (Gannet 3.0 left & Tarquin right). C) Mean creatine linewidth for all conditions. D) Mean GABA+ signal-to-noise ratio for all conditions. Mean GABA+ SNR and mean creatine linewidths measured with FID-A are depicted in C and D.

Figure 2 – Example raw 3-ppm GABA+ resonances. Frequency- and Phase-corrected 3-ppm GABA+ resonances without apodization or zero-filling for representative conditions. All 7 levels of creatine (Rows) and 13 representative noise levels (Columns) are depicted.

Figure 3 – Thalamic voxel position on representative T1-weighted image. A) Small voxel with V = (2 x 2 x 2) ml = 8 ml. B) Large voxel with V = (30 (AP) x 35 (LR) x 25 (HF)) ml = 26.25 ml.

Figure 4 – Quality metrics of 3-ppm GABA+ modeling with Gannet 3.0. Each metric is analyzed for all 427 conditions with 100 spectra per condition. A) Mean deviation from the known GABA+ resonance in % (GABA+$_{error}$). B) Mean fit error (GABA+$_{fit}$). C) Standard deviation of the model estimate (GABA+$_{SD}$). D) Number of rejected spectra (GABA+$_{rejects}$).

Figure 5 – Quality metrics of 3-ppm GABA+ modeling with Tarquin. Each metric is analyzed for all 427 conditions with 100 spectra per condition. A) Mean deviation from the known GABA+ resonance in % (GABA+$_{error}$). B) Mean fit error (GABA+$_{fit}$). C) Standard deviation of the model estimate (GABA+$_{SD}$). D) Number of rejected spectra (GABA+$_{rejects}$).
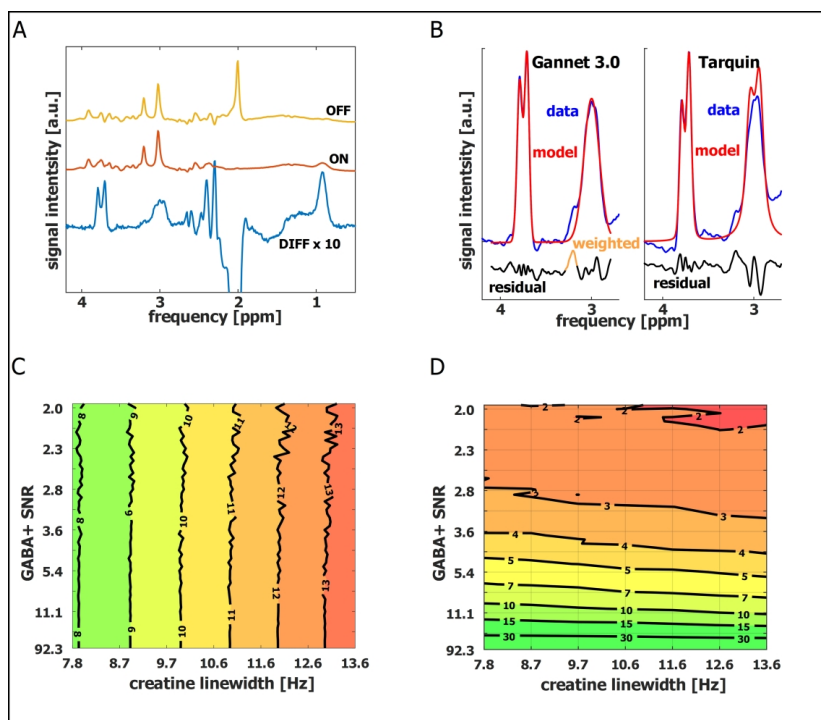
Figure 6 – Correlation coefficient r between the model estimates of Gannet 3.0 and Tarquin. The correlation analysis is performed between the 100 spectra of each condition. Areas with strong (r > 0.5), medium (r > 0.3), and small (r > 0.1) correlations are marked.

Figure 7 – In vivo spectra of the small (A and B) and large (C and D) voxel. Mean spectra, fit and residue are indicated through solid lines. Spectra, fit, and residue standard deviations are indicated through the shaded areas. The left column contains the mean spectra of both voxels, as well as the voxel positioning in the thalamus. The right column depicts the fitting results of the two quantification tools.

Figure 8 – In vivo GABA+ quantification. A) Distribution of GABA+-to-Cr ratios for the two voxels and two quantification tools. Successful quantifications (n) and the coefficient of variance (CoV) are reported in A. B) Distribution of fit errors for the two voxels and two quantification tools. C) Distribution of GABA+ SNR for the two voxels. D) Distribution of creatine linewidths for the two voxels. Dots indicate individual measurements.

Figure 9 – In vivo GABA+-to-Cr ratio correlation between the model estimates of Gannet 3.0 and Tarquin. A) Correlation analysis for the small voxel. B) Correlation analysis for the large voxel.
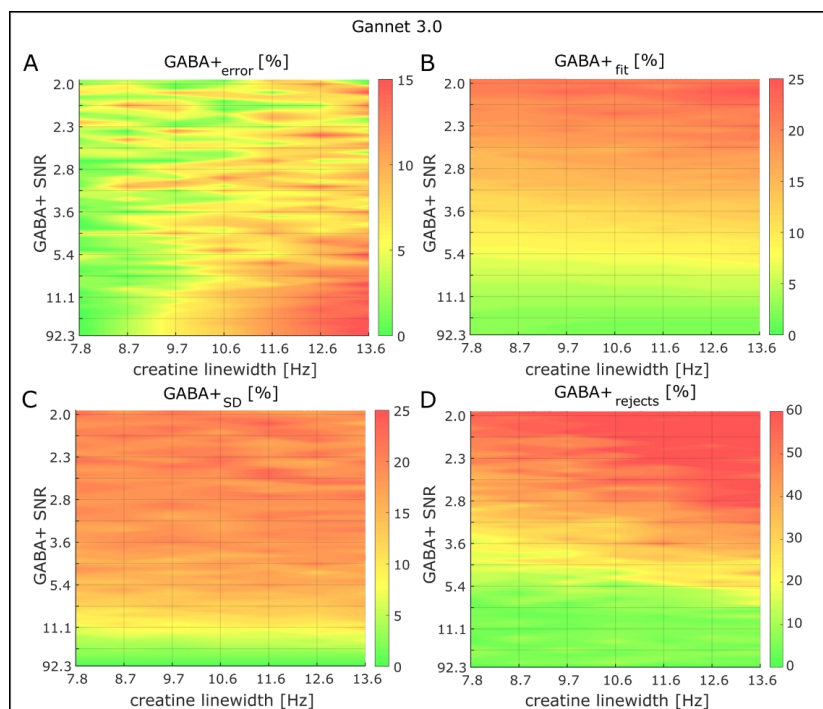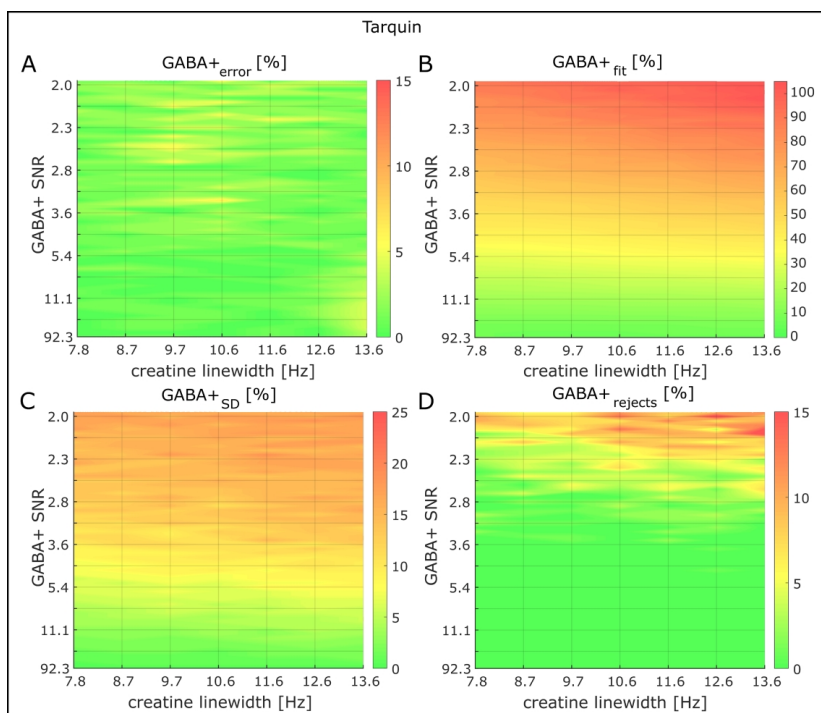
Template spectrum and spectral manipulation. A) Template ON/OFF spectra and resulting difference spectrum (magnified by a factor of 10) B). Quantified 3-ppm GABA+ resonance of the artificial difference spectrum without noise or line broadening (Gannet 3.0 left & Tarquin right). C) Mean creatine linewidth for all conditions. D) Mean GABA+ signal-to-noise ratio for all conditions. Mean GABA+ SNR and mean creatine linewidths measured with FID-A are depicted in C and D.

173x150mm (600 x 600 DPI)
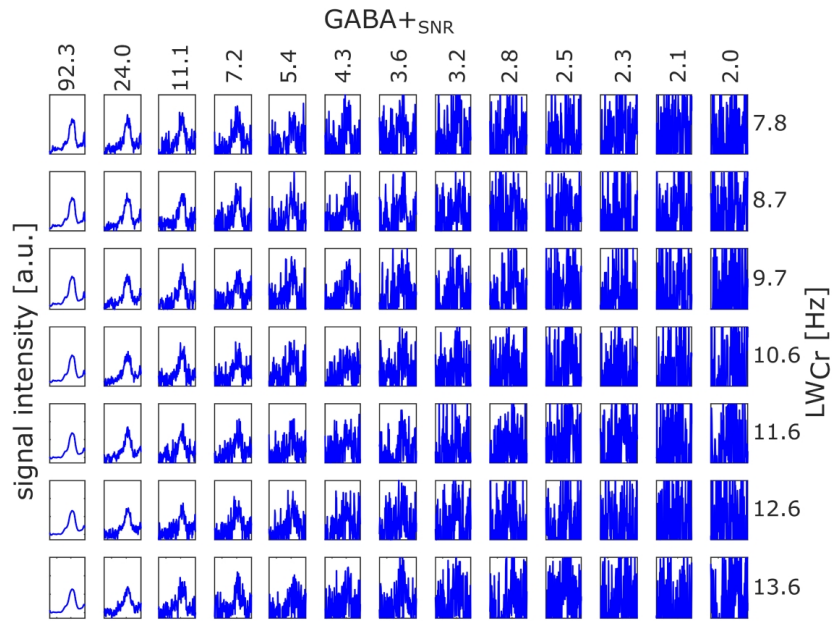
Example raw 3-ppm GABA+ resonances. Frequency- and Phase-corrected 3-ppm GABA+ resonances without apodization or zero-filling for representative conditions. All 7 levels of creatine (Rows) and 13 representative noise levels (Columns) are depicted.

175x139mm (600 x 600 DPI)
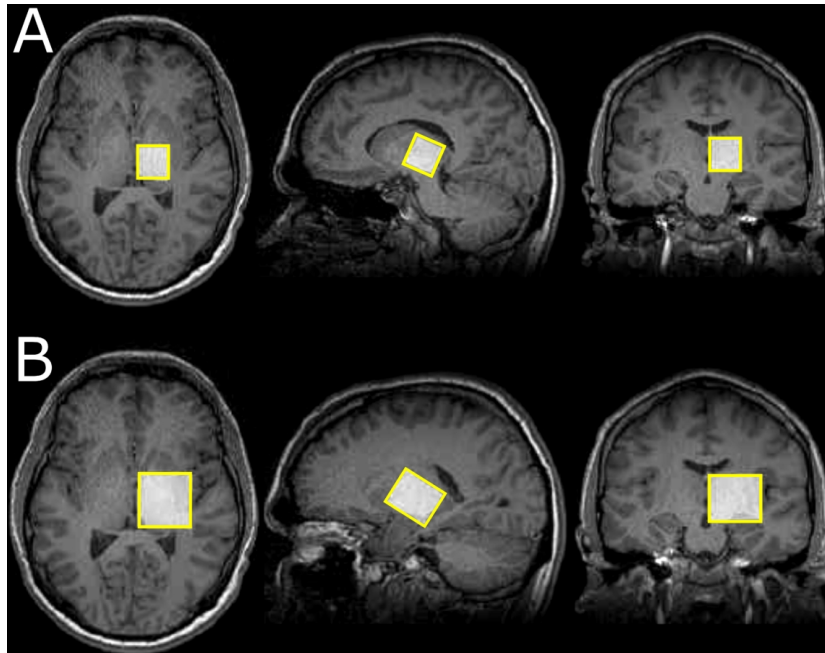
Thalamic voxel position on representative T1-weighted image. A) Small voxel with V = (2 x 2 x 2) ml = 8 ml. B) Large voxel with V = (30 (AP) x 35 (LR) x 25 (HF)) ml = 26.25 ml.

86x68mm (600 x 600 DPI)

1
2
3
4
5
6
7
8
9
10
11
12
13
14
15
16
17
18
19
20
21
22
23
24
25
26
27
28
29
30
31
32
33
34
35
36
37
38
39
40
41
42
43
44
45
46
47
48
49
50
51
52
53
54
55
56
57
58
59
60

Quality metrics of 3-ppm GABA+ modeling with Gannet 3.0. Each metric is analyzed for all 427 conditions with 100 spectra per condition. A) Mean deviation from the known GABA+ resonance in % (GABA+$_{error}$). B) Mean fit error (GABA+$_{fit}$). C) Standard deviation of the model estimate (GABA+$_{SD}$). D) Number of rejected spectra (GABA+$_{rejects}$).

175x149mm (600 x 600 DPI)

Quality metrics of 3-ppm GABA+ modeling with Tarquin. Each metric is analyzed for all 427 conditions with 100 spectra per condition. A) Mean deviation from the known GABA+ resonance in % (GABA+$_{error}$). B) Mean fit error (GABA+$_{fit}$). C) Standard deviation of the model estimate (GABA+$_{SD}$). D) Number of rejected spectra (GABA+$_{rejects}$).

175x149mm (600 x 600 DPI)

1
2
3
4
5
6
7
8
9
10
11
12
13
14
15
16
17
18
19
20
21
22
23
24
25
26
27
28
29
30
31
32
33
34
35
36
37
38
39
40
41
42
43
44
45
46
47
48
49
50
51
52
53
54
55
56
57
58
59
60

Correlation coefficient r between the model estimates of Gannet 3.0 and Tarquin. The correlation analysis is performed between the 100 spectra of each condition. Areas with strong (r > 0.5), medium (r > 0.3), and small (r >0.1) correlations are marked.

86x63mm (600 x 600 DPI)
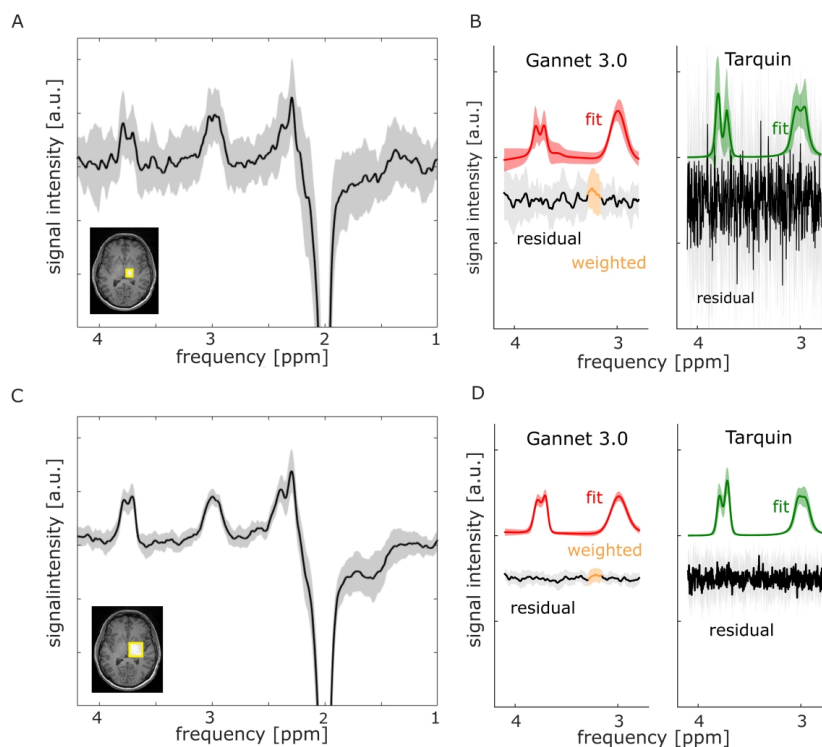
163

E Reprint Study 3

In vivo spectra of the small (A and B) and large (C and D) voxel. Mean spectra, fit and residue are indicated through solid lines. Spectra, fit, and residue standard deviations are indicated through the shaded areas. The left column contains the mean spectra of both voxels, as well as the voxel positioning in the thalamus. The right column depicts the fitting results of the two quantification tools.

175x159mm (600 x 600 DPI)
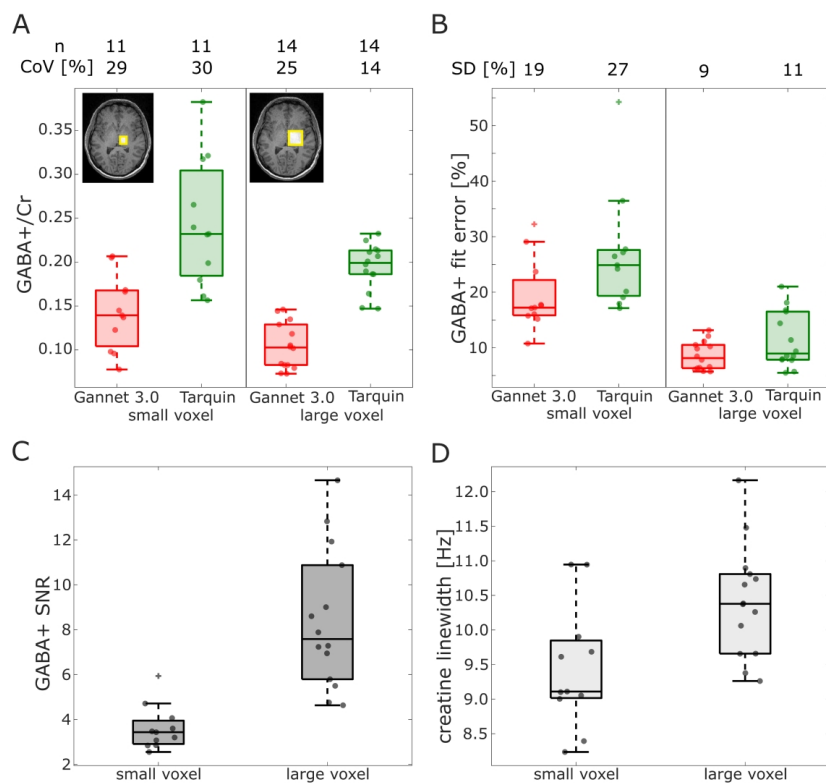
In vivo GABA+ quantification. A) Distribution of GABA+-to-Cr ratios for the two voxels and two quantification tools. Successful quantifications (n) and the coefficient of variance (CoV) are reported in A. B) Distribution of fit errors for the two voxels and two quantification tools.
C) Distribution of GABA+ SNR for the two voxels. D) Distribution of creatine linewidths for the two voxels. Dots indicate individual measurements.

175x164mm (600 x 600 DPI)

1
2
3
4
5
6
7
8
9
10
11
12
13
14
15
16
17
18
19
20
21
22
23
24
25
26
27
28
29
30
31
32
33
34
35
36
37
38
39
40
41
42
43
44
45
46
47
48
49
50
51
52
53
54
55
56
57
58
59
60
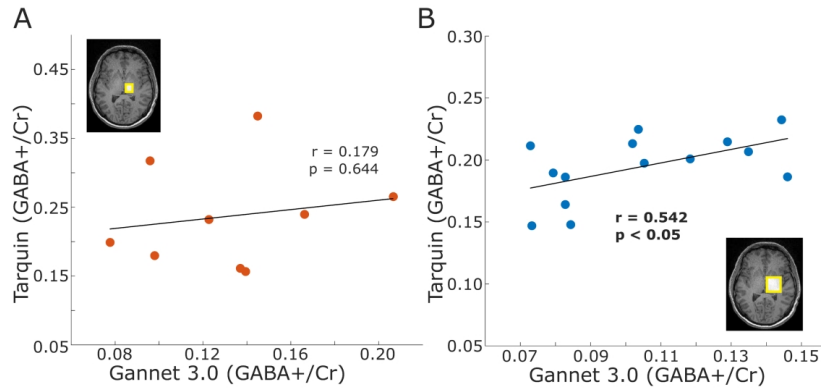
In vivo GABA+-to-Cr ratio correlation between the model estimates of Gannet 3.0 and Tarquin. A) Correlation analysis for the small voxel. B) Correlation analysis for the large voxel.

130x62mm (600 x 600 DPI)

1
2
3
4
5
6
7
8
9
10
11
12
13
14
15
16
17
18
19
20
21
22
23
24
25
26
27
28
29
30
31
32
33
34
35
36
37
38
39
40
41
42
43
44
45
46
47
48
49
50
51
52
53
54
55
56
57
58
59
60

In silico GABA+ MEGA-PRESS: Effects of signal-to-noise ratio and linewidth on modelling the 3-ppm GABA+ resonance – Helge Jörn Zöllner*, Georg Oeltzschner, Alfons Schnitzler, Hans-Jörg Wittsack
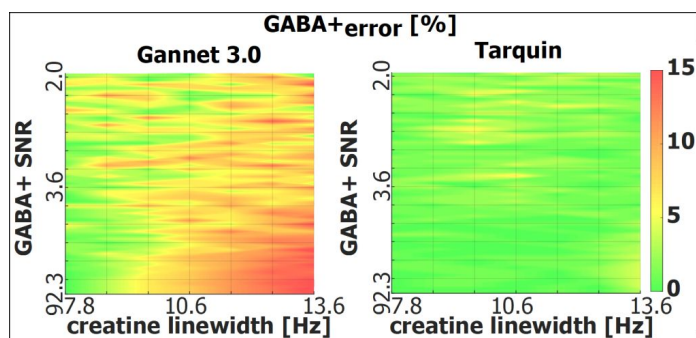
MEGA-PRESS difference spectra with various SNR and linewidth combinations were created by spectral manipulation of a noise free template spectrum and subsequently quantified via Gannet 3.0 and Tarquin. A comparison with the ground truth levels revealed time domain fitting to be more robust against linewidth changes than frequency domain fitting. No relation between the accuracy of the fit and commonly reported quality metrics was found.